THE UNIVERSITY OF HULL

Multiwavelength Photoconductivity of ZnO Nanoparticles Based on Surface Defects and Plasmonics

being a Thesis submitted for the Degree of

Doctor of Philosophy (PhD)

in the School of Mathematics and Physical Sciences,

University of Hull

by

Mohammed A. Ibrahem, B.Sc, M.Sc

October 2017

Declaration of authorship

I declare that the work presented in this thesis entitled "Multiwavelength Photoconductivity of ZnO Nanoparticles Based on Surface Defects and Plasmonics" is undertaken by myself under the supervision of Prof. Mary O'Neill to fulfil the requirements of the University of Hull, Doctor of Philosophy (PhD) degree in Physics. Part of this work is presented and published in the following conference and publication journal respectively:

Conference

- Attending the Material Research Society (MRS) spring meeting in Phoenix 2016, USA- Poster presentation.

Publication

- "Dual-Wavelength (Ultraviolet and Green) Photodetectors Using Solution-Processed Zinc Oxide Nanoparticles", *ACS Appl. Mater. Interfaces* **2017**, *9* (42), 36971–36979.

Professor Mary O'Neill
Dean of the School of Science and Technology
Nottingham Trent University
Nottingham, NG11 8NS
United Kingdom
E-mail: mary.oneill@ntu.ac.uk
Direct Tel: +44 (0)115 848 3281

Abstract

ZnO is distinguished as the semiconductor of choice in a variety of applications such as in optoelectronics and photodetectors owing to its superior light sensitivity, the ease of synthesis in a wide range of nanostructure forms and its tuneable optical and electrical properties. Herein, ZnO photoconductivity is investigated for two purposes; firstly, to assess device stability with different preparation conditions and environments and secondly, to improve and extend photodetection of ZnO into the visible and near-infrared by stimulating surface defects and plasmonics effect.

Persistent photoconductivity resulting from UV irradiation of ZnO NP films is highly affected not only by oxygen adsorption but also by other organic species and water in atmospheric air. The stability of ZnO photodetector is found to be enhanced in terms of current magnitude and sustainable photocurrent cycles when the device is prepared, annealed and tested in a nitrogen environment. A noticeable difference is identified in the ZnO NP surface composition, represented by surface organic complexes when the film is prepared and annealed in air compared to nitrogen. The aforementioned species are found to be removed efficiently in oxidized fabrication environment such as in air while partially decomposed in nitrogen. This enables the ZnO surface to build new organic species and surface carbonates by electrochemical reaction with atmospheric CO_2 leading to promote electrically active defects surface states.

Narrow-band photoconductivity, with a spectral width of 0.16 eV, is obtained by irradiating ZnO NP films using green light. A new model involving electron transfer from deep defects to discrete shallow donors is introduced to explain the narrow spectrum and the exponential form of the current rise and decay transients. The green

photocurrent responsivity can be enhanced by storage in air and this correlates with the formation of carbonate surface species by the capture of carbon dioxide during storage. We successfully demonstrated a solution-processed ZnO NP photodetector using a low-cost and scalable photolithographic approach to fabricate dual (ultraviolet and green) and single (ultraviolet only) wavelength detecting ZnO pixels on the same substrate using the same mask.

We also show that the plasmonic effect can be used to extend the photoconductivity of ZnO NPs into the deep red/infrared spectral region utilizing gold nanoislands as a light absorber and source of hot electrons in a vertical device configuration involving PEDOT: PSS.

To my parents.

Acknowledgments

This thesis would not have been possible to finish without the help and support of many people to whom I'm incredibly grateful. First and foremost, I would like to express my deepest appreciation and sincere gratitude to my supervisors, Prof. Mary O'Neill and Dr Ali Adawi for their insight, guidance and unlimited support all the way through my PhD study.

Prof. O'Neill is a very knowledgeable supervisor and a great advisor and mentor. She provided me with innumerable opportunities and gave me the freedom to work independently. She continually encouraged and supported me, giving me the confidence to explore new options and ideas. I learned a lot from our uncounted meetings and deep discussions over the years. It was a great privilege working closely with you. You will always be my advisor and mentor. Also, thanks for sharing lots of coffee with me, it was my favourite.

I would like also to express my deep appreciation and gratitude to Dr Emanuele Verrelli and Dr Jean-Sebastian Bouillard for their countless help and valuable support. Emanuele has a broad knowledge in experimental physics, I was lucky to have him around during my PhD work. He helped me all the way and was very keen and patient to answer all my questions, both good and stupid ones. Our discussions helped improve my ability and confidence to conduct high-quality experiments. We shared great laboratory time together over the years and a lot of coffee and hot chocolate. Emanuele will always be my mentor and a friend. I also would like to thank Dr Steve Myers for being the first person showing me how to work in the lab and helping me at the earlier

stage of my PhD. I would like to extend my gratitude to Dr Fei Cheng for the synthesis of ZnO nanoparticle solution investigated in this work.

During my five years at Hull, I was lucky to meet incredible people that become very special and close to me. I'm very grateful to Verena Fleischanderl for being very kind and patient with me and supporting me unconditionally right from the start. Her kindness helped me pass through many tough times. For that and more, thank you. I also would like to thank her parents, Theresia and Robert Fleischanderl for their encouragement and hosting me in their lovely and warm home in Austria on many occasions, making me feel at home.

I would like to thank my friends and work colleagues for their help, support and advice in and outside the laboratory: Addison Marshall, William Harrison and Brian Lambert. Addison and I started our PhD together and with time we become close friends. I also would like to extend my gratitude to my friends Hassan Moayed and Jwan Oday for their support and help throughout my stay at Hull.

I would like to take this opportunity to thank Dr Bassam G. Rasheed, my M.Sc supervisor for his help, support and friendship. Thank you for believing in me.

Also, special thanks to all my colleagues and staff in the Physics and Astrophysics research group at the University of Hull to create such a great working environment during the four years of my study. I also would like to extend my sincere gratitude to the Iraqi Ministry of Higher Education and Scientific Research represented in the UK by the Iraqi Cultural Attaché in London and to my home university in Baghdad, University of Technology, for funding my scholarship.

Finally, I would like to express my deep appreciation and gratitude to my parents for believing in me, supporting me all the way and for their invaluable prayers which

enabled me to only meet the good people through my journey. For that and more, thank you.

Imagination is more important than knowledge.

– Albert Einstein

Contents

Chapter 1

Introduction and Background Theory

This chapter introduces some basic theory and physics principles relevant to the topics studied in this thesis. ZnO is the main semiconductor used in this work and therefore, an overview of its optical and electrical properties is given.

1.1 Introduction

In our daily life, photodetectors are considered as the most ubiquitous type of technology that electronic devices use such as in smartphones, computers, wearable and flexible display devices and cameras. However, the rapid advancements in these technologies create a high demand for innovations in device processing and integrations in addition to low production cost accompanied with high device performance. Therefore, metal oxide semiconductors such as ZnO found to meet the requirement due to its novel functionalities, transparency, and wide band gap that can allow low cost and unconventional processing technologies like sol-gel methods which are compatible for integration with flexible and low-temperature processing substrates. The advent of ZnO has revolutionized the electronic devices by moving from rigidly based electronics to a high-end technology based on flexible and transparent electronics which invade the commercial market where oxide-based devices expected to grow to nearly 7.1 billion dollars by 2018 [1].

ZnO has witnessed a resurgence in the last few years as a strong competitive candidate to GaN in optoelectronics and optical display devices. Research on ZnO blossomed in the early 1930s with some initial work on light emission followed by the recording of the first electron diffraction data in 1935 [2,3]. A few years afterwards, the native n-type conductivity in ZnO was confirmed by Hall effect measurements [4]. Following a systematic study on ZnO up to the 1970s, new material properties emerged such as the discovery of the piezoelectric effect and light emitting diodes (LEDs) [5]. Figure 1.1 illustrates the development of research on ZnO and its related materials by showing the number of publications between 1920 and September 2017. The data were collected from ZnO publications registered in ScopusTM. It is clear that the number of publications starts to increase significantly in the early 1990s when a good

understanding of the electrical and optical properties of ZnO was realized, in addition to the big interest in nanotechnology. Hence ZnO was incorporated in different device configurations such as transparent thin film transistors (TFTs), light emitting diodes (LEDs), solid state lasers, varistors, gas sensors and UV photodetectors.

In this chapter, a brief introduction to ZnO structure as well as its optical and electrical properties are presented. Furthermore, the main defects types abundant in ZnO are introduced and briefly reviewed in addition to some practical applications. A general background to the theory behind photodetection in semiconductors is described. Finally, we will discuss work motivation and introduce the thesis structure in brief sections.

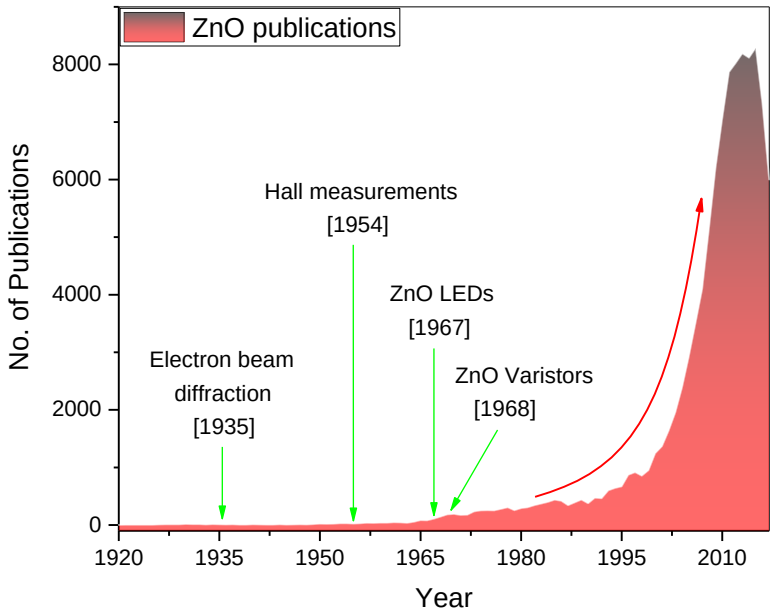

Figure 1.1: The number of publications involving Zinc Oxide (ZnO) per year, from 1920 to September 2017, which are registered in *Scopus* database search engine. 13th Sept. 2017.

1.2 ZnO structure

ZnO is an important semiconductor among the II-VI group, with a wide direct band gap and intrinsic n-type conductivity with an energy gap of 3.37 eV at room temperature and 60 meV exciton binding energy [6]. It crystallizes in three different structure forms;

hexagonal wurtzite, zinc blende and cubic rocksalt. The zinc blende crystalline structure can be stabilized by growing it on cubic substrates, while cubic rocksalt can be formed under high-pressure conditions [5]. The wurtzite structure is defined by a and c axes, with lattice constants of $a = 3.25\ A^o$ and $c = 5.21\ A^o$, as shown in figure 1.2. It represents the most common crystalline structure form of ZnO because of its thermodynamic stability in ambient pressure and temperature. Along the c-axis, the zinc atoms are stacked tetrahedrally with four oxygen atoms in a typical sp^3 covalent bond (a chemical bond involving electrons shared between the Zn and O atoms). On the other hand, the oxygen and zinc bond has also a significant ionic character owing to the big difference in their electronegativity (oxygen = 3.44 and zinc = 1.65). Therefore, ZnO can be classified as a mixed ionic (ionicity of 39%) and covalent metal oxide [7,8].

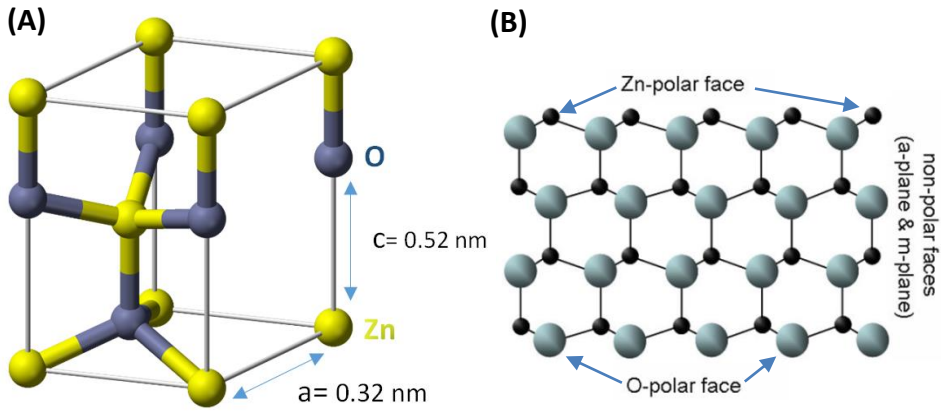

Figure 1.2: (A) The unit cell of the hexagonal wurtzite structure of ZnO. (B) The Zn and O polar and nonpolar plane surfaces in the ZnO lattice [8].

The distribution of the zinc cations (positively charged ions) and the oxygen anions (negatively charged ions) in the unit cell can take different configurations, where anions or cations can cover the entire surface leading to the formation of polar surfaces. In the wurtzite crystalline structure, ZnO normally has four different surfaces, two of which have surface dipoles with polar surfaces; Zn-(0001) (Zn atoms covering the entire outer

plane surface) and O-$(000\bar{1})$ (O atoms covering the entire outer plane surface). These are believed to be responsible for the material's optical and electrical properties. The other two surfaces are $(10\bar{1}0)$ and $(11\bar{2}0)$ which are non-polar. The polar surfaces are found to be more intriguing and energetically favourable in scientific and technological points of view compared to the nonpolar counterparts which consist of an equal number of oxygen and zinc atoms with mixed termination [6] as shown in figure 1.2-B. The polar surfaces are also believed to be responsible for the gas sensing activity and surface reactions at the surface of ZnO nanostructures [9].

1.3 Optical properties of ZnO

The optical properties of ZnO have been the subject of intensive research in the last decades due to their importance in deciding the material's applications. ZnO has a direct band gap of 3.37 eV and a high exciton binding energy of 60 meV (which enables the formation of a high number of excitons), both at room temperature. Owing to its high excitonic binding energy and direct wide band gap, ZnO is considered as a very efficient UV light emitter at room temperature [10] and also has a broad visible emission related to native defects. Among other elements in its group, oxygen anions in ZnO have the highest ionization energy leading to a strong interaction between Zn3d and O2p orbitals which give rise to its direct band gap as shown in figure 1.3. Its conduction band (CB) is constructed from the s-like state and formed from $4s^2$ electrons related to Zn. On the other hand, its valence band (VB) is formed from $2p^4$ electrons related to the O and so has a p-like state. ZnO VB has three split-off bands in wurtzite ZnO resulting from the effect of the crystal field (the effect of the electrical field of the neighbouring ions on the energies of the valence orbitals of the ion in the crystal) and spin orbital interactions. Upon light absorption, electrons are promoted from the valence band to the conduction band leaving behind positively charged holes. Owing to their charge

difference, the excited electrons bond with the holes through a Coulombic force and forms what is called an exciton (electron-hole pair) illustrated in figure 1.4-A. When electrons and holes recombine, a narrow line spectrum is emitted with energy (E_X) slightly below the optical band gap by the amount of the binding energy. This slight difference comes from the binding energy associated with exciton formation. Therefore, exciton binding energy can be given by [11]:

$$E_X = E_g - E_B \tag{1.1}$$

Where $\hbar$ is the reduced Planck constant ($\hbar = \mathrm{h}/2\pi$), ω is the angular frequency ($\omega = 2\pi\upsilon$), E_g representing the band gap, E_B is the binding energy or ionization energy of free exciton.

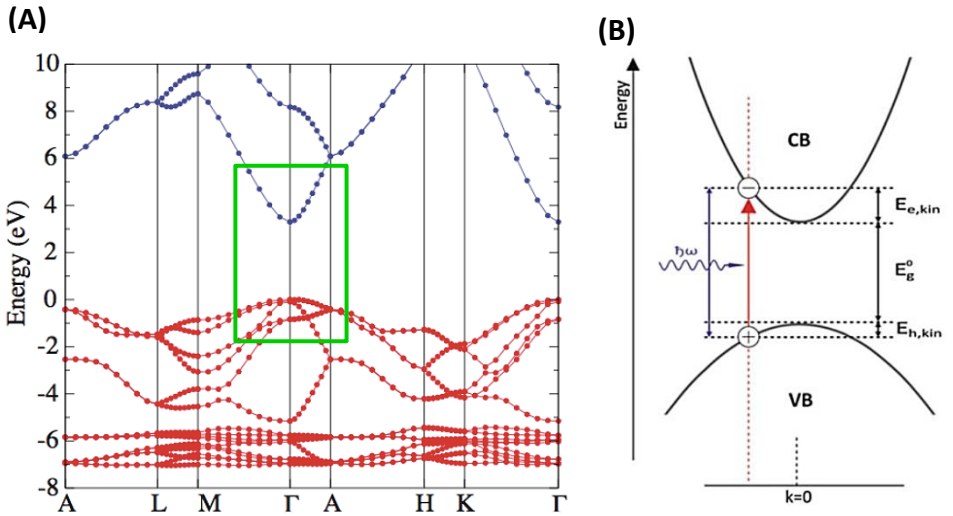

Figure 1.3: (A) The band structure of ZnO as calculated by HSE hybrid functional [30]. (B) The direct transition of an electron from the valence band (VB) to the conduction band (CB) leading to hole generation in the valence band. This results from of the absorption of light with photon energy equal to or higher than the fundamental band gap [11].

The behaviour of the exciton (electrons orbiting the holes) resembles the hydrogen atom and hence its binding energy can be calculated from the hydrogen-like model and given by:

$$E_B = \frac{m_r^* e^4}{2h^2 \varepsilon^2 n^2} \tag{1.2}$$

where m_r^* is the reduced mass of the electron-hole pair, e is the electron charge, h is Planck's constant, ε is the dielectric constant and finally, n is an integer representing the quantum number corresponding to the energy state. Due to this strong attraction force (which is a characteristic of an ionic crystal), the electron is tightly bound to the hole until they recombine giving rise to photon emission with energy given in equation 1.1. The large binding energy (60 meV) of free excitons in ZnO enables them to be highly stable and give rise to photon emission at room or even higher temperature ($K_B T$ = 25.9 meV). Excitons can be described by two different models depending on how tightly bound the electron-hole pair is, namely: Frenkel exciton and Wannier-Mott exciton shown in figure 1.4-B and C. The Frenkel model describes tightly bound electron and hole confined within a single lattice constant and is more relevant to organic semiconductors. The Wannier-Mott model describes the loosely bound hole and electron with an average bound radius larger than the lattice spacing and is more relevant to inorganic semiconductors [5].

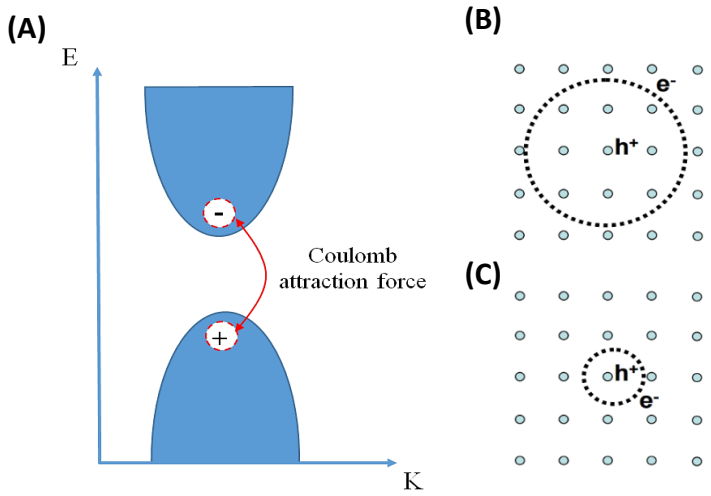

Figure 1.4: (A) An illustration of exciton formation resulting from the Coulombic attraction between the free electron in the conduction band and free hole in the valence band. (B) and (C) describing the Wannier-Mott and Frenkel exciton models respectively.

1.4 Electrical properties of ZnO

It is hard to put in context the electrical behaviour of ZnO owing to the great impact of surface defects on its electrical properties. ZnO films of high quality have a carrier concentration around 10^{16} electrons cm^{-3}, while the electron concentration can reach 10^{20} electrons cm^{-3}, with heavy n-doping. The electron and hole effective masses in ZnO are found to be 0.24 m_e and 0.59 m_h respectively [12,13]. Owing to its large band gap, ZnO can work reliably under large electric fields, powers and temperature without breaking down. ZnO is also well known for its piezoelectricity (electrical charges stimulated by mechanical stress) [14].

ZnO has an intrinsic n-type conductivity originating from the unintentional doping during fabrication or material processing. It is well known that ZnO has an ambipolar doping problem meaning that it can only reliably work as an n-type semiconductor (the unintentional existence of shallow donors) due to the donors' compensation when acceptors are introduced. Electrons mobility in bulk ZnO is limited at low temperatures,

equal or lower than 10 K, owing to intrinsic processes such as scattering with ionized impurities. The electron mobility of bulk ZnO at room temperature is found to be 205 cm^2/V s as reported by Look et al. [15], while it increases to 440 cm^2/V s for thin films as reported by Ohtommo and Tsukazaki [16]. On the other hand, the hole mobility of ZnO at room temperature is reported by Ryu et al. [17] to be 5 to 30 cm^2/V s which is much less than the electron mobility as expected.

1.5 Defects in ZnO

High-quality ZnO films and crystals are normally accompanied by defects and impurities. The fabrication environment and processing conditions, such as working in an oxygen-rich or zinc-rich environment, normally dictate the formation energy of the defects (the difference between the total energy of the perfect crystal structure before and after the defect formation). It is important but not easy to identify the defects and their locations within the band gap. A combination of theoretical calculations based on the first principles theory and experimental techniques have made great contributions to help resolve this problem. In the last few years, many semiconductors with very interesting properties have not been considered for device applications because of the lack of control over their conductivity due to defect formation. The defects alter the electronic structure of ZnO by introducing additional energy levels within the band gap which help trap the charge carriers leading to a major difference from the properties of the pure semiconductor. The energy of the defect levels varies depending on their thermal ionization energies. For instance, shallow and deep defects levels correspond to defects which are likely to be ionized and nonionized at room temperature respectively. The deep levels are transition levels located energetically far away from the band edges (conduction band minimum and the valence band maximum) and require energy much larger than the thermal equilibrium to move electrons. On the other hand, shallow

defects levels are energetically located close to the band edges (either below the conduction band or just above the valence band) where electrons can be ionized with little thermal energy [18]. Those levels are very important in controlling the materials conductivity type by either accepting electrons from the valence band leading to the generation of holes (p-type) or donating electrons to the conduction band leading to an increase of the free electrons (n-type). A variety of experimental and theoretical techniques are utilized to help identify and calculate the defects concentrations such as electron paramagnetic resonance (EPR) [19], deep-level transient spectroscopy [20], cathodeluminescence (CL) [21], secondary ion mass spectrometry (SIMS) [22], positron annihilation spectroscopy (PAS) [23] and density-functional theory (DFT) with first principle calculations [24].

The formation of a defect in the lattice mainly depends on the experimental conditions represented by the environmental abundance and the Fermi level, in the case of a charged defect. For instance, preparing or annealing the sample in environments rich or poor in one particular constituent, Zn and O atoms in the case of ZnO, could lead to the formation of point defects. An oxygen vacancy is formed as a result of oxygen atom removal from the lattice. Therefore, by utilizing the density functional theory (a powerful tool used to investigate defects formation in semiconductors) the formation energy (E^f) of oxygen vacancy arising after the removal of an oxygen atom can be given by [25]:

$$E^f\left(V_O^q\right) = E_{tot}\left(V_O^q\right) - E_{tot}(ZnO) + \mu_O + qE_F \qquad (1.3)$$

where $E_{tot}\left(V_O^q\right)$ represents the total energy of the crystal with the charged oxygen vacancy, $E_{tot}(ZnO)$ is the total energy of the perfect crystal in the same system, μ_O is the oxygen chemical potential (a temperature and pressure dependent potential energy

describing the reactivity of any given species to perform a reaction or phase transition) which varies depending on experimental conditions such as O-rich or Zn-rich environment and finally, E_F is the Fermi level. From equation 1.3, the formation energies of zinc and oxygen vacancies are affected by Zn and O-rich fabrication conditions as seen in figure 1.5-A. Under Zn- and O-rich conditions, the formation energy of oxygen vacancy (V_O) is reduced when the Fermi level approaches the valence band maximum (VBM) ($E_F = 0$). In contrast, the formation energy of zinc vacancy (V_{Zn}) is reduced when the Fermi level approaches the conduction band maximum (CBM). Figure 1.5-A also shows that under a Zn-rich environment, V_O is likely to form only when E_F is located very close to the VBM, while it is unlikely to form under an O-rich environment despite the position of E_F. On the other hand, V_{Zn} is likely to form in an O-rich fabrication environment when E_F is close to the CBM and has a slight chance to form in a Zn-rich environment.

Zn and O atoms are bound together by covalent bonds to form the ZnO lattice. When an oxygen atom is removed from the lattice, four bonds surrounding the Zn atoms will be broken leading to the formation of a new symmetric energy state, occupied by two electrons in the natural state of the charged oxygen vacancy, located close to the valence band maximum in the ZnO band gap and another three states located above the conduction band minimum which are always empty [26].

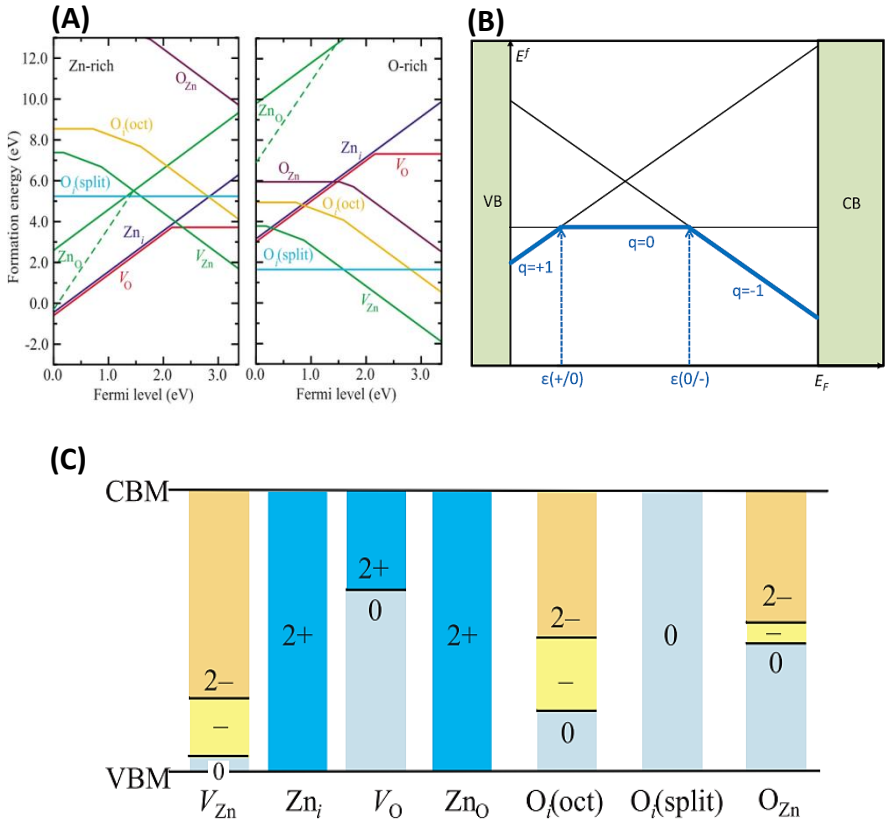

Figure 1.5: The calculated formation energies of the common point defects as a function of Fermi level of ZnO. (A) The calculated defects energy levels with respect to the preparation conditions (Zn-rich and O-rich environments) where the valence band maximum corresponds to the zero Fermi level. (B) The defect formation energy (E^f) versus Fermi level (E_F) showing a system consisting of three charge states, +1, 0, -1, with two transition levels represented by $\varepsilon(+/0)$ and $\varepsilon(0/-)$ for the deep donor and acceptor levels respectively. The black lines correspond to the defects formation energy, while blue lines are the favourable charge states corresponding to E_F [28]. (C) Showing the defects transition levels positions inside the ZnO band gap as calculated by LDA and LDA+U [26].

Energy levels are introduced in the ZnO band gap by the presence of defects which often involve transition levels which take place between different charged states within the same defect. The transition level, $\varepsilon(q_1/q_2)$ is the Fermi energy at which the formation energies of two charge states, q_1 and q_2, are the same, where the defect charge state is denoted as q [27]. If $q = 0$, the defect is considered natural, whereas when $q = +1$ or -1 indicates that the defect is lost or gained one electron respectively. Figure 1.5-B shows the formation energies of three possible charge states in ZnO with

two transition levels. The stability of the formed charge state is determined by the position of Fermi level corresponding to the transition level. For instance, when the Fermi level is located below the transition level $\varepsilon(q_1/q_2)$, the charge state q_1 is stable, whereas when the Fermi level is located above the transition level, q_2 becomes the stable charge state [28]. Figure 1.5-C shows the positions of the native point defects in ZnO band gap based on local density approximation (LDA) in addition to LDA+U approach calculated by Anderson Janotti and Chris G. Van de Walle [26].

ZnO is an excellent host for surface defects and has a rich defect chemistry especially when it is structured in nanoscale dimensions [29]. In this thesis, we try to explore the effect of surface defects on the electrical properties by looking at their role when the material has nanoscale dimensions.

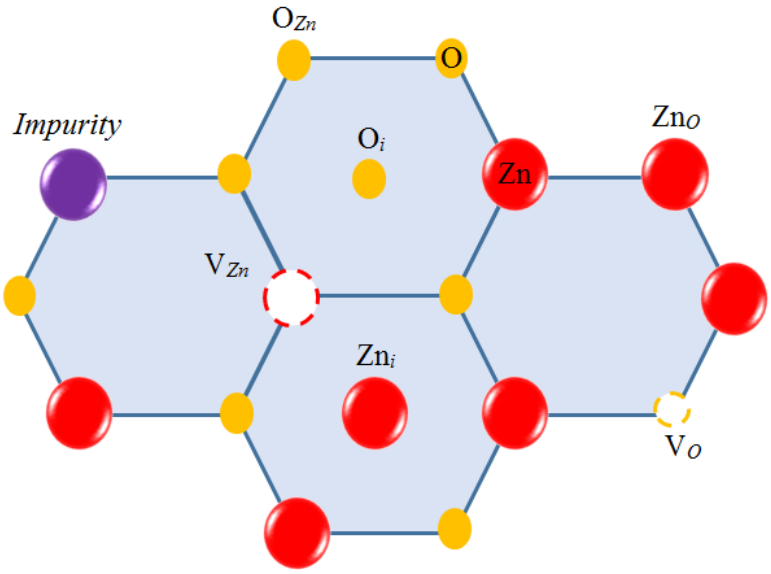

Figure 1.6: An illustration of the intrinsic and extrinsic point defects in ZnO crystal structure, where (Zn) is a zinc atom, (O) an oxygen atom, (V_O) an oxygen vacancy, (V_{Zn}) a zinc vacancy, (Zn_i) a zinc interstitial, (O_i) an oxygen interstitial, (Zn_O) a zinc antisite, (O_{Zn}) an oxygen antisite and a substitutional impurity at zinc site.

1.5.1 Intrinsic defects

Intrinsic defects are often referred to as native defects, which include vacancies, interstitials and antisites. These are usually named according to the production method and are denoted as V_O and V_{Zn}, O_i and Zn_i and O_{Zn} and Zn_O respectively as shown above in figure (1.6) . Vacancies have the missing atoms at regular positions in the ZnO lattice, while interstitials refer to extra atoms (either O or Zn) occupying the gaps in the lattice. Antisites represent the complementary substitution of an atom in the lattice with the other type, i.e. Zn occupies the place of O and vice versa. Generally, neglecting defects interactions, the defect concentration, c, in a lattice structure at thermal equilibrium can be calculated using the following equation [30]:

$$c = N_{sites} \exp\left(-\frac{E^f}{K_B T}\right) \tag{1.4}$$

where N_{sites} is the number of defects sites per volume, E^f represents the defects formation energy, K_B is the Boltzmann constant and T is the temperature. Equation (1.4) shows that defects with high formation energy exist at low concentration and vice versa. It represents the likelihood of defect formation, where defects with low formation energy are more likely to exist over the defects with high formation energy. The formation energy of the defects strongly depends on the location of the Fermi level as well as the potential energy of Zinc or oxygen.

1.5.1.1 Oxygen vacancies

The removal of an oxygen atom from the ZnO lattice results in the formation of an oxygen vacancy (V_O) as shown in figure 1.6. This vacancy has long been considered as a shallow donor responsible for the n-type conductivity of ZnO. This assumption is based on observing the conductivity of ZnO prepared in a Zn-rich environment [26]. First principle calculations proved that oxygen vacancies are deep donor rather than shallow

defects with high formation energy in n-type ZnO and that the transition level between charge state 2+ and natural charge state 0 $(2+/0)$ is located ~1 eV below the conduction band [31], which make it impossible to contribute electrons to the conduction band. Therefore, being considered as deep donor together with its high formation energy even at Zn-rich conditions indicate that these defects are not likely to be responsible for the intrinsic n-type conductivity of the ZnO [25]. However, despite the DFT calculations which predicted that oxygen vacancies have high formation energies in ZnO and therefore likely exist at low concentrations, different conditions may occur at the surface of ZnO nanostructures owing to their large surface area. The oxygen vacancy can exist in three possible charged states depending on the Fermi level energy; fully occupied (V_O^0), singly occupied (V_O^+) and empty (V_O^{2+}) [30]. The fully occupied defect state is found to be energetically stable in n-type ZnO and has a high formation energy in O-rich conditions, which makes it unlikely to exist at a high concentration, while the singly occupied state is found to be energetically unstable, always having higher energy than the fully occupied and the empty states for any given Fermi level position.

1.5.1.2 Zinc vacancies

A Zinc vacancy (V_{Zn}) is formed when a Zn atom is missing from the lattice structure leading to the formation of energy states within the band gap resulting from breaking four bonds with the neighbouring oxygen atoms. It is a deep acceptor defect with low formation energy in n-type ZnO. Therefore, this defect is unlikely to be the responsible for the n-type conductivity of ZnO. However, this defect is believed to be accounted for the green photoluminescence (PL) centred between 2.4 and 2.5 eV [32,33,34] which is in good agreement with the calculated transition state by Janotti and Van de Walle [27]. Different experimental investigations tried to better understand the relation of these defects with the visible PL. For example passivating the Zn vacancies with hydrogen

plasma was found to reduce the green PL. However, electron irradiation is also found to reduce the green PL despite Zn vacancy formation [35,36].

1.5.1.3 Oxygen and zinc interstitials

The tetrahedral and the octahedral sites represent the two possible interstitial sites for excess atoms in the ZnO wurtzite lattice. Each site has a unique location where the interstitial atoms neighbour a specific number of Zn and O atoms at a specific distance. Therefore, the sites have different stabilities based on the geometrical constraint on the interstitial atom. For instance, in a tetrahedral site, there are one zinc and one oxygen atom neighbouring the interstitial atom at a distance of about $0.833\,d_o$, where d_o represents the Zn-O bond along the c-axis of the lattice. On the other hand, in an octahedral site, the interstitial atom neighbours three zinc and three oxygen atoms at a larger distance of $1.07\,d_o$ [37]. The O_i interstitial represents an added oxygen atom in the lattice of ZnO. Calculations show that this defect has high formation energy in equilibrium conditions. Therefore, it is not likely to contribute to the n-type conductivity of the ZnO. Moreover, it can be electrically active or inactive depending on its location in the lattice and the material conductivity type [26].

The Zn_i interstitial is an extra Zn atom normally located in the octahedral site of the wurtzite structure. This defect is located above the conduction band and has two electrons which enable it to be a shallow donor in ZnO. However, calculations show that this defect has high formation energy (about 6 eV) in an n-type sample making it non-viable in equilibration conditions. Hence, those defects are not considered responsible for the native conductivity of the ZnO [26,18].

1.5.1.4 Oxygen and zinc antisites

Oxygen antisite defects occur when an oxygen atom occupies the site of a Zn atom in the lattice and are denoted as O_{Zn}. This defect has a high formation energy in an n-type material at equilibrium conditions (its formation is favoured in an O-rich environment) and is found to act as a deep acceptor with transition levels 1.52 eV and 1.77 eV above the valence band maximum [26]. Zinc antisite defects, denoted as Zn_O, occur when a zinc atom occupies the site of an oxygen atom in the lattice structure. The defect is a deep donor with a high formation energy in equilibrium conditions (its formation is favoured in a Zn-rich environment) [34]. Both types of antisite defects do not explain the n-type conductivity of ZnO due to their high formation energies.

1.5.2 Extrinsic defects

Extrinsic defects refer to external atoms (impurities) that can exist intentionally or unintentionally in the lattice structure of ZnO. These defects also introduce donor or acceptor energy levels in the band gap depending on their formation energies [38]. As mentioned above, many intrinsic point defects have high formation energies and hence are unlikely to exist in thermal equilibrium. Alternatively, they may exist at low densities so they do not effectively contribute to the ZnO n-type conductivity. There are many dopants/impurities that can play an important role in ZnO conductivity, such as aluminium (Al), boron (B), gallium (Ga), indium (In), lithium (Li), hydrogen (H) and more.

1.5.2.1 Hydrogen in ZnO

The incorporation of hydrogen impurities during the deposition of ZnO is almost unavoidable whatever the fabrication technique is. Generally, hydrogen was first considered as a shallow donor in ZnO in 1956 when Thomas and Lander [39]

experimentally indicated that hydrogen increased the conductivity of ZnO as a result of its possible reaction with an oxygen ion. Further investigation of the role of hydrogen in ZnO conductivity was conducted by Van der Walle [40] using density functional theory (DFT) calculations. His work shows that hydrogen interstitials exist in ZnO in their positive charge state (H_i^+), which is the thermodynamically stable form of hydrogen. They act as shallow donors located independently of the Fermi level energy [30,41]. It is found that hydrogen is normally incorporated in most semiconductors in its negative charge state in n-type and in its positive charge state in p-type. Therefore, it is not likely to be considered as a dopant candidate. However, in ZnO, hydrogen behaves differently and exists in its stable positive state. This behaviour can be explained by the strong H-O bond which helps to reduce the formation energy of H_i^+ and hence increase the hydrogen solubility. Hydrogen in ZnO has a low formation energy and can takes two different forms, either as an interstitial or a substitution by replacing the oxygen [30]. There is a strong belief that hydrogen could be responsible for the n-type conductivity of ZnO. Using electron paramagnetic resonance (EPR) and electron nuclear double resonance spectroscopy (ENDOR), hydrogen was linked to one of the two observed shallow donors in commercially undoped ZnO crystals characterized by a thermal activation energy of 35 meV and concentration of about 6 x 10^{16} cm^{-3} [41]. Moreover, a Hall effect measurement recorded ZnO conductivity an order of magnitude higher, when treated with hydrogen plasma [42].

1.5.3 Defects in ZnO nanostructures

The massive development in nanofabrication techniques enables the production of a large variety of nanostructures with complex shapes and sizes. ZnO among semiconductors has a wide range of different nanostructure forms such as nanoparticles, nanowires, nanorods, nanobelts and much more. Furthermore, ZnO also has a rich

defects chemistry which has made it a very interesting subject of investigation for over 50 years. However, with having different nanoscale structures, defects studies need updating in the context of nanostructured materials. In such a small size (few nanometres) defects have a great impact on tailoring the ZnO properties owing to the large surface-to-volume ratio relative to the bulk which enables large density of defects to exist compared to bigger crystals [29]. Furthermore, the large surface area of the nanoparticles increases the density of the atomic sites and therefore increases the surface capability of molecules adsorption such as oxygen and carbon dioxide. Despite the dependence of surface defects on their formation energy, their concentration is found to increase based on the high surface area of nanostructured materials. For instance, Nasiri et al. [43] have reported the impact of reducing the ZnO particle size on its photoconductivity compared to the bigger particles due to the high concentration of surface adsorbed oxygen which leads to a high density of surface states. This study is supported by Park et al. [44] which shows that the carrier dynamics in nanostructured ZnO, characterized by PL and photoconductivity, are affected by the surface layer, which is size and morphology dependent, owing to the high density of surface defects.

Zhang et al. [45] show the dependence of photocatalytic activity of ZnO nanostructures on its aspect ratio. Despite the huge amount of literature trying to identify surface defects by utilizing PL measurements, defects identity and origin are still controversial due to the broad PL spectrum which makes it hard to confirm the defect transition responsibility. However, an important observation is that PL intensity in the visible is related to the ZnO nanostructures size and shape [46,5]. Manipulating the size and shape of ZnO do not only alter the density of defects on the surface but also stimulates different types of those defects. In a study by Han et al.[47], two ZnO structure forms were prepared and investigated using time-resolved photoluminescence, hexagonal

cones with 100 nm size and hexagonal plates with 30 nm size. Oxygen vacancies were found to dominate the hexagonal cone-shaped nanostructures while zinc vacancies appear in addition to the oxygen vacancies when the size and shape of ZnO changed to hexagonal plates.

1.6 Applications of ZnO

1.6.1 Light emitting diodes (LEDs)

The ease of material processing and the high exciton binding energy of ZnO (60 meV) enable the material to be highly appreciated in the light emitting diodes (LEDs) industry. It is still very challenging to successfully fabricate high-quality p-type ZnO because of its native n-doping nature. Nevertheless, great efforts have been paid to develop blue and UV LEDs based on heterojunctions with ZnO using a variety of organic and inorganic materials. However, the lattice mismatch with the p-type materials gives rise to possible dislocations defects which impact the device performance. The first LEDs based on hybrid heterojunction with Cu_2O as a p-type conductivity material are believed to have been fabricated in 1968 by Drapak [48]. Thereafter, tremendous research work has been done to improve LEDs by incorporating ZnO with p-type materials such as some conductive oxides, Si, GaN, AlGaN and more [49]. Furthermore, an organic-inorganic heterojunction LED emitting at 390 nm was fabricated using a diode structure consisting of ZnO nanorods embedded in insulating polystyrene and sandwiched between SnO_2 and p-type organic hole transport layer (PEDOT: PSS) [50].

1.6.2 Thin film transistors (TFTs)

ZnO has been implemented in electronic circuits as an active semiconductor layer in thin film transistors (TFTs) due to its wide band gap, the possibility of low-temperature processing (can be deposited even at near room temperature) and its outstanding electrical properties. Its optical transparency and stability enable ZnO to be considered as a successful candidate in the revolutionary development of flexible and transparent thin film transistors, with fast operating speeds. ZnO can be prepared using a wide range of fabrication techniques such as chemical vapour deposition (CVD), pulsed laser deposition (PLD), molecular beam epitaxy (MBE) and by sol-gel methods. Most of the aforementioned techniques utilize high temperature in the fabrication process which hinders the development of low-cost TFTs. However, solution-processed ZnO nanostructures with different sizes and shapes based on sol-gel fabrication technique are considered to be cost-effective, relatively simple and require a low synthesis temperature which is compatible with transparent, low weight flexible platform technology [51].

ZnO was first realized in 2003 as a transparent active material in TFTs [52,53,54]. Soon after, a considerable amount of research was conducted to build a general understanding of its operation. TFTs based on ZnO normally have a higher effective channel mobility than other traditional semiconductors like hydrogenated amorphous silicon (about 42 cm^2/V s as compared to about 1 cm^2/V s for silicon) [55]. Despite the advantages of using ZnO in TFTs, there are still some problems to be overcome such as the electrical instability under ambient environments.

1.7 Metal-semiconductor interface

Ideally, when a metal is brought into contact with a moderately doped semiconductor, a barrier is formed in the contact area. This results from the difference in the work functions between the metal and the semiconductor and the misalignment in their Fermi levels. The Fermi level in metals represents the highest occupied energy state at room temperature. While in semiconductors, it represents the lowest available energy level for electrons and ideally lies within the band gap and close to the conduction band (valence band) in n-type (p-type) semiconductors. Upon contact, electrons transfer to the metal leaving behind a region depleted of electrons called the depletion region or space charge region located close to the metal-semiconductor interface. This region stimulates an internal electric field as shown in figure 1.7. This field bends the energy bands of the semiconductor upwards (downwards) in n-type (p-type) semiconductors at the interface leading to the formation of a Schottky barrier with the metal. This barrier acts as a rectifying junction which allows electrons to move in one direction only, from the semiconductor to the metal. The height of the Schottky barrier normally depends on the difference between the electron affinity of the semiconductor ($q\chi$) (distance from the bottom of the conduction band to the vacuum level) and the metal work function ($q\emptyset_m$) and can be calculated theoretically from $E_B = q(\emptyset_m - \chi)$ where q is the electron charge. However, for p-type semiconductors, the barrier height will be $E_B = E_g - q(\emptyset_m - \chi)$ where E_g represents the semiconductor band gap. It should be noted that all the above mentioned descriptions are based on an ideal contact between the metal and the semiconductor. However, in reality, the Schottky barrier height will be different based on the presence of localized surface states due to impurities. The barrier heights can be optically determined based on Fowler's theory of internal photoemission by fitting the square root of the photocurrent responsivity as a function of photon energy

[56]. The intercept of the linear fit with the photon energy represents the Schottky barrier height. The current transport through the barrier is mainly due to the majority carriers which are electrons in n-type semiconductors. Due to the difference in the work functions between the semiconductor and the metal, electrons are in favour to cross the barrier to the metal [57].

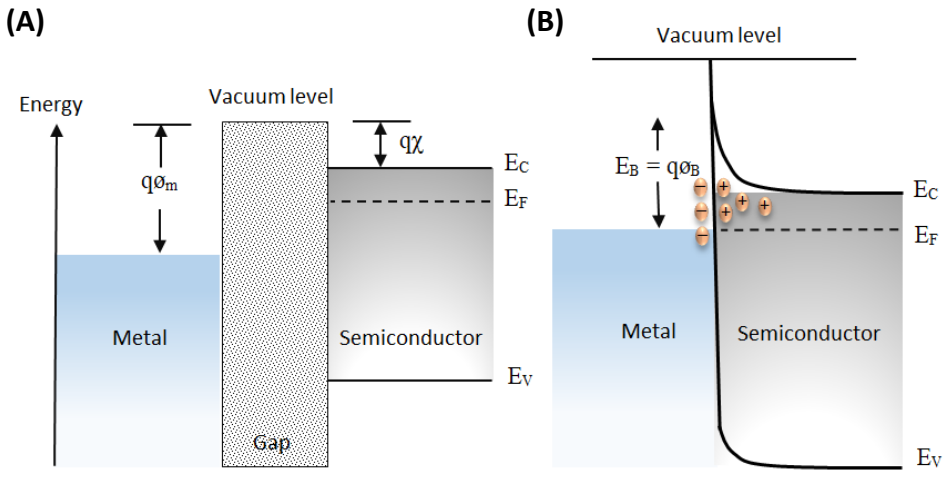

Figure 1.7: An energy level diagram showing the semiconductor and metal in the case of (A) no contact and (B) the formation of a Schottky barrier at a metal-semiconductor (n-type) interface [57].

On the other hand, an ohmic contact is formed if the work function of the metal is the same as the electron affinity of the semiconductor (no or very low barrier at the interface) so that electrons are free to move in and out of the semiconductor. Ohmic contact is preferable for long lifetime operation of devices, to minimize device failure by thermal stress or degradation by the resistance at the contact interface. Several approaches are followed to reduce the potential barrier with the metal electrodes such as: modifying the surface of ZnO by surface cleaning technology, evaporating an ultra-

thin metal interlayer between the semiconductor and the metal electrode and post-deposition annealing.

1.8 Photodetection in semiconductors

The general principle of photodetection in semiconductors is based on a combination of three main processes, namely: electron-hole generation by light absorption, charge separation and finally, charge transportation to their respective electrodes, and contributes to an output signal. Upon light illumination, photons with energy equal or greater than the semiconductor's band gap are absorbed promoting electrons intrinsically by a direct transition from the valence band to the conduction band. Photons with energy lower than the semiconductor's bandgap can also be absorbed in an extrinsic process promoting electrons from the defects or impurities levels to the conduction band. The electrons either move freely to their respective electrodes under the influence of an externally applied field or get trapped. The promoted electrons leave positively charged holes which move in the opposite direction to the electrons. As a result of the electron-hole separation process, a photocurrent will be generated over the device with a magnitude depending on the collected photogenerated charge carriers at a given wavelength. In principle, photoactive devices can be categorized as photoconductors and photovoltaics based on the mechanism by which charge separation occurs. Photoconductor devices normally consist of a single semiconductor layer electrically connected to two metal electrodes on each side. Charge separation occurs through the application of an external electric field across the electrodes. On the other hand, photovoltaic devices normally utilize two semiconductor layers with different carrier majorities (p-n). The internal field achieved at the interface of the p-n junction is used to separate the generated photo-charge carriers. This working principle can also be

extended to cover the Schottky diode photodetectors and metal-semiconductor-metal photodetectors.

1.8.1 Photodetector considerations

1.8.1.1 Responsivity

Responsivity (R) in photodetectors can be defined as the ratio of the photocurrent magnitude flowing through the device (I_{ph}) to the incident light power (P). It is a wavelength-dependent parameter and varies with applied voltage and temperature. Responsivity has units of A/W and can be calculated using the following equation [57]:

$$R = \frac{I_{ph}}{P} \tag{1.5}$$

Another important photodetector parameter is the detectivity (D) which characterizes the photodetector performance. It is inversely proportional to the noise equivalent power (NEP), that is the minimum optical signal required to generate a photocurrent signal which depends on the photon energy ($h\upsilon$), quantum efficiency (η) and the spectral band width of the incident signal (B). Therefore, the detectivity, with unit W^{-1}, can be expressed by:

$$D = \frac{\eta}{2h\upsilon B} \tag{1.6}$$

The specific detectivity (D^*) of the photodetector can also be defined as the photodetector figure of merit that is independent of the photodetection area (A) and spectral bandwidth with units of Jones ($cm.\sqrt{Hz}/W$) and can be given by:

$$D^* = \frac{\sqrt{AB}}{NEP} \tag{1.7}$$

1.8.1.2 Quantum efficiency

The quantum efficiency (η) is defined as the number of photogenerated electrons divided by the incident number of photons. It is normally given by a value between 0 and 1, but may be higher if there is gain. In other words, it quantifies the device performance. It reflects the efficiency of light absorption by the photoactive material, since not all the light is absorbed so that there are reflection and transmission losses. The value of the quantum efficiency may also be affected by intrinsic processes within the active material and the presence of surface defects, which may act as traps or recombination centres for electrons and holes. Quantum efficiency can be linked to the optical responsivity (R) and the incident wavelength in nanometre (λ) and can be expressed by the following equation [58]:

$$\eta = \frac{R \times 1240}{\lambda} \tag{1.8}$$

1.8.1.3 Gain

The gain represents the average number of the electrons generated in the circuit per electron-hole pair. Some photodetectors have an internal gain coming from the difference between electrons and holes speed in addition to the long recombination lifetime as a result of the presence of charge trapping. Normally, electrons travel much faster than holes owing to the difference in their effective mass $m_e < m_h$. Therefore, upon light irradiation, electrons travel to the cathode much faster than holes to the anode. This enables the electrons to pass through the circuit more than once leading to a high internal gain. The number of the circuits the electron makes before recombination with the hole is given by the following equation [59]:

$$G = \frac{\tau}{\tau_e} \tag{1.9}$$

where G represents the internal gain, τ is the carrier recombination lifetime and τ_e is the electron transient time across the device and is related to the device length and the electron speed. This means that an electron-hole pair generated by the absorption of a photon delivers a charge (q) equal to the gain of electrons. The above assumption is true in cases the recombination time is long. If electrons recombine shortly before reaching the electrode, the internal gain will be less than unity and only a fraction of electrons can be delivered [60].

1.8.2 Photoconductors

An ideal photoconductor is a light-sensitive resistor consisting of a semiconductor with two ohmic metal contacts as shown in figure 1.8. It converts light into an electrical signal by changing the electronic energy distribution within the semiconductor [58]. Generally, incident light with photon energy equal or higher than the material's band gap is absorbed by the semiconductor creating electron-hole pairs which are separated by the applied electrical field. The material's conductivity increases in proportion to the number of incident photons.

This type of photodetector device is considered the simplest possible type of the photodetectors family. Despite the simplicity, photoconductor devices show a very fast time response, several orders of magnitude higher than other types of photodetectors in addition to a high gain. On the other hand, photoconductors have limited practical applications due to the poor selectivity in the UV/Visible region and short photodetection spectral bandwidth compared to the p-n or Schottky junction photodetectors [61].

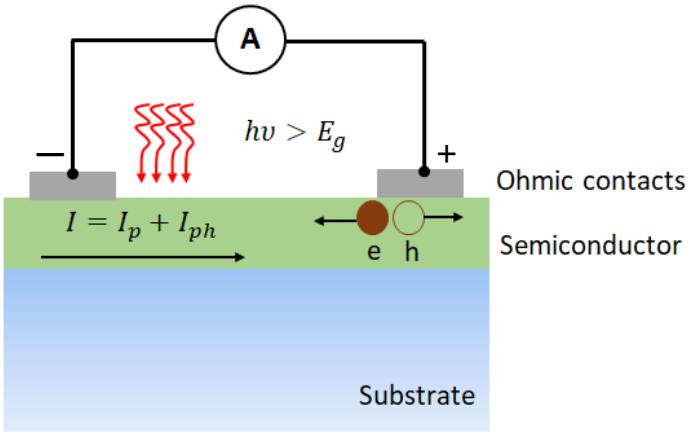

Figure 1.8: A schematic illustration of the photoconductor operation. I_p represents the current stimulated by the bias voltage and I_{ph} is the photocurrent.

1.8.3 P-n junction photodetector

A p-n junction photodiode is one of the most common forms of photodetectors. It consists of interfacing n-type and p-type doped regions often of the same semiconductor. The photodiode operates by absorbing the incident light in the depletion region, a space charge region formed by charge exchange at the interface between the n-type and p-type semiconductors [62]. In the dark, the device current is effectively zero because electrons in the n-type semiconductor are prevented from diffusing to the p-type semiconductor by the effect of the built-in potential barrier at the junction. A similar effect occurs for the holes in the p-type semiconductor. However, with light illumination, electron-hole pairs are created and then separated by drifting in opposite directions by the internal electric field across the depletion region. This leads to photocurrent generation. The device normally works in reverse bias in order to achieve a wide depletion region which maximizes the light absorption. A schematic illustration of the working principle of the photodiode accompanied with its energy band diagram is shown in figure 1.9.

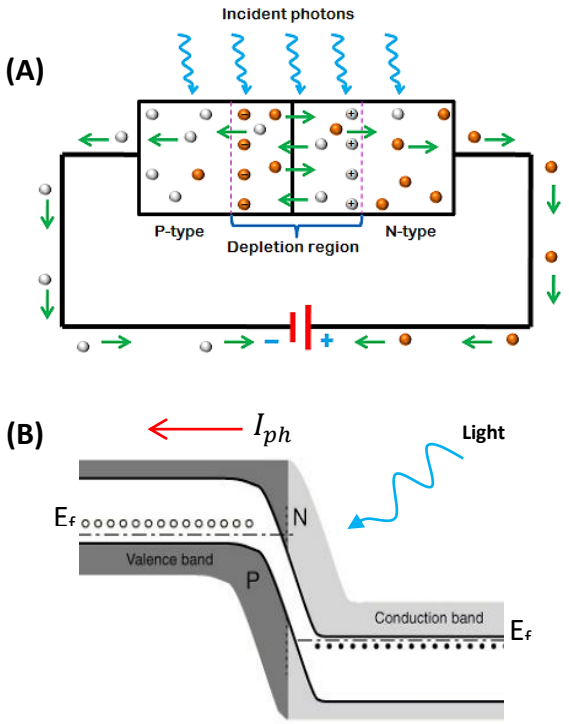

Figure 1.9: (A) An illustration of a typical reverse biased p-n junction photodiode [62]. Electrons and holes are denoted in the orange and white colours respectively. (B) Energy band diagram of a p-n junction in the reverse bias upon light illumination. Black and white dots represent the electrons and holes respectively.

1.8.4 Schottky barrier photodiode

This photodetector device is based on a unilateral junction where an n-type semiconductor makes a Schottky junction at one end and an ohmic contact at the other end with metal electrodes as shown in figure 1.10. The current in this type of device is conducted through the majority carriers and moves only in one direction, conventionally from the metal to the semiconductor. Upon light illumination, electron-hole charge carriers are created in the semiconductor close to the interface with the metal. The built-in potential resulting from the space charge region (depletion region) will help to separate the charge carriers and eventually create a photocurrent. Photoelectrons drift through the semiconductor and get extracted by the cathode, while holes diffuse by the upward band bending and get extracted by the metal anode. The intensity of the built-in

electric field can be modified by applying a bias voltage over the device to enhance the charge separation and device performance. In the forward bias for instance, where positive voltage is applied to the metal side and negative on the semiconductor, the Fermi level of the metal will decrease relative to the Fermi level of the semiconductor leading to a decrease of the potential energy across the semiconductor which reduces the electric field at the metal-semiconductor interface as shown in figure 1.10-A. In this case, a high current will flow across the junction. On the other hand, when a negative voltage is applied to the metal and positive voltage on the semiconductor (reverse bias), the Fermi level of metal will increase relative to the semiconductor leading to an increase of the electric field at the interface resulting from the high built-in potential across the semiconductor as shown in figure 1.10-B [63]. The current crossing the junction is very low compared to the case of the forward bias. The device is normally irradiated either from the front side or the back side depending on the device structure and configuration as illustrated in figure 1.10-C. General characteristics of this type of photodetectors are the fast switching speed owing to the rectification behaviour of the junction and the low electrical noise. Moreover, it can work in two different modes based on the irradiated photon energy [57]. A direct band-band transition of electrons from the semiconductor occurs when the incident light has energy equal or higher than the band gap, while at low photon energy (less than the band gap of the semiconductor), photocurrent can also be realized by the internal photoemission of electrons from the metal.

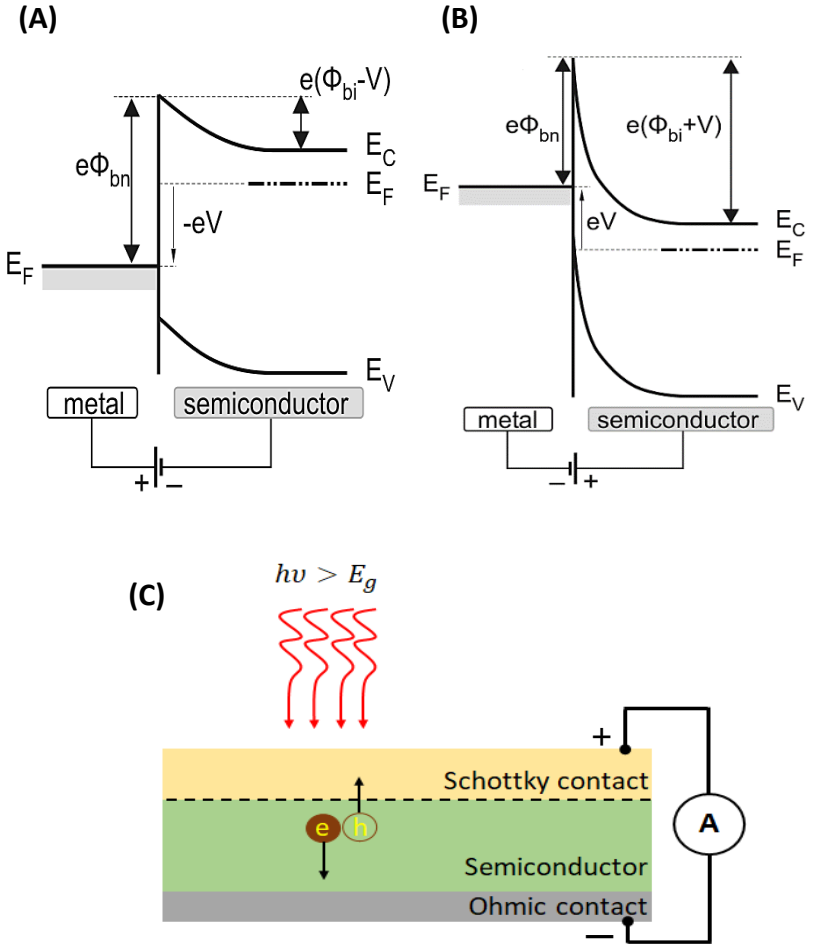

Figure 1.10: (A) and (B) represent the Schottky junction formation at the metal-semiconductor interface in the forward and reverse bias respectively. $e\phi_{bn}$ represents the Schottky barrier height and ϕ_{bi} is the build-in potential across the semiconductor [63]. (C) Illustrates the Schottky barrier photodiode working principle. The front metal contact should be transparent to allow light penetration.

1.8.5 Metal-semiconductor-metal photodetector (MSM)

An MSM photodetector device consists of two metal electrodes making Schottky contacts on both ends of the semiconductor as shown in figure 1.11. The electrodes normally take the structure of interdigitated fingers separated by a very short distance, around a few micrometres. Initially, no current is recorded across the MSM device unless an external bias voltage is applied [64]. As such, one contact is reverse biased while the other is forward biased based on the voltage polarity [65]. Upon light

irradiation, electron-hole pairs are generated in the semiconductor. The charge carriers generated close to the reversely biased contact, where a depletion region is formed, will more likely contribute to the photocurrent. The internal electric field originating from the upward band bending at the semiconductor-metal interface will separate the photogenerated electrons and holes which then travel in opposite directions towards the cathode and anode respectively. This device structure provides the advantage of not having an ohmic contact which is difficult to control for a wide range of semiconductors due to the presence of surface states defects. It is possible to use different metal electrodes on each end of the semiconductor to optimize the barrier height and therefore reduce the dark current for instance.

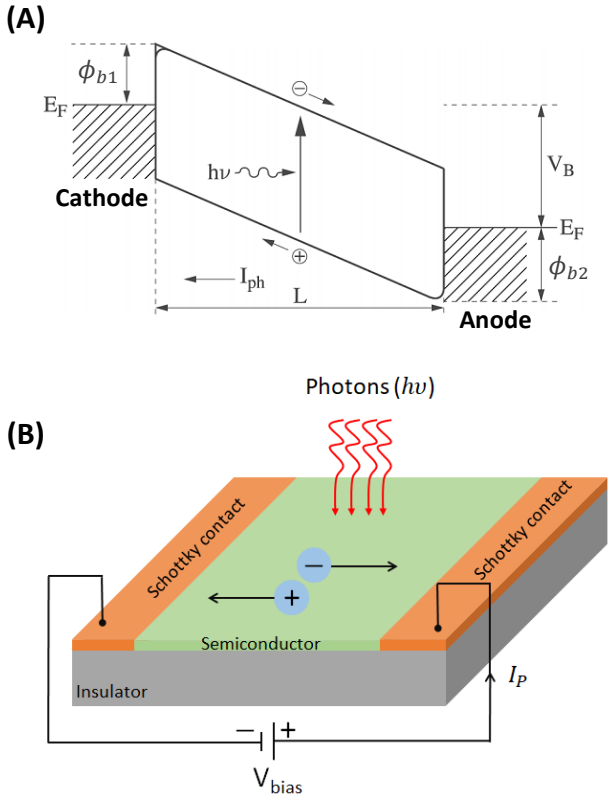

Figure 1.11: (A) Energy band diagram of MSM photodetector showing the difference in Schottky barriers (ϕ_b) at the two ends of the semiconductor separated by a distance (L) under bias voltage (V_B) [65]. (B) A schematic structure of an MSM photoconductor device. Light will be absorbed by the semiconductor material leading to electron-hole generation moving to their respective electrodes derived from the applied bias voltage.

1.8.6 Photovoltaic device

The photovoltaic effect is the mechanism by which the solar cell operates. Solar cells are photosensitive devices used to convert the sunlight into electrical power. Photocurrent and photovoltage are generated without the use of external bias voltage. The device mainly consists of a semiconductor with different doping concentrations, n and p-type, and the most famous example of this is the crystalline silicon solar cell panel. Furthermore, solar cells can also be fabricated from two different semiconductors such as organic solar cells where the active area normally consists of electron donor and electron acceptor materials both sandwiched between two contact electrodes normally

from different metals. A typical solar cell device structure in addition to energy band diagram is schematically illustrated in figure 1.12. The semiconductor is carefully chosen to maximise absorption for most of the sunlight spectrum. The solar cell operates by the generation of electron-hole pairs by light absorption. Electrons are raised to the conduction band while the holes are in the valence band. The electrons and holes are bound together by Columbic force depending on the semiconductor material. This bond is broken by the effect of the built-in electric field created by the depletion region leading to separation of the charge carriers and therefore, a photocurrent and electromotive force (emf) generation (this is the potential difference created by the depletion region which exerts force on the charge carriers leading to a current flow).

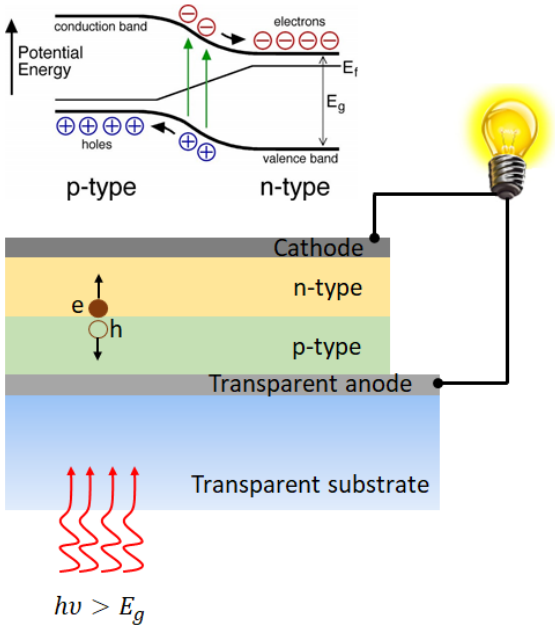

Figure 1.12: A schematic structure showing a typical solar cell configuration in addition to the energy band diagram of the p-n junction.

1.9 Overview of UV photodetection

Ultraviolet radiation (UV) was first realized in 1801 by J. Ritter and demonstrated soon after by T. Young in 1804 [66]. After this crucial observation, scientists started to investigate invisible electromagnetic radiation with wavelengths below the blue end of the spectrum. UV radiation is categorized into three wavelength bands based on their impact on the biosphere; the wavelength band from 320 nm to 400 nm is called UVA and is mainly useful for photocatalysis. The second band is called UVB and spans from 280 to 320 nm. This band is mainly blocked by the atmospheric ozone. The small portion arriving at ground level is considered very harmful to human beings with excessive exposure leading to skin cancer and burns. However, UVB band also has some benefits such as the stimulation of vitamin D in the human body. Finally, the UV band ranging from 100 nm to 280 nm is called UVC. This band is the most energetic band of the three bands. The UV wavelength range below 180 nm is known as deep UV and can only be generated under vacuum conditions. Scientists conduct extensive research to find suitable materials and device structures which can be used to build high-quality UV photodetectors. A table categorizing the different types of UV photodetectors is given by M. Razeghi and A. Rogalski [58] and shown in figure 1.13.

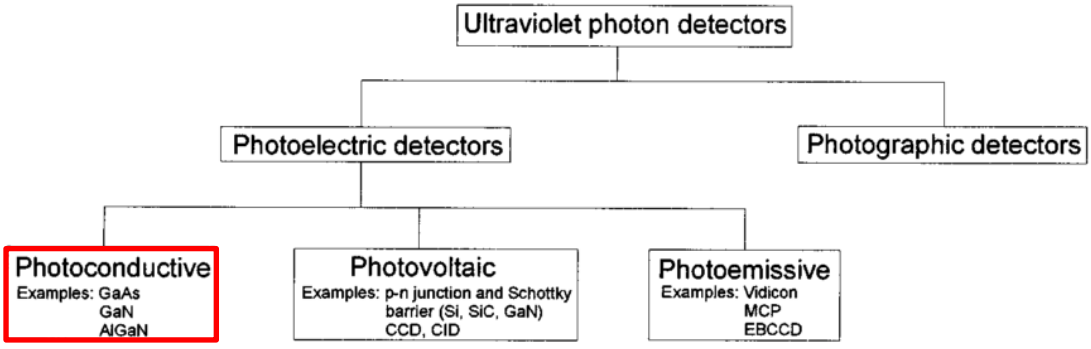

Figure 1.13: UV photodetectors classified according to their detection mechanism [58]. In this thesis, we are interested in the photoconductive type of detectors which have highlighted in red.

UV light can be detected in two main ways based on the photodetector operating principle; photographic and photoelectric. Each of them has advantages and disadvantages based on the application requirements. For instance, photographic detectors are based on molecular electronic transitions of photographic emulsion and best known for the store and read the electric charge generated by light absorption. However, they have slow responsivity and a nonlinear response over certain wavelengths [67]. On the other hand, photoelectric detectors are well known by their high sensitivity to the UV light with a fast light response. The photoelectric detectors are divided into three different types based on their working principle; photoconductive UV detectors, photovoltaic UV detectors and photoemissive UV detectors. The photoemissive photodetector's working principle is based on the photoelectric effect in metals. The detector consists of two metal electrodes, anode and cathode fixed in a phototube under vacuum. With the light on, electrons emitted from the cathode are accelerated towards the anode by the high voltage leading to a photocurrent signal. The optical sensitivity mainly relies on the cathode workfunction. On the other hand, photoconductive and photovoltaic UV photodetectors are based on semiconductors and they operate by photo-charge separation as discussed earlier. Therefore, their light sensitivity and bandwidth mainly depend on the semiconductor and the device configuration [58].

1.10 Persistent photoconductivity in ZnO

Persistent photoconductivity is observed in several semiconductors and can be defined as the long photorecovery of current (could reach minutes, hours or days) after light illumination. This phenomenon is mainly related to the presence of interband defects states, which help maintain the photocurrent and prevent the sudden decrease of current

after switching off the light. This phenomenon has a great impact on the photodetector performance by limiting its response speed while increasing the photocurrent magnitude. Great attention has been given to understand the cause of persistent photoconductivity. This phenomenon is first reported a few decades ago in GaAsP and attributed to the DX centres (D stands for donor and X is for unknown lattice defect such as a vacancy), which are deep donor levels located in the band gap responsible of charge capturing and emission, observed in many III-V semiconductors [68,69]. The general explanation to the long-time conductivity is that during light illumination, photo-charge carriers are generated in semiconductors (electrons-holes). Holes are believed to be trapped leading to increasing the lifetime of the photogenerated electrons and therefore, current takes a long time to saturate. After switching off the light, electrons will relax taking different recombination paths such as direct recombination with holes in the valence band (fast process) and/or recombine with trapped holes in the defects states (slow process) [70,71].

Persistent photoconductivity in ZnO has been explained differently. A long time ago, Broich at al. [72] suggested that long-lived photoconductivity in ZnO is mainly originated from the surface by photoexcited electrons localized in the charged surface layer. Furthermore, persistence photoconductivity is also attributed to the photoexcitation of carriers from deep donor defects in the presence of hole traps [73]. Lany et al. [74] and Janotti et al. [75] show that metastable oxygen vacancies could be the responsible of the long-lived photoconductivity. ZnO is well known for its persistent photoconductivity in a variety of structures such as in thin films [76], nanowires [77] and nanoparticles [43] due to the surface electron depletion region caused by oxygen adsorption [78,79]. The photogenerated electron-hole pairs normally having a very short lifetime, shorter than a nanosecond [10]. However, in reality, the lifetime is substantially

longer resulting from the presence of surface defects. The generally accepted mechanism for persistent conductivity is as follows. In the dark, atmospheric oxygen molecules are adsorbed on the ZnO surface, capturing electrons from the valence band leading to form a depletion region. Upon light irradiation, photogenerated holes are drifted to the surface by energy band bending (caused by the depletion region) and release the adsorbed oxygen. By doing so, the trapped electrons are released back and contribute to the overall photocurrent. When light switched off, oxygen molecules are re-adsorbed back on the surface and resume the electrons capturing process. This leads to a slow decay in the photocurrent depending on the efficiency of the adsorption process. Furthermore, persistence photoconductivity in ZnO is also studied in vacuum and photocurrent found to continue increasing in low oxygen pressure confirming the responsibility of oxygen adsorption assumption [80,81]. However, Collins and Thomas [82] suggested that the removal of adsorbed oxygen from the surface of ZnO could not be the only reason why photoconductivity increased under vacuum. They argued that surface photolysis of lattice oxygen could lead to creating a Zn-rich conductive layer on the ZnO nanostructures surface which could be accounted for the high conductivity in vacuum. The aforementioned suggestion is also supported by Bao et al. [83] which also attributed the high photocurrent in vacuum to the photodecomposition of ZnO under UV irradiation.

1.11 Motivation

Interest in ZnO has grown enormously in the last 20 years or so with nearly 6000 papers published already in this year up to Sep 2017, as recorded in the Scopus database. Many of these involve solution processable colloidal ZnO, photodetection and nanoparticles, which are among the subjects of this thesis. The rapid increase in interest comes from the fact that ZnO has a potential advantage over GaN such as the ability to produce

high-quality crystals at low cost, compatibility with solution processing and high exciton binding energy, which is more than double that of GaN (~ 21-25 meV) [84]. In theory, this would help ZnO to be a brighter UV light emitter than GaN at room temperature. However, the outstanding challenge of producing stable and high-quality p-type ZnO in addition to other unresolved issues related to identifying and controlling defects on the surface make it hard to predict its electrical and optical properties, therefore limiting ZnO commercial applications. The aforementioned limitations attract considerable research efforts to investigate ZnO in order to realize a breakthrough which could change ZnO's destiny. Nowadays, the low-end technology in optoelectronic devices requires the combination of low fabrication cost, novel functionalities and the compatibility of integration with flexible and low-temperature processing substrates. ZnO has superb photodetection ability, especially in the UV. Unfortunately, its photoconductivity is mostly persistent meaning that photocurrent is sustained after light irradiation due to surface electrochemical reactions. Often, persistent photoconductivity is considered as a problem but for some applications, it may be useful such as in bioelectronics [85], phototransistors [86] and photocatalysis [87].

A primary motivation of this study is investigate the impact of different atmospheric environments on the photoconductivity of solution-processed ZnO. We want to qualitatively explain, with reference to the photoconductivity mechanism, why the time dependence and responsivity of the PC signal varied with processing and measuring conditions. This might help us find the conditions to obtain temporally stable devices.

A second long-term aim of the study is towards a solution processed imaging detector, where different pixels detect different colours of light. These would be laterally displaced, or vertically in a more sophisticated device, to make a low-cost camera. Hence we investigated ZnO photoconductivity below its bandgap. We studied spectrally

narrow photoconductivity in the green spectral region and a plasmonic approach to obtain photoconductivity in the deep red/infra-red.

1.12 Thesis structure

Chapter 1 provides a general theoretical background to ZnO in addition to other subjects relevant to the areas investigated in the subsequent chapters. Chapter 2 goes through the experimental methods and equipment utilized in this study. Chapter 3 presents a study of how the device preparation, storage and measurement environment can influence the magnitude and time dependence of persistent photoconductivity in ZnO nanoparticles. The experiments are correlated with surface wettability and FTIR measurements to elucidate the surface mechanisms which impact the UV photoconductivity. Chapter 4 investigates the spectrally narrow, persistent photoconductivity obtained in the green of solution-processed ZnO nanoparticles (NPs). A model involving electron transfer from deep defects, tentatively assigned to neutral oxygen vacancies, to discrete shallow donors is introduced to account for the narrow spectrum and the exponential form of the current rise and decay transients. Furthermore, a low-cost and scalable photolithographic approach is developed to pixelate dual-wavelength photodetectors. One pixel works in the UV only and the other in both green and UV.

Chapter 5 presents a vertically configured photodetector based on a simplified hybrid plasmonic geometry, which utilizes the plasmonic effect to obtain photoconductivity in the deep red/near-infrared (IR). Gold nano-islands serve as a photosensitized material, which absorbs light within the spectral region of the plasmonic resonance and generates hot charge carriers by the plasmon decay. Finally, in chapter 6 we summarize and conclude the experimental findings in addition to suggestions of future work.

Chapter 2

Experimental Techniques

This chapter illustrates the experimental techniques and procedures followed in this thesis. It goes through the steps followed to make the active photodetector devices starting from ZnO NPs synthesis, thin film processing, device fabrication and characterization.

2.1 ZnO nanoparticles synthesis and functionalization

The ZnO nanoparticle (NP) solution was synthesised by Dr Fei Cheng of the Chemistry Department of the University of Hull using literature methods with some modification [88,89]. A new solution batch was prepared for almost every new experiment indicating the consistency and repeatability of the results. Zinc acetate ($Zn(OAc)_2$, 0.8182 g, 4.46 mmol) and 0.25 ml of water were added to a three-neck flask containing 42 ml of methanol. The solution was heated to 60 °C and then a solution of potassium hydroxide (0.4859 g, 7.22 mmol) in methanol (23 ml) was slowly dropped into the flask. The reaction took place at 60 °C for 2 hours. White ZnO NPs were obtained after centrifuging and washing with methanol twice. These were dried in air for 30 min and then dissolved in a solution of chloroform (6.2 mL) containing a small amount of octylamine (0.2 mL). The amine ligands helped to enhance the dispersion of the particles and prevent agglomeration within the solution. Finally, a clear ZnO nanoparticle solution was obtained after filtering through a 0.45 μm PTFE filter. The prepared nanoparticles have a good size uniformity and reproducibility as confirmed by TEM.

2.2 Device fabrication

Planar and vertical photodetector device configurations were prepared and investigated for the work of this thesis. The main fabrication procedure, such as substrate preparation and cleaning, the spin speed, baking temperature and the used materials were mostly the same and are detailed here.

2.2.1 The substrate

In this work, polished soda lime, float glass (15 mm × 20 mm), coated with interdigitated Indium Tin Oxide fingers (ITO) (20 Ω/square) with overall channel

dimensions of 30 mm × 50 µm, shown in figure 2.1, were bought from Ossila and used as substrates. The substrates were cleaned thoroughly in an ultrasonic bath for 10 minutes using deionised water (DI), acetone and propanol respectively. Thereafter, the substrates were dried with a dry nitrogen gun and treated with UV/Ozone for 3 minutes in order to remove any organic contamination on the surface as well as to improve the surface wettability for better film uniformity.

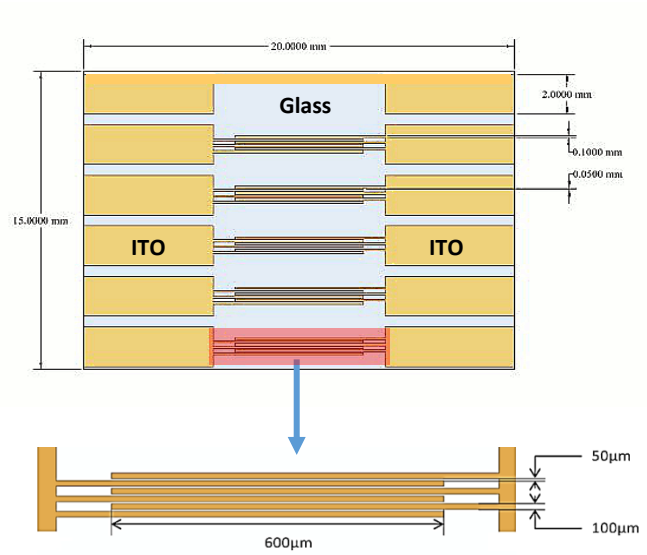

Figure 2.1: A pre-patterned ITO OFET substrate, bought from Ossila, used to prepare the photodetectors and plasmonic devices in this thesis.

2.2.2 Thin film deposition

ZnO nanoparticles with the concentration of 2.5 wt. % and an average diameter of 11.8 ± 1.7 nm (based upon analysis of more than 100 particles by TEM) dissolved in chloroform were prepared using the modified sol-gel method mentioned earlier. Generally, the ZnO nanoparticle solution was spin coated, using a spin coater very similar to the one showing in figure 2.2 [90], in air or in N_2 on ITO interdigitated substrates at 2000 rpm for 30 sec through a 0.45 µm syringe filter. This was followed by soft baking in the chosen environment at 100 °C for 10 min. The baking process is

important to remove any remaining solvent from the film. After that, samples were post-annealed on a hot plate at different temperatures in air or nitrogen environments to modify the properties, and hence the electrical and optical behaviour. The conductive polymer (poly(3,4-ethylenedioxythiophene) polystyrene sulfonate) PEDOT: PSS layer, bought from Ossila, was also used as a hole transporting layer in the preparation of plasmonics devices. The material was filtered and then spin coated in air at 2000 rpm for 30 sec followed by soft baking at 150 °C for 10 min.

Figure 2.2: Photograph of a typical spin coating instrument [90].

2.3 Device configurations

There are two main device configurations utilized in this thesis, namely planar and vertical. The planar configuration is mainly used to investigate ZnO NPs photodetector devices in chapters three and four. A vertical configuration is used to investigate the role of plasmonic gold nanoislands on the near-IR photoactivity of ZnO NPs, as discussed in chapter five.

2.3.1 Planar device configuration

The photodetector device structure is shown below in figure 2.3-A. Simply, a layer of Zinc oxide colloidal nanoparticles (ZnO NPs) was spin coated on top of a glass\pre-patterned ITO (100 nm thickness, 20 Ω/□ resistance) OFET (organic field effect transistor) substrate which has five channels, each of which represents an active working device. Aluminium contact legs were attached to the substrate after film deposition to make electrical connections from the ITO channels to a measuring circuit board bought from Ossila and illustrated in figure 2.3-B. The connection legs are also used as contact pads for electrical measurements using the needle probes. The thin film was irradiated from the top (the film side) for the photocurrent measurements. The device active area is 0.15 mm^2 (the active ITO finger length (0.6 mm) × the distance between two fingers (0.05) mm × the number of fingers (5)).

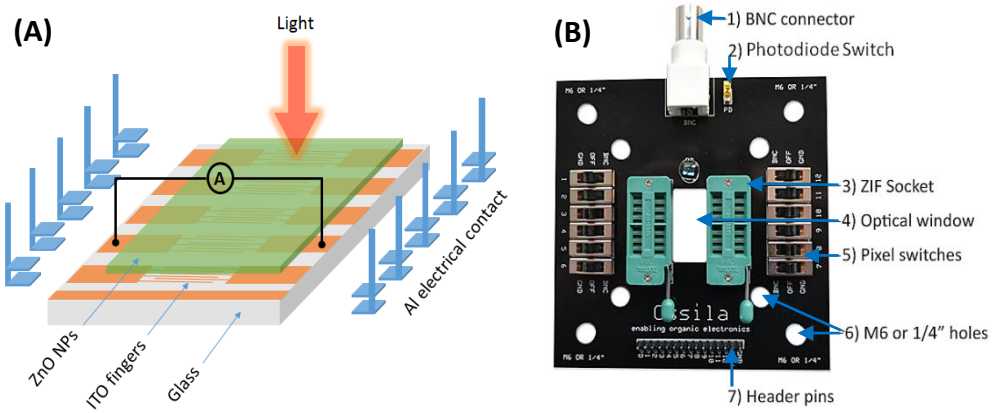

Figure 2.3: (A) A schematic illustration of the planar device configuration layout and (B) a labelled image of the circuit board (from Ossila), which holds the substrate to measure the photocurrent. The connection legs go through the ZIF socket and the pixel switches on each side of the board determine which current pathway is measured.

2.3.2 Vertical device configuration

The vertical configuration indicates the device structure where multiple layers were deposited on top of each other to build the working device. In this structure, the current is measured between the ITO fingers and the Aluminium (Al) back electrode which was thermally deposited on top of the ZnO NPs layer. This structure was used to investigate the plasmonic devices used in chapter five. The device is built by spin coating the PEDOT: PSS layer on top of the ITO channels followed by ZnO NPs and then evaporating the Al electrode. In some devices, a gold thin film (Au) was deposited on top of the PEDOT: PSS layer by thermal evaporation before the spin coating of ZnO NPs. Vertical configuration devices were optically irradiated through the glass/ITO for the photocurrent measurement as shown in figure 2.4. Each ITO pad is connected to three ITO fingers; therefore, there are 10 working devices on each substrate, 5 devices on each side.

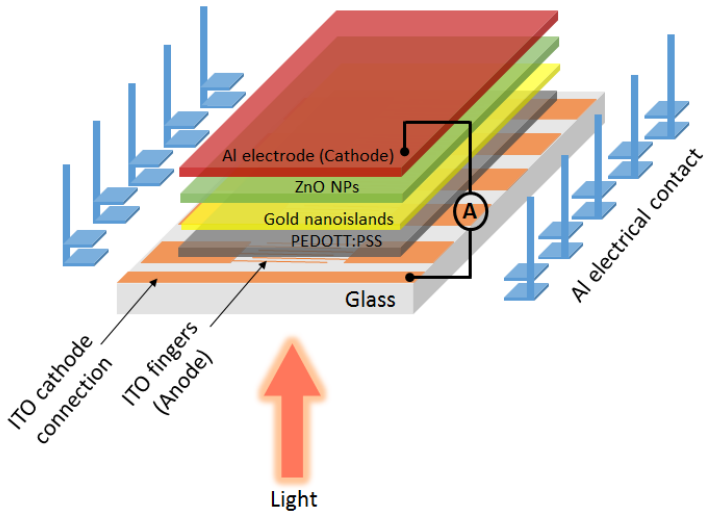

Figure 2.4: A schematic illustration of the vertical device configuration.

2.4 Thin film processing

2.4.1 UV/Ozone treatment

UV/Ozone treatment is a well-known technique for cleaning the surfaces by removing contaminants. It represents a non-destructive, easy and fast way of removing organic species from surfaces. The cleaning process is performed using a home-made system containing a low-pressure UV discharge mercury lamp fixed at the top of and inside an aluminium metal box. The aluminium box is surrounded by a bigger box made from perspex, to absorb any UV light outside the aluminium box and also to keep the generated ozone in the irradiated area as shown in figure 2.5. The outer box is fitted with a ventilation pipe to introduce fresh oxygen and safely remove ozone via an exhaust line.

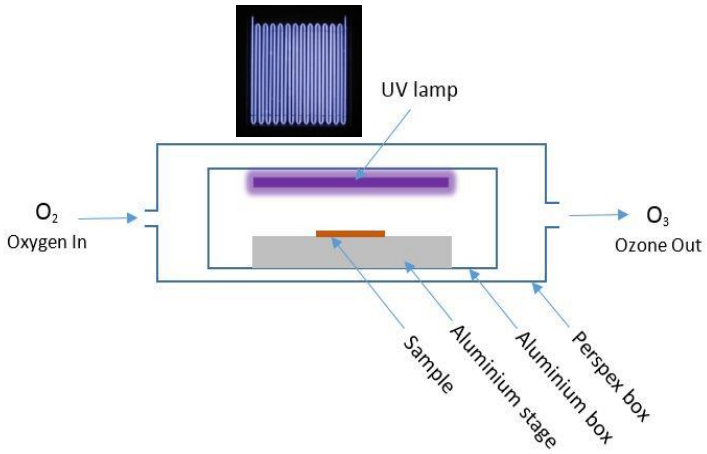

Figure 2.5: Schematic diagram of the UV\Ozone irradiation system.

The working mechanism is simple. A low pressure, high-density mercury grid lamp emits UV light dominated by the wavelengths 184.9 nm and 253.7 nm. Absorption of the short UV wavelengths helps dissociate oxygen molecules and form two free oxygen radicals (O^*). The free radicals react with another oxygen molecule (O_2) and generate

the ozone molecule (O_3). Ozone molecules can absorb light of wavelength 253.7 nm to generate highly unstable active oxygen molecules which decompose the organic compounds on the film surface to form volatile gases such as CO_2 and H_2O as explained by the following reactions [91,92]. The resulting gases are removed by the ventilation pipe.

$$O_2 + h\upsilon\,(184.9\,nm) \rightarrow O^* + O^* \quad (2.1)$$

$$O^* + Organic\ compounds \rightarrow CO_2, H_2O \quad (2.2)$$

$$O_2 + O^* \rightarrow O_3 \quad (2.3)$$

$$O_3 + h\upsilon\,(253.7\,nm) \rightarrow O_2 + O^* \quad (2.4)$$

2.4.2 Thermal evaporation

An automated thermal evaporation system, Auto500 supplied by HHV Ltd, was used to evaporate the back electrode metals as well as very thin gold films for plasmonic devices. The metal is heated and evaporates in an ultra-high vacuum so that particles can travel directly to an overlying substrate where they condense to form the thin film. An ultra-high vacuum, in the range of 10^{-7}mbar, is obtained before the start of every evaporation process. The system has two different evaporation sources: Resistive heating is used to heat and evaporate metals with low melting points whilst an electron gun is a more effective and localised heating source for other metals. Different metals can be evaporated alternatively without breaking the vacuum for better film quality. Film thickness as low as 1 nm in addition to a very slow evaporation rate of 0.1 A/sec are accurately achievable.

2.4.3 Solution-processed photolithography

ZnO NPs films can be spatially patterned following a simple yet innovative solution processed photolithography technique. A positive photoresist AZ5214 (Microchemicals Gmbh) was used to define the ZnO NPs pixels using UV irradiation through a homemade mask. The size and shape of the pixels were designed using a Microsoft power point document and then printed over a transparent plastic film. The photo-pixellation process is based on a selective reaction of ZnO NPs film with the developer solution and the acetone. ZnO is insoluble in the solvent, acetone, which dissolves the photoresist. The photoresist developer (AZ726MIF) dissolves both the exposed photoresist and ZnO NPs film. This technique offers a simple and scalable approach to the fabrication of pixelated ZnO thin film where pixels can vary in their photoconductive spectral responses by either applying different surface treatment and/or changing the pixel thickness. Pixels with the same size, shape and approximately the same thickness can be easily reproduced by following precisely the experimental procedure. A two-pixel device can be made with one mask. The first pixel can detect light in the UV and green while the second pixel can only detect the UV light, where green PC is suppressed by using different surface treatment. Results on pixels performance can be found in chapter four, section 4.3.4. Detailed descriptions of the fabrication steps that were followed to prepare and pattern the ZnO NPs device are illustrated schematically in figure 2.6 and given by the following points:

1. The substrate was cleaned thoroughly by sonication for 10 min in deionised (DI) water, acetone and propanol. Then, ZnO NPs (2.5%, dissolved in chloroform) were spin-coated on top of the substrate at 2000 rpm for 30 sec. The solution was filtered with 0.45 μm PTFE filter to remove the aggregated particles. After spin coating, the substrate was soft baked at 100 °C for 5 min in air.

2. The photoresist (AZ5214) was spin coated on top of the ZnO NPs at 3000 rpm for 30 sec. Then, the substrate was baked at 100 °C for 1 min.
3. The first pixel was defined by covering the wanted area by a mask (printable transparent plastic film) and then the film was irradiated uniformly with UV light using a UV exposure system (contains two UV lamps with 8 Watts each) for about 90 s.
4. The substrate was washed with the developer by dipping it in and out for about 40 s, followed by washing with deionised water. In this step, the irradiated photoresist and the ZnO NPs beneath it were removed by the developer leaving the area covered by the mask protected.
5. The pixelated ZnO NPs were washed with acetone to remove the protecting photoresist layer on top. This is by immersing the substrate in acetone for about 1 min, then dried with N_2 and baked at 100 °C for 5 min. The device was annealed at 350 °C in air for 1 hour, to improve the photoconductivity of the ZnO NPs in the green.
6. The first pixel was covered with the photoresist for protection. This was done by spin coating the photoresist at 2000 rpm for 30 s. The protective photoresist layer was relatively thick so that the UV light would not significantly penetrate to P1. After that, the substrate was baked at 100 °C for 2 min. Then, the same mask was used as for step 3 to cover P1 and irradiate the rest of the area with UV light for 90 s. After that, the substrate was washed with the developer and DI water, so that photoresist only overlaid P1.
7. The substrate was spin-coated with ZnO NPs at 2000 rpm for 30 s, followed by baking at 100 °C for 5 min.

8. The photoresist layer was spin coated at 3000 rpm for 30 s on top of the ZnO NPs, followed by baking at 100 °C for 1 min.
9. The second pixel, P2, was defined using the same mask to cover the required area and irradiating the rest of the substrate (including P1) with UV for 1 min.
10. The substrate was washed with the developer and the DI water leaving both P1 and P2 covered with the photoresist.
11. The substrate was washed with acetone and DI water to remove the protecting photoresist on P1 and P2. Then, the substrate was soft baked at 100 °C for 10 min to remove the remaining solution.

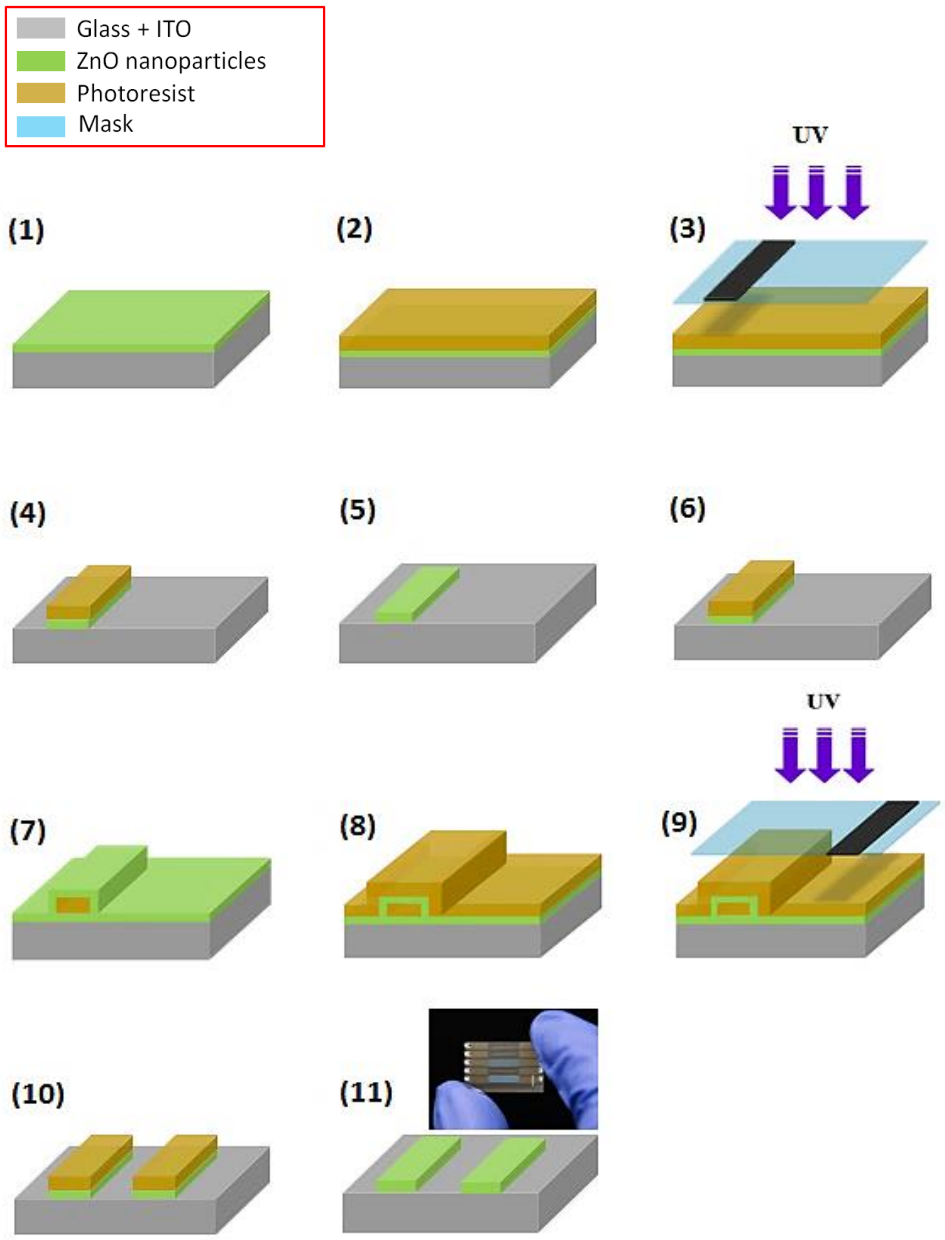

Figure 2.6: Schematic illustration of the key steps followed in photolithographically processing a two pixel device on top of a pre-patterened ITO substrate. The optical image shows the actual device prepared using the above procedure.

2.5 Characterization methods

We now discuss the characterization techniques that are used to investigate the optical, electrical and structural properties of the fabricated devices. We summarise below the working principles behind these techniques in addition to the procedures followed.

2.5.1 UV-Vis absorption

Light-matter interaction gives very important information about the optical identity of the material. The UV-visible instrument consists of a light source, which generates a spectrum covering the UV, visible and near-IR regions (200-1100 nm), a monochromator to separate the light according to its wavelengths, a slit with a specific width (depending on the required resolution) and finally a detector to record the optical signal. The transmission of light through a semiconductor depends on the Lambert-Beer's law [57]:

$$I = I_o e^{-\alpha t} \tag{2.5}$$

where I is the intensity of the transmitted light, I_o is the intensity of the incident light, α is the absorption coefficient, which is strongly dependent on the incident wavelength, and finally t is the film thickness. The absorbance, $A=\alpha \times t$, of a thin film is obtained as a function of wavelength by rearranging equation 2.5. The absorbance of the blank substrate is similarly measured. This is subtracted from the sample measurement in order to identify the absorption of the required material precisely. In an ideal semiconductor, only light of photon energy higher than the optical band gap can be absorbed. The semiconductor is transparent at wavelengths longer than $\lambda = \frac{hc}{E_g}$, where h is Planck's constant, c is the speed of light in vacuum and E_g is the semiconductor band gap. In reality, there may be residual absorption below the band-gap because of defect states.

2.5.2 Film thickness

A computerized Bruker thin film profilometer (DektakXT), illustrated below in figure 2.7, was used to monitor the surface uniformity and measure film thickness. This

technique has the ability to measure thicknesses over a millimetre to nanometer scale with a minimum error of ± 5 nm. The working principle of this instrument is quite simple. The vertical profile of the surface is measured electromechanically by moving a diamond tip over the area of interest. The profilometer is connected to a microscope and a 2D translation stage so you can easily specify the required measurement area on the surface as well as other parameters depending on the sample. The film is scratched with a very sharp tool with uniform edges to give a uniform scratch for high data accuracy. The height variation between the top surface of the film and the bottom of the scratch causes the profilometer tip to move vertically resulting in an electrical signal. This calculates the difference in movement as the film thickness changes. The vertical variation precision varies from about 5 nm to 1mm. The data resolution is highly dependent on the tip radius, scan speed, scan length and on the force applied to the tip (0.03-15 mg.).

Figure 2.7: An image of the DektakXT profilometer used in this work.

2.5.3 Contact angle measurement

The contact angle that a drop of liquid makes with a surface is considered a good indication of the surface wettability. It can be defined as the angle that the liquid droplet makes with a given solid surface. If the contact angle value is higher than 90º, the surface is considered as hydrophobic, while if the contact angle value is less than 90º, the surface is considered as hydrophilic. Generally, the arrangement of the material's atoms on the surface is different than in the bulk. In the bulk, atoms are evenly surrounded leading to balance the cohesive forces between the atoms in all directions. On the other hand, atoms arrangement on the surface is on one side only which leading to generate a cohesive force towards the surface to minimize its area. If considered as a force rather than energy, then this force is called the surface tension (γ) measured in (Newton/m) which can be defined as the surface force (or energy in Joule/m^2) exerted to form one unit area and its equal to the surface energy if there is small or no strains. When a deionized (DI) water drop is placed on the surface, three interfaces forces are generated, two of which are impacting the value of the contact angle namely; the solid-liquid interface (γ_{SL}) and the solid-vapour interface (γ_{SV}) as shown in figure 2.8. If the surface energy at the solid-liquid interface is larger than the surface energy at the solid-vapour interface, the droplet spreads, wetting the surface. On the other hand, the droplet makes a defined compact shape when the surface energy of the solid-vapour interface is larger than the surface energy at the solid-liquid interface.

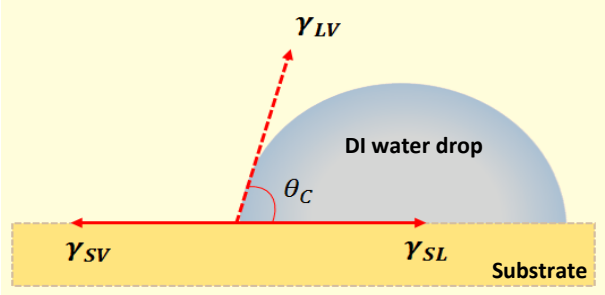

Figure 2.8: A schematic illustration of the water drop on the solid surface indicating the forces applied on the drop by the three interfaces it makes namely; solid-liquid interface (γ_{SL}), solid-vapour interface (γ_{SV}) and liquid-vapour interface (γ_{LV}).

In this work, the wettability of ZnO NPs films was evaluated by measuring the contact angle using a computerized Drop Shape Analysis System; model DSA10-Mk2 from KRÜSS. The DI water droplet is analysed using a drop analysing software. The measuring procedure can be summarized as followed. A precise DI water drop (about 10 µl) is put on the surface of ZnO NPs and left to sit for about 5 sec. The droplet is viewed by a CCD camera connected to the computer. The droplet background light can be adjusted in order to get a high contrast of the droplet boundaries. The contact angle is measured using image analysis software installed on the computer. The software recognizes the droplet boundaries and by performing a numerical fitting to the edges and droplet profile, the value of the contact angle is revealed.

2.5.4 Fourier transform infrared (FTIR) spectroscopy

The term infrared generally refers to the spectral radiation starts after 700 nm (0.7 µm). However, most of the fundamental vibrations of functional groups such as the organic molecules, important for chemical analysis are laid in the spectral range from 2.5 to 25 µm, which is equivalent to the wavenumber (the number of electromagnetic waves at a specific distance (one centimetre)) range (4000 to 400 cm^{-1}). The wavenumber ($\tilde{v}$) is normally measured in cm^{-1} unit and it is linearly with energy (E) and inversely proportional to wavelength (λ) as described in the following relations:

$$\tilde{\upsilon} = \frac{1}{\lambda} = \frac{\upsilon}{c} \quad , \quad E = h\upsilon = hc\tilde{\upsilon} \tag{2.6}$$

Where h is Planck's constant, c is the speed of light in vacuum and υ is the optical frequency. FTIR is a vibrational spectroscopy technique by which molecular vibrations of a specific function group is excited by absorption photons within the infrared energy. Molecular vibration can be expressed by the inharmonic motion of atoms within the molecule. The molecules are normally having three vibrational degrees of freedom represented by the vibration modes (atoms in the molecule are moving in periodic motion without affecting the chemical bond), stretching modes (stretching the chemical bonds by the action of atomic movement along the chemical bond) and finally bending modes (bending the chemical bond by changing its angle when atoms are not moving along the bonding direction).

The FTIR instrument normally consists of a Michelson interferometer which includes a beam splitter and two planar mirrors [93]. One of these, M1, is stationary, and the other, M2, is moveable as illustrated in figure 2.9. By mechanically scanning the position of M2, a time-dependent variation in the transmitted infrared radiation is created in a process called interferogram resulting from the difference in path length between the mirrors. The reflected IR radiation from M1 and M2 are recombined at the beam splitter and directed towards the sample. The detector then records the transmitted IR radiation through the sample as a function of optical path difference (at each wavelength) in the form of intensity versus time. The sample absorbing specific wavelengths (depending on the surface composition) leading to reduce their intensity. The recorded spectrum is computed using Fourier transform function to transfer the recorded signal to a readable spectrum in the form of intensity versus frequency. FTIR measurement records all the wavelengths simultaneously rather than stepping at each wavelength. This means that

the signal-to-volume noise ratio is proportional to the acquired data points in the spectrum (the larger the data point's acquired, the higher is the spectrum resolution).

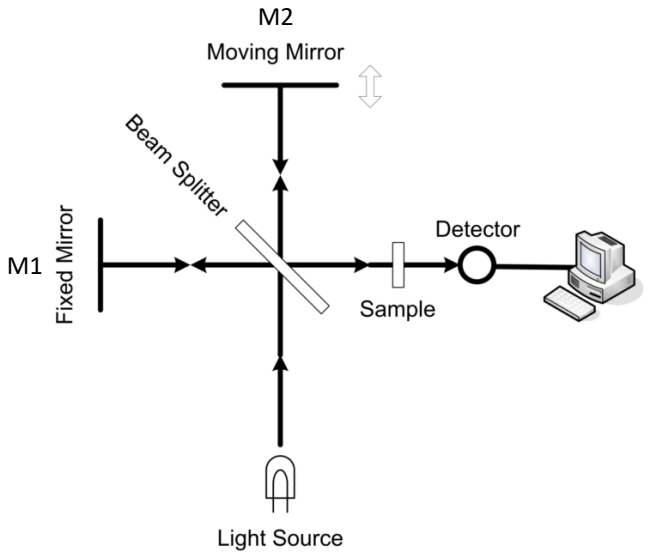

Figure 2.9: A schematic diagram of the FTIR working principle [93].

A Bruker IFS 66/S Fourier transform infrared spectrometer equipped with a water-cooled glowbar source, a potassium bromide (KBr) beam splitter and a deuterated triglycine sulphate detector was used to measure the transmittance of the samples at 300 K (where transmittance is equal to I/I_o, I is the intensity of the transmitted light through the sample and GaAs substrate and I_o is the intensity of the transmitted light through the GaAs substrate only). The GaAs substrate spectrum was taken under the same conditions as each sample measurement in order to eliminate any inherent artefacts. The scanning resolution was 4 cm^{-1} and 1000 scans were collected for each spectrum. The sample compartment was continuously purged with dry air to reduce absorption due to atmospheric water vapour and carbon dioxide. FTIR measurements were performed at the School of Engineering and Computer Science at the University of Hull with the help from Dr Khue T. Lai.

2.5.5 X-ray diffraction measurement

X-ray diffraction (XRD) is a non-destructive characterization technique mainly used to identify the atomic structure and composition of materials. This technique gives a quantitative analysis based on X-ray scattering from the sample, with each material having a distinctive scattering pattern as a function of detection angle. The instrument consists of three main elements; an X-ray tube, a holder for the sample and an X-ray detector. X-rays are generated in the cathode ray tube under vacuum as follows: Electrons are emitted from a heated filament and then accelerated in an electric field towards a target (copper in our case). The accelerated electron collides with an inner shell electron from the target ejecting it from the copper atom leaving a hole. An outer shell electron within the atom fills the hole emitting an X-ray photon so that energy is conserved. The X-ray diffraction set-up is illustrated in figure 2.10 [94]. The emitted photons are collimated, filtered, and then directed towards the sample. Both the sample and the detector are rotated at specific angles and a light diffraction signal is recorded when Bragg's law is satisfied ($n\lambda = 2dsin\theta$), where λ is the X-ray wavelength, θ is the angle between the incident rays and the irradiated crystal surface, d is the inter atomic layer spacing and n is an integer [59].

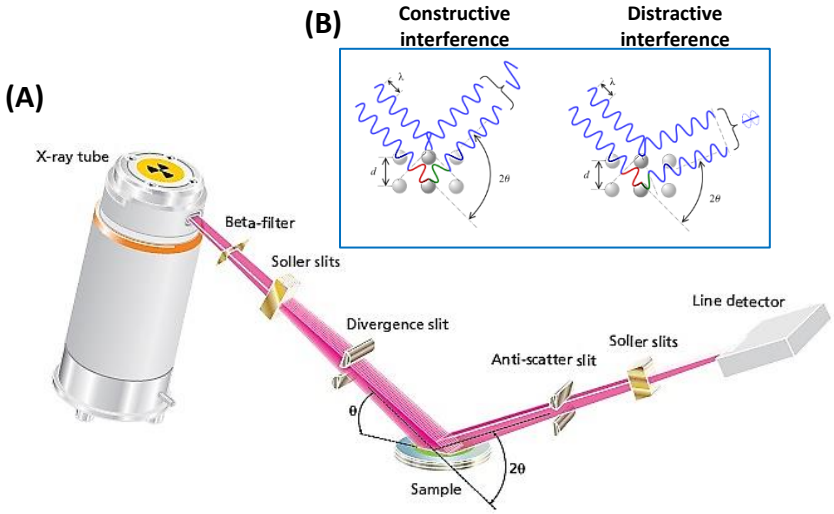

Figure 2.10: A schematic illustration of (A) the X-ray diffraction measurement and (B) Bragg's scattering principle [94].

X-Ray diffraction patterns were measured using a PANalytical Xpert Pro system equipped with an Empyrean diffractometer that can be used in reflection or transmission mode. The diffraction spectra of ZnO NPs in the powder form were recorded from 20^o – 80^o with scan steps of 0.026^o using CuKα radiation (λ = 1.5406 A^o) operating at 40 mA and 40 KV with a reflection mode.

2.5.6 X-ray Photoelectron Spectroscopy (XPS)

X-ray photoelectron spectroscopy (XPS) is a powerful surface analysis technique used to examine the surface chemistry and elemental composition within 10 nm from the surface of a film [95]. Its operation is based on the photoelectric effect explained by the following Einstein's question [96] which determines the binding energy of electrons in a given substance:

$$E_k = h\nu - E_B - \emptyset \qquad (2.7)$$

where E_k is the kinetic energy of the emitted electron, $h\nu$ is the incident photon energy, E_B is the binding energy of the photoexcited electron, $\emptyset$ is the workfunction and h is

Plank's constant. The binding energy of any given electron can be defined as the minimum energy required to remove an electron from its atom. For any given substance, electrons in the atom have a set of specific binding energies, which represents a fingerprint of that substance. Therefore, substances can be identified by analysing the speed and energy of the emitted electrons when irradiated with a monochromatic light source of well-known energy. X-ray photoelectron spectroscopy was further developed by the Swedish physicist Kai Siegbahn and his co-researchers at the University of Uppsala in early 1960s [97].

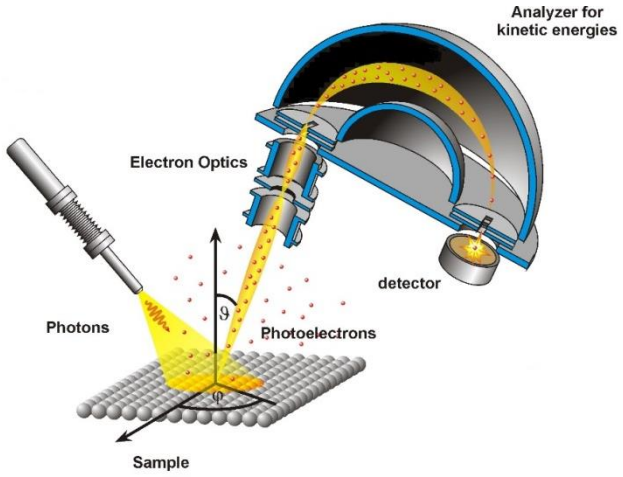

Figure 2.11: Schematic illustrating the three main requirements for X-ray photoemission spectroscopy [98].

XPS spectra were collected and measured using an experimental set-up similar to that illustrated in figure 2.11 [98]. A powerful monochromatic X-ray beam is normally used to irradiate the sample causing the removal of core electrons from the surface. This process occurs in ultra-high vacuum to maximize the collection of electrons. The ejected electrons have a range of kinetic energies. Most electrons ejected in XPS have energies in the range of 0 to 1500 eV. The ejected electrons have a range of kinetic energies and can be classified as primary and secondary electrons based on their kinetic

energy. The primary electrons are the ones with higher kinetic energy ($E_k = hv - \phi_{sample}$) which emitted directly from the Fermi level or somewhere close. On the other hand, the secondary electrons are the ones excited from deeper energy states and lost most of their kinetic energy by inelastic scattering process and barely made it to the surface. The primary and secondary electrons emitted from the surface are accelerated as they pass through the analyser, by a potential created as a result of work function difference between the sample and the energy analyser ($\emptyset_{sample} - \emptyset_{analyser}$) when they electrically connected through the sample holder, and collected using a hemispherical energy analyser (HEA) where electrons are dispersed based on their kinetic energy as shown in figure 2.11. The kinetic energy of the accelerated electrons reached the HEA are shifted to a higher value as a result of the acceleration process (to the amount of $\emptyset_{sample} - \emptyset_{analyser}$). In consequence, electrons with different kinetic energies are then counted by a detector located at the end of the HEA [99].

In this work, XPS spectra were acquired using on a Kratos AXIS HSi spectrometer equipped with a charge neutralizer and monochromatic Al Kα excitation source (1486.7 eV), with energies referenced to carbon at 284.6 eV. The samples were stored and handled in air. Spectral fitting was performed using the CasaXPS program. The measurement was performed in collaboration with Dr G. Kyriakou and Prof. A. Lee from Aston University's European Bioenergy Research Institute, Birmingham.

2.5.7 Transmission Electron Microscopy (TEM)

Transmission electron microscopy (TEM) is an electron microscopy technique that images samples using accelerated electrons. Here, electrons need to penetrate through the sample and are then collected on a screen contain a phosphorescent plate. The recorded image represents the number of transmitted electrons. Hence, only thin

samples which allow electrons transmission or porous materials can be measured with this technique. A schematic illustration of the TEM instrument, outlining the electromagnetic lens system and other imaging parts, is shown in figure 2.12 [100].

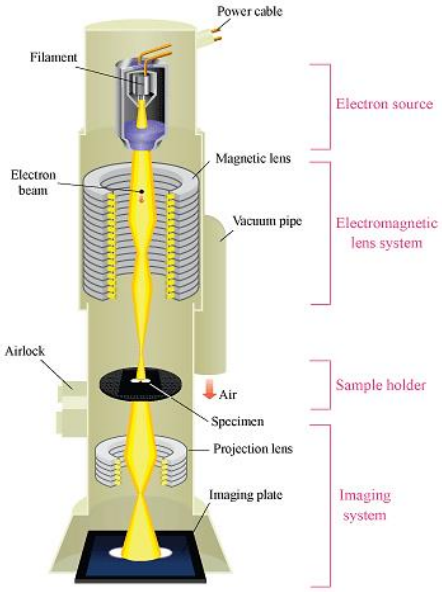

Figure 2.12: A schematic representation of the TEM and its optical components [100].

A High-Resolution Transmission Electron Microscope (TEM) recorded using a Cs aberration-corrected JEOL 2100F microscope at 200 kV was used in this work. A diluted solution of ZnO NPs (about 0.001%) was prepared and drop casted on carbon-copper grids bought from Electron Microscope Sciences (USA) so that individual nanoparticles could be imaged. The carbon-copper grids are made from pure carbon (30 nm) deposited on one side of the copper grid with 200 meshes.

2.5.8 Atomic Force Microscopy (AFM)

Atomic force microscopy (AFM) is normally used to characterize the morphology and surface topography of thin films irrespective of the material's conductivity status. This technique can efficiently measure, analyse and quantify the material's properties and

dimensions with a sub-nanometer image resolution provided in two and three dimensional illustration. The sample can be directly measured without the need for any coating or mounting. The measurement can be carried out not only in air but also in liquids and samples under pressure or at elevated temperatures [101,102]. The working principle of the AFM is based on measuring the interatomic force between the surface atoms and the AFM tip. The tip is connected to a flexible cantilever and has a diameter depending on the application. When the tip approaches the surface, the interatomic forces, either repulsive or attractive, vary with the distance between the tip and the surface, causing deflection in the cantilever. This deflection is measured and transformed to image the surface topography of the scanned area.

AFM can be performed in different modes based on the distance between the tip and the surface during the scanning process. The tapping mode, TM-AFM working principle is based on cantilever oscillation, at near resonance frequency, close to the sample's surface as shown in figure 2.13-B. During this process, the oscillation amplitude of the cantilever is monitored relative to any variations on the sample's surface which may cause deflection in position or change in the amplitude. This measuring mode is highly favourable when measuring samples with soft surfaces to reduce any possible damage from tip-surface contact.

On the other hand, the contact mode, C-AFM works with constant contact between the tip and the surface during the measurement as illustrated in figure 2.13-A [103]. The bending in cantilever resulting from the repulsive interatomic forces with the surface will form the AFM topography image. This technique is not suitable for soft materials since dragging the tip on the surface during the scan can damage the surface and the tip as well [104].

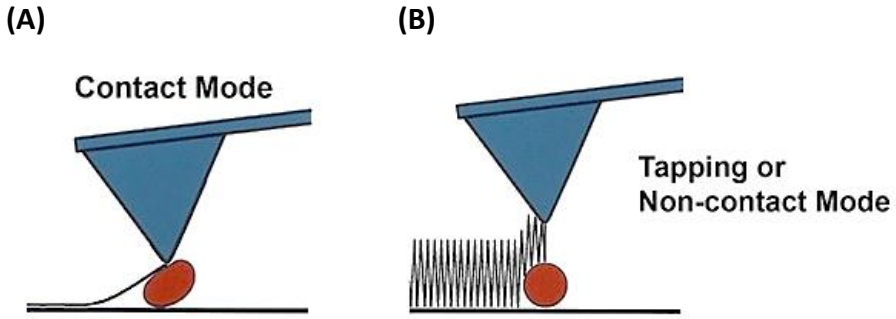

Figure 2.13: An illustration of (A) AFM operating in contact mode and (B) AFM operating in tapping mod. The solid line shows the path that the cantilever follows in each case [103].

In both modes, the movement of cantilever reflects the nature of the surface. The deflection of the cantilever can be measured using a light beam from a laser diode focussed on a reflective area located at the back of the cantilever. The reflected light is directed to a position-sensitive photodetector which detects any deflection or change in position of the cantilever in relating to features on the sample's surface.

A Dimension Edge with ScanAsyst AFM from Bruker was used to characterize the topography. The topography was recorded with the tapping mode using TESP-V2 etched silicon probes (42N/m, 320kHz, without reflecting coating to the back of the tip). The Dimension Edge AFM instrument used in this work is illustrated in figure 2.14.

Figure 2.14: A photograph of the Dimension Edge AFM from Bruker. [103].

2.6 Photocurrent-Voltage characteristics (I_P-V)

This characterization technique represents the cornerstone of testing the electrical properties of any photodetection device. It simply measures the current flow through the device by sweeping the voltages in the dark and/or on irradiation with light. The photocurrent characteristics of the photodetector device were tested on excitation with a150W Xenon light source (Bausch & Lomb) equipped with a 5 nm bandwidth, triple grating monochromator model (TMc300) and a set of lenses to collimate and focus the beam and make a uniform rectangular shape light beam covering the active device. The spectral response of the lamp extends from the UV to the near infrared. A solar simulator from ABET Technologies (DC Xenon Arc lamp, model 10500) was also used as an efficient white light source to measure the IR photoresponse of the plasmonic photodetector devices using a set of bandpass filters, purchased from THORLABS, covering the optical range from 600 nm to 950 nm with 10 nm FWHM. Furthermore, a tuneable energy, mercury UV lamp from OmniCure model (S1500) equipped with a liquid light guide and optical collimator was also used as an additional UV light source.

The optical system was interfaced with a Keithley 2400 source meter using BenWin+ software to acquire the photocurrent as a function of wavelength and time. For statistical reliability, two to four devices out of five on each substrate were measured. The optical power at each wavelength was calibrated using a computerized digital optical power meter PM200D from THORLABS.

Samples were electrically probed using different approaches. The first one is used the Ossila circuit board shown in figure 2.3-B to characterize the photodetector devices in the planar configuration. Secondly, probe needles were applied to characterize the electrical properties of ZnO NPs in different environments. The measurements were calibrated to give similar data accuracy. The measurements conducted in a CO_2 environment used a custom design sealed vacuum chamber consisting of a quartz window, a ventilation/pumping valve and electrical connection pins as shown in figure 2.15. The pins are wired and numbered in order to switch between devices on the same substrate. The wires were connected through a cable to an outside testing board, which was connected to the Keithley via two needle probes. After fixing the sample inside, the chamber was filled with CO_2 to a pressure of 150 mbar.

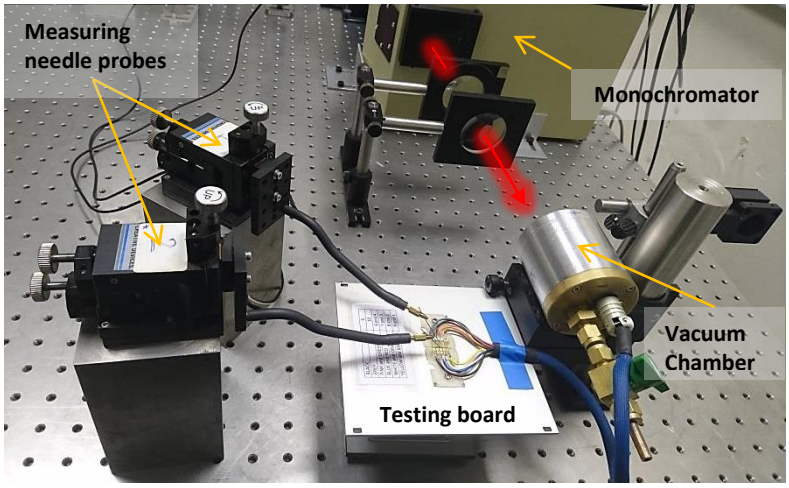

Figure 2.15: The electrical measuring setup used to study the electrical properties of ZnO NPs device under CO_2 environment.

I-V and photocurrent transient measurements were also performed in controlled atmospheric conditions using a motorized, custom designed microscopic probe station system installed in an isolated glove box. The glove box is surrounded by Faraday cage to help exclude any external electrostatic effect. The probe station equipped with two motorized needle probes, high-resolution camera and a UV light source (OmniCure) integrated with the system by liquid optical fibre. The probes are connected to two channels source meter model (Agilent B2912). The glove box atmosphere (nitrogen, dry air and humidity) can be controlled automatically with a custom designed controlling panel designed by Dr Emanuele Verrelli.

Chapter 3

UV Photodetection of Solution-Processed ZnO Nanoparticles

This chapter presents a study of how the device preparation and storage environment can influence the magnitude and time dependence of the UV photodetection of solution-processed ZnO nanoparticles. The generally accepted UV photoconductivity mechanism in ZnO involves oxygen adsorption. However, here we find that humidity and surface carbonates are found to have a big influence on the photoresponse of ZnO nanoparticles. The electrical observations are correlated with surface wettability and FTIR spectra to elucidate the surface mechanisms which impact the photoconductivity.

3.1 Introduction

ZnO is a wide band gap metal oxide semiconductor with some unique optoelectronic properties such as the high optical transparency and an exciton binding energy of 60 meV at room temperature [105]. Optoelectronic devices based on ZnO nanoparticles (NPs) have witnessed revolutionary developments in their applications such as photodetectors, wearable and flexible display devices. However, in order for those applications to be industrially viable, a very good understanding of the effects of storage environment on the photoactivity of the ZnO NPs is needed, since mostly all the optoelectronic devices are exposed to the ambient environment in one way or another.

ZnO mainly absorbs light in the UV which enables it to be very efficient in UV photodetection applications. However, ZnO in the nanostructure form has a number of very active surface defects, which are found to affect the material's electrical and optical properties. With a variety of advanced fabrication techniques, solution-processed ZnO nanostructures are considered to be low-cost, relatively simple to fabricate and compatible with mass production. However, organic ligands are often added to the ZnO nanoparticles to improve solubility in organic solvents and aid device fabrication. This approach has disadvantages since they electrically isolate the ZnO particles and hinder electronic transport in the resulting thin films. There may be other organic residues from the starting precursor in the processed thin film, which may also affect the film quality. Therefore, it is important to remove ligands and other contaminants after the fabrication process. Normally, organic ligands are carbon-based complexes which can be removed or partially decomposed by either UV irradiation or annealing. Another important issue is the interaction with the environment. Solution-processed ZnO NPs photodetection is widely affected by the surrounding environment, specifically oxygen and humidity.

In this chapter, we present a study of how the device preparation, storage and measurement environment can influence the magnitude and time dependence of the photoconductivity. The experiments are correlated with surface wettability and FTIR measurements to elucidate the surface mechanisms which impact the photoconductivity.

3.2 Chemical reactivity of ZnO nanostructures surface

ZnO has a wide and direct band gap and has great potential in optoelectronics and gas sensing applications. The optical and electrical properties of ZnO are varied when the material is reduced in size to the nanoscale, mainly due to the quantum confinement effect where optical absorption is blue shifted with reducing the particle size [106]. The surfaces of ZnO nanostructures also have a rich defect chemistry [107] and are considered as attractive sites for oxygen molecule adsorption. For example, oxygen [108] and ozone [109] represent oxidative gases which help trap electrons from the conduction band of ZnO leading to a decrease in its conductivity. A space charged region is then formed on the surface of ZnO as a result of electron trapping, as shown in figure 3.1. The diameter of this region is known as Debye length (λ_D) and it may be comparable to the material's diameter depending on the concentration of electrons and temperature. For ZnO with dielectric constant of 8.2 and carrier concentration of 10^{18} to 10^{19} cm^{-3}, the depletion region area (λ_D) was found to be 1-3 nm [110]. Kolmakov et al. [111] found that the diameter of the depletion region could reach 30 nm for undoped ZnO. On the other hand, CO [112] and H_2O [113,114] represent reductive gases which react differently with the ZnO surface. These gases release the trapped electrons by desorbing the oxygen molecules on the surface leading to an increase in electrical conductivity and therefore, reducing the depletion layer [8]. This represents the vital role by which ZnO or other metal oxide semiconductors can function as a gas sensor. The smaller the size of the

material (equal or smaller than the Debye length), the higher the sensitivity. The mechanism by which electrons are captured by oxygen molecules has been explored over many years. The ionization energy of these electrons is very low owing to the small energy gap with the conduction band. Therefore, large numbers of electrons are easily ionized and transferred to the conduction band at room temperature or lower. This is believed to be the responsible of the material's n-type conductivity [111].

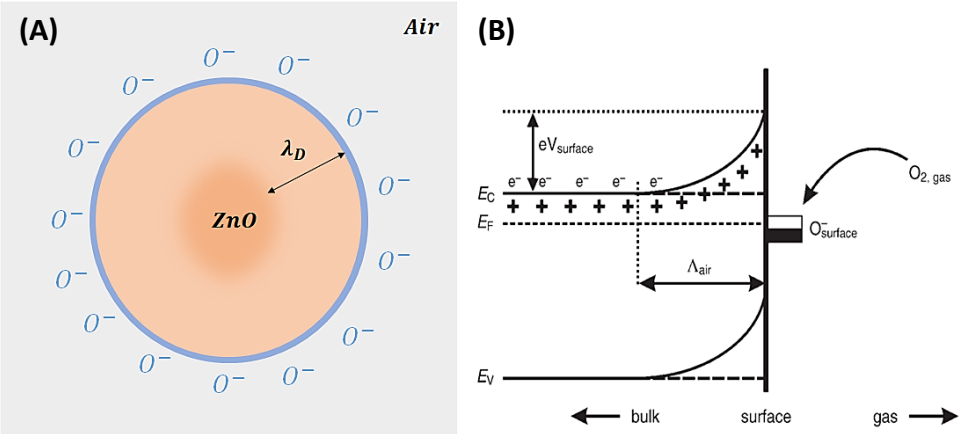

Figure 3.1: (A) An illustration of the surface reaction of ZnO nanoparticles located in air. Oxygen molecules are adsorbed on the surface of ZnO creating a space charged region with thickness equivalent to the Debye length, λ_D. Adapted from ref. [111]. (B) A model illustrating the energy band bending at the surface of a wide band gap semiconductor after chemisorption of oxygen and the formation of the space charged region denoted as Λ_{air} [119].

The electrical properties of ZnO nanostructures are closely related to the space charge region on the surface, which is very sensitive to the surrounding atmosphere. For instance, when ZnO interacts with CO gas or water vapour, the region is affected by the interaction of atmospheric gases with the adsorbed oxygen on the surface. Normally, oxygen molecules and water vapour (in the form of either molecular or hydroxyl moieties) compete to react with the oxygen vacancies sites on the surface of ZnO [115]. On the other hand, CO gas interacts with adsorbed oxygen ($O^-_{(ads)}$) leading to release the trapped electrons (e^-) and the formation of carbon dioxide gas $CO_{2(g)}$ [111,116,117].

Furthermore, CO is also found to react with the lattice oxygen on the surface giving carbonate groups at temperature between 150 to 400 ºC and carboxylate groups at temperature between 250 to 400 ºC as indicated by FTIR [118].

Surface reactions with atmospheric gases could help reduce the Schottky barrier because the captured electrons are released to the conduction band increasing the electrical conductivity. In this situation, the semiconductor conductance (G) can be given by the relation [119,120]:

$$G \approx \exp\left(\frac{-eV_{\text{surface}}}{K_B T}\right) \tag{3.1}$$

where V_{surface} represents the height of the surface potential barrier. The surface charging or the depletion region causes a potential barrier on the surface (which is denoted as a Schottky barrier) with height depending on the oxygen adsorbed concentration (captured electrons) [121] as shown in figure 3.1-B. The depth of the energy band bending is related to the Debye length (λ_D) which is a characteristic of the semiconductor and strongly depends on the concentration of surface defects, surface adsorbed oxygen, dielectric constant of the metal oxide semiconductor (ε) as well as the carrier concentration (N_D), as calculated from the following question [119]:

$$\lambda_D = \left(\frac{\varepsilon K_B T}{e^2 N_D}\right)^{1/2} \tag{3.2}$$

where K_B is Boltzmann constant, T is the operating temperature and e is the electron charge. The increased potential barrier resulting from the surface depletion region affects the mechanism of electron transport between the grains of two neighbouring nanoparticles. Therefore, the metal oxide conductance is highly related to the surrounding environment. As illustrated in figure 3.1, the space charge region has a stronger effect on small particles compared to larger ones. When the particle size is

small and the depletion region is of the order of the radius of the particle, any reduction in the depletion length greatly increases the conductivity because of the greater ease of inter-particle hopping between the high conductivity regions of the particles. This feature is the cornerstone of gas sensors based on metal oxide nanostructures, where the sensitivity substantially increases with reduced structure size [122,123]. More information about how the grain size affects surface potential can be found in ref. [121,124,125]. It is also found that the particle size has a significant effect on the carrier concentration of ZnO. In air with oxygen adsorption onto the surface, large particles of size 50 nm have carrier concentrations between two and four order of magnitude higher than smaller particles of size 20 nm [110].

The change in surface conductivity resulting from this charge transfer is governed by a few important parameters, such as the surface atomic composition, bonding and ZnO surface polarity. The ZnO crystal orientation (polar and nonpolar facets where ZnO surface has either a Zn terminated plane or an O-terminated plane) is believed to potentially affect the UV photoconductivity. Chao et al. [126], have used plasma-enhanced chemical vapour deposition to synthesize the polar and nonpolar thin film UV detector. The Zn-terminated plane is found to be more chemically active than the O-terminated surface which is useful in detection applications.

Oxygen can be adsorbed onto the surface as either molecular (O_2^-) and/or atomic (O^-) species based on the provided temperature. It was found that oxygen is adsorbed as a molecule at a temperature below 150 ºC, while atomic adsorption is dominant at a temperature greater than 150 ºC [125].

3.2.1 Water reaction on the surface of ZnO

A Schottky junction is normally created when ZnO is intimately interfaced with ITO metal oxide electrodes due to the relative difference in their Fermi level energies as discussed earlier in chapter 1, section 1.7. Upon contact, the Fermi levels of both materials come into equilibrium and a potential barrier is established at the interface limiting electrons flow between the ZnO and the ITO. The barrier height can be increased or decreased by applying a negative or positive bias voltage respectively on the metal. Schottky junctions are found to be sensitive to the presence of humidity especially when forward biased, owing to the water electrolysis at the positive (oxidation) and negative (reduction) side of the junction [127].Water vapour on the ZnO surface can be adsorbed and electrolyzed at the interface with a metal electrode. Therefore, water can be decomposed to form oxygen at the anode whilst hydrogen can be formed at the cathode, according to the reactions [128]:

$$2H_2O \leftrightarrow O_2 + 4H^+ + 4e^- \qquad (\textit{at the anode}) \qquad (3.3)$$

$$2H^+ + 2e^- \leftrightarrow H_2 \qquad (\textit{at the cathode}) \qquad (3.4)$$

Water electrolysis on the surface results in proton conductivity. In the work of Chatman et al. [128], the current generated by protonic conduction resulting from water electrolysis is about 10 mA which is significantly higher than the Schottky current which is in the range of 10-100 μA. Electrical conductivity of adsorbed water is carried out by protons, by means of a mechanism explained by Grotthus and given his name [129]. The protons transfer between the water molecules by the formation and breaking of covalent bonds via hydrogen bonding with neighboring molecules in the liquid phase as illustrated in figure 3.2.

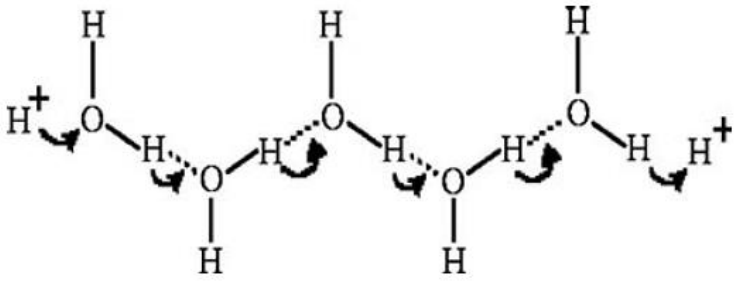

Figure 3.2: An illustration of proton transfer between adjacent water molecules as explained by the Grotthus mechanism [129].

Normally, ZnO behaves differently in the presence of humidity. With the very high level of water vapour, water molecules are physisorbed and chemisorbed on the surface leading to protonic conductivity. Water adsorption on the surface takes place in three different stages as shown in figure 3.3-A. At the beginning, a water molecule is chemically adsorbed onto a surface active site to form an adsorption complex. This adsorption complex eventually forms surface OH^- ions. Thereafter, another water molecule approaches the surface and is physisorbed by two hydrogen bonds to the hydroxyl groups. It is believed that no proton conduction takes place at this stage owing to the missing hydrogen bond between them. However, the first physisorbed and chemisorbed layers can help with electron tunneling between the adsorbed water molecules on the surface [130]. With a high level of water molecules approaching the surface, water forms an extra layer on top similar to bulk liquid water, by the formation of a hydrogen bond. This process is illustrated in figure 3.3-B and leads to protonic conduction as described above by the Grotthus mechanism [129].

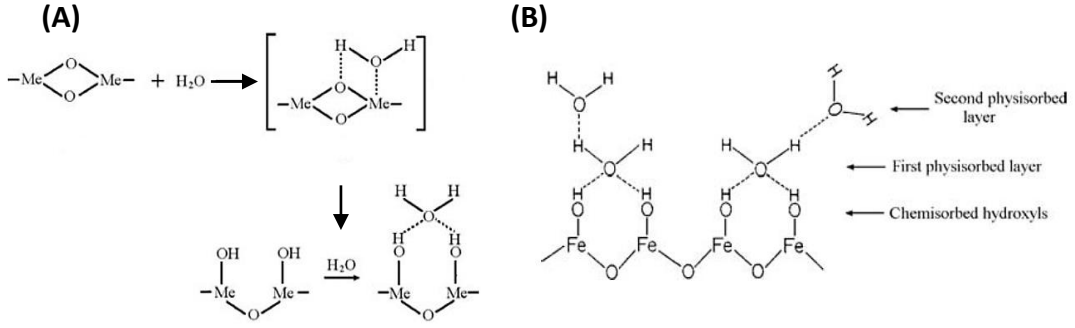

Figure 3.3: An illustration of (A) the three stages of water adsorption to a binary metal (Me) oxide semiconductor, and (B) the multilayer structure of water adsorption on iron oxide Fe_2O_3 [129,289].

The interaction of OH^- with the surface of ZnO greatly affects the surface chemical and electronic properties. Generally, there are two different known types of OH groups originating from the interaction of hydrogen, produced by electrolysis, with ZnO at room temperature. The first one resulting from water dissociatively adsorbed on the oxygen and zinc sites, similar case to stage two illustrated above in figure 3.3-A which give rise of strong IR signals at 3498 cm^{-1} and 1708 cm^{-1} assigned to the stretching vibration of OH and ZnH respectively. The water adsorbed on the ZnO surface, which eventually dissociates to hydroxyl groups, shows surface orientation and crystallographic dependence. Noei et al. [131] found that the polar and nonpolar ZnO surfaces respond differently to the water adsorption. Different OH species were created when water is dissociated on ZnO surface with different atomic terminations.

3.3 ZnO as a UV photodetector

ZnO has received great attention due to its superior performance in photonic and electronic applications. The wide direct band gap enables ZnO to be the material of choice in photodetection applications especially in the UV part of the light spectrum. ZnO has a band gap of 3.37 eV at room temperature which made it a very good light

absorber in the spectral range from 320 to 400 nm, also known as UV-band A. ZnO has a great history as a UV photodetector started from the late 1980s [132] with simple structured devices having poor performance until the current generation of very advanced device structure with outstanding performance. High-performance ZnO UV photoconductors were developed by adopting a variety of techniques such as n-doping the ZnO, utilizing different metals electrodes and different device structures. Moreover, ZnO based nanostructures are considered as a promising approach to modifying the electrical and optical properties by changing the size and shape of ZnO [64]. Upon irradiation with UV light, electron-hole pairs are photogenerated. The holes migrate to the ZnO surface along the potential gradient resulting from the energy levels band bending and desorb the oxygen molecules from the surface leading to the release of trapped electrons to the conduction band as shown in figure 3.4. Electrons generated by the photoabsorption in addition to the electrons released from the surface significantly increase the ZnO conductivity [133]. Oxygen adsorption/desorption on the surface of the ZnO is found to play a crucial role in the optical responsivity of the ZnO photodetector. As we know, oxygen adsorption introduces energy levels (traps) within the band gap. The photocurrent value and the response time of the detector depend on the number of traps levels, so it is important to control trap levels for reliable device fabrication.

Metal-semiconductor-metal (MSM) is the common device configuration with ZnO as an active medium. This type of configuration has the advantage of high internal gain based on hole trapping which enables electrons to pass the circuit many times before recombine. However, it normally has a high dark current and slow decay time.

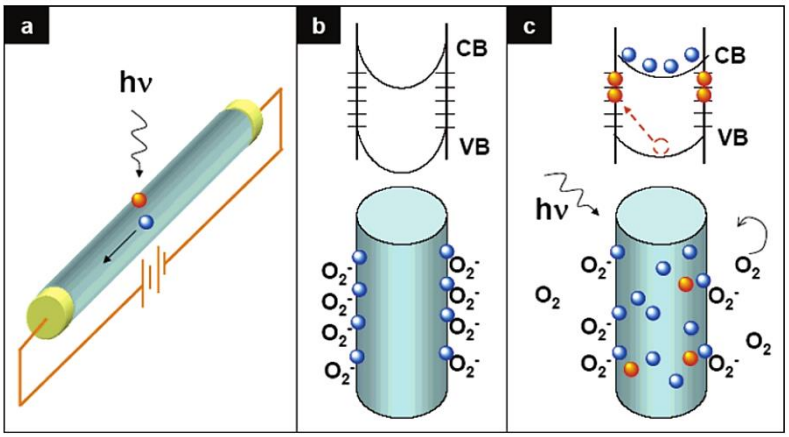

Figure 3.4: An illustration of the photoconduction mechanisms in ZnO nanowires. (a) Photogenerated electron-hole pairs are created with light absorption, (b) prior to photoexcitation, oxygen molecules are adsorbed on the surface of ZnO nanowire trapping electrons, and (c) oxygen molecules are discharged by the photogenerated holes, releasing the trapped electrons [133].

There are a variety of ZnO thin film preparation techniques including chemical vapour deposition (CVD), electron beam lithography, thermal evaporation, solution processing and more. Solution processing using sol-gel preparation method is a low-cost approach to fabricate photodetector devices, compatible with large-scale production. However, solution processed UV photodetector devices are not yet commercialized due to their low performance as compared with gallium nitride (GaN) photodetectors. One of the main problems is the charge transport in the solution processed film. Nanoparticles, for instance, have many grain barriers in addition to extra barrier to electron transport caused by the organic ligands added to processes the film. Great progress has been achieved concerning the device fabrication and photoresponse. For example, solution-processed ZnO colloidal nanostructures blended with organic ligands show very low dark current with high UV responsivity of 61 A/W [78].

In this short review, we summarise work on persistent conductivity in solution-processed ZnO photodetectors to provide context to our own research results. Solution-processed fabrication technology represents a future vision for low-cost manufacturing

due to the ease of processing, large-scale production, less energy consumption and relatively low cost as compared with conventional fabrication methods. All those factors have encouraged more research in this promising field. Therefore, a variety of ZnO nanostructures, such as nanoparticles [78], nanowires [134,135], nanobelts [136], nanorods [137], etc have been fabricated and used in photodetector devices. A highly UV sensitive, single ZnO nanowire photodetector prepared by vapour phase transport was reported for the first time by Yang et al. [81] The UV photoresponse of the wires was high and the dark current was low. It was found out that the photoconductivity is highly sensitive to the environment with a slow response time in vacuum and inert gases and a fast response time in air owing to the adsorption of oxygen molecules. Solution-processed ZnO polycrystalline UV photodetector were prepared and investigated by D. Basak et al. [138] with gold electrode contacts. The device shows a low responsivity of 0.040 A/W at 350 nm with 5V bias and 14% quantum efficiency. The search for solution processed photodetectors with high optical response led researchers to chemically dope the ZnO with different metals. Zi-Qiang Xu et al. [139] reported the fabrication of MSM photodetectors based on solution processed, Al-doped, ZnO films with gold electrodes for lower dark current and hence better signal to noise ratio as well as tuneable UV photodetection. The low dark current results from the high Schottky barrier that ZnO made with the Au. The device shows a photocurrent of 58.05 μA at 6V bias. Greenham et.al. [78] used ZnO colloidal nanoparticles as a UV light absorber in MSM photodetector using gold electrodes. The device was visible blind and showed good reproducibility with very low dark current and responsivity of 61 A/W at 370 nm with 120V bias. The photocurrent mechanism was dominated by electrode injection rather than oxygen adsorption on the surface. The injection barrier between the ZnO and the metal contacts played an essential role in controlling the dark and photocurrent as

shown in figure 3.5. Moreover, adsorbed oxygen at the ZnO/metal contact interface altered the density of defects states and hence the injection barrier height. By switching off the UV light, readsorption of oxygen at the ZnO/Au electrode interface will help increase the barrier height leading to a fast decay in photocurrent compared to the ZnO interfaced with Al where the barrier height is very small.

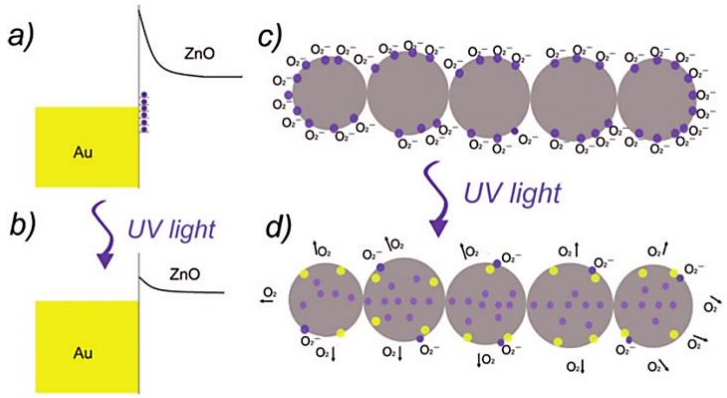

Figure 3.5: The effect of oxygen adsorption on the electrons injection barrier between the ZnO and the Au electrode is shown. The Schottky barrier at the electrode is shown (a) in the dark and (b) on photoirradiation. The adsorption of oxygen on the surfaces of the nanoparticles traps electrons in the dark in (c). (d) Photogenerated holes results in the removal of adsorbed oxygen, releasing electrons and reducing the injection barrier upon UV irradiation [78].

Chen et al. [140] investigated the effect of the crystallization on the photodetection properties of sol-gel ZnO film. The device showed low dark current with a responsivity of 1.1 A/W at 360 nm with 5V bias. Sangsig Kim et al. [141] also reported the fabrication of UV photodetector based on ZnO nanoparticles. Their device showed a high light to dark current ratio of about 10^6 with 0.1 mA/W at 1V bias at 325 nm. Liqiao Qin et al. [142] reported a big improvement in MSM based ZnO NPs UV detectors with a responsivity of 371.42 A/W at 345 nm with 20V bias. They showed that surface defects such as Zn^{2+} ions and oxygen vacancies were passivated by coating the ZnO nanoparticles with polyvinyl-alcohol (PVA) to give a reproducible device with high

optical responsivity. Afal et al. [134] reported a lateral UV photodetector based on solution processed ZnO nanowires grown hydrothermally. The device was in situ heated at 150 ºC on the hot plate during the responsivity measurements to remove any water molecules remaining or adsorbed on the surface of the ZnO wires and also to enhance the oxygen molecules adsorption for better responsing time. The device measured at 150 ºC showed shorter response and recovery times compared to the one measured at room temperature, with responsivity of 0.46 A/W at 380 nm with 2V bias measured at 150 ºC. The UV photoresponsivity of ZnO was also enhanced by the incorporation of plasmonic gold nanoparticles. The Au nanoparticles work as hole trapping points which improve the device performance [143]. ZnO photodetectors have also been grown on environmentally friendly paper substrates at low temperature [137]. This reflects the technological development and the great potential of ZnO to lead in the photodetection industry. Solution processed ZnO nanoparticles with film thickness of 5 nm deposited on flexible PET substrate, exhibited a remarkable transparency of 90% and UV responsivity of 1.51×10^5 A/W owing to the incorporation of 2-4 nm Au nanoparticles on top of the film. The depletion layer created by the adsorbed oxygen molecules on the ZnO surface, in addition to the localized Schottky junctions between the ZnO particles with the Au nanoparticles, helped to significantly reduce the dark current of the photodetector device [144].

3.4 ZnO surface wettability

Surface wettability is indicated by the value of contact angle of the surface with water. For materials to be defined as hydrophobic, the water contact angle with the surface has to be larger than 90º. On the other hand, if the water contact angle is smaller than 90º, the material is classified as hydrophilic. The surface wettability of ZnO can be

transformed by either covering the surface with specific coatings or by irradiation with UV light. It was shown that the surface changes from hydrophilic to highly hydrophilic after UV irradiation. This effect is found to be reversible: after removing the UV light the sample returns to its original state of hydrophilicity after time. The suggested mechanism is that carbon contamination adsorbed on the surface is released by UV irradiation and adsorbed back onto the surface after the UV [145]. However, later results showed that carbon removal from the surface did not produce a hydrophilic surface [146]. This suggests that the photocatalytic removal of surface contamination by UV irradiation might not be an accurate explanation to what is going on. Sun et al. [146] reported changes in the wettability of ZnO and TiO_2 after irradiation with UV. Their study shows that an oxygen environment with humidity < 10% plays an important role in returning the surface wettability of ZnO from hydrophilic to hydrophobic after UV irradiation. On the other hand, the contact angle was found to increase much less when storing the sample in pure argon with humidity < 10%. They suggest that upon UV irradiation, oxygen molecules adsorbed on the surface are released and water molecules adsorb dissociatively on the defect sites on the surface. They also found out that, after annealing at a temperature higher than 300 ºC, the contact angle decreased remarkably resulting from the increase in the density of surface defects and hence adsorbed water molecules. This result is supported by Hu et al. [147] who theoretically investigated the surface wettability of ZnO with and without oxygen vacancies by simulating the surface bond between Zn in ZnO and O in H_2O in the presence of one water molecule, a water monolayer and a water film. Water adsorption on the surface of ZnO was found to increase with increasing the oxygen vacancies. It also reveals that the surface hydrophilicity of the ZnO strongly depends on the density of oxygen vacancies on the surface.

It was observed that hydrophilic ZnO (irradiated with UV) tends to change its wettability to hydrophobic when stored in dark places. The time needed to convert wettability depends on the sample and treatment but could take a few weeks in the dark to reverse the wettability. Surface roughness was also found to play an important role in the value of the contact angle. A low contact angle is observed with rough surfaces [148]. Another study suggested that, for TiO_2, ZnO and other wide band gap semiconductors, the contact angle starts to return to its original value before the UV by irradiation with visible light [149].

Upon UV irradiation, water can better penetrate the film grooves so that it covers a higher surface area on the ZnO giving high hydrophilicity. On the other hand, in the dark, the lack of OH on the surface prevents water from penetrating and so leads to high hydrophobicity. This comes about because the surface is energetically unstable after OH^- adsorption, while oxygen is thermodynamically stable when strongly bonded to the defects sites. It is also suggested that this adsorption/desorption of oxygen and hydroxyl takes place on the surface of the metal oxide leaving the core bulk untouched, which explains the long term durability in wetting switching [150].

The wetting states of metal oxide semiconductors are normally controlled by two main key factors, the surface morphology and surface defects. Defect radicals attached to the surface can be efficiently detected by FTIR. Water wettability is linked to the concentration of hydroxyl and carboxyl groups on the surface of ZnO nanowires with the surface showing higher wettability when the density of these groups on the surface is high. The surface converts to hydrophobic when the density of these groups decreases or disappears (due to their thermodynamic instability) when the sample stored in dark. Yadav et al. [151] reported the effect of oxygen and hydrogen gases on the surface contact angle of ZnO. The water contact angle followed a consistent trend with a higher

contact angle when annealing in hydrogen and lower contact angle with oxygen annealing, as shown in figure 3.6.

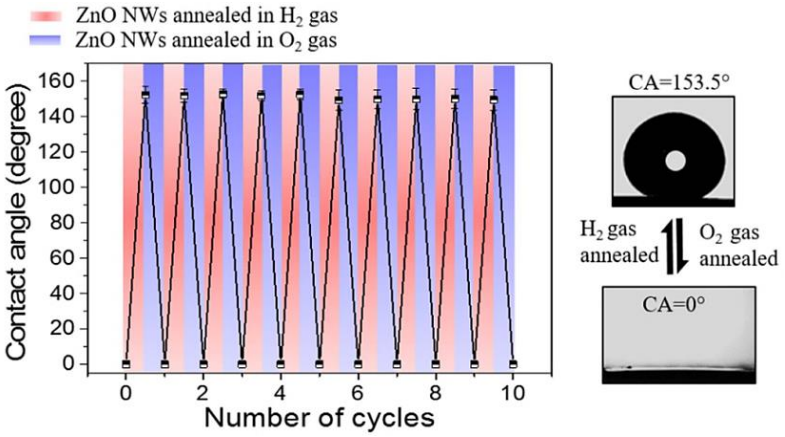

Figure 3.6: The ZnO contact angle following annealing in different ambient gases, oxygen and hydrogen [151].

3.5 Methodology

3.5.1 Device preparation

ZnO nanoparticle suspensions of 2.5 wt. % concentration in chloroform was incorporated as the active layer in UV photodetectors with a planar configuration. The layer was spin coated either in air or nitrogen on a glass/interdigitated ITO substrate at a fixed spin speed and baking temperature for device comparability. Moreover, the particles have a uniform size distribution of 11.8 ± 1.7 nm according to TEM (figure 3.8-A). The device thickness was about 120 nm (± 5 nm) unless stated otherwise. After spin coating and baking, the film was annealed at 350 ºC in air, oxygen or nitrogen for better film uniformity and also to remove the capping octylamine ligands for better electrical connection. The device area and ITO substrate specifications are specified earlier in chapter 2 section 2.3.1. The photodetector fabrication process did not involve

any vacuum evaporation or any harsh processing steps. A schematic representation of the ZnO UV photodetector is shown in figure 3.7.

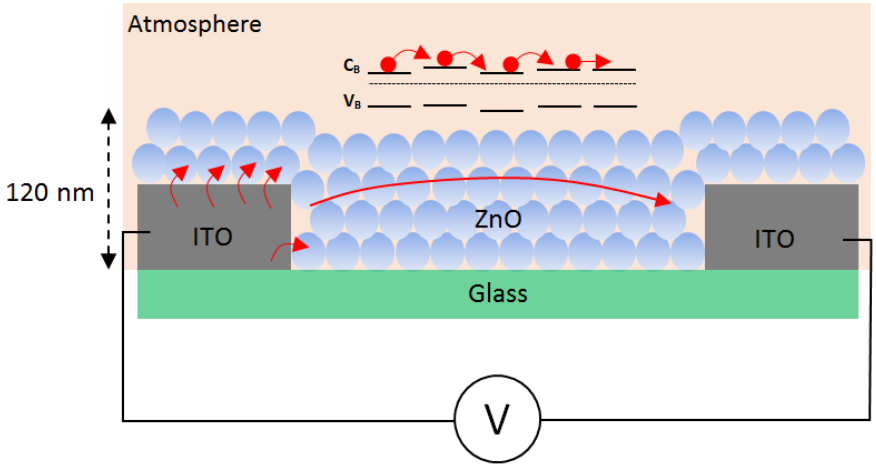

Figure 3.7: 2D schematic illustrating the solution processed ZnO UV photodetector used in this study. It also illustrates electrons injection from the electrode to the ZnO nanoparticles. The ZnO thickness is about 120 nm. The inset depicts electron transport by hopping between the particles.

The interface between the particles and the electrodes is not continuous owing to the spherical particles' shape. Therefore there are voids where gases in the atmosphere can easily penetrate to the interface region. Moreover, in this planar device configuration, the ambient environment influences the electrical and optical properties of the ZnO and its photocurrent response. It is also suggested that electrons are more likely to be injected to the ZnO from the large ZnO/ITO electrode contact area on top of the electrodes rather than the sides, where a very small area of the nanoparticles is in direct contact with the ITO. Furthermore, the electrons' percolation path will be dictated by the interface, environment and voids within the film.

3.6 Experimental results

3.6.1 Physical characterization

Solution-processed ZnO NPs structural properties were characterized using different techniques including dark field HR-TEM, XPS, FTIR and XRD. The crystallinity of the ZnO NPs is confirmed using the dark field HR-TEM as shown in figure 3.8-A. The average particle diameter is found to be 11.82 ± 1.7 nm (based upon analysis of more than 100 particles) with a lattice spacing (d-spacing) of 0.26 nm for the (002) lattice plane. Moreover, an XRD scan shows a typical diffraction pattern of the ZnO wurtzite crystal structure as shown in figure 3.8-B.

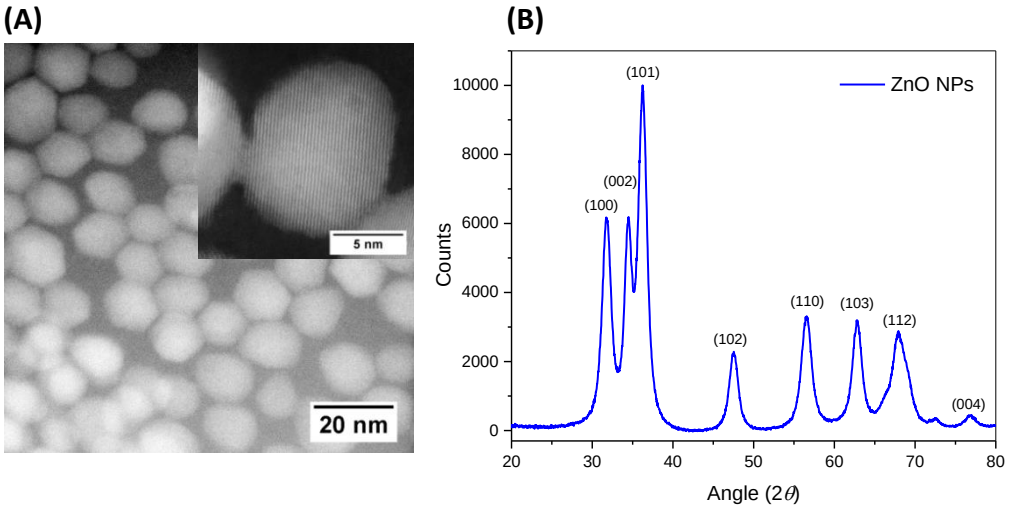

Figure 3.8: (A) A TEM dark field image of the as-synthesized ZnO NPs. The inset shows a dark field high resolution TEM image of crystalline ZnO nanoparticles, (B) X-ray diffraction of the ZnO nanoparticles prepared by the sol gel method. The spectrum of ZnO was taken in the powder form.

ZnO NPs films spin-coated on silicon substrates and annealed at 350 °C in air or nitrogen were investigated using X-ray photoelectron spectroscopy (XPS). The XPS spectra of O 1s, C 1s and Zn 2p spectral regions of the ZnO NPs after the annealing are shown in figure 3.9. The Zn:O atomic ratio was essentially the same for annealing under

both environments at ~0.65, somewhat lower than expected for stoichiometric ZnO indicating the presence of oxygen vacancies. In contrast, the C:O atomic ratio was higher for the sample prepared via N_2 versus air annealing (0.86 versus 0.65 respectively). This also contained trace surface nitrogen, together suggesting an incomplete decomposition of the octylamine stabiliser during nitrogen thermal processing. Zn 2p XPS spectra (figure 3.9-A) exhibited a single chemical environment at 1021.4 eV binding energy consistent with Zn^{2+} in ZnO [152]. The O 1s spectra (figure 3.9-B) exhibits three distinct chemical environments and can be fitted with three peaks according to Zhang et al [153]. The three peaks are associated with the oxygen lattice (O_L) in ZnO at 530.14 eV, oxygen vacancies (O_V) at 531.24 eV, and either a dissociated oxygen species (O_C) or surface hydroxyls (which possess a higher intensity following annealing in air) at 532.2 eV [146]. The ratio of (O_L) : (O_V) : (O_C) components for the nitrogen annealed sample was 1.0 : 0.24 : 0.14 while that for the air annealed sample was extremely similar at 1.0 : 0.27 : 0.21, indicating similar surface concentration of oxygen vacancies following both pretreatments and different level of surface hydroxyl in the two samples. The C1s XPS spectra (figure 3.9-C) of both samples exhibit two distinct chemical environments, a strong feature at 284.4 eV consistent with an aliphatic hydrocarbon chain arising from the octylamine stabiliser, and a weak high binding feature at 288.9 eV indicative of a carboxylate [154,155]. This is due to either partial decomposition of the acetate precursor or adsorption of atmospheric CO_2 during sample storage and handling in air. Since the ZnO NPs were annealed to 350 °C prior to XPS analysis, sufficient to fully decompose the zinc acetate precursor [156], the former possibility can be discounted for the sample annealed in air, with carbonate formation simply reflecting atmospheric CO_2 adsorption.

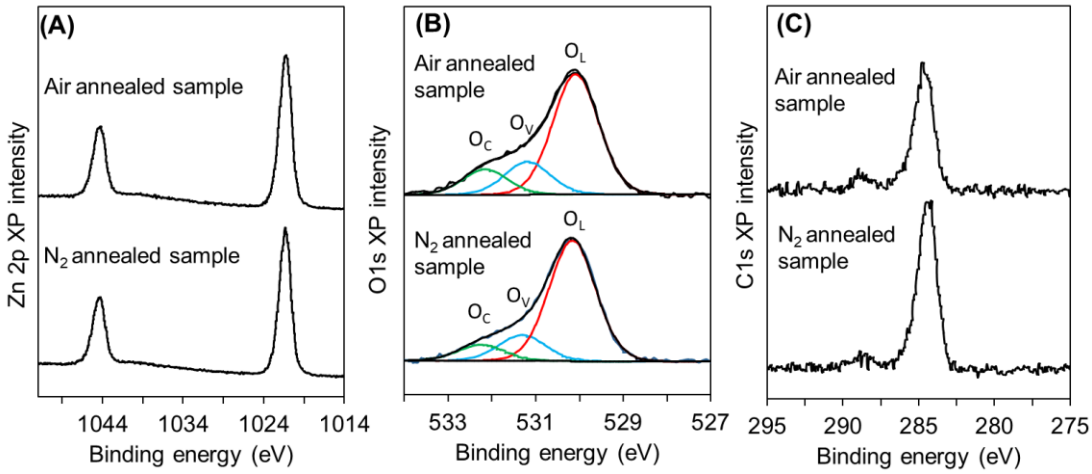

Figure 3.9: XPS spectra of ZnO NPs spin coated and annealed at 350 °C for 1 hour in air and N_2 showing the spectral regions of (A) Zn 2p, (B) O 1s and (C) C 1s. Spectral fitting was performed using CasaXPS with help from G. Kyriakou and A. Lee, Aston University, Birmingham.

3.6.2 Surface morphology

Atomic force microscopy (AFM) working in the tapping mode was used to investigate the surface topography and roughness of ZnO NPs films prepared and annealed in air and nitrogen. This section sheds light on the impact of preparation environment and annealing on the ZnO NPs surface morphology.

3.6.2.1 ZnO NPs films prepared and annealed in air

AFM images shown below reveal the porous nature of ZnO NPs films prepared and annealed in air. Figure 3.10-A and B show the surface morphology of ZnO NPs films after baking and annealing respectively. Regardless of the particle size, spin coating the ZnO NPs in air followed by baking at 100 ºC for 10 min results in dense particle-like features distributed semi-uniformly on the surface as shown in figure 3.10-A. The average surface roughness (is a property of the surface which describes the irregularities of the sample morphology) extracted from the full-size AFM image is 8 nm. Figure 3.10-B shows the 2D and 3D topography images of the ZnO NPs prepared and annealed

in air at 350 ºC for 1h. Film morphology in the two processing conditions (after and before annealing) looking similar with ridge-like features and roughness of 8 nm.

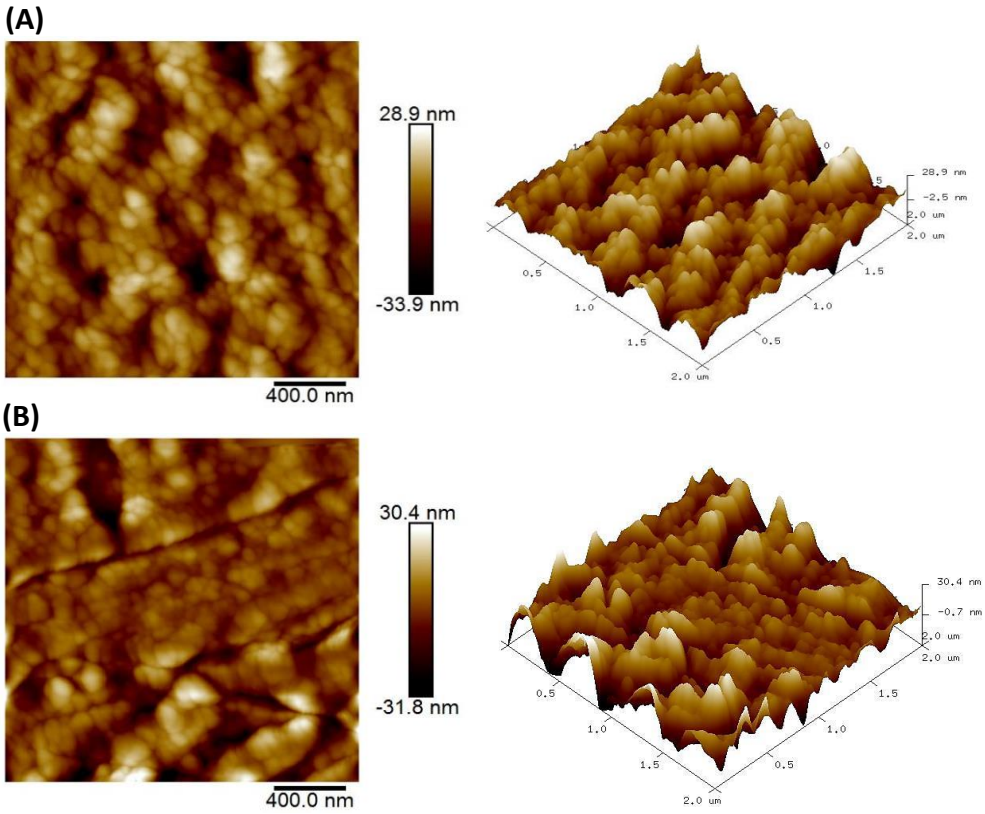

Figure 3.10: 2D AFM images with their corresponding 3D topography of ZnO NPs films prepared in air with (A) baking at 100 ºC for 10 min and (B) annealed after baking at 350 ºC for 1h. Surface roughness, as represented by the average root mean square of the overall AFM image, is 8 nm for both samples.

3.6.2.2 ZnO NPs films prepared and annealed in nitrogen

ZnO NPs films prepared and annealed in nitrogen environment were also imaged by AFM. Figure 3.11-A shows the 2D and 3D AFM images of ZnO NPs film prepared in a nitrogen environment and baked at 100 ºC for 10 min. The film shows particle-like structures with bigger agglomeration features compared to the air sample shown in figure 3.10-A. The surface roughness after baking was 8 nm which is the same as the sample prepared in air. After annealing the sample for 1h at 350 ºC in nitrogen, the

surface morphology shows some particle agglomeration, which increases the film roughness to 15 nm.

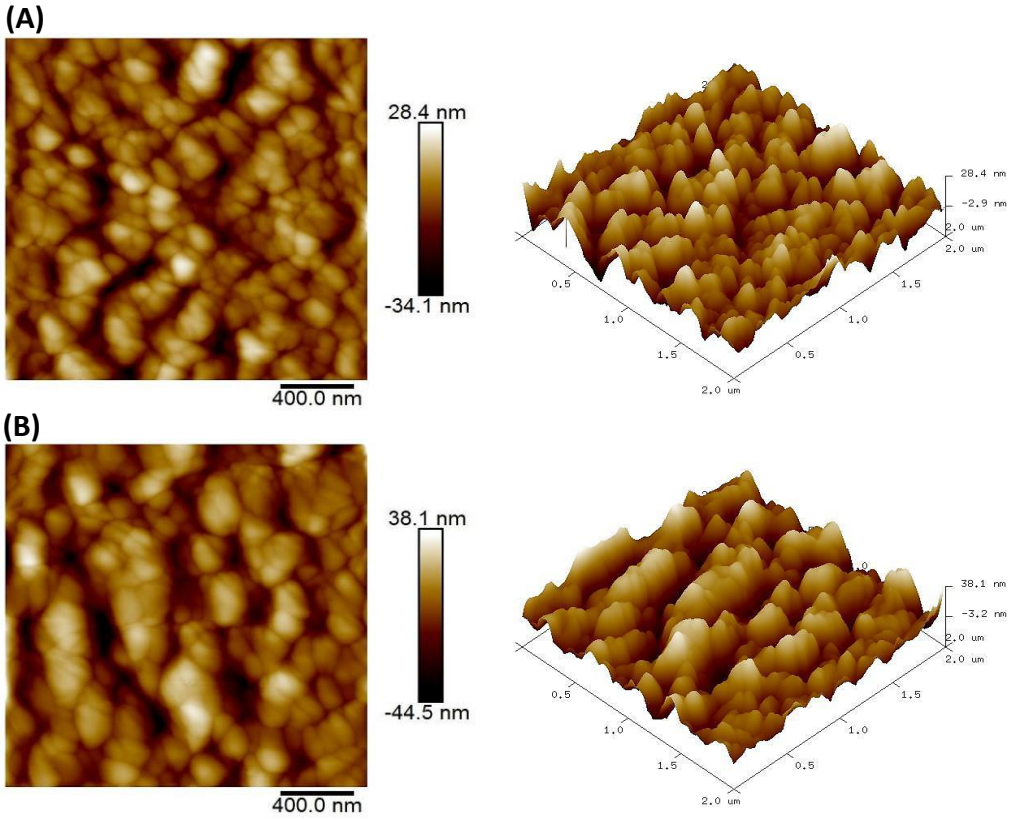

Figure 3.11: 2D AFM images and their corresponding 3D topography of ZnO NP films prepared in nitrogen with (A) baking at 100 ºC for 10 min and (B) annealed after baking at 350 ºC for 1h. Surface roughness is 8 nm and 15 nm for (A) and (B) respectively.

3.6.3 FTIR analysis

Solution-processed ZnO nanoparticles drop cast onto GaAs substrates were investigated by Fourier transform infrared spectroscopy (FTIR). Figure 3.12 shows the FTIR spectra of (A) a ZnO NPs film prepared from the zinc acetate, (B) the octylamine stabilizing ligands and (C) the ZnO NP thin film with the octylamine ligands following baking the film at 100 ºC for 10 min in air. The assigned modes in figure 3.12 represent the main absorption peaks which are believed to give an important indication of the effect of surface treatment on the surface composition.

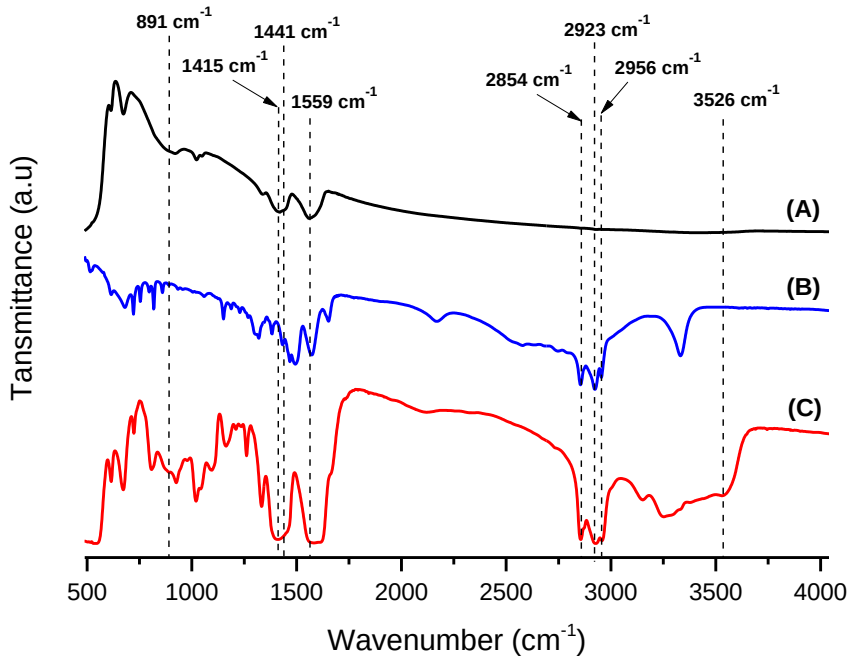

Figure 3.12: The FTIR spectrum of (A) ZnO NPs film prepared from zinc acetate precursor, (B) octylamine ligands, (C) ZnO NPs presented in (A) after adding the octylamine ligands. ZnO samples were prepared on GaAs substrates.

The ZnO NPs film fabricated from zinc acetate precursor shows transition peaks at 500 cm^{-1} assigned to ZnO backbone transitions and a broad absorption peak at 891 cm^{-1} which is reportedly assigned to the substitutional hydrogen at oxygen site (H_O) bound to the lattice zinc site ($Zn\text{-}H_O$) [157,158]. This substitution has the potential to act as a shallow donor in ZnO [158]. The absorption peaks around 1559 cm^{-1}, and the poorly resolved doublet at 1415 and 1441 cm^{-1} are related to the stretching C═O and C-O bounds respectively, which are believed to be associated with the acetate complex (CH_3COO^-) groups chelated on the ZnO surface [116,159,151] although some papers associate them also with the weakly bond water [159,160]. Moreover, these peaks are also reportedly assigned to the asymmetrical and symmetrical stretching of the zinc carboxylate [161,151]. Figure 3.12-B shows the FTIR spectrum of the octylamine ligands as a film drop-casted on GaAs substrate. Figure 3.12-C shows the FTIR of ZnO NPs film after the addition of octylamine ligands. Both films show absorption peaks at 2854

cm^{-1}, 2923 cm^{-1} and 2956 cm^{-1} which are related to the asymmetric and symmetric C-H stretching vibrations of hydrocarbon chains [151,162,163].

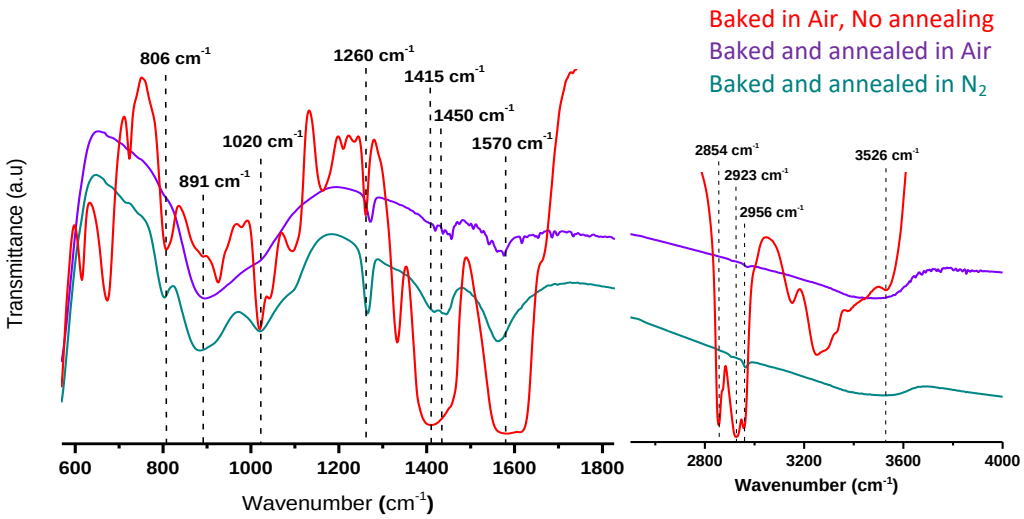

Figure 3.13: FTIR spectra of ZnO NPs thin films deposited on GaAs substrate following different processing. The baking temperature was 100 °C for 10 min. The annealed conditions were 350 ^{o}C, for 1h in air or nitrogen.

Figure 3.13 shows the effect of preparation conditions and surface treatment on the chemical composition of ZnO NPs films as indicated by FTIR spectra. The baked sample serves as a reference. It shows a large number of transitions mainly originating from the remaining unbounded carbons and/or acetate groups from the starting precursor. The assignment of FTIR transitions relevant to these studies are shown in table 3.1. The reference sample used in this experiment was thick which explains the saturated absorption of some of the stretching vibrations of the surface carbonates. However, when ZnO NPs films are annealed at 350 ^{o}C, for 1h in air and nitrogen, some of the transition peaks are slightly shifted and the FTIR spectra become smoother compared to the reference sample, resulting from decomposing most of the remaining carbons and unreacted chemical groups. The spectrum shows a significant reduction in the characteristic peaks at 1570 $cm^{-1,}$ 1415 and 1450 cm^{-1}, assigned to acetate groups originating from the precursor when the ZnO NPs film is annealed in air compared to

nitrogen. This suggests its incomplete decomposition for the latter condition. While preparing and annealing the ZnO NPs in an oxidizing environment shows a semi-complete decomposition of the ligands attached in addition to higher relative absorption of water as shown in figure 3.13. Furthermore, the transition peak at 1260 cm^{-1} is assigned to the adsorbed carboxylate group (COO^-) on the surface [164], which shifted to 1267 cm^{-1} after annealing, shows higher absorption in nitrogen compared to ZnO annealed in air. The C═O transition peak at 1570 cm^{-1} is slightly blue shifted to 1565 cm^{-1} after annealing for 1 h in air and nitrogen in addition to the C-O doublet at 1415 and 1450 cm^{-1} which are shifted to about 1419 cm^{-1} and 1454 cm^{-1} respectively. The three transition peaks assigned to the octylamine ligands are significantly reduced and/or removed after annealing in air and nitrogen and show a small absorption peak at 2956 cm^{-1}, while the other two peaks at 2854 and 2923 cm^{-1} are almost completely removed. FTIR spectrum of ZnO NPs film prepared and annealed in nitrogen shows two transition peaks located around 806 cm^{-1} and 1020 cm^{-1} believed to be assigned to the C-H bending modes of surface hydrocarbons [165] and carbonate ions CO_3^{2-}stretching mode [160] respectively. Those two transition peaks are completely removed when ZnO NPs prepared and annealed in air as shown in the purple spectrum in figure 3.13. The broad absorption peak from 3000-3650 cm^{-1} is related to the adsorbed water which shows high absorption after annealing in air.

The above observations are in good agreement with the XPS results shown earlier in figure 3.9. The calculated C:O ratio is found to be higher when ZnO NPs prepared and annealed in nitrogen versus air which supports the incomplete decomposition of organic ligands in a nitrogen environment. Moreover, the results also suggest the presence of higher hydroxyl absorption when the sample is prepared and annealed in air rather than nitrogen. This is also discussed in more detail later. In order to investigate the effect of

the storage environment and ageing in more detail, new experiments were performed involving measuring the FTIR spectra of ZnO NPs films prepared and annealed in air and nitrogen and stored in their respective environments for 51 days.

Table 3.1: Illustrate the important FTIR transitions locations in ZnO NPs before annealing and their assigned chemical composition. Few transitions peaks are shifted with annealing treatment.

FTIR transition (cm^{-1})	Assigned chemical composition	References
801, 1020	C-H bending modes of surface hydrocarbons from octylamine ligands.	[165]
891	Substitutional hydrogen at oxygen site (H_O) bound to the lattice zinc site (Zn-H_O).	[157,158]
1260	Adsorbed carboxylate group (COO^-) on the surface.	[164]
1570, 1415 and 1450	Stretching C═O and C-O bounds respectively.	[116], [159], [151]
2854, 2923, 2956	Asymmetric and symmetric C-H stretching vibrations of hydrocarbon originated from the octylamine ligands.	[151],[162],[163]
3000-3650	Stretching mode of the hydroxyl groups (O-H) originated from the atmospheric moisture.	[159], [151], [162],[166],[167]

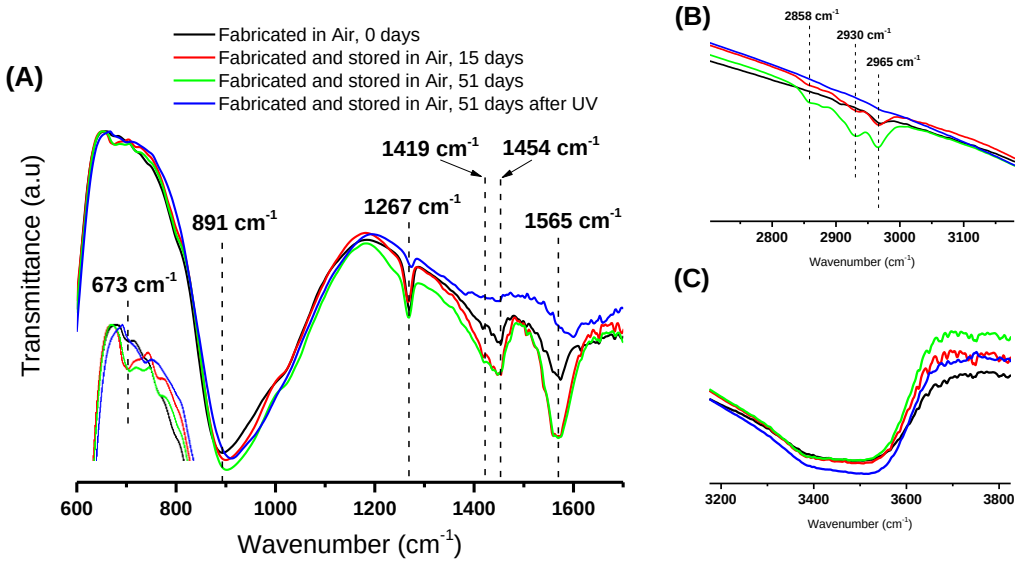

Figure 3.14: The FTIR spectra of ZnO NPs prepared and annealed in air and measured immediately after preparation, storing and UV irradiation for 40 min in air. (A), (B) and (C) show different spectral regions with (B) displaying the C-H stretching vibrations of hydrocarbon chains and (C) O-H hydroxyl groups respectively.

Figure 3.14 shows the FTIR spectra of ZnO NPs film prepared, annealed and stored for 51 days in air. The sample aged for 51 days then irradiated with UV light of power density 0.45 W/cm^2 for 40 min in air and retested immediately. As shown in figure 3.14-A, the absorption peaks related to the carbonates stretching bonds around 1565 cm^{-1}, 1419 and 1454 cm^{-1} increased after storing in air for 15 days. Further storing the sample for 51 days shows no change in their absorption intensities indicating that 15 days are enough for the adsorbed carbonates to saturate on the surface. A small absorption band grows also around 673 cm^{-1} assigned to the transitions developed from the interaction with atmospheric CO_2 [164]. A small absorption peak assigned to the adsorbed carboxylate group (COO^-) is also observed at 1267 cm^{-1} which found to slightly increase and widen after 51 days storage in air. Figure 3.14-B shows the C-H stretching modes, which arise from adsorbed hydrocarbons. By storing the sample in air for 51 days, three transition peaks, 2858 cm^{-1}, 2930 cm^{-1} and 2965 cm^{-1}, are found to develop suggesting a possible chemical adsorption reaction of aliphatic organic

components from the air. The transitions are slightly red-shifted from the transitions originating from the octylamine ligands of the unannealed sample, see figure 3.13. Figure 3.14-C indicates the adsorption of the hydroxyl group onto the surface of ZnO NPs film with time.

After irradiating the sample with UV for 40 min in air, significant and interesting changes in the FTIR transition lines took place. The transition line at 1267 cm^{-1} is dramatically reduced and slightly red-shifted upon UV irradiation. FTIR absorption peaks at 1565 $cm^{-1,}$ 1419 and 1454 cm^{-1} are reduced substantially with UV irradiation. Moreover, the three absorption peaks of the hydrocarbons stretching modes are completely removed with UV irradiation. The hydroxyl group transitions related to the adsorbed water shows an interesting reduction of 12.5% in its relative absorption after UV irradiation. What is more, the transition line assigned to the substitutional hydrogen at the oxygen site (H_O) bound to the lattice zinc site (Zn-H_O) at 891 cm^{-1} is red shifted and slightly reduced in strength after UV irradiation.

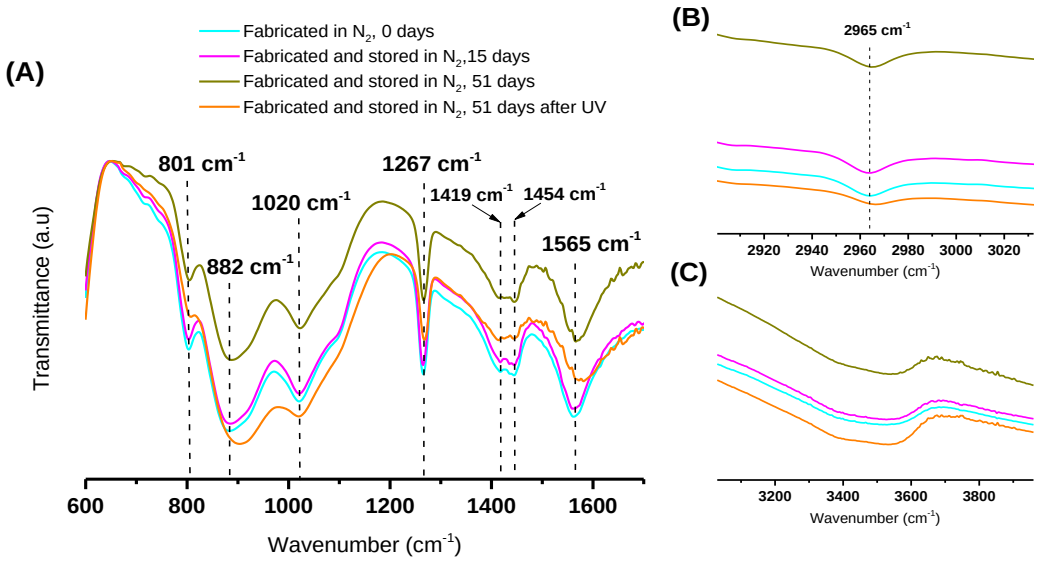

Figure 3.15: The FTIR spectra of ZnONPs prepared and annealed in nitrogen and measured immediately after preparation, storing in nitrogen and UV irradiation for 40 min in air.(A), (B) and (C) show different FTIR spectral regions with (B) displaying the C-H stretching vibrations of hydrocarbon chains and (C) O-H hydroxyl groups originated by water adsorption.

Figure 3.15 shows the FTIR spectra of ZnO NPs prepared, annealed and stored in a nitrogen environment and measured immediately after preparation, storing in nitrogen and UV irradiation for 40 min in air. Most of the absorption peaks have approximately the same strength after preparation and following storing the sample in nitrogen for 15 and 51 days as shown in figure 3.15-A. The transition peak at 891 cm^{-1} observed when ZnO prepared and annealed in air is shifted to 882 cm^{-1} when ZnO prepared and annealed in nitrogen. The stretching vibrations of the hydrocarbon chains shown in figure 3.15-B only contain a single absorption peak at 2965 cm^{-1} which is found to be unaffected by storing the sample in nitrogen for 51 days. Figure 3.15-C shows a comparison of water absorption on ZnO NPs film just after the preparation (0 days), storing for 15 and 51 days. The spectra look similar suggests that OH transition hardly changes with time when ZnO NPs film stored in nitrogen. Irradiating the sample with UV significantly decreases the absorption peaks of the transition lines associated with

the C-H bending modes of surface hydrocarbons (801 cm^{-1} and 1020 cm^{-1}). In addition, the absorption peak of the adsorbed carboxylate at 1267 cm^{-1} is also reduced and slightly red-shifted with UV irradiation. The peaks at 1565 cm^{-1}, 1419 and 1454 cm^{-1} are also reduced with a slight red shift in the later transition position. Moreover, the absorption peak at 882 cm^{-1} is also shifted after UV treatment. In contrary, hydroxyl group related to water adsorption shows a significant increase by 50.6% in its relative absorption spectrum after UV irradiation in air as shown in figure 3.16.

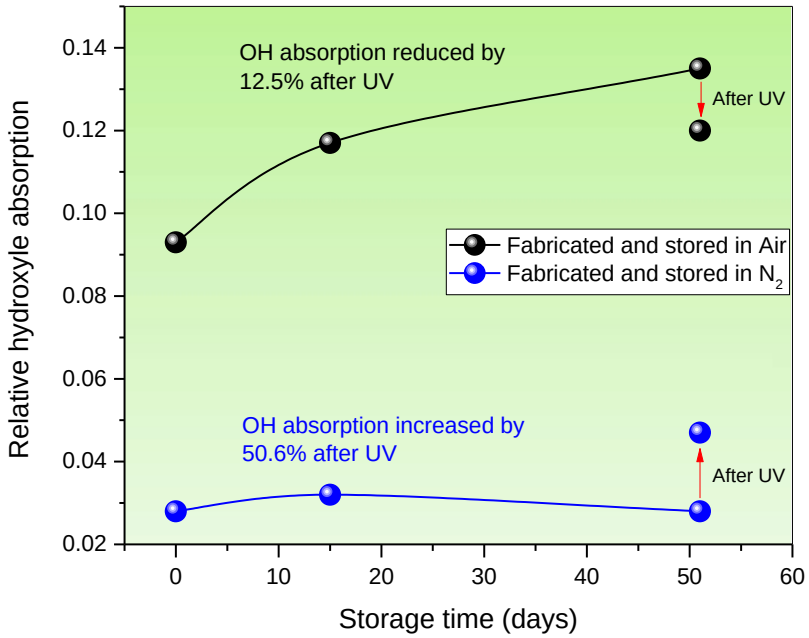

Figure 3.16: The absorption strength of the hydroxyl group located in the spectral region 3000-3650 cm^{-1}, as a function of sample storage time for the ZnO thin films annealed at 350 ºC, 1h in their fabrication environments and stored in air and nitrogen. The figure also shows the effect of UV irradiation in air on the OH adsorption strength. The relative absorption is calculated by subtracting the transmittance minimum from the background as illustrated by the red line in figure 3.18-B.

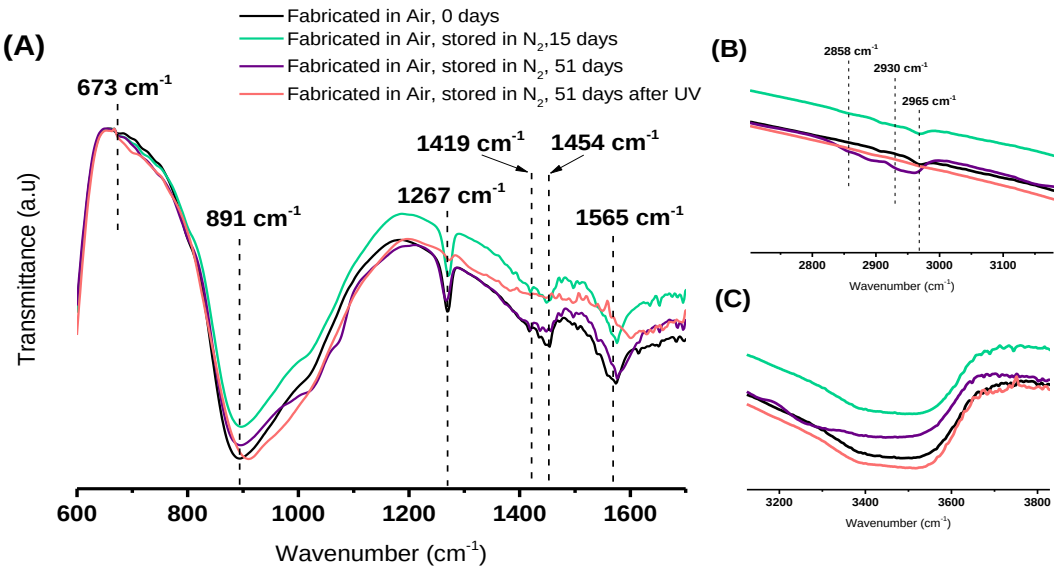

Figure 3.17: The FTIR spectra of ZnO NPs prepared and annealed in air and measured immediately after preparation then stored in nitrogen for different times and UV irradiation for 40 min in air. (A), (B) and (C) show different FTIR spectral regions with (B) displaying the C-H stretching vibrations of hydrocarbon chains and (C) O-H hydroxyl groups originated by water adsorption.

Figure 3.17 shows the FTIR spectra of ZnO NPs prepared and annealed in air and measured immediately after preparation. Then, the sample is stored in a nitrogen environment for 15 and 51 days and then irradiated with UV light for 40 min in air. Figure 3.17-A shows that there is not a big change in the absorption peaks of the surface carbonates after ageing the sample in nitrogen for 15 and 51 days. Moreover, the C-H stretching modes, which arise from adsorbed hydrocarbons, show a slight change in its absorption intensity after storing the sample for 51 days as shown in figure 17-B. Whereas, water adsorption is reduced with storing the sample in nitrogen as shown in figure 3.17-C. Figure 3.18-A shows the FTIR spectra of the hydroxyl transition for ZnO NPs films fabricated and stored in air and nitrogen for 51 days in addition to a sample fabricated in air and stored in nitrogen for the same amount of time. The spectra show a big difference in water absorption for all three samples. The higher water absorption is found in the sample fabricated (prepared and annealed) and stored in air, whilst the

sample fabricated and stored in nitrogen shows the lowest water absorption, by a factor of three. The ZnO sample prepared in air and stored in nitrogen has an intermediate value of water adsorption. These results correlate with the presence of humidity in air compared to the isolated nitrogen environment. As discussed above in section 3.2.1, ZnO NPs is well-known as a hygroscopic material. Figure 3.18-B shows the FTIR spectra of a single sample annealed in air and then stored in a nitrogen environment for 51 days. The spectra show that water absorption decreases by about 8% when stored in nitrogen implying desorption of hydroxyl groups from the surface.

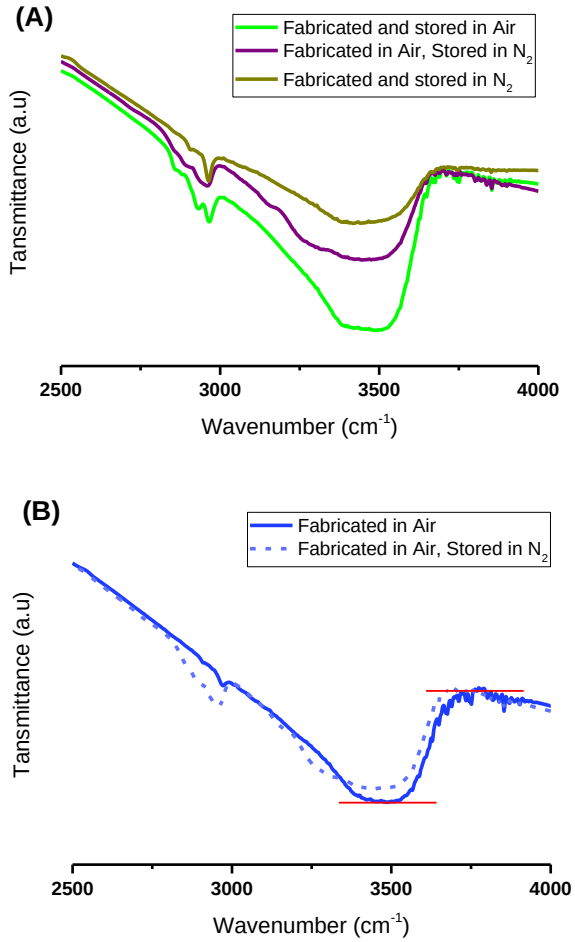

Figure 3.18: (A) the FTIR spectra of ZnO films processed and stored in air and nitrogen for 51 days. The figure illustrates the difference in the adsorbed hydroxyl group (OH) depending on the processing and storage environment (B) The FTIR of a single sample measured immediately after the fabrication in air and again after storing in nitrogen for 51 days.

The absorption of water on the surface of ZnO is generally linked to the presence of surface defects sites. Annealing the ZnO in air leads to form surface defects by the decomposition of organic ligands and precursor acetate. This happens to a greater extent in an oxygen atmosphere and not in nitrogen. With storing in air, atmospheric water is likely to be adsorbed on the defects sites (with concentration proportional to the defects density) as indicated by Grotthus mechanism discussed earlier in this chapter, section 3.2.1. This is in a good agreement with XPS results (figure 3.9) which indicate that surface hydroxyls (at 532.2 eV binding energy) possess a high intensity following annealing in air versus nitrogen.

Water adsorption on the ZnO surface is also affected by UV irradiation. Feng et al. [150] attributed the increase of surface hydroxyl (OH) with UV irradiation to the competition between water and oxygen adsorption on the surface vacancy sites resulting from the reaction of photogenerated holes with the ZnO lattice oxygen. Herein, FTIR spectra show that water adsorption increases with UV irradiation in air for the sample fabricated and stored in nitrogen, while the sample fabricated and stored in air shows reduction in its water absorption after the UV irradiation. Interestingly, the absorption peak of the transition line 891 cm^{-1} is slightly reduced after UV irradiation for the sample fabricated in air as shown in figure 3.14. However, the same transition (slightly shifted to 882 cm^{-1} in nitrogen) shows 18.2% relative increase in its absorption after UV irradiation as shown in figure 3.15. This transition peak is assigned by Senthilkumar et al. [158] to the substitutional hydrogen at oxygen site (H_O) bound to the lattice zinc (Zn-H_O). This increase in hydrogen on zinc sites could be linked to the passivation of nitrogen bonded on the ZnO surface fabricated and stored in nitrogen where hydrogen is more likely to bind with nitrogen and forms N_O-H complex [168]. The presence of nitrogen traces could help decrease the surface states by passivating the surface defects. UV

photoluminescence (PL) of ZnO NPs prepared in air and nitrogen was also measured. PL normally originates from the radiative recombination of electrons and holes. The ZnO NP film prepared in nitrogen shows PL, three times higher than the sample prepared in air as shown in figure 3.19-A. This higher PL could be related to the nitrogen bonded on the surface of ZnO NPs during and\or after the preparation process which helps increase the recombination process owing to its role in passivating the surface defects which trap the carriers [169]. This is also consistent with XPS results which indicate the presence of nitrogen traces at a binding energy about ~ 400 eV [170] in the sample fabricated in nitrogen as shown in figure 3.19-B.

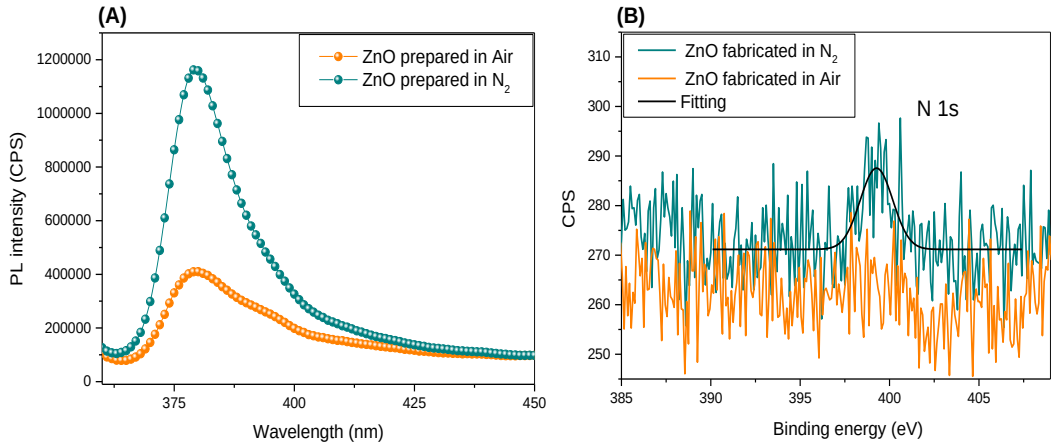

Figure 3.19: (A) Band transition PL spectra of ZnO NPs prepared (spin coated and baked) in air and nitrogen excited with 350 nm. (B) XPS scan showing the N 1s core levels of nitrogen traces in ZnO NPs fabricated in a nitrogen and an air environment.

Table 3.2 shows the relative difference in absorption values for the asymmetrical and symmetrical stretching of the surface carbonates adsorbed on annealed ZnO surface before and after storing for 51 days in air and nitrogen (extracted from figures 3.14 and 3.15 respectively). The table illustrates the significant increase in absorption in both transitions when sample fabricated and stored in air versus nitrogen. The change in the surface carbonates is much bigger in air than in nitrogen suggest that surface reactions,

involving the formation of both bidentate and monodentate adsorbed carbonate are taking place, by the interaction of ZnO surface (oxide anions and oxygen vacancies (V)) with atmospheric gaseous carbon dioxide ($CO_{2(g)}$) in air as shown in the reactions below [171]:

$$Zn - O + CO_{2(g)} \rightleftarrows ZnCO_3 \text{ (}monodentate\text{)} \quad (3.5)$$

$$Zn - V - Zn - O + CO_{2(g)} \rightleftarrows ZnCO_3 \text{ (}bidentate\text{)} \quad (3.6)$$

Table 3.2: The relative absorption strength of the stretching vibrations of the surface carbonates originated from the acetate complex (CH_3COO^-) groups chelated on the ZnO surface. The relative absorption is calculated by subtracting the absorption peak from the higher point as illustrated by the red lines in figure 3.18-B.

Transition peak (cm^{-1})	Fabricated in Air		Relative increase by (%)	Fabricated in Nitrogen		Relative increase by (%)
	0 days	51 days		0 days	51 days	
1454	0.053	0.096	56.7	0.088	0.102	14.7
1565	0.083	0.194	80.1	0.198	0.223	11.8

This interesting observation suggests that ZnO is developing new organic compounds on the surface, probably by a surface reaction involving CO_2 adsorption from the air. To get further insight into this, a new experiment was performed by fabricating ZnO NPs in air and storing it in a vacuum cell filled with CO_2 (150 mbar). FTIR spectra were measured immediately after the fabrication, as a reference, and after storing for 3 and 6 days as shown in figure 3.20. It is realized that OH absorption increases after storing the ZnO in CO_2, by about 53% after storing for 6 days.

It is interesting to see that the characteristic absorption peaks at 1565 cm^{-1}, 1419 and 1454 cm^{-1} related to carbonates group become broader and much stronger after storing

the sample for 3 and 6 days in the CO_2 environment while no corresponding growth in aliphatic groups was observed. This could be related to the adsorbed carbonate species from CO_2 uptake on the ZnO surface. The absorption bands at 1486 and 1552 cm^{-1}, appearing after storing, could be assigned to the asymmetric $\nu_3(O-C-O)$ and symmetric $\nu_3(O-C-O)$ vibrational modes of monodentate and bidentate carbonate species respectively [171]. The carbonates and carboxylates groups' absorption is saturated after 3 days in CO_2. The peak shown at 2338 cm^{-1} is related to the physisrobed bent CO_2 in the ZnO and could be assigned to the asymmetric stretching mode of CO_2. This peak is also attributed to the trapped CO_2 in porous structure of ZnO [116,162,172]. It has been suggested by Baltrusaitis et al. [173,174] that CO_2 will interact with surface adsorbed water and form carbonate species when catalysed by water. The interaction will results in the production of bicarbonate intermediate and ultimately forms carbonic acid which is stabilized by the strong hydrogen bond with surface adsorbed hydroxyl groups.

FTIR results indicate the formation of surface carbonates on the ZnO surface with time when sample stored in air. Surface composition is varied when ZnO prepared and annealed in air and nitrogen because of the remain organic ligands and acetate groups from the precursor when ZnO annealed in nitrogen compared air. Water adsorption is increased with time when sample stored in air.

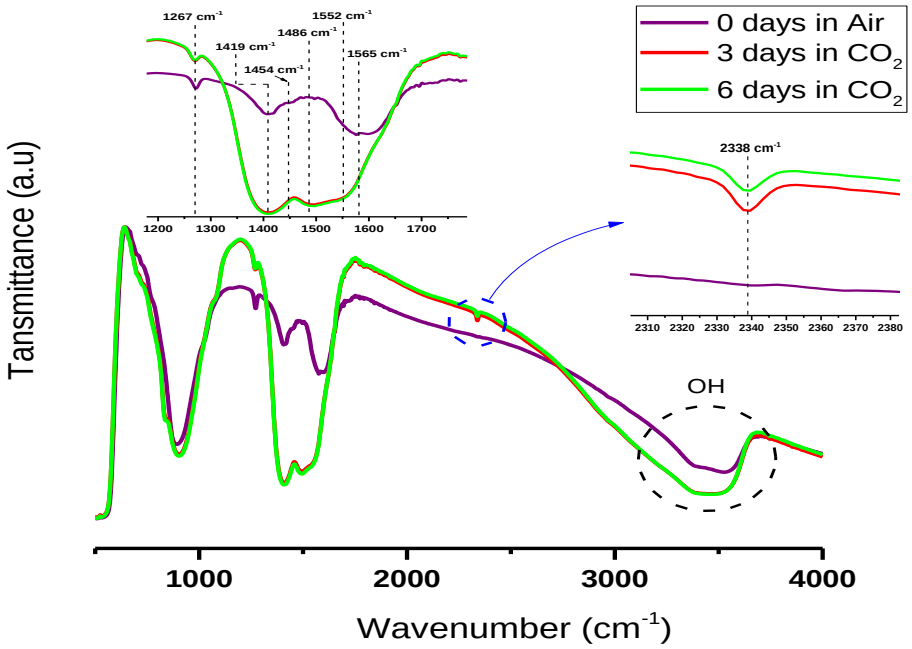

Figure 3.20: FTIR spectrum of ZnO NPs film stored in CO_2 environment. The sample is fabricated in air on GaAs substrate and then stored in a vacuum cell filled with CO_2 (150 mbar) above the atmospheric pressure.

3.6.4 Contact angle measurements

Contact angle (CA) measurements were performed to further examine the effect of surface treatment and storage environments on the ZnO NPs surface and its wettability. The surface wettability together with FTIR spectroscopy provides a powerful tool to study the chemisorption and bonding molecules on the surface. All films were prepared by spin-casting onto glass substrates following the same procedure and from the same ZnO suspension. The ZnO NP film thickness for all samples was about 120 nm (± 5 nm). Figure 3.21 shows optical images of the deionized water drop on the surface of ZnO NPs films prepared and treated with different conditions. The ZnO NPs films are hydrophilic and hydrophobic with contact angles of 55.3º and 91.1º when baked at 100 ºC for 10 min in air and nitrogen respectively, as shown in figure 3.21-A and B.

The contact angle decreased to 11.5º and 25.2º after annealing at 350 ºC for 1h in air and nitrogen respectively as shown in figure 3.21-C and D.

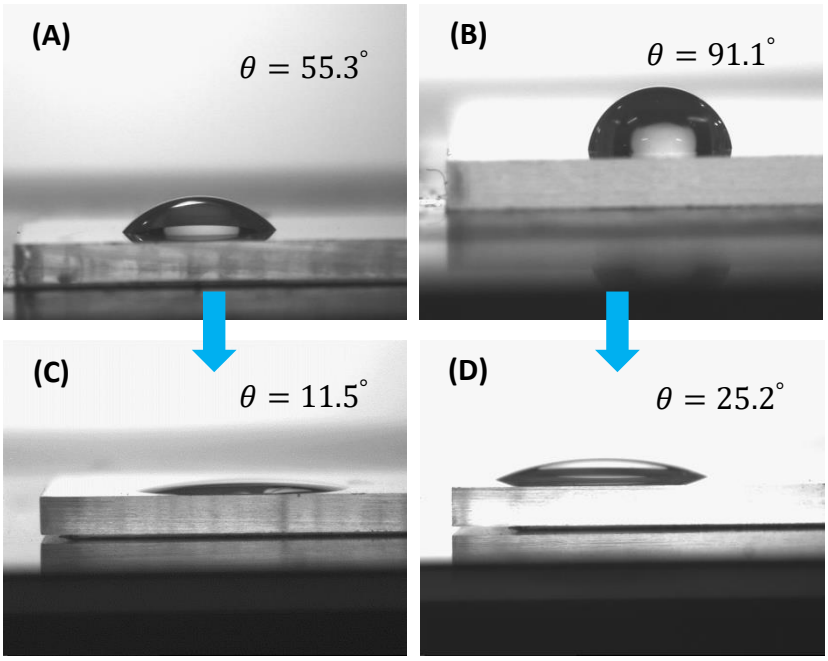

Figure 3.21: Optical images of the DI water drop on the surface of ZnO NPs films (A) baked in air, no annealing, (B) baked in N_2, no annealing, (C) baked and annealed in air and (D) baked and annealed in N_2. All DI water drops had the same volume and were released on the surface from the same height.

The effect of storing environments and UV irradiation on the surface wettability of ZnO NPs films were also investigated. Three samples were measured, two annealed in air at 350 °C for 1 hour and the other in nitrogen for the same conditions. Table 3.3 shows the variation in contact angle (CA) values for the three samples, following storage in air and nitrogen. For all samples, the contact angle increases with storage time, reaching a value of 87° when stored in air and 50°-57° when stored in nitrogen. In other words, the ZnO NP surface becomes highly hydrophobic after storing in air for 51 days compared to a lower degree of hydrophobicity when stored in nitrogen.

Table 3.3: The contact angle (CA) of samples prepared and annealed in air and nitrogen and stored for up to 51 days in their respective environments. The reference samples represent the CA measured immediate after baking and before annealing, while 0 days indicates immediate measurement after annealing. The table also shows the CA after irradiating the Ref. and ZnO sample stored for 51 days with 0.45 W/cm^2 of UV light for 40 min in nitrogen and in air respectively.

Aging time (days)	Contact angle of ZnO NPs films (°)		
	Fabricated and stored in Air	Fabricated in Air and stored in Nitrogen	Fabricated and stored in Nitrogen
Ref.	55.3	55.3	91.1
0	11.5	14.9	25.2
15	73.2	35	41.9
51	87.6	50.4	56.9
UV in Air	8.2	7.4	11.3
UV in N_2	11.5	----	42.2

The CA of ZnO NP films were also measured after irradiation with 0.45 W/cm^2 of UV light for 40 min in air and in nitrogen. The reference samples (baked at 100 ºC in air and nitrogen) were irradiated in a nitrogen environment, while the annealed samples stored for 51 days were irradiated in air. For the latter set, the contact angle obtained after irradiation was approximately the same, 7°-8°, for the two samples annealed in air, irrespective of the storage conditions. The sample annealed in nitrogen had a slightly higher value post-irradiation. The reference samples irradiated in nitrogen both showed a drop in contact angle, to a significantly lower value for the sample annealed in air. The contact angle results are summarised in figure 3.22.

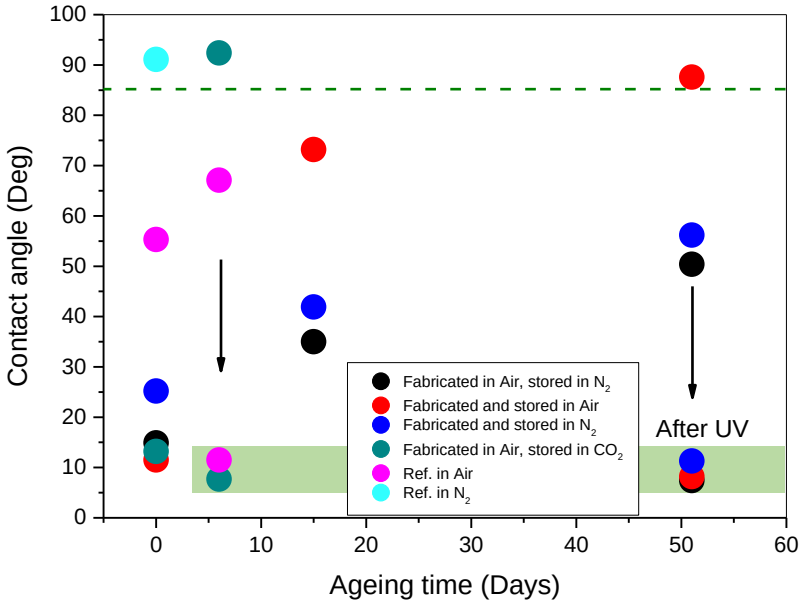

Figure 3.22: Time dependence of the contact angle of various annealed sample fabricated and stored in air, nitrogen and CO_2. The ref. values represent the CA of unannealed ZnO films. The arrows show the fall in CA (high surface wettability) after UV irradiation in air.

The CA of ZnO NPs film stored in the CO_2 environment for 6 days is also measured. The sample is annealed in air, measured and then introduced into a small vacuum chamber filled with 150 mbar CO_2. The CA for the sample stored in CO_2 increased substantially from 13.2º to 92.4º after only 6 days in CO_2. After UV irradiation in air, the contact angle dropped to 7.7º. An inspection of figure 3.22 shows that the highest CA values belong to the samples that are fabricated and stored in air and CO_2, in addition to the reference sample baked in nitrogen. Interestingly, after UV irradiation in air, all CAs are dropped to very similar values as shown by the shaded area in figure 3.22. This observation indicates that the compounds or surface bond which responsible for increasing the contact angle could be the same.

The CA change induced by the surface treatment and storage environments could be linked to the change in water absorption, surface hydrocarbons and CO_2. First of all, let

us consider the relation between water absorption and CA change. One might expect that hydrophilicity (low CA) is associated with water absorption. As discussed in section 3.6.3 above, the extent of water absorption on the surface of ZnO NPs depends on the fabrication conditions. ZnO absorbs more water when fabricated in air than nitrogen. Indeed the ZnO surface wettability is higher (lower CA) when the sample is fabricated in air rather than in nitrogen. When storing in air, the extent of water absorption increases gradually with time up to 51 days, as indicated by FTIR data in figures 3.16 and 3.18. In contrast, water absorption does not increase when ZnO is stored in nitrogen for 51 days. However, the CA of both samples increases significantly with storage time which does not correlate with changes in OH adsorption. Figure 3.16 also shows that OH absorption decreases following UV irradiation of the sample annealed and stored in air, whilst surface wettability substantially increases. Based on the above, we suggest that water absorption is not responsible or has a low impact on surface wettability and CA change. This observation contradicts the work by Ren-De Sun et al. [146] which reported the important role of water absorption and surface defects such as oxygen vacancies in promoting the surface wettability in metal oxide semiconductors especially ZnO.

Now, let us discuss the change in stretching vibrations of the C-O groups, at 1565 cm^{-1} 1419 and 1454 cm^{-1} in relation to CA measurement. These transitions originate from the acetate complex (CH_3COO^-) groups from the precursor materials chelated on the ZnO NPs. The absorption strength of the transition peaks significantly decrease after annealing the ZnO in air, as the groups are decomposed. However, absorption at these wavenumbers increases substantially with storage time in air (slightly shifted). This is attributed in section 3.6.3 to carbonate formation by surface reaction with CO_2. The carbonate groups are finally decomposed by UV irradiation. The CA of an identically

processed sample is substantially reduced by annealing, then increases with storage time and finally drops to a very low value on irradiation. Therefore we suggest a correlation between high CA and carbonate formation on the NP surface. This hypothesis is supported by results from the sample annealed and stored in nitrogen, where smaller changes in both CA and carbonate absorption are observed with storage time. Similarly, the sample stored in a CO_2 environment develops very strong carbonate transitions and a hydrophobic surface.

3.6.5 Conductivity and photoconductivity

3.6.5.1 Photocurrent and responsivity measurements

The electrical properties of metal-semiconductor-metal (MSM) planar devices based on solution-processed ZnO NPs were evaluated to identify the mechanism of persistent photoconductivity as well as what influences its magnitude. We measured I-V characteristics in the dark and on irradiation with UV as well as the photocurrent spectrum and transients. We investigated ZnO NP devices fabricated in air and nitrogen and tested in different controllable atmospheres in order to study whether these factors affected photocurrent generation. It is generally accepted that the UV photoresponse of ZnO is impacted by the adsorption of oxygen molecules from the ambient environment on the surface of ZnO NPs, as outlined in section 3.3. However, air is a mixture of molecules including water and carbon dioxide, which may also affect the photocurrent generation when testing the device in air. We aim to show that many other surface species, such as water and/or surface carbonates, are also relevant.

Figure 3.23 shows the I-V characteristics in addition to the photocurrent transients of ZnO NP devices prepared and annealed in air and nitrogen. Devices were prepared following the preparation and fabrication procedure illustrated in section 3.5.1. The

devices were tested in air at room temperature. The device prepared in air (spin coated and baked at 100 ºC for 10 min) is used as a reference to the other two ZnO NP devices, fabricated (prepared and annealed at 350 ºC for 1h) in air and nitrogen. ZnO NPs prepared in air show an asymmetric I-V behaviour in the dark, indicating charging effects. At a bias of 20 V, the dark current density was about 4.77×10^{-6} A/cm^2. When ZnO NPs were fabricated in air, the device also shows asymmetric I-V behaviour with a dark current density of 4.27×10^{-7} A/cm^2 at 20 V. The lowest dark current is found for ZnO NPs fabricated in nitrogen, with a current density of 5.27×10^{-9} A/cm^2 at 20 V as shown in figure 3.23-A.

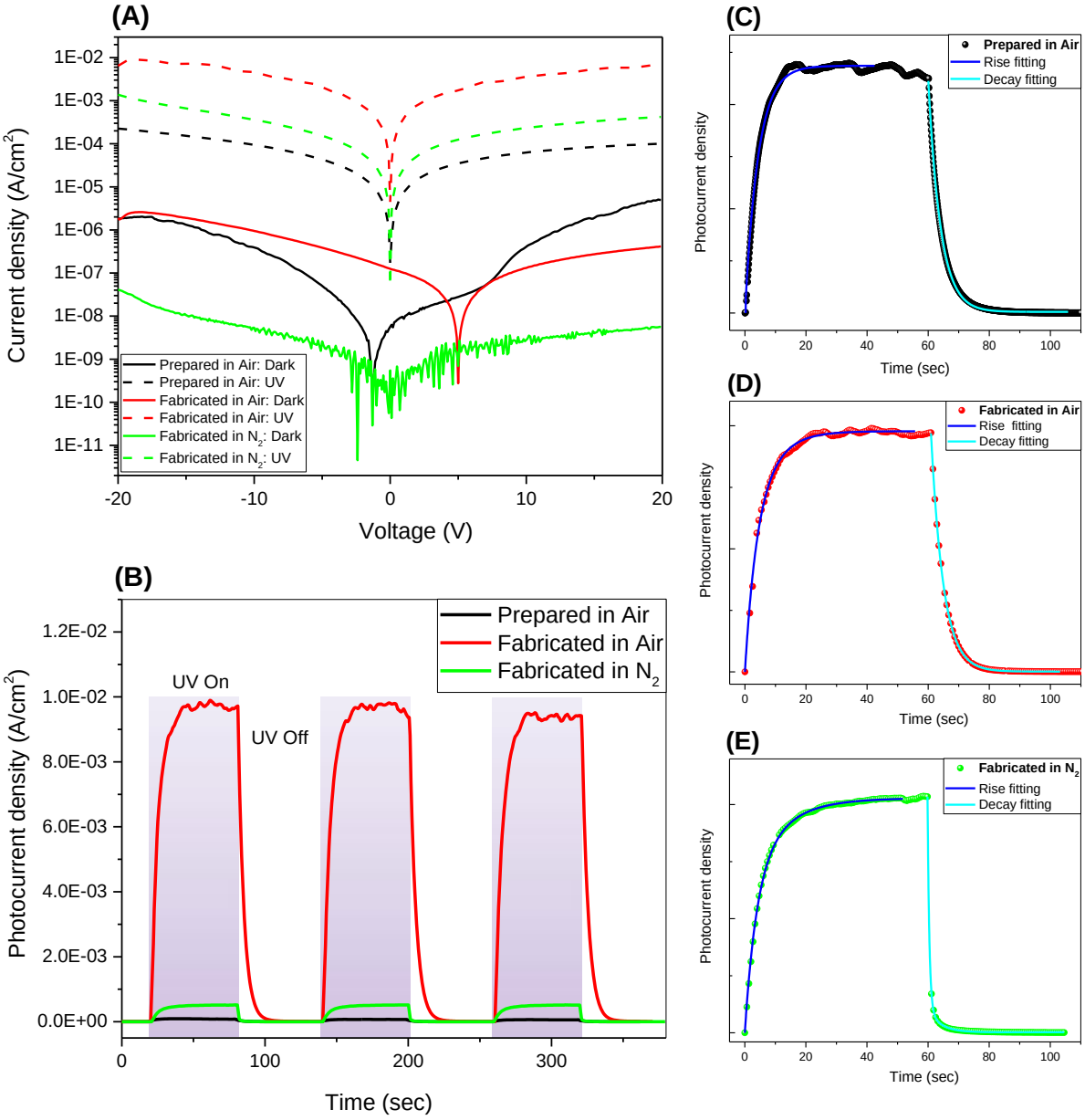

Figure 3.23: (A) Semi-log plot of dark and photoinduced I-V characteristics of ZnO NP films fabricated (prepared and annealed) in air and nitrogen. The sample prepared (spin coated and baked) in air represents the reference device. (B) The photocurrent transients of the ZnO films shown in (A). The devices were measured in air with 20 V biased. (C), (D) and (E) show the photocurrent transients and the corresponding time constants fitting for devices prepared in air, fabricated in air and fabricated in nitrogen respectively. The devices were measured in air.

The I-V characteristics devices were also measured on illumination with UV light of wavelength 363 nm and intensity 0.31 mW/cm^2 in air. The highest photocurrent density was recorded for the sample fabricated in air followed by the sample fabricated in nitrogen and finally the reference device with a recorded responsivity of 11.3, 1.77 and

0.23 A/W respectively. All three devices show a consistent and repeatable photocurrent cycles when irradiated with UV light. The temporal response of the devices was also characterized by illuminating the samples at 1 min time intervals separated by 1 min gaps, as shown in figure 3.23-B. The ZnO NPs prepared in air show the lowest photocurrent of 7.07×10^{-5} A/cm^2, about an order of magnitude higher than the dark. The device fabricated in air shows the highest photocurrent density of 9.7×10^{-3} A/cm^2, about four orders of magnitudes higher than the dark current density. Finally, the device fabricated in nitrogen shows a photocurrent density of 5.15×10^{-4} A/cm^2, five orders of magnitudes higher than its dark current density. However, these observations contradict that of Hatch et al. [175] who found that photodetectors of ZnO-nanorod/CuSCN annealed in nitrogen exhibited the highest photocurrent in the UV, about 30 μA, compared to oxygen and air annealed samples. This is attributed to N-related shallow donor defects formed during the highly reducing nitrogen-anneal coupled with the absence of V_{Zn}^{2-} trap states.

The photocurrent transients shown in figure 3.23-C to E show slow response times confirming persistent photoconductivity. Figure 3.24 shows the log plot of the photocurrent density as a function of the incident UV light power density, albeit over a limited range, for ZnO NPs fabricated in air and nitrogen. Both devices follow the power law function with power variations given by $I_{Light} \propto P^{\alpha}$ where α represents the power law factor which is related to the charge generation, trapping and recombination processes [136]. The values of α for devices fabricated in air and nitrogen were extracted by linearly fitting the photocurrent data and are equal to 0.8 and 0.9 respectively as shown in figure 3.24. The difference between the α values may be related to the variation in charge generation and/or electron-hole traps with fabrication environment.

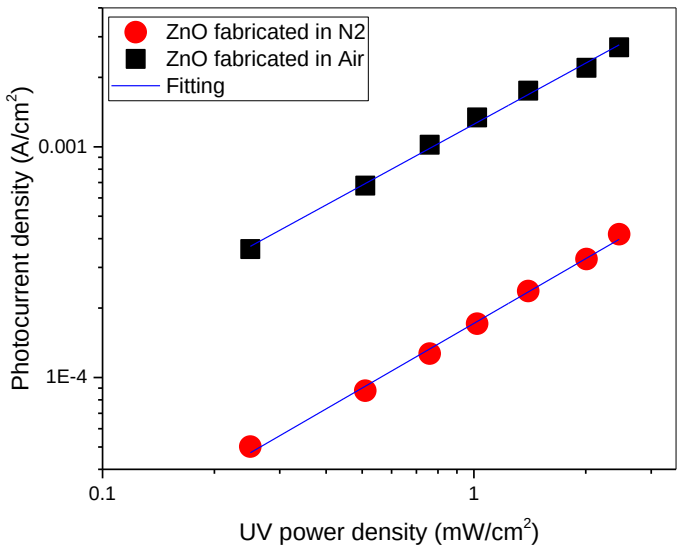

Figure 3.24: A log plot of the photocurrent as a function of the incident UV light power for devices fabricated in air and nitrogen and tested in air. The blue line represents the fit to the power law function defined in the text.

3.6.5.2 Conditioning of photoconductivity with storage

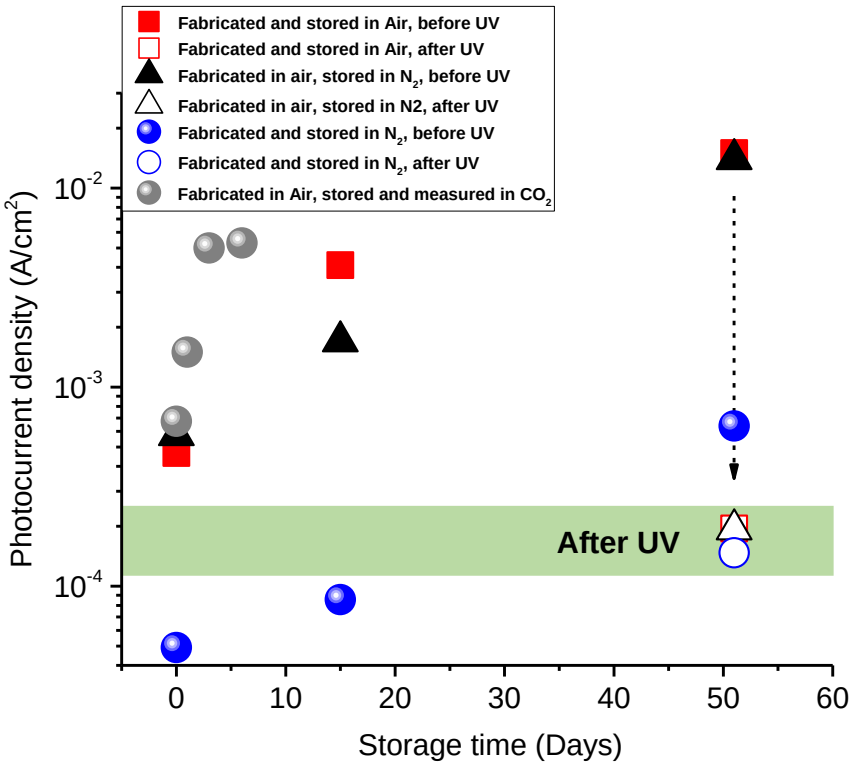

Figure 3.25: The semi-log plot of the evolution of the UV photocurrent density evolution with time of ZnO NP devices fabricated in air and nitrogen and stored in different environments. The devices stored in air and nitrogen were irradiated with UV and retested again as shown in the highlighted area. All devices were tested in air except for the sample stored and measured in CO_2.

We have shown in section 3.6.3 and 3.6.4 that the surface composition of ZnO NPs is affected by storage in different environments. For example, surface carbonates are formed by storage in air and CO_2 and the contact angle also changes significantly with time. We now consider how the storage environment affects photoconductivity. Figure 3.25 shows the UV photocurrent of ZnO NP devices fabricated in air and nitrogen as a function of storage time up to for 51 days in two environments namely; air and nitrogen. For a better understanding of the effect of a nitrogen environment on the photocurrent, a ZnO NP device fabricated in air but stored in nitrogen was also examined. The three

devices were then irradiated with UV of 0.45 W/cm^2 for 40 min in air and then retested immediately. A fourth device was stored and measured in CO_2. All devices irradiated and electrically tested following the same conditions and light source for comparable reasons. It is clear from the figure that the performance of all devices improves with storage time. Persistent photoconductivity occurs because normal electron-hole recombination is prevented because the photogenerated holes are quickly removed from the system, possibly by reaction with adsorbed oxygen, or by trapping. There is an excess of long-lived electrons and the photocurrent is proportional to the density of excess electrons according to the conductivity equation outlined in chapter 4, section 4.1. Therefore the increase in photocurrent on storage may originate from the more effective removal of holes. Alternatively "conditioning" in the storage environment may involve the removal of electron traps which reduce the density of electrons. This may occur by the adsorption of moieties onto the ZnO NP surface, eliminating a surface trap. We note that conditioning occurs irrespective of whether there is an oxygen, nitrogen or CO_2 environment. It would be interesting if we could correlate the formation of carbonate groups on the ZnO surface with the improvement in photoconductivity on storage. Unfortunately, this is not the case. The FTIR result in figure 3.17 shows that there is no significant formation of carbonates when the device, fabricated in air, is stored in nitrogen. However, the photoconductivity of this device increases with storage time, albeit initially more slowly than for the device stored in air. Figures 3.17-A, B and C show that irradiation with high-intensity UV light removes material from the surface of ZnO. This may be associated with the large drop of responsivity following irradiation using similar conditions, possibly resulting from the photogeneration of a high density of electron traps or recombination centres.

3.6.5.3 Temporal characteristics of persistent photoconductivity

We now consider in more detail the temporal characteristics of the three devices discussed in figure 3.23. The photocurrent response times were found by fitting the rise and decay current transients to separate exponential curves, with the time constants tabulated in table 3.4. The equations used to fit the transient photocurrent with different time constants are given below:

$$J(t) = J_o + A\left[1-\exp\left(-\frac{t}{\tau}\right)\right] \tag{3.7}$$

$$J(t) = J_o + A_1\left(1-\exp\frac{-t}{\tau_1}\right) + A_2\left(1-\exp\frac{-t}{\tau_2}\right) \tag{3.8}$$

$$J(t) = J_o + A\ \exp\left(-\frac{t}{\tau}\right) \tag{3.9}$$

$$J(t) = J_o + A_1\exp\left(-\frac{t}{\tau_1}\right) + A_2\exp\left(-\frac{t}{\tau_2}\right) \tag{3.10}$$

Where J_0 representing the photocurrent, A is the photocurrent amplitude coefficient, t is the irradiation time and τ is the increasing time constant. Equations 3.7 and 3.8 calculating the rising transient with single and double time constants respectively, while equations 3.9 and 3.10 used to calculate the decay transient with single and double time constants respectively.

The fitted curves are given along with experimental data, in figures 3.23-C to E. The temporal response of the device prepared in air is well described by the mono-exponential rise and decay functions shown in figure 3.23-C. The device fabricated in air has an additional slower component to the rising transient, which is well described

by a double exponential function with two time constants. The decay can be fitted with one time constant as shown in figure 3.23-D. Finally, the device fabricated in nitrogen requires double exponential functions for both the rising and decaying photocurrent transients as shown in figure 3.23-E.

Let us now discuss the significance of these exponential temporal characteristics. Persistent photoconductivity in ZnO requires an excess of long-lived electrons and the photocurrent is proportional to the density of excess electrons. On irradiation, the density of electrons grows with time until equilibrium is reached over the timescale of the excess electron lifetime. This may depend on trapping times or scavenging by surface electrochemical reactions. When the light is switched off, the photocurrent decays over a timescale depending on the excess electron lifetime. A simple exponential decay curve is observed if there is a single dominant decay mechanism. A second component in the rising photocurrent signal relates to a second independent contribution to the generation of excess electrons. This occurs for the two samples fabricated in air and nitrogen respectively and may indicate electron release from shallow traps. The relative coefficients A_1 and A_2 for the sample fabricated in air are 3.7 and 6.3 respectively (note that the photocurrent is normalized for clarity). While, the relative coefficients for the sample fabricated in nitrogen are 4.23 and 5.67 for A_1 and A_2 respectively. This indicates that the second component in the rising photocurrent signal is the dominant of the overall photocurrent response in both samples.

The photocurrent decay transient, observed on switching off the light source, is related to the excess electron lifetime and may also have two components, as observed in figure 3.23 (E), for the sample fabricated in nitrogen. A stretched exponential (not observed here) may result if relaxation to/from multiple trap levels is involved.

Table 3.4: Time constants calculated from the fitted curves describing the photocurrent transients shown in figure 3.23.

Devices	Rise time constants		Decay time constants	
	τ_1 (sec)	τ_2 (sec)	τ_1 (sec)	τ_2 (sec)
Prepared in air	4.3	----	4.0	----
Fabricated in air	3.6	7.1	4.0	----
Fabricated in N_2	3.9	11.2	0.57	4.0

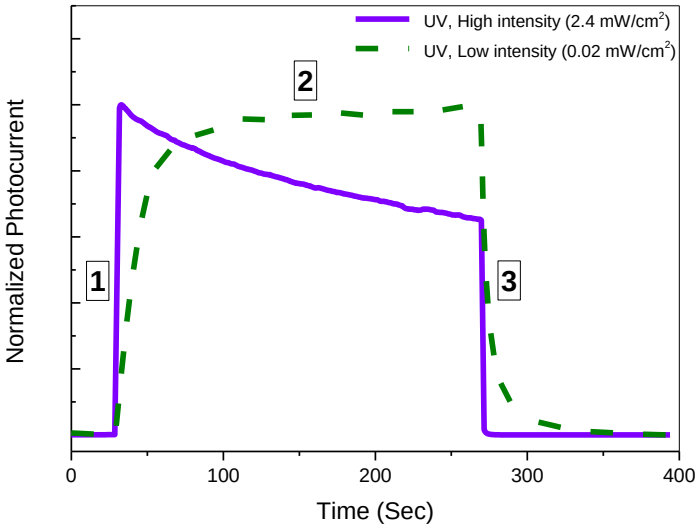

Figure 3.26: The normalized UV photocurrent transients for the same ZnO NPs device (fabricated and tested in air) measured on irradiation with UV light of intensity 2.4 and 0.02 mW/cm^2 for 4 min. A voltage of 20V is applied for the measurement. .

Figure 3.26 shows the normalized time dependence of the photocurrent for the same ZnO device in response to light pulses of 4 min duration measured in air. Neutral density filters were used to vary the UV light intensity from 2.4 mW/cm^2 to 0.02 mW/cm^2 to make the two measurements. The different temporal regions are labelled (1), (2) and (3) for clarity of discussion. The relatively long response time of region (1) at low intensity is explained in the literature by trap filling. At high intensity the traps become filled. In this case the sharper rise time indicates a shorter electron lifetime

maybe involving reactions with surface species or electron-hole recombination [176,177]. If the latter mechanism dominates, it involves recombination with trapped holes, as the lifetimes are still orders of magnitude longer than those typical for interband recombination. For similar reasons, on switching off the light source, the photocurrent decay, shown in region (3), is shorter for the higher intensity light source. Region (2) shows a slow exponential like decay of the photocurrent even when illumination is maintained, but only when the incident intensity is high. Therefore the new decay mechanism is nonlinear and so we may assume that it involve electron-hole recombination. An inspection of figure 3.27-B, which shows multiple photocurrent transients for a similarly prepared device, reveals further information about the mechanism. The generation of new recombination centres is photoinduced. Secondly the centres are permanent rather than volatile over the timescales of the experiment, since the original photocurrent is not restored by subsequent pulses of light. Therefore we can rule out the mechanism of carriers being scavenged by adsorbed groups to form volatile molecules which escape from the surface. For example, water dissociation on the surface of ZnO was found to capture charge carriers and therefore, reduce the photocurrent [178]. However the current would be restored in the subsequent pulse which is not that is observed. Instead we suggest that the photo-decomposition of adsorbed moieties, observed by FTIR, results in the creation of long-lived defects on the surface which act as recombination centres which remain active to quench carriers created by subsequent pulses of light.

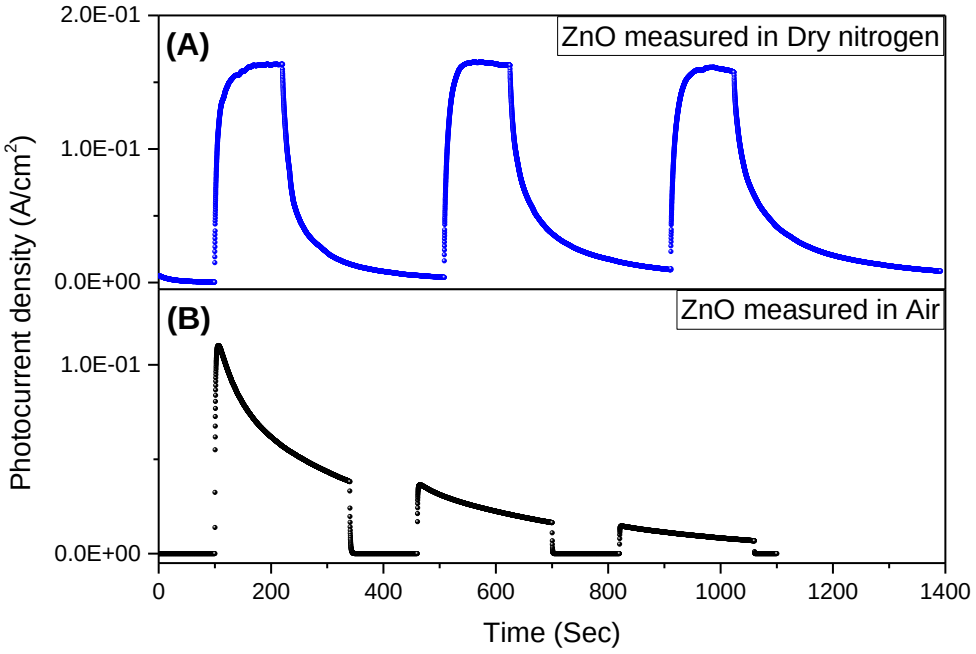

Figure 3.27: The UV photocurrent transient of ZnO NPs, but measured in air and dry nitrogen respectively. Both devices were irradiated with UV light of intensity 2.4 mW/cm^2 and measured on application of 20 V.

A second sample, prepared and annealed in nitrogen, was illuminated under the same conditions and its photocurrent transient is shown in figure 3.27-A. The initial photocurrent of both devices is about the same. However, the latter device is stable over a number of pulses. This suggests either that the surface groups involved in defect formation are not present or that the photochemical reaction is oxidative.

3.6.5.4 Measurements in wet and dry environments

A probe station was mounted in a glove box (GB) in order to compare devices measured in four distinct environments. For clarity, devices fabrication and testing conditions are summarized in table 3.5. Four devices fabricated in air are labelled (A), whilst those fabricated in nitrogen are labelled (B). The latter devices were transferred to the probe station glove box in a sealed container and so did not interact with air. After introducing to the GB, samples were stored for about 30 min in the GB before taking the measurement. The samples were tested in 4 different environments: dry nitrogen (1);

dry oxygen (2); wet oxygen (3) and wet nitrogen (4). The relative humidity was about 3% for conditions 1 and 2 and 90% for conditions 3 and 4. A different sample was used for each testing condition. All devices were baked at 100 ºC for 10 min and annealed at 350 ºC for 1 hour in their fabrication environment.

Table 3.5: Gives device preparation and testing conditions for glove-box experiments. The A and B letters included in the device number refer to the device annealing condition, where A represents the device annealed in air and B in nitrogen. The low water content indicator corresponds to a relative humidity of about 3%, while the high is about 90%.

Devices	Testing conditions			
	Condition	*Oxygen*	*Water*	*Description*
1A and 1B	1	Low	Low	Nitrogen
2A and 2B	2	High	Low	Oxygen
3A and 3B	3	High	High	Wet oxygen
4A and 4B	4	Low	High	Wet nitrogen

Figures 3.28 and 3.29 show the dark I-V and the photocurrent characteristics in addition to the time dependent photocurrent measurements of all the devices. Each sample was irradiated using the same conditions of a UV light pulse of duration 5 min and intensity 2.4 mW/cm^2. We do not discuss all the data in depth but present a few key results. First let us recall the generally accepted mechanism of persistent photoconductivity in ZnO, illustrated above in figure 3.5. The adsorption of oxygen on the surfaces of the nanoparticles traps electrons in the dark. Free electrons and holes are created by excitation at energies above the semiconductor band-edge. The photogenerated holes react with the adsorbed oxygen, according to equation $O_2^- + h^+ \rightarrow O_{2(g)}$ resulting in its removal and the release of the trapped electrons. The lifetime of the excess electrons is determined by the capture rate of molecular oxygen to reform the adsorbed ionic species. This mechanism was used to explain the slow recovery times often found when

samples are measured in an inert atmosphere, e.g. nitrogen or vacuum [78]. The electron lifetime is long because of the low density of oxygen, however it is clear from the results that something more complicated is going on.

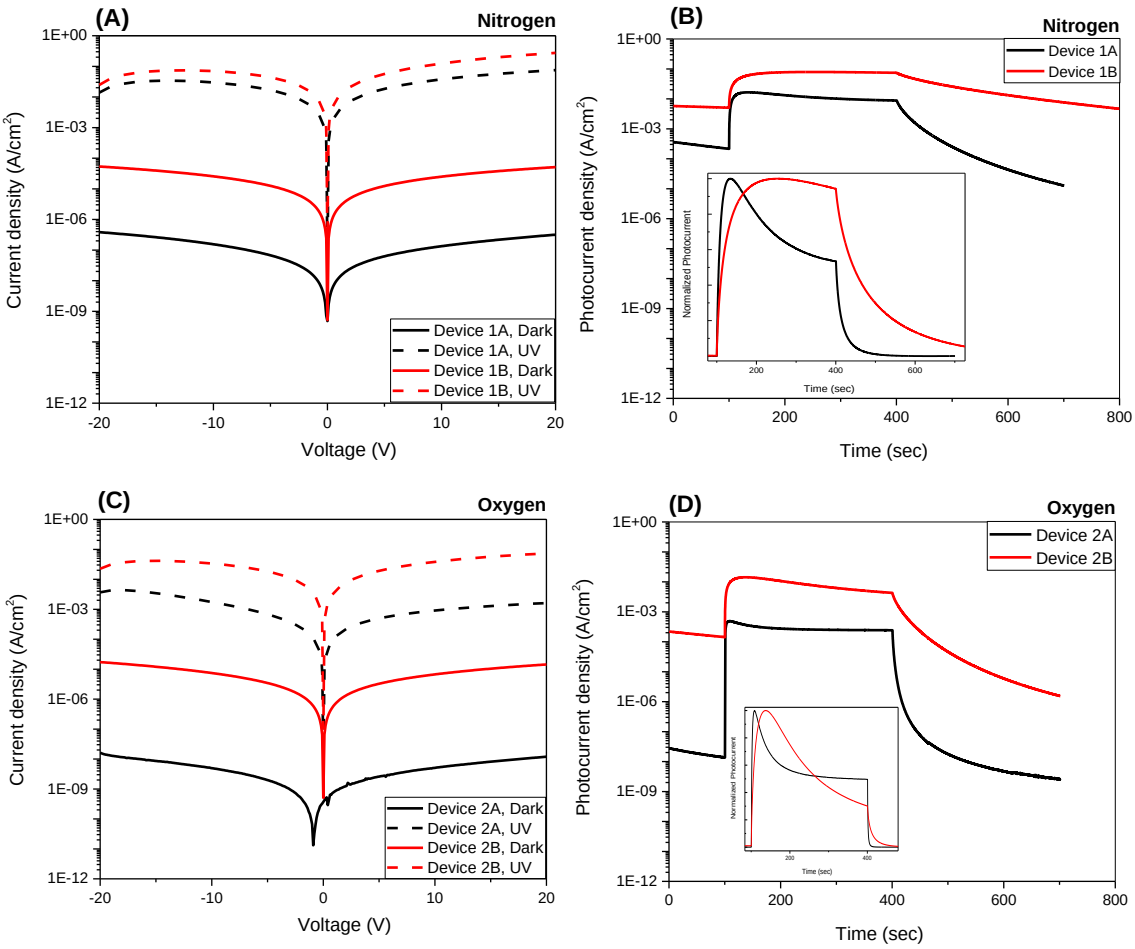

Figure 3.28: The semi-log plot of dark and photo- I-V characteristics for the set of devices tested in (A) dry nitrogen and (B) dry oxygen. The photocurrent transients of the devices tested under both conditions are shown in (B) and (D). The insets show the normalised transients. The devices were irradiated with 2.4 mW/cm^2 UV for 5 min with an applied voltage of 5V.

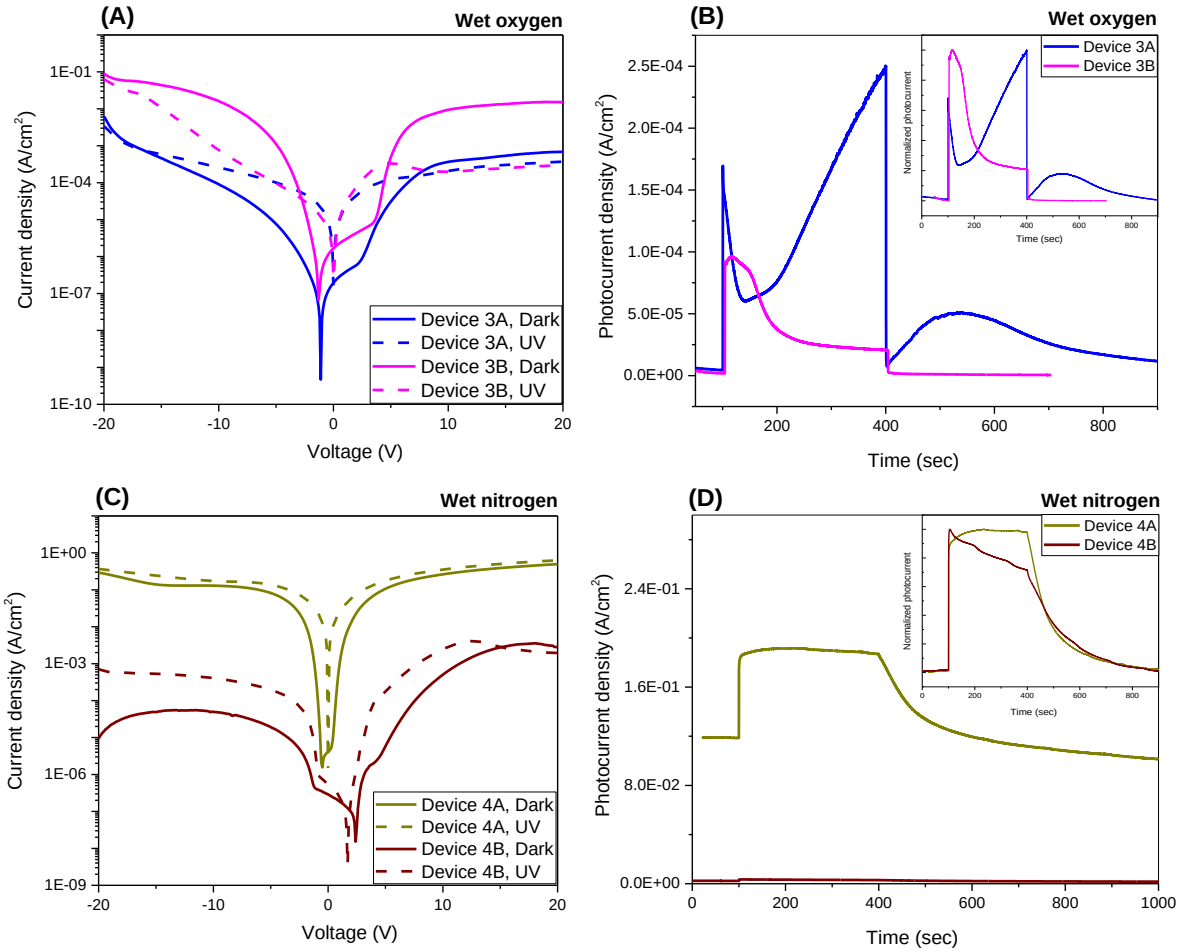

Figure 3.29: The semi-log plot of dark and photo- I-V characteristics for the set of devices tested in (A) wet oxygen and (B) wet nitrogen. The photocurrent transient of the devices tested under both conditions is shown in (B) and (D). The insets show the normalised transients. The devices were irradiated with 2.4 mW/cm^2 UV for 5 min with an applied voltage of 5V.

Firstly, there are significant differences between the A and B devices for all testing conditions. FTIR, see figure 3.13, tells us that annealing of the A devices in air more effectively decomposes precursor acetate group and the octylamine ligands, so creating more surface states than the B samples annealed in nitrogen. It is unlikely that device 1B, annealed and tested in nitrogen, has a high concentration of surface adsorbed oxygen, yet photogenerated holes are efficiently removed to generate a large number of excess electron to produce the large photocurrent maximum of 8×10^{-2} A/cm^2 shown in

figure 3.28-B. A comparison of the photocurrent decay timescales (when light is switched off) in figures 3.28-B and 3.28-D shows that the electron lifetime is much slower when tested in a nitrogen rather than an oxygen environment. This implies that surface reactions with atmospheric species affect the excess electrons lifetime and that these are more likely in an oxygen environment. A comparison of the decay transients of the A and B devices of the same two figures shows a correlation between a shorter electron lifetime and a higher density of surface traps.

Figure 3.29-A and C shows that devices tested in a highly humid oxygen or nitrogen atmosphere have extremely high dark currents. These results are in agreement with the work of Lai et al [178], who find that the dark current of a ZnO nanorod device increases with relative humidity in air. As discussed in section 3.2.1, electrical conductivity by adsorbed water is carried out by protons, by means of the Grotthus mechanism. Indeed, figure 3.29-A shows that the dark current is higher than the photocurrent in the higher voltage regions of the two devices tested in wet oxygen. In both cases, the photocurrent measurement begins at a voltage of -20V. The observed photocurrent appears asymmetric with respect to voltage as it reduces over time as the devices are scanned. This suggests that photo-electrochemical reactions are removing protons as well as electrons (or creating holes) and further implies that the adsorbed water is removed by oxidative reactions. The temporal characteristic of device 3A is particularly complicated showing competition between current generating and current reduction mechanisms, both under irradiation and in the dark. The proton mediated dark current of the device 4A, which was annealed in air and tested in wet nitrogen, appear to be unaffected by irradiation, as the photocurrent sits on a stable background. This suggests that the adsorbed water is not removed by irradiation and that it does not appear to quench the photocurrent of the device. Since device 4B was annealed in a nitrogen environment, it

is unlikely that hole capture by adsorbed oxygen to release molecular oxygen is unlikely to be the mechanism of persistent conductivity. Despite this the electron decay time is fast, see figure 3.29-D.

3.7 Summary

The objective of this chapter was to investigate how the device preparation, storage and testing environment influences the magnitude and time dependence of the ZnO NPs photoconductivity. Solution processed ZnO NPs devices were fabricated in air and nitrogen and electrically tested in air and in a controlled environment in a glove box. The experiments are correlated with surface wettability and FTIR measurements to elucidate how surface states affect the photoconductivity.

FTIR indicates some important observations related to the surface composition of ZnO NPs after fabrication in air and nitrogen. We found that annealing the ZnO NP film in an oxidizing environment, i.e. air, decomposes most of the organic ligands and the residual acetate from the starting precursor, and so creates surface states. However, CO_2 is adsorbed from air on storage to form carbonate groups which possibly passivate the surface states and so increase photoconductivity. NP films annealed in nitrogen retain a significant fraction of precursor acetate and ligand groups and show different photoconductivity behaviour. Water absorption is found to increase gradually with time when ZnO NPs are stored in air but not in nitrogen. Irradiation with high intensity UV light in air removes many surface groups. This affects the stability of devices.

The contact angle (CA) of ZnO NPs is very sensitive to the surface treatment and storing environments. The NP thin film is initially hydrophobic and then becomes hydrophilic following annealing in air. The change towards hydrophobicity on storage in air is attributed to carbonate formation.

A major aim of the work was to fabricate a ZnO persistent photoconductive device, which was temporally stable. Though not tested for extended periods, the ZnO NP film annealed and tested in dry nitrogen appears to be a very promising device. We find that UV light irradiation in an oxidative environment creates permanent recombination centres. These quench photoconductivity may be associated with the photochemical removal of surface groups. We were unable to elucidate the exact mechanism of persistent photonductivity in ZnO NPs, although it is clear that electrons can be generated or quenched by a number of different interactions with surface states or atmospheric species. It is evident from this work that the standard mechanism, involving the adsorption and desorption of molecular oxygen, cannot be valid for many of the devices discussed.

Chapter 4

Dual Wavelength (UV and Green) Photodetection of ZnO NPs

In this chapter, steady-state and transient measurements are discussed to probe the origin of persistent narrow-band green photoconductivity. Surface defects associated with the photoconductivity mainly originate as a result of the production method and are highly affected by the surface treatment and storage environment. FTIR spectroscopy of the ZnO surface after and before annealing shows the evolution of the compounds which might cause this phenomenon.

4.1 Introduction

ZnO colloidal nanoparticles are potentially useful semiconductors in electronic and optoelectronic applications due to their compatibility with low-cost and highly scalable manufacturing for the next generation of smart products for the Internet of Things, wearable technologies, mobile medical devices, security etc. The direct, wide band gap at room temperature (3.37 eV) and the high exciton binding energy (60 meV) enable ZnO to be the material of choice for some photonics applications [61]. Simple production techniques and ease of processing are considered advantageous for any material to be technologically viable for low-cost applications. Hence, solution-processable ZnO nanoparticles have many applications in device technologies such as transistors, light-emitting diodes, photodetectors, sensors etc. Due to its superior electronic properties, ZnO represents the most reported metal oxide semiconductor in thin film transistors (TFTs) to date [179]. From an optoelectronic perspective, it is often combined with organic materials to improve electron injection or collection in hybrid OLEDs, photovoltaics and photodiodes [180,181]. Furthermore, there is a tremendous research interest in solution-processed ZnO nanoparticles due to their remarkable ultraviolet photoconductivity (PC) [138,182]. Recently, ZnO has been used as core-shell nanorods with CdS to make a self-powered dual wavelength photodetector ZnO CdS operating in both ultraviolet and blue-green spectral regions [183]. Such multispectral photodetectors are interesting for applications such as discrimination of objects, lab on a chip, environmental and biological sensing. Low-cost, electronic and optoelectronic materials must be easily patterned in order to achieve the promise of the disruptive technologies mentioned above, but there is limited work on the patterning of ZnO to date. Thin ZnO seed layers are often used to seed the growth of vertical ZnO nanowires by solution-processing or chemical vapour deposition and the growth can be patterned by masking

the seed layers with patterned photoresist [184]. Alternatively, the seed layers can be patterned photolithographically or by inkjet printing [185]. Zinc oxide vertical nanowire arrays have also been sculpted to form three-dimensional patterns using photolithography [186]. A photolithographic approach was used to pattern ZnO, deposited by spray pyrolysis, to modify the electron injection barrier of a gold/organic semiconductor interface and therefore improve the efficiency of a light-emitting, organic field-effect transistor [187].

The conductivity σ of a semiconductor is given as $\sigma = (ne\mu_e + pe\mu_h)$ where *e* is the elementary charge, *n* and *p* are the density of electrons and holes respectively and μ_n and μ_p their respective mobility. Photoconductivity (PC) results in a change of conductivity by irradiation with light, normally due to the increase in *n* and/or *p*. No energy is generated and the current is provided by the external circuit via the contacts, reducing to zero as the applied field goes to zero. ZnO shows PC with response times in the nanoseconds regime determined by electron-hole recombination [188,133] but there are also many examples of persistent PC [138,133,189]. ZnO is an *n*-type semiconductor with a very deep valence band so it is generally assumed that the persistent photocurrent is carried by excess electrons. The generally agreed mechanism is that a low conductivity depletion region is generated at the surface of ZnO in the dark because electrons are trapped by the adsorption of gaseous oxygen according to the reaction $O_2(g) + e^- \rightarrow O_2^-$. Free electrons and holes are photogenerated by absorption of light with above band-gap energy. The holes migrate to the ZnO surface along the potential gradient produced by band bending where they release the adsorbed oxygen according to the reaction $O_2^- + h^+ \rightarrow O_2(g)$. The persistent photocurrent build-ups over the timescale, seconds or longer, of the electron lifetime, which is determined by trapping or scavenging via

surface electrochemical reactions etc. A photoconductive gain (equal to the number of electrons generated per photon) greater than one is often observed as the electrons pass across the circuit multiple times. The PC signal may also have a contribution from the reduction of the injection barrier at the Schottky contacts due to the trapping of photogenerated holes in the depletion layers [133,78]. There are reports of nominally undoped ZnO showing PC below band-edge and in the visible spectral range. The visible PC is spectrally broad and is attributed to transitions between various defect states and the conduction or valence band [189,190,191].

Surface defects become very effective when the material structure is brought down to nanoscale size because of the large surface to volume ratio. The effect of surface defects on the optoelectronic properties of ZnO nanostructures has been investigated by many research groups. Great efforts are made to identify the surface defects by linking the visible photoactivity to the material's light emission [107]. However, due to the wide distribution of surface defects with different sub-bandgap energy levels, visible photocurrent in ZnO nanostructure has a broad spectrum. M. Kavitha et al. [192] investigated the visible photocurrent from ZnO nanostructures prepared by different methods. They tried to identify the dominating surface defects by comparing the photoresponse with their photoluminescence (PL) emission. Visible PL emission and photocurrent were found to be quenched and reduced respectively when the sample was annealed at 550 °C suggesting the reduction in oxygen vacancies density. Moazzami et al. [73] also realized a visible photocurrent from ZnO epilayers prepared by plasma-assisted molecular beam epitaxy. They studied the carrier trapping associated with the presence of surface defects using photoconductive transients under white light. They claimed that persistent photoactivity in the visible is related to deep hole traps with a small electron-hole recombination rate. Reemts and Kittel [70] suggested that persistent

photoconductivity from porous ZnO film prepared by electrodeposition is attributed to the lattice relaxation process after the photoexcited electrons are distributed in sub-energy levels within the ZnO band gap. Dipanwita Sett et al. [193] tried to identify the defects by studying the photocurrent transient and correlating it with PL emission from chemically grown ZnO nanorods. They investigated the relation of annealing with the number of hole and electron traps using the photocurrent transient at different wavelengths. A relevant study correlating surface defects of ZnO nanorods with the surface morphology has recently been conducted by K. Bandopadhyay and J. Mitra [194]. By spatially resolving the photocurrent using the conductive mode AFM with a green excitation light source at 532 nm, the photoconductive regions related to the surface defects were found to be distributed within the grain boundaries of the ZnO rods where lattice dislocations normally take place.

In this chapter, we discuss narrow-band persistent PC below the band-edge of colloidal ZnO nanoparticles. The transitions observed in the green spectral region are sharp, which suggests that charge transfer occurs between discrete states rather than to the broad conduction or valence band. We propose a model based on defect and shallow donor states to explain the spectral and temporal dependence of the photocurrent. This is different to most sub-bandgap PC, which occurs over a broad spectral range, resulting from optical transitions between defect states and the conduction or valence band. We show how device processing and storage can be controlled to increase the density of defects and thereby enhance PC in the green. The photoconductive thin films are solution-processable and we demonstrate that they can be patterned using photolithography to obtain a dual wavelength photodetector. Multi-step photolithography allows different pixels to have different spectral responses; one is

sensitive to both green and ultraviolet light whilst the green response is suppressed in another.

4.2 Photodetector device fabrication

The photodetector device used in this study was designed with a planar configuration, as shown in figure 4.1. More details about the substrate, device specifications, synthesizing of ZnO NPs solution and device fabrication procedures are mentioned in chapter two. A new solution batch was prepared for almost every new experiment indicating the consistency and repeatability of the results. The ZnO NPs annealing temperatures were varied as mentioned later in device pixilation procedure. The resulting ZnO layer thickness was kept almost the same, around 120 nm (±5nm) with good uniformity. Depending on the surface treatment, the device preparation environment is changed to be either air or nitrogen, following the same preparation parameter to assess and control the surface defects of the ZnO NPs film. ZnO NPs devices were electrically tested in air and nitrogen using the I-V characterization measurement discussed in section 2.2 in chapter two. The light beam intensity typically was about 0.31 mW/cm^2 and 0.5 mW/cm^2 at 363 nm and 550 nm respectively. The photocurrent transient was also measured in a nitrogen-filled glove box using a laser diode with a wavelength of 532 nm and a power of 0.15 mW. The electrical measurements were performed using a testing circuit board bought from Ossila connected to a Keithley 2400 source meter and interfaced with the computer using BenWin+ software to measure the photocurrent density as a function of wavelength and time. All electrical the measurements were performed at room temperature.

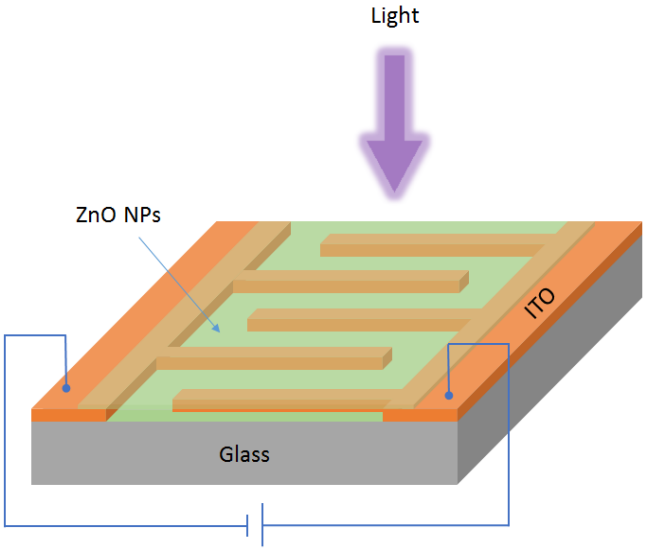

Figure 4.1: The photodetector device structure used in this study showing the ZnO NPs film on top of ITO inter-digitated electrodes. ITO edges have been wiped for direct electrical contact.

4.3 Results and Discussions

4.3.1 Visible photoconductivity of ZnO nanostructure

Surface defects of ZnO represent a rich subject of investigation. The high surface to volume ratio of ZnO nanoparticles enables those defects to significantly affect the material properties and hence its applications. The simple chemical formula of ZnO encourages the defects such as Zn interstitials and O vacancies to accommodate sites in its open structure. Those native defects have different ionization energies by which they alter the electrical and optical properties of ZnO [29]. ZnO has a wide band gap of around 3.37 eV at room temperature, enabling it to be an excellent photoconductive material in the UV. However, due to the surface defects, ZnO NPs also have photoactivity in the visible, depending on the defects densities and types. Here, solution-processed ZnO nanoparticles exhibiting photoactivity in the UV which originates from the band transition and a defects-based narrow-band photocurrent peaking at 550 nm with a shoulder at 596 nm, as shown in figure 4.2, are investigated.

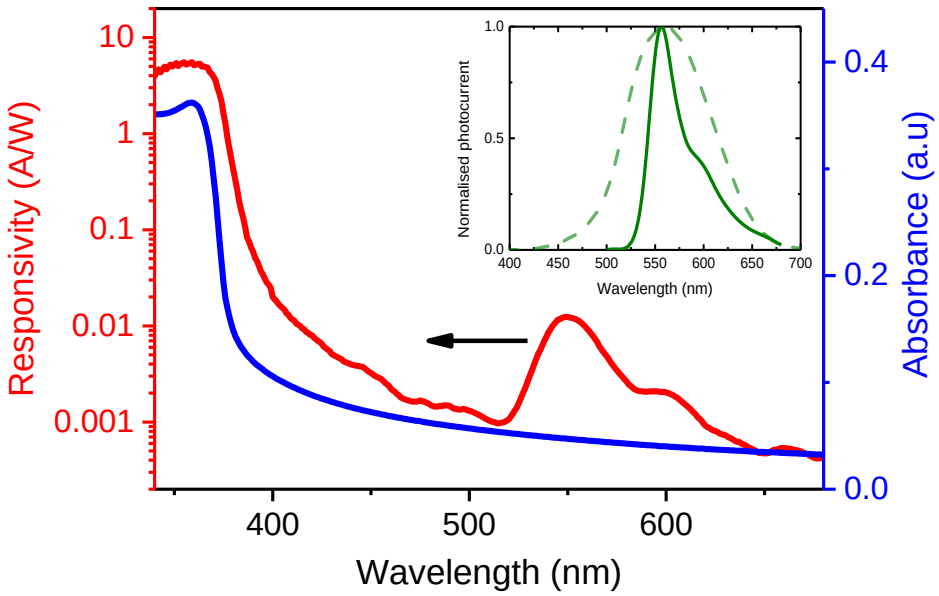

Figure 4.2: Semi-log plot of absorbance and photocurrent responsivity spectra from a thin film of ZnO nanoparticles following annealing at 350 °C in air for 2 hours. The inset shows the visible photocurrent spectrum (solid line), measured on application of a voltage 20 V across a device length of 5 μm, and the green colour matching function (dashed line) of the CIE colour system.

The figure above shows semi-log plot of the optical absorption and photocurrent responsivity spectra of a ZnO film. The strong excitonic absorption peak around 360 nm shows a small quantum confinement effect compared with the peak of bulk ZnO at about 370 nm. A weak absorption tail decays into the visible region of the spectrum, which is attributed to defect states. The responsivity of the photocurrent peaks at 5.3 A/W in the UV. The expected tail in the visible is accompanied by a remarkable narrow-band photocurrent with a peak responsivity of 10.2 mA/W at 550 nm and a shoulder at 596 nm. Noting that the responsivity of ZnO photodetector depends on defect concentration, the UV responsivity reported here is comparable to that reported by others, i.e. 61 A/W for colloidal NPs by Greenham et al [78] and 1.1 A/W for a sol-gel ZnO film by Chen et al [140]. The reduced responsivity in the visible spectrum is compatible with the literature. For example, ZnO nanowires show a UV responsivity of

2×10^{-2} A/W, whilst the corresponding broad-band responsivity in the visible is 10^{-5} A/W [195]. The inset of figure 4.2 shows the visible PC spectrum on a linear scale. Its full width at half maximum (FWHM) is about 40 nm with some sample-dependent variation in the relative heights of the peak and shoulder. There is no corresponding visible feature in the absorption spectrum, indicating that a low density of the defect states is associated with the PC, which must have a much higher photoactivity than the defects associated with broadband visible absorption. As the inset shows, the green PC spectrum is completely contained within the green colour matching function of the CIE colour system (International Commission on Illumination), showing its applicability for green imaging devices. The UV PC spectrum is also narrow with FWHM of 32 nm, although the high-energy spectral range may be limited by the declining output of the measuring light source below 340 nm.

The time dependence of the photocurrent in the UV and green is shown in figure 4.3-A using a semi-log plot. Figure 4.3-B shows the UV and green photocurrent as well as the dark current as a function of voltage, again with a semi-log plot. The UV signal has a rise time of less than 0.5 sec and this increases as the intensity of the irradiation decreases as discussed earlier in chapter three. Slower response times are found for the green signal.

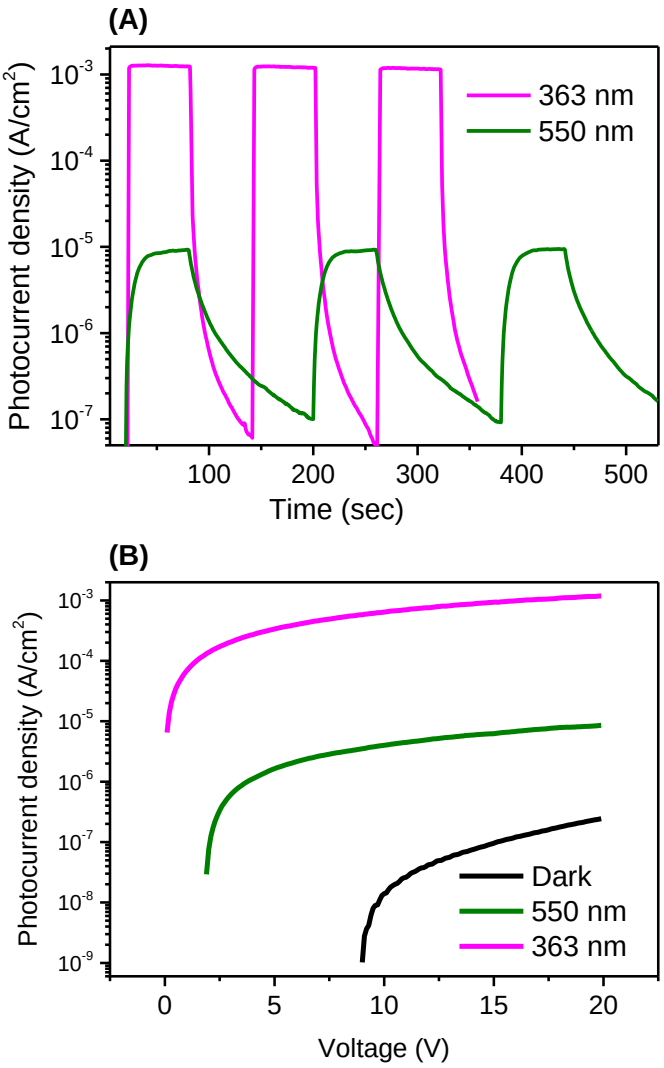

Figure 4.3: (A) A semi-log plot of the current transients of ZnO nanoparticles in response to the light in the UV (363 nm) and green (550 nm) for the same working device. The device was annealed at 350 °C for 2 hours in air. The incident light pulse length was 60 seconds for both, and the time interval between each light pulse was 60 seconds for the UV and 120 seconds for the green. The responsivity in the UV and green is 8.6 A/W and 0.18 A/W respectively, (B) Current density versus field in the dark and on application of light of intensity of 0.31 mW/cm^2 and 0.5 mW/cm^2 at a wavelength of 363 nm and 550 nm respectively.

4.3.2 Origin of green photoconductivity

There is a fundamental difference between the visible PC reported here and reports in the previous literature [189,191,73,193,196,80] which show PC over a broad spectral range, with typical spectral width >> 100 nm. These are attributed to optical transitions between defect states and the conduction or valence band. For example, Kavitha et al. [192], and others [44,74] studied the ZnO photoconductivity in the visible and assigned it to the electron transitions between sub-bandgap ionized energy levels introduced by the oxygen vacancies and the conduction band. Furthermore, Kang et al. [197] have proposed a different mechanism based on first principles calculations suggesting that, hydrogen-zinc vacancy defect complex ($H - V_{Zn}$) formation is the responsible of persistence photoconductivity in ZnO. Upon light absorption, the zinc defect complex results in a $O - O$ bond which give rise to metastable conducting states. The spectrally narrow visible photoconductivity from undoped ZnO observed in our devices has not yet been explored for the best of our knowledge. Moreover, surface reactions involving CO_2 adsorption from the atmosphere have been suggested to be the responsible of defects formation which causing the narrow photoactivity. In a study by Liu et al. [198] CO_2 can be photoreduced (by illumination with solar simulator light source) on the surface of TiO_2 to CO and CH_4 with the presence of oxygen vacancies. That is to say, the presence of oxygen vacancies on the surface could promote CO_2 activation both in dark and under illumination by generation of CO_2^- intermediates by the surface reaction with surface adsorbed H_2O or OH groups. This study suggests an association between carboxylate formation and the presence of oxygen vacancies.

The visible photocurrent spectrum shown in the inset of figure 4.2 cannot involve transitions to a continuous band because of the two transitions, peak at 550 nm and shoulder at 596 nm, are spectrally narrow and so must involve discrete states. In

suggesting a model to explain the origin of PC, we are hampered by the huge variation in the attribution of defect states to spectral transitions in the literature. Therefore, our proposed model can only be tentative. For example, the green luminescence in ZnO has been linked to transitions involving Zn vacancies [27], O vacancies [191,199] etc. Jannotti and Van de Walle have calculated the transition energies of various defects. These are the Fermi energies at which the formation energies of two charge states are the same [27]. They, as well as others [200], show that the Zn vacancy is a deep acceptor with a low formation energy. It exists in its double ionised state, V_{Zn}^{2-} in n doped ZnO, since the transition from the - to 2- charge state occurs at a Fermi energy of 0.87 eV above the valence band maximum. It is often passivated by hydrogen substitution, since strong O-H bonds are formed. Oxygen vacancies are deep donor states in ZnO and can exist in one of three different charge states. The neutral state V_O^0 contains two electrons which may be removed to form V_O^+ and V_O^{2+} respectively. In n type conditions, where the Fermi level is near the conduction band, the neutral state is stable with a calculated energy about 2.0 eV below the conduction band minimum. The concentration of defects has an inverse exponential dependence on the formation energy which is proportional to $exp(\frac{-E^f}{KT})$ [27]. The calculations predict that oxygen vacancies have high formation energy and therefore exist at low concentrations. However, the surface density of oxygen vacancies in ZnO nanoparticles should be much higher because of their large surface area. The XPS results in chapter three (figure 3.9) show a large concentration of oxygen vacancies in our samples.

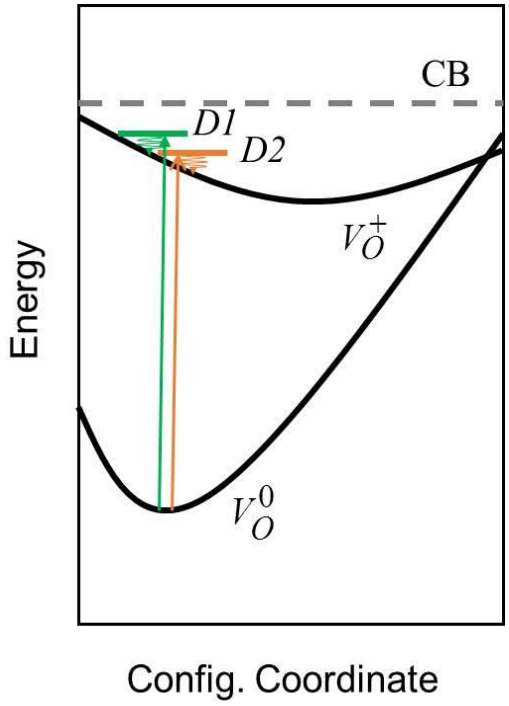

Figure 4.4: Illustration of the proposed model to describe discrete PC transitions. The minimum energy of the oxygen vacancy defect occurs at different values of the lattice configurational coordinate for the V_O^0 and V_O^+ states. The electron is transferred from the V_O^0 state to a nearby ionised donor according to equation (4.1). Two discrete donors, *D1* and *D2*, account for the PC peak at 550 and shoulder at 596 nm respectively. The ionised V_O^+ state then relaxes by lattice deformation to its equilibrium position.

We now discuss a model to explain PC at the two discrete wavelengths of 550 nm and 596 nm below the band-gap of ZnO. We assume that electron transfer comes from the V_O^0 defect because of the good match of its energy to theory, but a similar model would be relevant for the V_{Zn}^{2-}. The model is illustrated in figure 4.4. PC arises by electron exchange between the vacancy and two local and independent donors as follows:

$$V_O^0 + D1^+ + h\nu_{550} = V_O^+ + D1^0 \quad \text{and}$$
$$V_O^0 + D2^+ + h\nu_{596} = V_O^+ + D2^0 \tag{4.1}$$

The subscript in the photon energy term refers to the peak wavelength of each of the two transitions. The photon energy matches the energy difference between that of the neutral vacancy and the ionised shallow donor D^+, which gains an electron. First principle calculations show that the V_O^+ state is thermodynamically unstable [27,201,74]. However, as illustrated in the configuration coordinate diagram of figure 4.4, it can be stabilised by lattice interaction (i.e. displacement of nearest neighbour Zn atoms from their equilibrium positions) into a metastable state, the minimum energy of which occurs at a completely different lattice coordinate to that of the V_O^0 state. This means that there is a significant activation barrier for the decay of the metastable V_O^+ state to reform the V_O^0 state. Interestingly, electron paramagnetic resonance and Hall experiments with ZnO show the presence of two distinct shallow donors, one of which is associated with hydrogen [41].

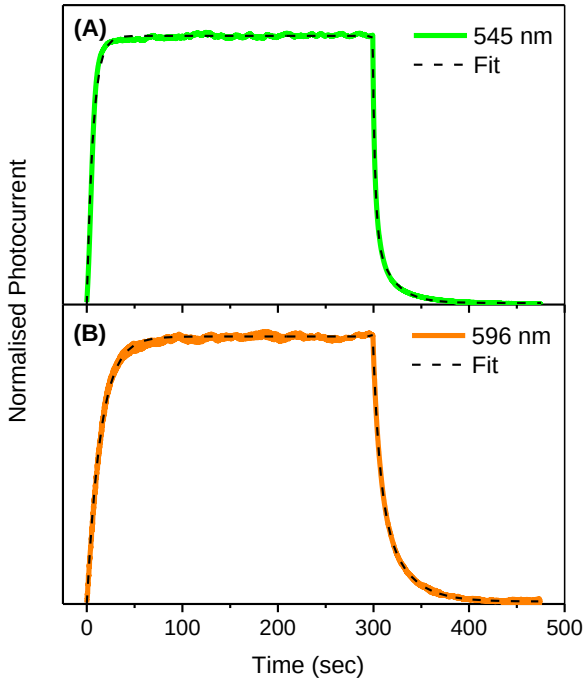

Figure 4.5: Normalised photocurrent as a function of time in response to an incident light pulse at (A) 545 nm and (B) 596 nm and length 300s. Both wavelengths have the same intensity of 0.52 ±0.03 mW/cm^2. The rising photocurrent part of the transients is fitted to the monoexponential function given in equation (4.2). The decay part of both curves is fitted to a biexponential function given in equation (4.6).

Let us now consider the temporal response to support the existence of two independent donors, *D1* and *D2*. As discussed above, it is generally assumed that photocurrent in ZnO is carried by excess electrons. Persistent photocurrent transients in ZnO often have long time constants, which can vary from seconds to hours, depending on the lifetime of the excess electrons [73,70,196,176]. Electrons can decay by recombination, trapping or by electrochemical reactions with surface groups or atmospheric species. The transients are mostly non-exponential because different traps have different trapping times and saturation effects. Figure 4.5 shows the normalised temporal response of the photocurrent at (A) 545 nm and (B) 596 nm in response to an optical pulse of length 300 sec. The rising transient of the current is well described by a single exponential, given as:

$$J(t) = J_0 + A\left[1 - \exp\left(-\frac{t}{\tau}\right)\right] \quad (4.2)$$

as shown by the fitted dash lines in figure 4.5. The time constant τ is 6.5 sec and 14.5 sec for the transitions at 545 nm and 596 nm respectively. The mono-exponential fits, with a different time constant for each transition, indicate that electron transfer occurs by a single but different route in each case. The time constant is a measure of the lifetime of the transferred electron, which includes the time taken for electron transfer from the neutralised donor to the conduction band and the reaction time with an electroactive species at the nanoparticle surfaces.

4.3.3 Variations of defect/dopant densities with processing conditions

We found large variations in the magnitude of the PC at 550 nm depending on device processing, storage conditions and storage environment. Here we attribute these variations to the density of defects/dopants and correlate these measurements to changes in the FTIR spectroscopic transitions of surface species in the ZnO thin films. Figure 4.6-A shows the FTIR spectrum of a thin film of ZnO without annealing. The ZnO backbone transitions are observed about 500 cm^{-1}. There are a number of transitions relating to the acetate ligand groups (from the starting precursor) chelated with zinc atoms on the surface of nanocrystals and the added octylamine ligands [202,203]. A thick sample was used so some of these transitions are saturated. Annealing in the air at 350 °C, see figure 4.6-B1, removes the octylamine and most of the acrylate groups. This is shown by the large reduction in the stretch C-O transitions between 1000 and 1150 cm^{-1}, the C-H bends between 620 cm^{-1} and 950 cm^{-1} and the sharp stretching C-H transitions between 2850 and 2950 cm^{-1}. Note the saturated unidentate transitions, C═O at 1570 cm^{-1} and C-O doublet at 1415 and 1450 cm^{-1}, from the precursor acetate groups are nearly completely removed by annealing in air, as shown in figure 4.6-B1 and C1.

However, transitions at similar wavenumbers, i.e. at 1565 cm^{-1}, 1419 cm^{-1} and 1454 cm^{-1}, increase significantly after storage of the thin films in the air for 15 days, see figure 4.6-B2. Only a very small increase in these transitions is observed when the sample is stored in a nitrogen environment with O_2, H_2O < 1.5-2 PPM, see figure 4.6-C2, for the same time. This is consistent with CO_2 adsorption by ZnO from the atmosphere to form surface carbonate.

The interaction of ZnO nanoparticle with atmospheric CO_2 can lead to a variety of adsorbed species depending on the presence or absence of humidity in the gas atmosphere. Possible adsorbed species include monodentate and bidentate carbonate species formed by the direct interaction of gaseous carbon dioxide ($CO_{2(g)}$) with surface oxide anions and oxygen vacancies (V) in the absence of water (Equations 4.3 and 4.4) and bicarbonate from the interaction of $CO_{2(g)}$ with surface hydroxyl groups present in humid environments (Equation 4.5) [171]. The strong IR absorption bands at ~1565 cm^{-1}, in addition to those at 1419 and 1454 cm^{-1} suggest that both bidentate and monodentate adsorbed carbonate are formed.

$$Zn - O + CO_{2(g)} \rightleftarrows ZnCO_3 \text{ (monodentate)} \quad (4.3)$$

$$\mathrm{Zn - V - Zn - O} + CO_{2(g)} \rightleftarrows ZnCO_3 \text{ (bidentate bridging)} \quad (4.4)$$

$$Zn - OH + CO_{2(g)} \rightleftarrows ZnHCO_3 \text{ (bicarbonate)} \quad (4.5)$$

The annealed samples have many transitions which do not change with annealing. These include the broad peak from 3000 - 3650 cm^{-1} and the strong peak at 900 cm^{-1}, both attributed to adsorbed –OH groups, as well as the sharp peak at 1267 cm^{-1}. A comparison of figure 4.6-C and D shows that an oxidising air rather than a nitrogen annealing environment assists the removal of the precursor acetate ligands from the

ZnO thin film. The FTIR spectrum of the nitrogen annealed sample does not change significantly following storage in nitrogen for 15 days.

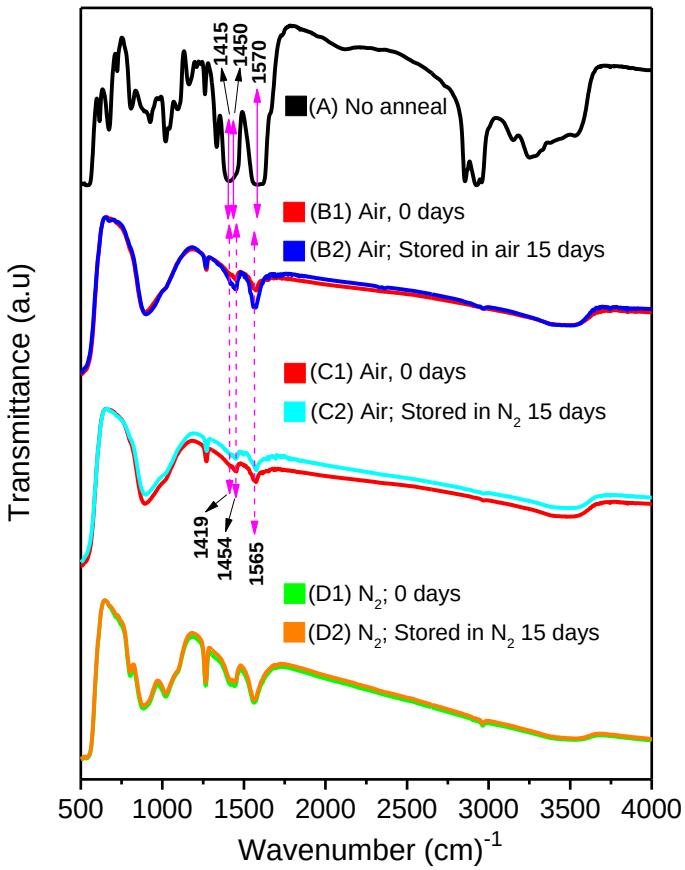

Figure 4.6: FTIR spectrum of thin films of ZnO drop-cast onto a semi-insulating GaAs substrate using different preparation and storage conditions: (A) Sample was baked at 100 °C to remove solvent; (B) Sample annealed at 350 °C in air for 1 hour, measured immediately (B1) and after storage in air for 15 days (B2); (C) Sample annealed at 350 °C in air for 1 hour, measured immediately (C1) and then after storage in nitrogen for 15 days (C2); (D) Sample annealed at 350 °C in nitrogen for 1 hour, measured immediately (D1) and after storage in nitrogen for 15 days (D2). The spectra are shifted vertically for clarity. The vertical lines and labelled transitions clarify the differences in wavenumber between the C-O transition in the unannealed sample and following annealing and storage in air.

Figure 4.7-A shows the dependence of the PC peak at 550 nm on annealing temperature and atmosphere. The highest photocurrent was observed following annealing in air at 350 °C for 2 hours. However, annealing at the same temperature in a nitrogen environment significantly reduces the visible conductivity. A correlation of these observations with FTIR results given in figure 4.6 suggests that samples, where the

precursor acetate groups are efficiently removed, give enhanced PC. Possibly, the removal of the acetate ligands creates oxygen vacancies, thus increasing the density of defect states V_O^0. Alternatively, or even simultaneously, the oxidising annealing environment may remove traps, which reduces the electron lifetime.

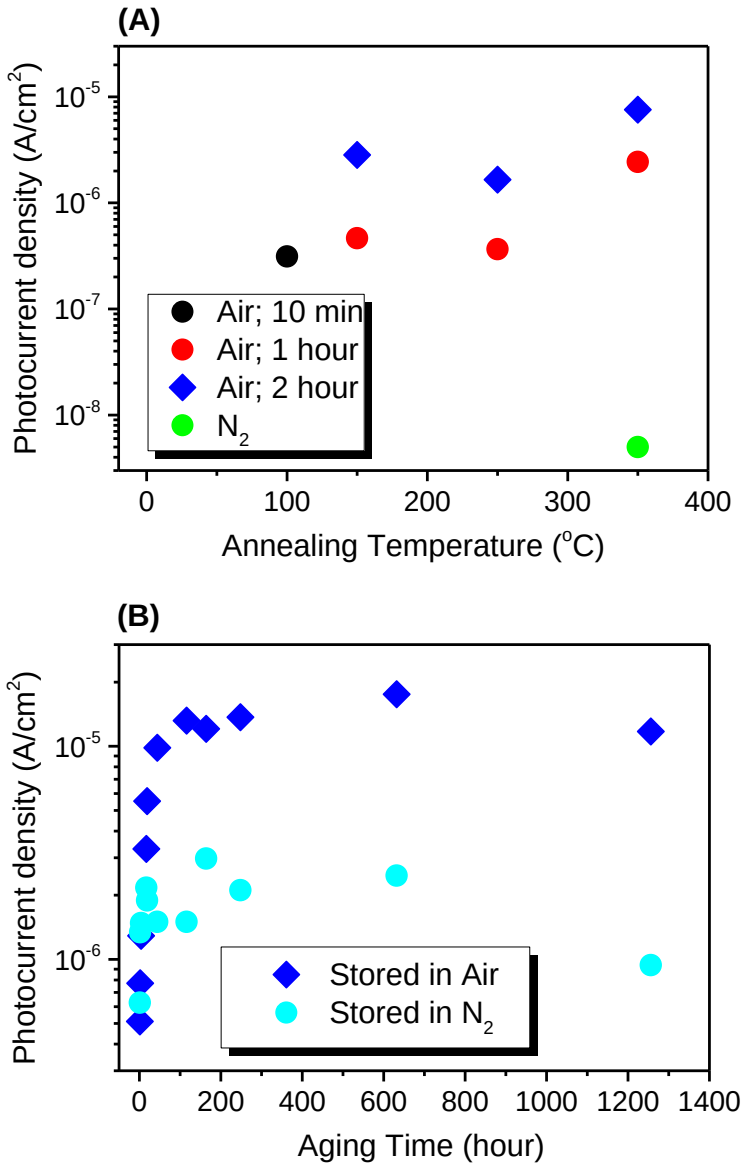

Figure 4.7: (A) Photocurrent of freshly annealed samples at 550 nm as a function of annealing temperature. The inset label refers to the annealing atmosphere and annealing time. (B) Variation of photocurrent as a function of storage time in different atmospheres. Both samples were prepared and annealed in air at 350 °C for 2 hours.

Figure 4.7-B shows that there are correlations between the FTIR spectroscopic changes (figure 4.6-B and C) to the ligands on storage and the magnitude of PC at 550 nm. Both samples were prepared and annealed in air but stored in different environments, air and nitrogen. When stored in air, the signal increases by ≈25 with storage before saturation. This correlates with the capture of CO_2 from the air, as shown by the increased carbonate signal in figure 4.6-B2 after 15 days of storage. Possibly, shallow donor states local to the vacancies are created by this electrochemical reaction. A much smaller increase in the PC signal is observed with storage in nitrogen, correlated to negligible changes to the carbonate transition in the FTIR spectrum, see figure 4.6-C. There are also significant differences between the FTIR spectroscopic C═O and C-O signals at 1565 cm^{-1}, 1419 and 1454 cm^{-1} on storage in air (figure 4.6-B) and nitrogen (figure 4.6-C), both following annealing in air. The intensity of these signals is approximately doubled on storage in air but hardly changes when stored in nitrogen. This is consistent with the capture of CO_2 from the air, as discussed above. It may be a coincidence that enhanced photoconductivity is associated with carbonate formation. Alternatively, it may suggest that shallow donor states local to the vacancies are associated with the adsorbed carbonates. A possible model for this is now discussed. Vacant oxygen interstitial surface sites (VOISSs) exist at the surface of ZnO NPs in addition to the neutral oxygen vacancy defect, V_O^0. However, the former defect is not charged in its neutral state [37]. It is suggested that photo-excitation can result in electron transfer from V_O^0 to VOISS [37]. This can be described by the reaction given in equation 4.1 with VOISS as D^+ and $(VOISS)^-$ as D^0. Furthermore, it is suggested that $(VOISS)^-$ facilitates the adsorption of CO_2 in the first step of methanol synthesis, so it may be stabilized here by the capture of free CO_2 to form the adsorbed carbonate CO_2^-. A

careful examination of the FTIR spectra before and after long storage in air, illustrated in figure 4.8, shows the development of transitions from neutral CO_2 at 673 cm^{-1}, 2332 cm^{-1} and 2362 cm^{-1} after storage [164,204]. We do not believe that water and oxygen in the atmospheric air are responsible for the narrow-band PC of ZnO NPs in the green. Water, for instance, is found to increase the electrical conductivity of ZnO by the protonic conduction [129]. On the other hand, it is well known that oxygen is associated with PC of ZnO NPs in the UV, particularly when the surface to volume ratio is high [43,27].

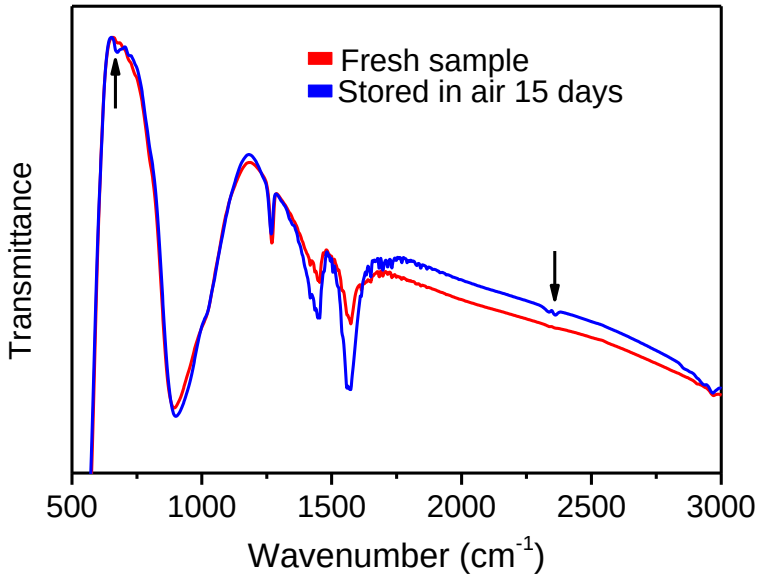

Figure 4.8: FTIR spectra from figure 4.6-B showing transitions due to free CO_2 at 673 cm^{-1}, 2332 cm^{-1} and 2362 cm^{-1}, indicated by arrows, increase in intensity following 15 days storage in air. The sample was annealed at 350 °C in air for 1 hour, measured immediately and after storage in air for 15 days.

Our results above clearly show that surface reactions play a major part in determining the PC by changing the density of defect or dopant states. Here we show that they also affect the lifetime. Since electron-hole recombination occurs on a nanosecond timescale very rapidly, the dynamics of persistent PC depend on the lifetime of the excess density of electrons over that of holes. Electrons can decay to intrinsic traps in the material or

can be scavenged by reaction with surface moieties. Let us consider the decay of the PC signals at 545 nm and 596 nm respectively when the optical pulse is switched off, shown in figure 4.5. Unlike the mono-exponential rising transient, a double exponential function given below is required to fit the decay curve:

$$J(t) = J_0 + A_1 \exp\left(-\frac{t}{\tau_1}\right) + A_2 \exp\left(-\frac{t}{\tau_2}\right) \tag{4.6}$$

This indicates that the carrier lifetime is different in the dark than in the presence of light, suggesting that photochemical reactions remove electrons. At 545 nm, the time constants are τ_1 = 2.5 sec and τ_2=18.8 sec respectively, whilst they are longer, τ_1 = 6.6 sec and τ_2=25.6 sec, for excitation at 596 nm. The two time constants for each wavelength of excitation show that there are at least two independent decay mechanisms. One of these decay times may reflect the time taken for electron transfer from the dopant to the conduction band, which would be longer for the deeper dopant *D2* and its subsequent decay time. The second time constant may indicate the timescale of surface reactions at the dopant site. The visible PC decay transient measured at 532 nm in a nitrogen environment, shown in figure 4.9, is non-exponential. At short times (< 500 sec) only, its decay can be approximated by equation 4.6 with two distinct timescales, τ_1=17.7 sec and τ_2=96.3 sec (calculated over the same temporal range as in figure 4.5), both much longer than those obtained with measurement in air, see figure 4.5. The figure also shows that there is no significant electron capture over the measured timescales by the metastable V_O^+ to reform the V_O^0 state. This is an intrinsic process and its timescale would be independent of atmospheric conditions. This suggests that the removal of electrons from the neutral dopant and conduction band in air involves reaction with an atmospheric species, such as oxygen, water or carbon dioxide. The

increase in response time when measuring in nitrogen compared to air also happens with ZnO UV photoconductors.

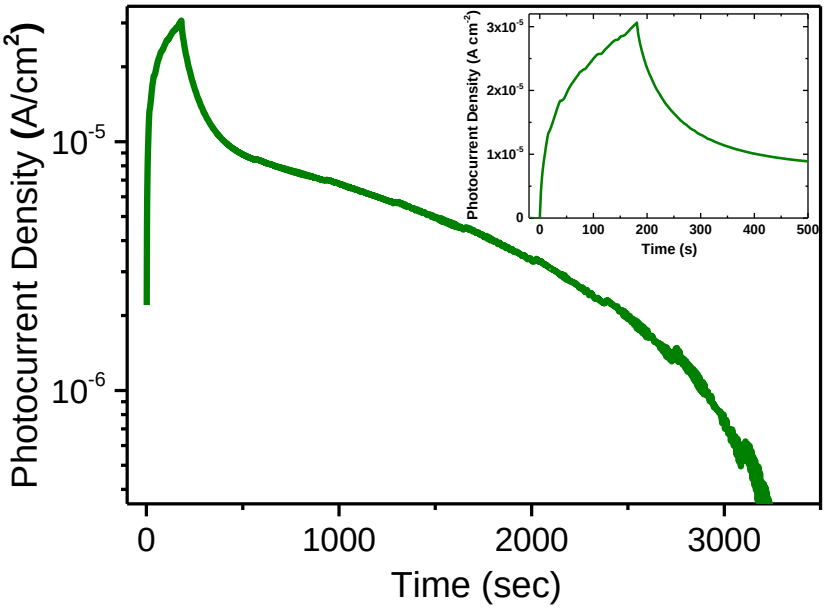

Figure 4.9: Semi-log plot of photocurrent from air annealed ZnO photoconductor, stored in air and tested in nitrogen. The sample was excited at a wavelength of 532 nm for a duration of 180 sec. The inset is a fitted linear plot of the PC transient taken over the same temporal range as in figure 4.5.

4.3.4 Pixelated dual wavelength detector

We now present a low-cost and scalable approach to the fabrication of pixelated ZnO thin film, with different pixels showing different spectral responses. A two-pixel device is produced where one pixel shows both a UV and green photoresponse, whilst the green response is suppressed in the second pixel. A photolithographic process based on the positive photoresist AZ5214 (Microchemicals Gmbh) is used to define the pixels. A solution-processed thin film of ZnO on pre-patterned ITO coated electrode is processed photolithographically to define a single pixel P1. This is annealed in air at 350 °C to optimise the efficiency of PC in the green spectral region. A similar photolithography step is used to mask P1 with an overlying photoresist layer before spin-casting a second

thin film of ZnO over the complete substrate. The second pixel is photolithographically patterned and developed. The substrate is finally washed with acetone to remove the photoresist overlying P1 and P2. Key steps of the photolithography process are schematically explained in figure 4.10, whereas a full description is discussed in chapter two.

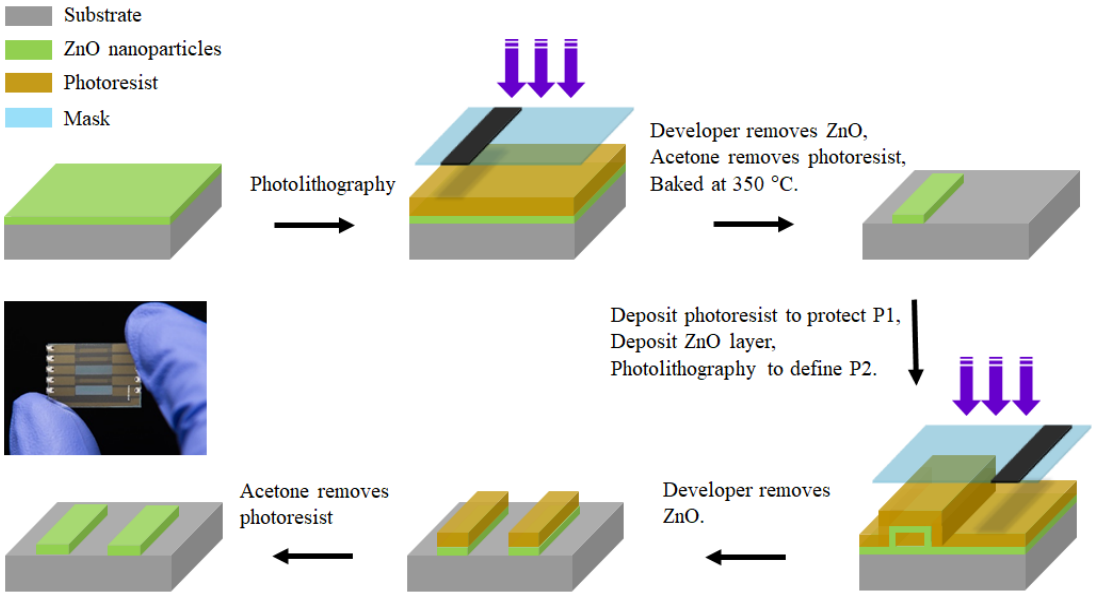

Figure 4.10: Photolithography steps to fabricate the pixelated photodetector. Each step is numbered as described in the text below.

Figure 4.11-A shows the spectrum from both pixels excited under the same conditions. P1 has the greater current density in the UV and green. The UV current density is decreased by a factor of 4.5 in P2, whilst its green PC is a factor of 44 less than that of P1. Figure 4.11-B shows that the photocurrent can drop below the dark current. This may result from photocatalytic reactions which remove groups, such as adsorbed –OH, which contribute to the dark current so that the dark current is lowered for some time after photoexcitation. Figure 4.11-B also shows that the voltage to the device can be adjusted, here to below about 10 V, as indicated by the arrow in the figure, so that the green photocurrent drops to a value below the dark current. Under these circumstances,

P1 can act as a dual wavelength photoconductor whilst P2 only detects the UV light. Note that the current density in the UV is over two orders of magnitude greater than that of the green. They can be equalised by coating the device with a UV absorbing thin film.

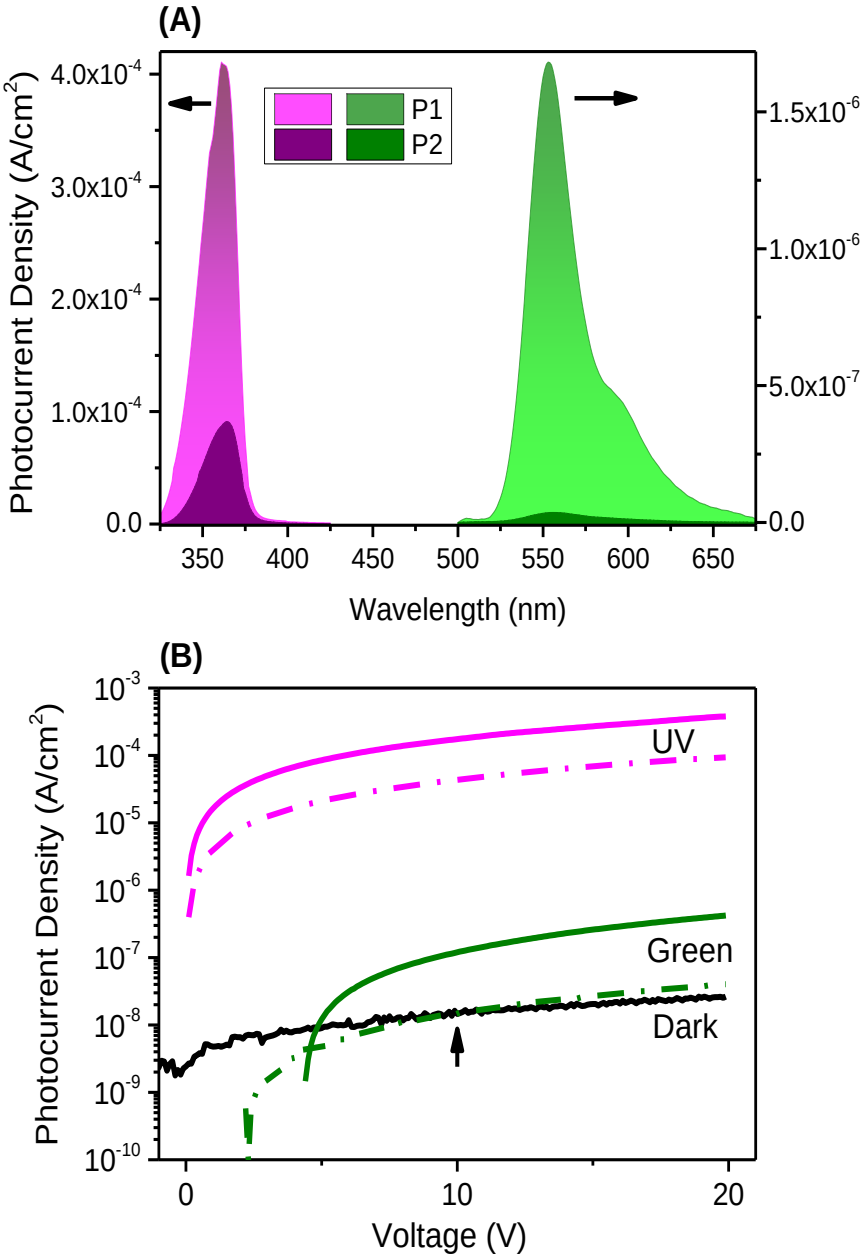

Figure 4.11: Photocurrent from two pixels on the same device. (A) Photocurrent spectrum showing UV and green signals from pixels P1 and P2. (B) Photocurrent versus voltage for both pixels. The arrow indicates the voltage at which the green signal equals the dark current in P2. The solid and dash-dot lines show data from P1 and P2 respectively.

4.4 Summary

A spectrally narrow PC at 550 nm and a shoulder at 596 nm (with a spectral width of 0.16 eV) are observed in ZnO nanocrystalline photoconductors. A model involving electrons transfer between the deep natural state of oxygen vacancy and two local and independent discrete shallow donors is introduced to account for the unusually spectrally sharp PC observed in the green spectral region of ZnO. The existence of those shallow donors are supported by the difference in rising time constants observed by measuring the temporal response for each wavelength. This is fundamentally different than what is proposed in literature where electrons transitions are normally taking place between the defects states and the continuous conduction band which resulting in spectrally broad PC.

The PC is enhanced by annealing and storing the photoconductor in air and the enhancement is correlated to the surface capture of carbon dioxide. We do not believe that water and oxygen in the atmospheric air are responsible for the narrow-band PC of ZnO NPs in the green. We exploit this control of PC to make low-cost dual wavelength photodetectors. The green PC response can be spatially patterned by multi-step photolithography so that dual (ultraviolet and green) and single (ultraviolet only) wavelength detecting pixels can be produced on the same substrate. Hence, a 2D detector array can be fabricated with a spatial response which varies with wavelength. This is interesting for security and imaging applications. A similar approach could be used for full-colour imaging, where gold or aluminium NP-doped ZnO pixels could be used to obtain blue and red PC via plasmonic effects [205,206].

Chapter 5

Near-infrared Photodetection with Plasmonic Gold Nanoislands

This chapter explores how hot electrons generated as a result of localized surface plasmonic resonances (LSPRs) in gold nanostructures can modify the ZnO photoresponse in the near-IR. We demonstrate a significant near-IR photocurrent by utilizing a simple device geometry incorporating a hole transporting layer in direct contact with the gold nanoislands. The device shows high photocurrent responsivity with slow rise/decay time constants due to hot electrons trapping by ZnO surface defects leading to persistent plasmonic photoconductivity.

5.1 Introduction

Plasmonics has emerged as a promising new technology that has a variety of applications in the field of biomedicine, biochemistry, optoelectronics and information technology [207]. It involves light-matter interactions which enable the electromagnetic fields to be localized and confined to the surface of metal nanostructures in dimensions smaller than the incident light wavelength. By manipulating the size and shape of the metals, and taking the refractive index of the surrounding medium in consideration, it is possible to tune the extinction spectrum of metals from the visible to the IR [208]. It is now possible to control the size and shape of metals on the atomic scale, due to the great development of nanofabrication technology. This helps to explore the plasmonic effect of metal nanostructures in a more detailed way rather than relying only on theory. Plasmonic nanostructures can be synthesized by a variety of techniques, such as wet chemical methods [209,210,211], nanosphere lithography [212], evaporation techniques [213], electron beam lithography [214,215] and more. Wet chemical nanofabrication is considered an easy and cheap way to prepare and size control metal nanoplasmonics.

Semiconductors are important optoelectronic materials because of their superb optical and electrical properties. Light absorption and photoconductivity in semiconductors are normally dictated by their optical band gap, although we have shown in chapter four that defects can result in sub-bandgap photoactivity. Photodetection of semiconductors at wavelengths below their band gap is also possible by utilizing the plasmonic injection of hot electrons from an interfacing metal. The physics of plasmonics has introduced a new generation of photodetectors with tunable photosensitivity independent of the semiconductor optical band gap. After plasmonic excitation by light, the strong electric field resulting from the metal's electrons oscillation dephases nonradiatively leading to the generation of energetic electron-hole pairs. Those electrons are energetic enough to

cross the Schottky barrier established with the semiconductor and are injected into its conduction band leading to a detectable photocurrent. This phenomenon has attracted great interest among many research groups who have tried to integrate plasmonic nanostructures into photodetectors [216,217] and solar cells [218,219]. Most of these are prepared using very expensive and complicated tools such as electron beam lithography. Solution-processed devices are considered to be cheap, easy to process and feasible on a large scale.

We report on a vertical configuration photodetector device based on a simplified hybrid plasmonic geometry, which utilizes the plasmonic effect to tune the optical response of ZnO NPs in the near infrared (IR) based on hot electron-hole generation. Gold nano-islands underlying a ZnO NPs thin layer serve as photosensitized material, which absorbs light within the plasmonic resonance and generates hot charge carriers by the plasmon decay. Plasmonic photoconductivity is observed when the gold nanoislands are interfaced with a thin hole transporting layer PEDOT: PSS (poly(3,4-ethylene dioxythiophene) polystyrene sulfonate).

5.2 Overview

Nanomaterials (materials with size smaller than 100 nm) were discovered and used several centuries ago, by the Romans in the late 4th century AD to decorate glasses and windows by metal nanoparticles to give vibrant colours [220]. The Lycurgus drinking cup, depicting the death of King Lycurgus exhibited in the British Museum illustrated in figure 5.1-A is a famous example of the incorporation of silver and gold nanoparticles within the fabricating glass matrix. The cup appears in two different colours, green and red resulting from light scattering and absorption by the metal nanoparticles. A similar

technique is followed to colour glasses and windows in old churches and cathedrals in Europe as shown in figure 5.1-B.

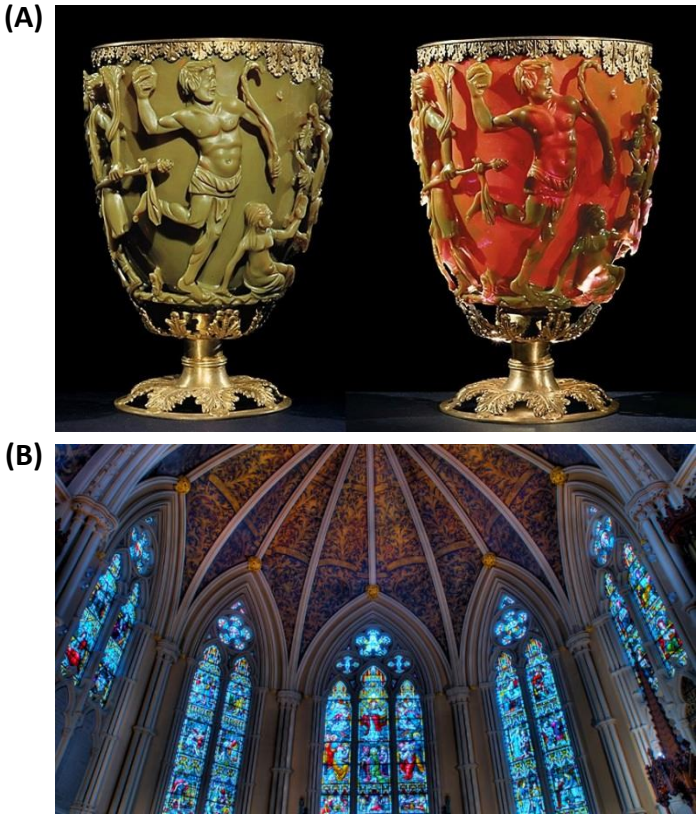

Figure 5.1: (A) the Lycurgus cup showing two colours by light scattering. (B) colour-stained glass windows in churches made by incorporating nano-sized metals with different sizes and shapes [220].

A plasmon is the collective oscillation (synchronized) wave of billions of electrons in the metal when excited by the external electromagnetic field with light frequency matching the plasmonic resonance. The secret of having different colours in the Roman cup and cathedral windows was scientifically revealed in 1908 by the German physicist Gustav Mie [221] with his study of the optical properties of metal spheres. Upon light excitation, the metal nanostructures show an intense absorption spectrum at the plasmonic resonance attributed to the collective oscillation of the free electrons on the metal surface. The plasmonic resonant frequency of the metal crucially depends on the metal size, shape, type and the surrounding medium as explained by Mie theory. Hence,

altering these parameters enables the manipulation of light on the nanometre scale. The structure of this chapter starts by giving a general theoretical background of the main concepts behind plasmonics accompanied by a short review on the possibilities of plasmonic energy transfer mechanisms and few examples of plasmonic photodetectors. The next part goes through the experimental results and discussion of the findings and ending with the conclusion.

5.3 Theoretical background

Plasmonics is a field of research that encompasses electrodynamics and light-matter interaction theory. Therefore, a good understanding of plasmonic dynamics requires good background knowledge of the above concepts. The following sections will provide a general introduction to some aspects of plasmonics applicable to the work undertaken in this chapter. However, more details and thorough explanations can be found in electrodynamics by J.D.Jackson [222], optical properties of solids by M. Fox [223] and plasmonics by S. Maier [224].

5.3.1 Maxwell's equations in matter

The plasmonic phenomenon is stimulated by light-metal interaction. As we all know, light is a combination of electric and magnetic fields propagating perpendicular to each other through space at the speed of light. In order to understand the physics behind plasmonics, we need to understand the conditions by which the plasmonic resonance is stimulated. Metals are electrical conductors with an abundance of free negative charges (electrons). When an electromagnetic wave (light) at a specific frequency (wavelength) impinges the metal, electrons start oscillating in relative to the positive nuclei in response to the applied electric field.

Maxwell's equations are a powerful tool to describe the behaviour of the electric and magnetic fields and their interaction with a solid medium. The equations link four macroscopic fields represented by the dielectric displacement **D**, the electric field **E**, the magnetic field **H** and finally the magnetic induction or flux density **B** with the external charge and current densities ρ_{ext} and $\boldsymbol{J}_{ext}$ respectively induced by the external field and given by [224,225]:

$$\nabla.\mathbf{D} = \rho_{\text{ext}} \tag{5.1}$$

$$\nabla.\mathbf{B} = 0 \tag{5.2}$$

$$\nabla \times \mathbf{E} = -\frac{\partial \mathbf{B}}{\partial t} \tag{5.3}$$

$$\nabla \times \mathbf{H} = \boldsymbol{J}_{ext} + \frac{\partial \mathbf{D}}{\partial t} \tag{5.4}$$

Equation 5.1 is representing Gauss' law which describes the behaviour of the electric field around electric charges. Equation 5.2 is known as Gauss' law of magnetism. Equation 5.3 is called Faraday's law which explains the creation of an electric field with a moving magnetic field. Finally, equation 5.4 is known as Ampere's law which describes the relation between current flow and magnetic field. The equations above indicate that the separation of any positive and negative charges induces an electric field. Therefore, this will give rise to an internal current and charge densities inside the medium representing the system response to the external field, which in total will be given as $\boldsymbol{J}_{tot} = \boldsymbol{J}_{ext} + \boldsymbol{J}$ and $\rho_{\text{tot}} = \rho_{\text{ext}} + \rho$. However, since the charge density is a property of the given system, a relation could be defined involving the electrical permittivity (ε_0) and permeability (μ_0) in free space linking the electric dipole moment per unit volume (**P)** inside the system and magnetisation (**M)** with the four macroscopic fields given by:

$$\mathbf{D} = \varepsilon_0 \mathbf{E} + \mathbf{P} \tag{5.5}$$

$$\mathbf{H} = \frac{1}{\mu_0}\mathbf{B} - \mathbf{M} \tag{5.6}$$

The electric dipole moment in equation (5.5) results from the internal charge density response to the external electric field and therefore, it can be linked to the internal charge density via the conductivity (ρ) by the relation $\nabla . \mathbf{P} = -\rho$. Moreover, since our interest is on the nonmagnetic medium, the magnetic response (**M)** is not considered further in this text.

In order to include material properties, a couple of constitutive relations for a nonmagnetic, linear and isotropic medium (meaning that **J** and **D** are parallel to **E**) can be given by:

$$\mathbf{D} = \varepsilon_0 \varepsilon \mathbf{E} \tag{5.7}$$

$$\mathbf{B} = \mu_0 \mu \mathbf{H} \tag{5.8}$$

$$\mathbf{J} = \sigma \mathbf{E} \tag{5.9}$$

$$\mathbf{P} = \varepsilon_0 \chi \mathbf{E} \tag{5.10}$$

where ε, μ, σ and χ are the dielectric constant or the relative permittivity, the relative permeability of the nonmagnetic medium (μ =1), the conductivity and dielectric susceptibility (which describes the medium polarization induced by bounded charges) respectively. These parameters vary with medium and frequency. However, they are independent of position, direction and fields, as the medium is linear and isotropic.

The dielectric constant is linked with the charges conductivity in the medium: at low frequency, ε describes the response of bound charges to the field while σ normally describes the contribution of free charges to the current flow, the latter of which is also

the responsible of the polarization of the medium. Both ε and σ can be used to determine the optical properties of the metal. Based on the consideration that conduction electrons are part of the dielectric medium, the parameters are linked by the complex dielectric function:

$$\varepsilon = \varepsilon_0(1 + \chi) + i\sigma\omega \tag{5.11}$$

where ω is the angular frequency. Maxwell's equations present a solution to understand the conduction electrons response to the applied electric field in terms of their dielectric function which is also linked to the complex index of refraction by $n = \sqrt{\varepsilon\mu}$.

5.3.2 Dielectric function of metal

To be considered as a dielectric, the charge carriers of a given material can be polarized in response to an external electric field. The material's response to the external electric field can be described by the dielectric constant which has two components, real and imaginary given by $\varepsilon = \varepsilon_1 + i\varepsilon_2$. The real component denoted by ε_1 describes the polarizability response to the electric field and is given by $\varepsilon_1 = n^2 - k^2$ while, the imaginary component represented by ε_2 shows the losses associated with responding to the electric field, such as the interband transitions in gold which dampen the plasmonic response. It can be given by $\varepsilon_2 = 2nk$ [226] where n and k are the refractive index and the extinction coefficient respectively. The refractive index describes the light refraction at the interface, while the extinction coefficient describes the light absorption inside the metal. Both are linked by the complex refractive index (N) and given by: $N = n + ik$ which is linked to the dielectric constant by: $\varepsilon = N^2$ [222].

The optical dielectric function is frequency dependent and can provide important information about the electronic structure and optical interactions of the metal. For instance, free electrons in gold respond differently depending on the applied photon's

energy. At low energy, intraband transitions of electrons within the conduction band dominate which gives useful information about the electrons scattering and mean free path. At higher energy, interband transitions from the d-band to the s-band are predominant, which reveal important information about the band structure of the metal [227].

5.3.2.1 Drude model

The optical properties of metals can be explained by Drude theory based on the plasma model where free electrons in the metal electrically interact with atomic nuclei through Coulomb force. In 1900, Paul Drude [228] proposed a theory to explain how electrons in noble metals respond to an external electromagnetic field with an optical frequency ranging from the visible to the IR. In this model, electron-electron interactions are neglected. However, the effective mass of electrons is accounted for. When an external electromagnetic field interacts with the metal system, free electrons start oscillating in response to the electrical component of the field. The Coulombic attraction force stimulated by the electrons displacement relative to the nuclei induces a restoring force characterized by the oscillation frequency. However, their oscillation is damped by collisions with the positive nuclei and/or impurities in the lattice. The damping constant (γ) of the electrons motion is inversely related to the collision time which gives the electron mean free path and can be given by $\gamma = \frac{1}{\tau}$, where τ is the relaxation time of the free electron. The resonant frequency of the collective electronic oscillation or the plasma frequency can be given by:

$$\omega_p^2 = \frac{ne^2}{\varepsilon_0 m_{\text{eff}}} \tag{5.12}$$

where ω_p represents the plasma frequency, n is the charge density, e is the electrons charge, ε_0 is the electric permittivity and m_{eff} is the electron effective mass. This oscillation is quantized and known as a plasmon which its frequency lies in the UV for most metals. In Drude model, the dielectric function of the electrons in the metal system, at a given frequency (ω), can be given by:

$$\varepsilon(\omega) = 1 - \frac{\omega_p^2}{\omega^2 + i\gamma\omega} \tag{5.13}$$

The dielectric function above is a complex and therefore, the real and imaginary terms can be separated and given by:

$$\varepsilon_1(\omega) = 1 - \frac{\omega_p^2\tau^2}{1+\omega^2\tau^2} \tag{5.14}$$

$$\varepsilon_2(\omega) = \frac{\omega_p^2\tau}{\omega(1+\omega^2\tau^2)} \tag{5.15}$$

That is $\varepsilon(\omega) = \varepsilon_1(\omega) + i\varepsilon_2(\omega)$. ε can be determined experimentally at optical frequencies by measuring the complex refractive index of the medium $n`(\omega) = n(\omega) + ik(\omega)$ from reflectivity. This leads to a relation between the imaginary part ε_2 and the extinction coefficient (k) which determines the optical absorption of the propagating electromagnetic waves through the medium. That is to say, the imaginary part is responsible of the optical absorption inside the medium.

Let us now examine Drude dielectric function given in equation 5.13 in two frequency regimes with taking in consideration the collision time. At low-frequency regime, $\omega\tau \ll 1$ indicates that the real part can be neglected and the imaginary part is predominant which results to dissipate the incident energy in the metal by optical

absorption. Therefore, the complex refractive index of the metal will be comparable to the imaginary part and can be given by:

$$n \approx k = \sqrt{\frac{\varepsilon_2}{2}} = \sqrt{\frac{\tau\omega_p^2}{2\omega}} \tag{5.16}$$

The incident electromagnetic wave penetrates in the metal for a distance called the skin depth, which has a characteristic value depending on the metal. On the other hand, at high-frequency regime with ω is large or above ω_P, ($\omega\tau \gg 1$), the damping coefficient in equation 5.13 become negligible and the dielectric function of the metal is predominantly real with a real refractive index and therefore, equation 5.13 can be re-written as:

$$\varepsilon(\omega) = 1 - \frac{\omega_p^2}{\omega^2} \tag{5.17}$$

From the above equation, two frequency regions can be distinguished: when $\omega < \omega_P$, the external electromagnetic wave will be screened by the electrons in the metal plasma leading to perfect light reflection in the wavelengths from the visible to the far infrared. On the other hand, when $\omega > \omega_P$, the external field will be transmitted into the metal where the electrons in the metal plasma are too slow to follow the external electric field. Therefore, the metal become transparent dielectric with wavelengths from the visible to the UV as can be seen in the reflectance graph of gold and silver shown in figure 5.2.

In the case where interband transitions of electrons take place at energies in excess of 1 eV, such as in noble metals like gold and silver, an additional term represented by Lorentz model is added to equation (5.13) which now can be written as [224,229]:

$$\varepsilon(\omega) = 1 - \frac{\omega_P^2}{\omega^2 + i\gamma\omega} + \frac{A_i}{\omega_i^2 - \omega^2 - i\gamma_i\omega} \tag{5.18}$$

where A_i is the oscillation strength taking place at electrons transition represented by ω_i, γ_i is the oscillation damping constant.

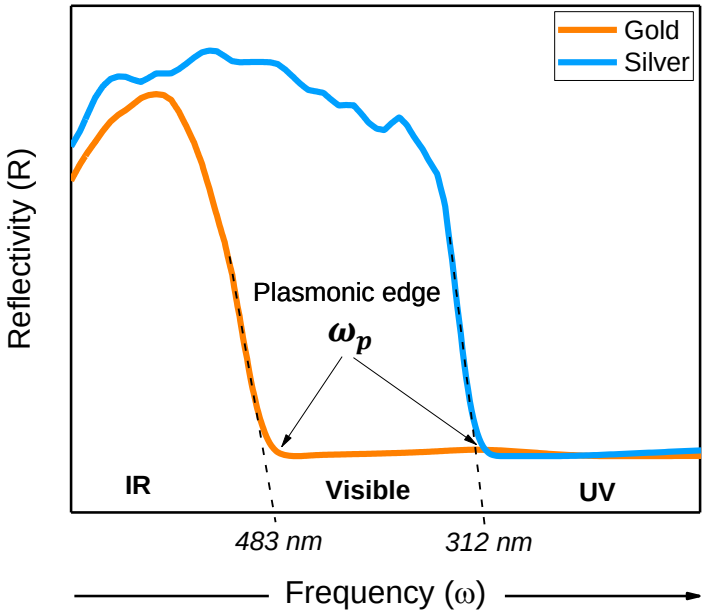

Figure 5.2: The reflectivity of both gold and silver as a function of frequency assigning the plasmonic edge in wavelength. The graph shows the plasmonic frequency cut-off by which a metal can be either a perfect reflector or transmitter with $\omega < \omega_P$ or with $\omega > \omega_P$ respectively. The reflectivity for gold and silver are calculated online using ref. [290].

5.4 Plasmon resonance modes

Surface plasmon can be defined as the interaction or coupling between the coherent oscillated charge carriers and the incident electromagnetic wave at the interface between two mediums with different permitivities, negative such as a metal and positive such as a dielectric. The ability to confine the electromagnetic field in a small volume, beyond the diffraction limit, enables plasmonics to be very valuable in photonics. Generally, plasmons can exist in different modes based on the metal dimension and/or geometry. Two main modes can be distinguished and given by; surface plasmon polariton (SPP) (a

propagating plasmon mode occurs at the metal-dielectric interface) and localized surface plasmon (LSP) (a localized plasmon mode occurs in nanoparticles and nanostructures). A brief description of each mode is presented in the following sections.

5.4.1 Surface plasmon polariton (SPP)

Surface plasmon polariton (SPP) describes the propagation of electromagnetic excitations along the interface between the metal surface and the dielectric [230]. The term polariton indicates the dipole-electromagnetic wave coupling [231], in other words, the coupling between the excited electrons in the metal plasma with the external electromagnetic field. The resulting charge displacement creates an internal electromagnetic field inside and outside the metal. Generally, there is a dielectric material at the interface with the metal, so that the created electromagnetic field is extremely confined and propagates along the metal-dielectric interface until it dissipates exponentially away in both media perpendicular to the interface as illustrated in the inset of figure 5.3. Due to the highly confined nature of the plasmon's electric field at the interface (stimulated by the electrons oscillation), its intensity (amplitude) is normally much higher than the external electric field causing the excitation leading to what is called near-field enhancement.

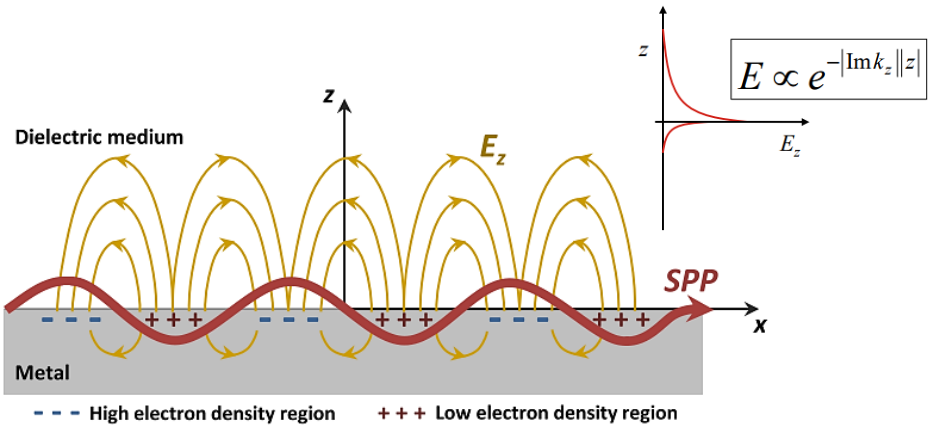

Figure 5.3: Illustration of the longitudinal surface plasmon polariton (SPP) wave propagation alongside the metal-dielectric interface. The schematic is taken from [291]. The figure inset showing the dissipation of the SPP away from the interface (Z=0) where metal is at Z < 0 and the dielectric is at Z > 0.

Now, let us discuss the surface plasmon propagation along the metal-dielectric interface by taking a look at the plasmon dissipation relation. In principle, the propagation of surface plasmon polariton is similar, yet more complicated than light wave propagation in a vacuum. An illustration of the surface plasmon dissipation relation compared to the light is plotted in terms of frequency versus wavevector and showing in figure 5.4.

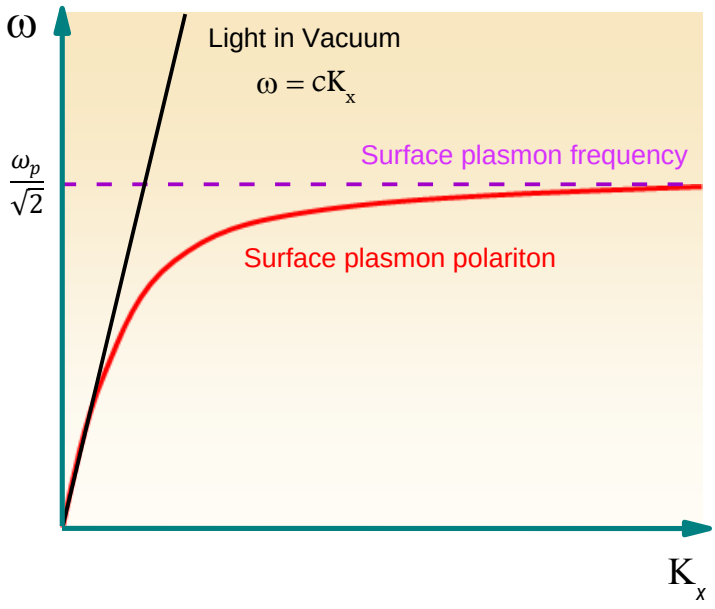

Figure 5.4: The surface plasmon polariton dispersion relation of metals with an air interface. The figure is inspired from [224].

Figure 5.4 shows the dispersion relations of light propagating in a vacuum and the surface plasmon shown in black and red lines respectively. The dispersion relation of SPP propagation along the metal surface can be derived by solving Maxwell's equations of the electric and magnetic fields components as a function of time and position to give the relation [225]:

$$\omega = \sqrt{\frac{\varepsilon_m + \varepsilon_d}{\varepsilon_m \varepsilon_d}}\, c k_x \tag{5.19}$$

where ω is the angular frequency of oscillation, ε_m and ε_d are the dielectric constants of the metal and the dielectric respectively. c is the speed of light in vacuum and finally k_x is the wavevector along the x propagation direction.

The SPP shows similar behaviour to light at low wavevector (k) as illustrated by the red line in figure 5.4. However, its propagation become sub-linear with increasing the wavevector until the frequency reaches a saturation value indicated by the surface plasmon frequency (ω_{sp}). The horizontal dashed line in purple represents a given surface plasmon frequency. At this plasmon frequency, surface plasmon polariton shown in red line has a higher wavevector (inversely proportional to wavelength) than light represented by the black line in figure 5.4. Hence the momentum of light is different than the surface plasmon for the same frequency, so light cannot excite the surface plasmon unless momentum is conserved. Various methods can be adopted to provide an additional momentum such as modifying the surface roughness, using a grating pattern or a prism. Each of those methods has a working mechanism and specific conditions which is not considered further in our discussion.

5.4.2 Localized surface plasmon (LSP)

This type of plasmon mode occurs in confined metal structures like some noble metal nanoparticles. It is a non-propagating oscillation of the electronic plasma coupled with an external electromagnetic field. It was not until 1908 when the German physicist Gustav Mie gave an explanation for the vibrant colours from metal nanospheres when excited at certain photon energies [221]. Charge oscillation redistributes the electrons over the metal particle surface so that negative and positive charges accumulate on each side of the particle, forming a dipole as shown in figure 5.5. The strength of the restoring force is a characteristic of the charge distribution and therefore governs the oscillation which occurs at a resonance frequency. This frequency is known as the localized surface plasmon resonance (LSPR). This plasmon mode stimulates an electric field, a few orders of magnitude higher than the exciting field. The electric field amplification occurs inside and outside the metal particle for a very short lifetime. This is followed by charge damping leading to energy generation in the material neighbouring the metal nanostructure. This process is further discussed later in this chapter.

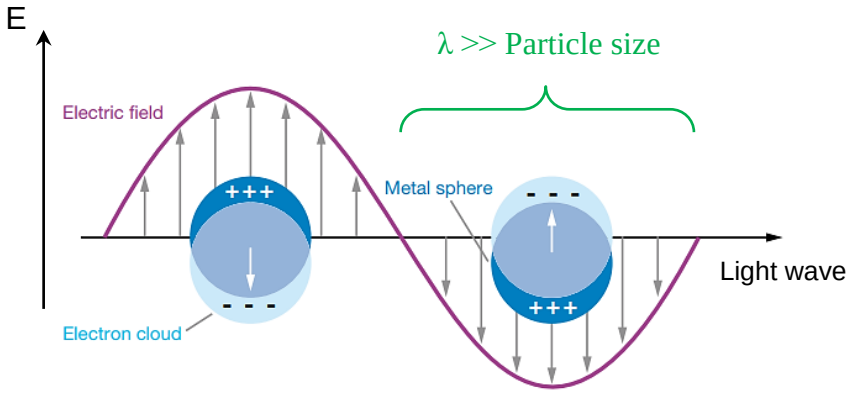

Figure 5.5: A schematic representation of the charge distribution on the metal particle surface as a result of localized surface plasmonic resonance (LSPR) excitation [292].

The direct excitation of the localized plasmon resonance by light is facilitated by the small size of the metal particle which enables the solution of the quasi-static approximation to be applied. This approximation describes the interaction of electromagnetic field with a metal particle of diameter, d, significantly smaller than the excitation wavelength, λ, i.e. $d \ll \lambda$ as shown in figure 5.5. Under this assumption, the exciting electric field distribution is practically uniform over the metal particle volume which enables the simplified case of a particle in an electromagnetic field to explain the plasmonic excitation field [224]. The quasi-static approximation can well describe the excitation field in the particle size range $d < 100$ nm. In order to do so, the Laplace equation of the electric potential (Φ) is used to calculate the electric field around a uniform, sub-wavelength metal nanoparticle by $\mathbf{E} = -\nabla\Phi$. This leads to define the electrons polarizability (α) of a metal particle located in a dielectric medium by utilizing the electrostatic approximation. This relation can be given by [224]:

$$\alpha = 4\pi r^3 \frac{\varepsilon_m - \varepsilon_d}{\varepsilon_m + 2\varepsilon_d} \tag{5.20}$$

where r represents the particle radius, ε_d and ε_m are the surrounding medium and the metal dielectric constants respectively. Equation 5.20 shows the polarizability dependence on the particle volume. The localized plasmonic resonance frequency can also be tuned, i.e red or blue shifted, when the aspect ratio and/or shape is altered. This can be understood by the difference in the oscillation path that electrons take when particle size is increased. The oscillation frequency decreases because of the longer pathway inside the particle, which leads to increase in the resonance wavelength.

5.5 Photoelectric effect of metals

In general, metals are characterized by the abundance of free electrons which are tightly bound to the nucleus by the positive attractive force. The electrons are free to move within the metal but they cannot escape because they do not have the energy needed to break the bond which is equivalent to the metal work function (the minimum energy needed for the electrons in metal to be emitted from the surface). When light with photon energy higher than the metal work function hits the metal surface, an energy transfer process takes place between the incident photons and the metal electrons as schematically shown in figure 5.6. As a result, electrons are excited and have enough energy to overcome the metal's work function and escape from the metal surface. This phenomenon is called the photoemission effect and was discovered many decades ago by Heinrich Hertz in 1887 [232]. In 1905, Albert Einstein [96] reported the key explanation of this phenomenon by suggesting that light consists of photons, each with a quantized energy (E) linked to its frequency (υ) by Planck's constant (h) and so given by $E = h\upsilon$. This represents the ground-breaking discovery by Einstein which reveals that the energy of both light and matter is discontinuous with particle/wave duality behaviour. The importance of this phenomenon is shown in applications in photoelectron spectroscopy, sensors and photodetectors.

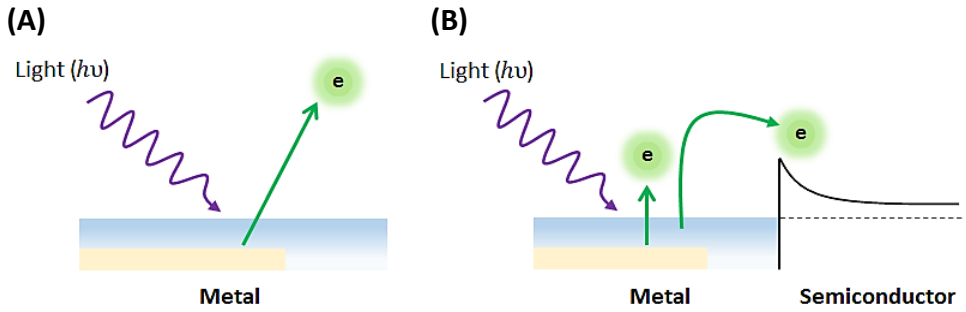

Figure 5.6: An illustration of (A) photoemission of electrons from a metal as a result of energy transfer from an incident light beam, (B) electrons photo-emitted from the metal can be injected in the neighbouring semiconductor when they have energy higher than the Schottky barrier. The schematic is inspired from [58].

The photoemission effect has opened a new understanding in fundamental research of the physical and chemical impact stimulated by energetic electron generation. Any electrons with energy higher than the Schottky barrier can overcome it to reach the semiconductor in a process called internal photoemission of electrons. Internal photoemission of electrons in metals is first realized in the 1930s by Fowler [56]. A few years later, the process has been quantitatively described by Spicer [233] in three main steps represented by: first, free electrons with isotropic momentum distribution will be generated in the metal as a result of light absorption. Second, excited electrons diffuse in the metal before getting thermalized. Finally, excited electrons with enough energy to overcome the metal work function can be emitted from the metal surface in an internal photoemission. The efficiency (η) of this process is described by Fowler's model in terms of the incident photon energy ($h\upsilon$), Fowler emission coefficient (device specific related to the work function) (C_F) and the Schottky barrier energy ($q\emptyset_B$) formed at the metal-semiconductor interface and given by the relation [56,57]:

$$\eta = C_F \frac{(h\upsilon - q\emptyset_B)^2}{h\upsilon} \tag{5.21}$$

Equation (5.21) indicates that the photoemission yield increases with the incident photon energy. However, energetic electrons generated by photoexcitation are emitted in all directions reducing the number of electrons crossing the Schottky barrier. Exciting electrons in plasmonic metal nanostructures solves this problem by adopting plasmonic nanostructures designs by which electron momentum is directed towards the interface to boost charge collection.

5.6 Plasmon-induced energy transfer

As discussed earlier, the plasmonic near field can be several orders of magnitude higher than the external driving field owing to its confined nature. These local electromagnetic field enhanced regions are normally called hot spots due to the high field intensity. After a few femtoseconds (10 – 30) fs [234], the intense field is dephased either radiatively by reemitting photons (scattering) or nonradiatively by either promoting electrons to higher energy states (hot electrons) or dissipating as heat (localized heating) as shown in figure 5.7. The nonradiative dephasing process can be controlled by manipulating the metal composition and dimensions [234]. We discuss now how the plasmonic near-field energy has the potential to be harnessed actively in a variety of applications such as the coupling with a nearby semiconductor.

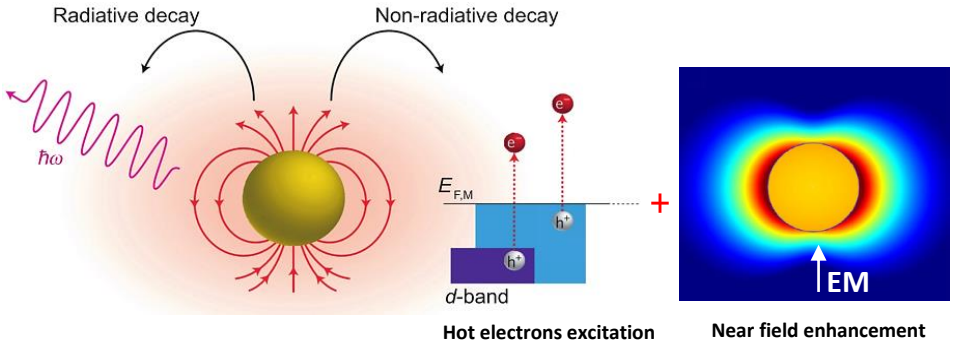

Figure 5.7: An illustration of the mechanisms by which localized surface plasmons decay and transfer energy; radiatively by reemitting photons or non-radiatively by promoting energetic electrons via inter-intraband excitation process and/or near-field enhancement which can stimulate electron-hole generation in the nearby semiconductor [279].

5.6.1 Plasmonic near-field enhancement (PNFE)

The evanescent electric field enhancement in the medium close to the metal nanostructure takes place as a direct consequence of electron imbalance over the metal surface by plasma charge oscillation. Its amplitude is limited by the ohmic losses in the metal volume such as absorption and scattering which leads to plasmon damping. The field decays rapidly away from the surface after very short time. Before reaching this stage, the strong plasmon dipole moment can stimulate energy transformation in the surrounding medium, such as in a neighbouring semiconductor, leading to local enhancement of absorption and hence, electron-hole pair generation below the optical band gap of that semiconductor. This process can be explained by the coupling reaction between the plasmon dipole and the nearby semiconductor interband transition dipole. This energy transfer is known as plasmon induced resonance energy transfer (PIRET) and generally characterized by balancing the dephasing times of the plasmon and semiconductor, and the distance between the metal and the semiconductor as illustrated in figure 5.8-B [235]. The dephasing time for the plasmon is defined as the time needed for the plasmon dipole to decay by losing its phase coherence. On the other hand, for the semiconductor, it is the interband transition time. This technique allowed a remote

transfer of energy from the metal dipole to the semiconductor dipole without the need of direct contact. However, the semiconductor still needs to be within the active region of the near field plasmon decay which is about 10 nm from the metallic interface [236]. Basically, when a semiconductor is put close to an excited plasmon, both systems interact by their dipoles until one system diphases which break the near-field interaction. If the plasmon in the metal dephases faster than the semiconductor, the dipoles interaction breaks and no energy is transferred. On the other hand, if the semiconductor diphases faster than the plasmonic dipole, energy is transferred to the semiconductor leaving the plasmon in the ground state [237]. The principal mechanism of PIRET can be shown in figure 5.8-A.

This phenomenon was proved experimentally by observing a long rise time in the absorption transient of Cu_2O as a result of resonance energy transfer from the gold despite the insulating SiO_2 barrier between them [235]. Another important condition for PIRET is the absorption spectral overlap between the plasmonic resonance in the metal and the semiconductor. This also has been confirmed experimentally by exploring the charge enhancement of TiO_2 with both Ag and Au core metals. PIRET was observed in Ag-TiO_2 core-shell by transition absorption spectroscopy, while no such energy transfer is observed when Au replaces the Ag. This is attributed to the absorption spectral overlap between the Ag and TiO_2 in the UV [238].

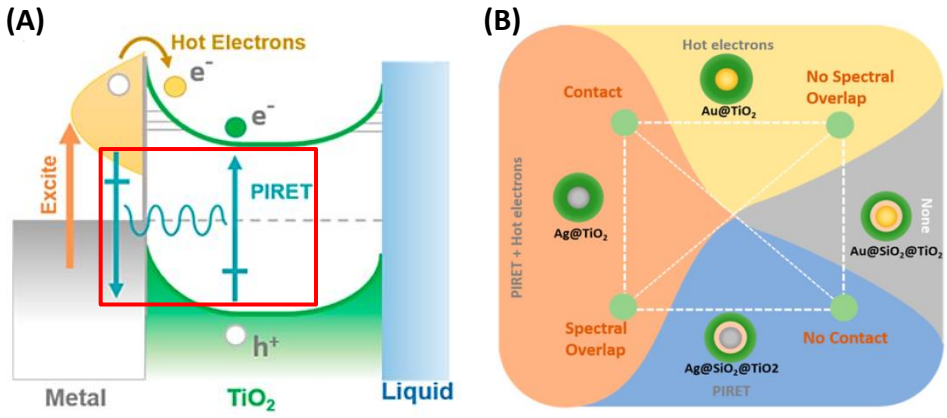

Figure 5.8: (A) A schematic representation of the PIRET operation principle represented by the highlighted red box. (B) The operating conditions required for which PIRET and hot electron injection leading to photoconversion in a neighbouring semiconductor [238].

5.6.2 Plasmon hot electrons injection (PHEI)

Hot electron injection is another mechanism whereby plasmon energy can be transferred to a semiconductor via a non-radiative plasmon dephasing process. The term *hot electrons* refer to the highly energetic electrons that are not in thermal equilibrium with the metal system. Hot electrons based on this technique crucially depend on a direct contact between the metal and the semiconductor, contrary to PIRET. The plasmon loses its coherent oscillation (dephasing), and energy is transferred to the metal volume leading to inter and intra-band excitation of free electrons as illustrated in figure 5.9. However, it should be noted that in order for electrons to be excited from the d-band energy levels, there must be an energy overlap between the resonance photon energy and the metal inter-band transition energy. For instance, in Au, the d-band energy levels are located at 2.4 eV below the Fermi level whilst the plasmonic resonance of Au is at about 530 nm (2.3 eV) [239,240]. Therefore, the possibility of exciting inter-band electrons in gold is weak. This leaves us with the intra-band transition where electrons are excited within the conduction band of gold nanostructure surface close to the Fermi level. The excited hot electrons are characterised by their wide energy distribution based

on their original energy before excitation. The distribution ranges from the Fermi level to the maximum energy $E_{max} = E_F + \hbar\omega$ as shown in figure 5.9-A. However, hot electrons still need to travel to the metal-semiconductor interface to be emitted. During this journey, the excited electrons further lose energy as a result of collisions with other electrons and/or lattice phonons. Therefore, only hot electrons reaching the surface with energy high enough to overcome the metal workfunction and the barrier are free to be injected in the semiconductor and contribute in the overall current. The most efficient way of capturing hot electrons is by adopting the photodiode principle by making a Schottky barrier with an appropriate semiconductor of high density of state (to insure fast charge injection). This technique allowed energetic hot electrons to move in one direction crossing the Schottky barrier and relax in the conduction band of the semiconductor as shown in figure 5.9-B. In addition, it is also possible yet unlikely that electrons will tunnel through the barrier towards the semiconductor.

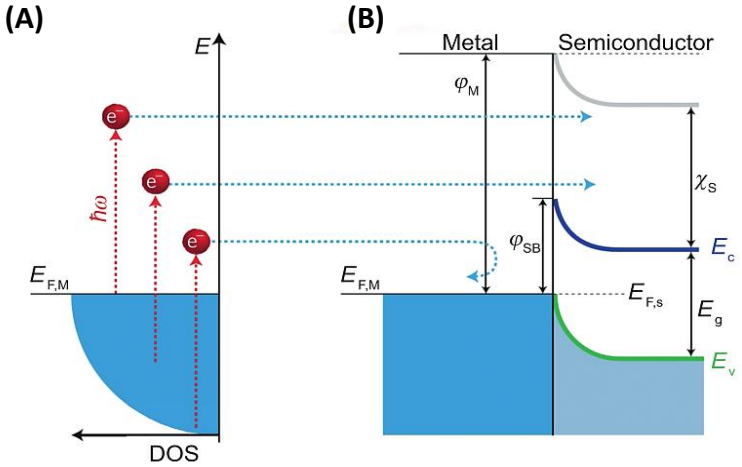

Figure 5.9: (A) Plasmonic hot electron excitation with different energy distributions. (B) Hot electrons with high energy cross the Schottky barrier and are injected into the conduction band of the neighbouring semiconductor [279].

Having enough energy to overcome the Schottky barrier is by no means the only requirement needed to ensure efficient collection of hot electrons. Several parameters need to be carefully considered such as the metal type, structure, metal-semiconductor interface quality and the overall system design. For example, the size of the metal particle size was important when optimizing the number of hot electrons. A study by Nordlander et al. [241] compared the lifetime, number and energy distribution of hot electrons generated from 25 and 15 nm silver spheres. Hot electrons emitted from the larger spheres had a large lifetime range of 0.05 – 1 ps with a large number of hot electrons. On the other hand, the smaller sphere had a resonance lifetime of 0.5 – 1 ps and generated fewer but more energetic hot electrons. Another important issue is the momentum distribution of the hot electrons following emission from the metal. The hot electron momentum distribution needs to be directed towards the contact area (the interface) with the semiconductor to increase the efficiency of injection. As shown in figure 5.10-A, when the plasmonic metal is on top of the semiconductor, the junction is limited to the contact area between the metal and the semiconductor. Only electrons with the momentum lying within the red cone can inject into the semiconductor conduction band. On the other hand, electrons directed parallel to the interface relax back to the metal causing heat losses [242]. Halas and co-workers [243] provide a possible solution to increase the hot electron injection efficiency by embedding the metal nanostructure into the n-type Si and making a three-dimensional Schottky junction as shown in figure 5.10- B.

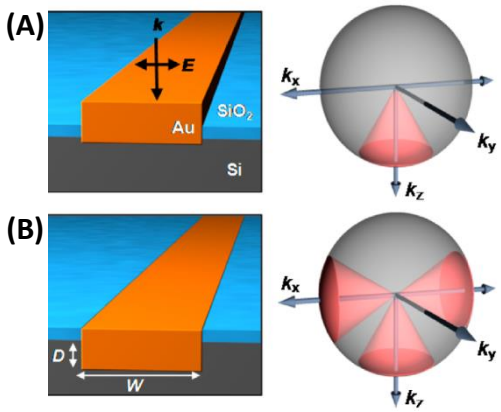

Figure 5.10: Hot electrons injection into the semiconductor is governed by the junction design. (A) 1D and (B) 3D junction. Having a three-dimensional Schottky junction by embedding the plasmonic structure within the semiconductor will improve electrons injection according to their momentum distribution [243].

Another important example reported by Zheng et al. [244] investigated the fundamental difference between photocarriers generated in gold by direct photoexcitation and by plasmon decay. Hot carriers generated by the former mechanism are based on light absorption by the bulk gold leading to the excitation of electrons from the d-band (high-density states). On the other hand, hot carriers generated by plasmon decay are stimulated by the strong enhancement in the near electric field close to the plasmonic nanostructure. Therefore, carriers generated by plasmon decay have more energy to overcome the barrier with the interfaced material. Interestingly, the photocurrent generated by both mechanisms can be distinguished by tailoring the interface with the semiconductor as shown in figure 5.11.

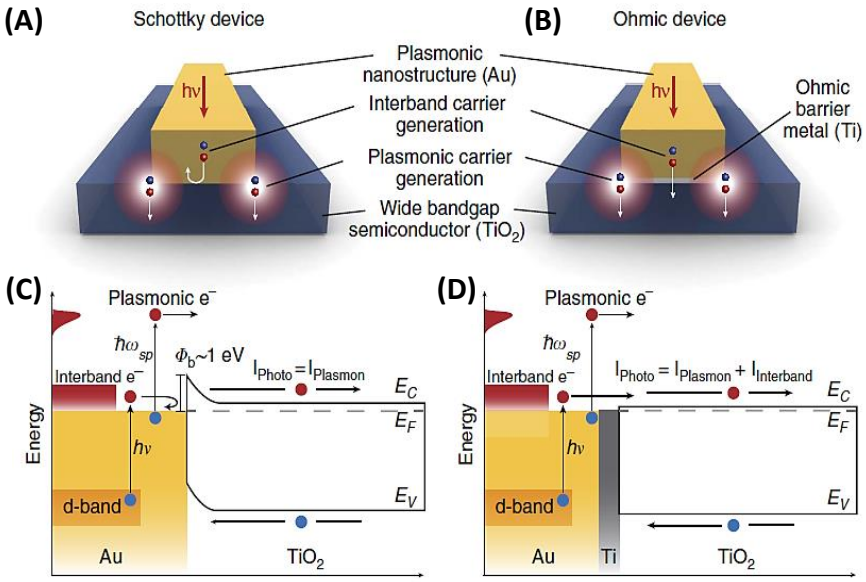

Figure 5.11: A schematic illustration of hot charge generation and transformation to the neighbouring semiconductor for (A) a Schottky barrier and (B) an ohmic contact, (C) and (D) show the band diagram established in the case of Schottky junction formation and ohmic contact respectively [244].

5.7 Plasmon photodetection devices

Photoelectrons ejected from the metal are a very promising approach to photovoltaic devices which rely on photocurrent and photovoltage generation by light absorption. The working efficacy of these devices depends on the active material, which normally absorbs light at a specific region of the spectrum depending on its optical band gap. Plasmonic hot electrons enable devices to extend their absorption spectrum and consequently their efficiency at longer wavelengths by hot electron injection. Photodetection based on internal photoemission in metals dates back to 1967 when Peters [245] utilizes internal photoemission over the Schottky barrier between silicon and gold as a detection mechanism of infrared. However, this field is re-explored over the last few years by applying the knowledge of plasmonic hot electrons to enable sub-bandgap photodetection over a wider spectral range, from UV to the infrared. Plasmonics enable photodetection in semiconductors by either a direct injection of hot

electrons in the conduction band or by stimulating the generation of charge carriers in semiconductors by amplifying the optical absorption through near-field enhancement.

The concept of hot electron generation and injection has been experimentally proved by many research groups. However, the real challenge is to make an efficient working device based on the hot electrons. Herein, we will briefly review some examples of photodetection with plasmonic enhanced charge generation at different spectral wavelengths. Charge separation originating from a plasmonic resonance was first reported by Zhao et al. [246] when a visible photocurrent was noticed from wide-band gap solution-processed TiO_2 (3.3 eV) containing a suspension of gold and silver nanoparticles. Tian et al. [211,247] reported a visible photocurrent from TiO_2 nanoporous film incorporating Au nanoparticles by plasmon-induced photoelectron-chemistry using an electrochemical cell with a coexisting electron donor. It was found that the lifetime of the hot electrons in Au and Ag NPs is usually very short, on the subpicosecond time scale [248]. Therefore, in order to have efficient electron collection, electron injection needs to be faster than the hot electron's lifetime. Furube et al. [249] used a femtosecond transient absorption spectroscopy with an IR probe to calculate hot electrons transfer from 10 nm gold nanoparticle to the TiO_2 nanoparticles porous film. The film was heated at 500 °C to decompose any organic ligands separating the Au and TiO_2. They have found out that hot electron transfer takes place within 240 femtoseconds with 40% yield.

Energy generation was realized by coupling the strong plasmonic near-field resonance with the semiconductor leading to amplification of the light absorption of the semiconductor at sub-bandgap wavelengths and therefore enhancing the overall power conversion efficiency. In a study by Bob Y. Zheng et al. [206], visible photodetection was demonstrated based on plasmonics near-field enhancement effect magnified by optical

interference effects. The MSM device is fabricated by integrating an aluminium grating on top of a silicon substrate. The responsivity was spectrally filtered by changing the Al grating configuration. Pitches of 500, 400 and 300 nm were used in order to measure red, green and blue respectively. The responsivity recorded was 11.18 A/W, 12.07 A/W and 12.54 A/W for the red, green and blue respectively. The high responsivity is partially explained by the strong coupling between plasmonic resonance from the aluminium grating fingers and the silicon despite the separating thin SiO_2 oxide layer. This provides more evidence of indirect energy transformation through the insulating oxide layer between the grating and the silicon via PRIET as shown in figure 5.12.

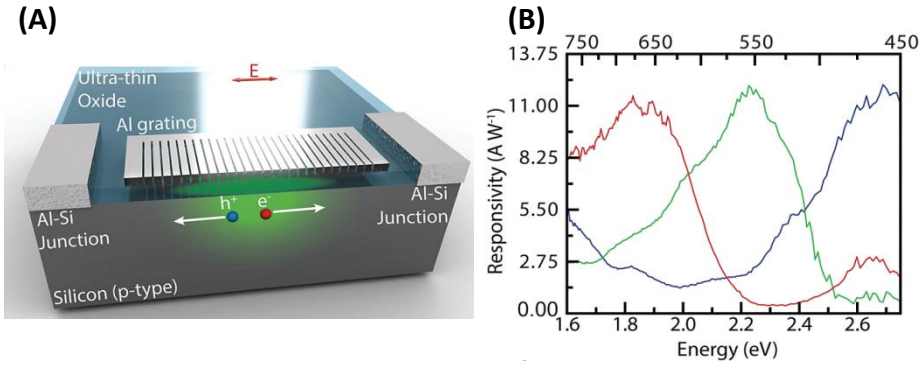

Figure 5.12: (A) MSM plasmonic photodetector incorporating an Al grating to filter the plasmonic resonance and hence the spectral responsivity of the detector. (B) The experimental spectral responsivity data recorded by changing the pitch of the grating. Near field enhancement and light interference result on high responsivity and photocurrent selectivity [206].

As discussed above, the excitation of localized surface plasmons results in a hot electron-hole generation. Hot holes are just as important as hot electrons in stimulating energy transfer and have been investigated. Tapan Barman et al. [250] reported a plasmonic photodetector working at 0V bias in the region 400-500 nm based on a polyaniline-gold nanocomposite thin film as shown below in figure 5.13. Gold nanostructures with different sizes and shapes were incorporated in a p-type organic semiconductor polymer matrix to tune the resonance absorption spectrum and hence the

spectral response of the photodetector. The study attributed the responsivity in the blue region to hot holes generation as a result of electrons excitation from the d-band in the gold nanostructures. The hot electrons were blocked by the conduction energy level of the polymer matrix. The confirmation of hot hole involvement in plasmonic photodetection could be very useful to further understand the physics of hot charges generation and injection.

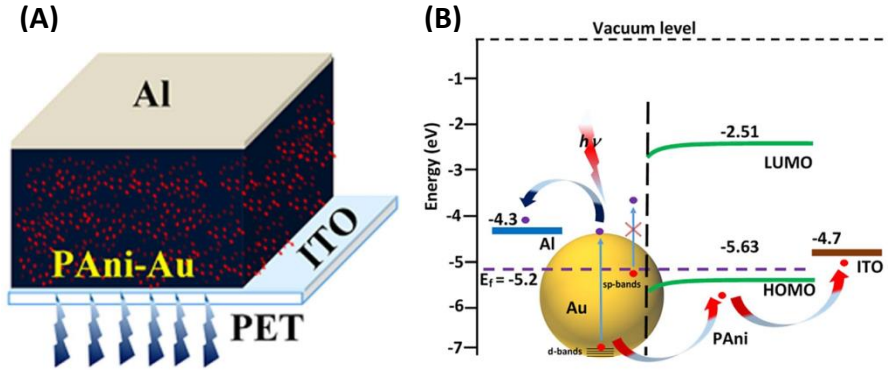

Figure 5.13: (A) A schematic representation of the plasmonic-organic photodetector. (B) Energy band diagram of the gold polyaniline system showing hole conduction through the polymer [250].

Ran Jia et al. [251] reported a dual-band plasmonic photodetector actively working in the UV and green based on gold nanostructures sputtered under vacuum on Ga-polar gallium nitride (GaN). Gold nanostructures were annealed at 300 and 500 ºC to control the surface coverage of the devices. GaN is an n-type wide band-gap semiconductor known to have an abundance of defects. By incorporation of gold nanostructures, the photoelectric responsivity in the UV and green is increased by 50 times compared to the blank GaN as illustrated in figure 5.14. They attributed the enhancement in photoresponsivity in the UV to interband electrons (excited from the d-band) which are injected from the gold nanostructure, while the photocurrent enhancement in the green to hot electrons excited close to the surface (intraband transitions) amplified by

coupling with sub-bandgap trapped electrons in GaN surface defects leading to external quantum efficiency of 27.6%.

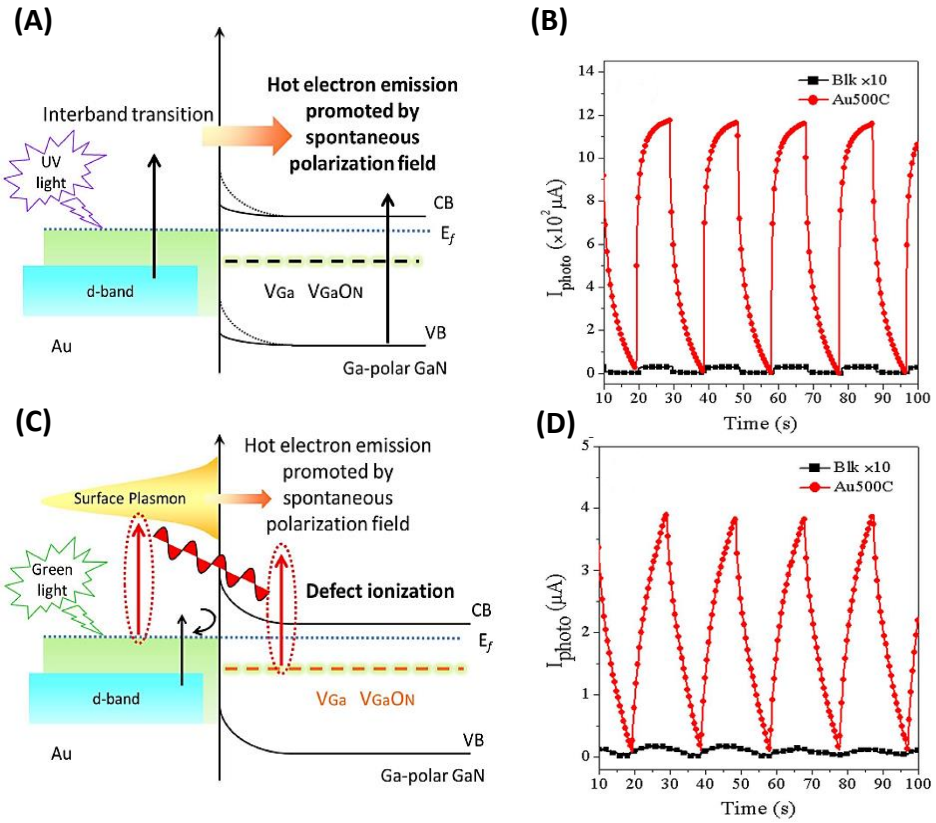

Figure 5.14: An illustration of the dual wavelength plasmonics photodetection mechanism in a GaN device. (A) and (B) show the interband excitation of hot electrons when gold NPs are irradiated in the UV and the corresponding time dependence of the UV photocurrent respectively. (C) and (D) show the intraband excitation in gold NPs when irradiated at the plasmonic resonance wavelength and its corresponding time-dependent photocurrent in the green [251].

Mubeen et al. [205] were among the first to demonstrate the sub-bandgap photoactivity of TiO_2 in the visible by direct electron injection from gold nanoparticles. The device shown in figure 5.15 is fabricated by the insertion of multilayers of evaporated gold nanoparticles with a diameter of 14 nm between layers of TiO_2 of thickness 200 nm. The gold particles are separated by about 14 nm and each layer is well isolated by the TiO_2. The study shows that the visible photoconductance increases with the number of layers of gold nanoparticles since more hot electrons are injected via localized surface

plasmon decay. However, this device shows no direct electrical contact between the plasmonics structures and the electrodes which mean that gold, nanoparticles are theoretically isolated. This means that near-field enhancement of gold nanoparticles could also be responsible for visible photocurrent by stimulating light absorption in TiO_2. Moreover, the author didn't mention any effect of near-field coupling between nearby Au particles owing to the short separation distance.

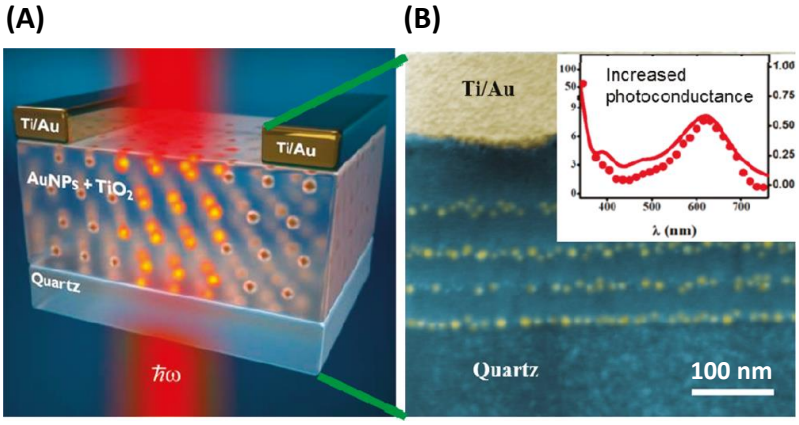

Figure 5.15: An illustration of the Au-TiO_2 plasmonic composite for sub-bandgap photodetection. (A) Schematic illustration of the device. (B) SEM cross-section showing the incorporation of multilayers gold nanoparticles embedded in TiO_2. The inset showing the optical absorption and the photocurrent spectrum of the plasmonic device [205].

Lee et al. [252] constructed a plasmonic photodiode by depositing a 10 nm gold film on top of TiO_2 as shown in figure 5.16. The gold film was modified to form connected islands by thermal annealing at different temperatures in air. The plasmonic photocurrent recorded from the modified gold islands (after annealing) is significantly higher than the untreated film. This enhancement in photon to electron conversion efficiency is attributed to the localized surface plasmonic resonance supported by the formation of gold islands, which enable the generation of hot electrons. It was suggested that the plasmonic photocurrent based on hot electrons can be significantly improved by roughening the metal-semiconductor interface area [253,254].

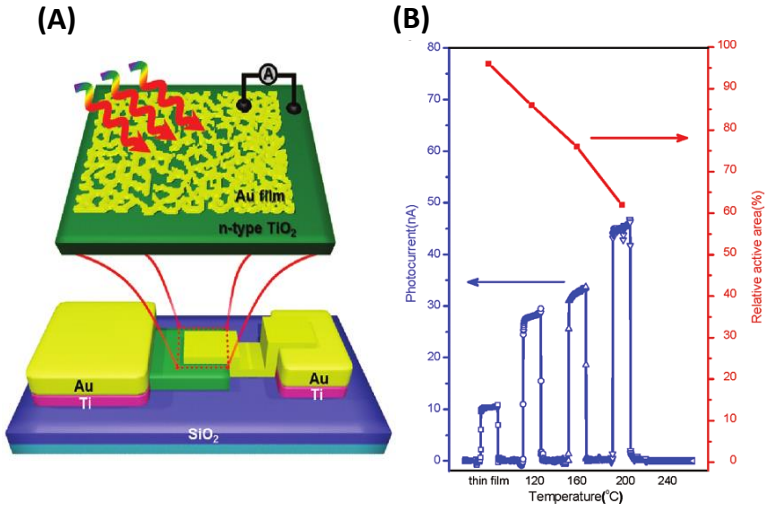

Figure 5.16: (A) Schematic illustration of the hot electrons driven by plasmon absorption from the gold islands developed on top of TiO_2. (B) The relation between the active surface area of gold nanoislands on the TiO_2 surface (created by different annealing temperatures) and the visible photocurrent by plasmon effect. Low surface area of gold nanostructures enhances the plasmon photocurrent [252].

Plasmonic photodetection is also observed in the near infrared (IR) region by both hot electron injection and PIRET. Knight et al. [255] reported an example of hot electrons excitation and extraction by embedding an optical nano-antenna of gold nanorods in n-type Si substrate. They show that utilizing different gold nanorods dimensions changes the photocurrent response accordingly, following the antenna's plasmonic resonance as shown in figure 5.17. They also show that modification of the Schottky barrier height enhances the hot electron photocurrent efficiency. Therefore, a very thin layer of 1 nm Ti film was used between the Au NRs and the Si to reduce the barrier and also to improve the gold adhesion. The device quantum efficiency was low, close to 0.01%, It is believed that this could increase to about 2% by considering a different Ti layer thickness as well as different experimental parameters.

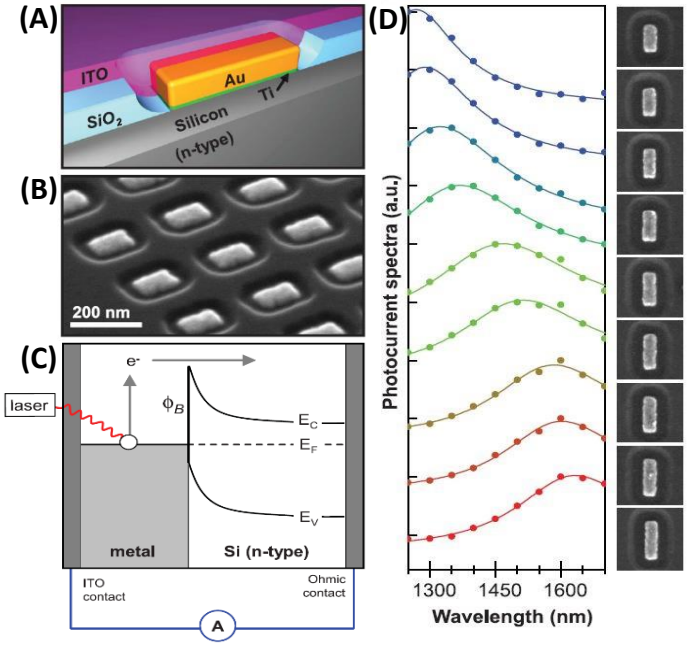

Figure 5.17: Plasmonic photodetection based on gold nanorod optical antenna: (A) A schematic representation of the hot electron plasmonic device incorporating gold nanorods on an n-type silicon substrate with a transparent ITO front electrode. (B) SEM image of the optical nanodiode arrays. (C) Energy band diagram illustrating the energy band alignment and charge injection through the Schottky barrier. (D) Optical photodetection from the embedded plasmonic photodiodes with different gold antenna lengths [255].

A plasmonic photodetector with a narrow band optical response was successfully reported by Ali Sobhani et al. [256] using an Au grating on a silicon substrate shown in figure 5.18. They utilize the plasmonic modes from the enhanced light transmission through the subwavelength periodic gold slits to couple the light with the gold and generate hot electrons. In this plasmonic structure design, the optical response was tuned by changing the Au thickness, slit width and interslit distance. The photocurrent responsivity is highly dependent on the gold thickness resulting because of surface plasmon interactions between the top and the bottom of the Au fingers. By changing the thickness, the plasmon interference can be controlled to maximize hot electron generation at the bottom interface of gold/silicon. The spectral photoresponse can be tuned by changing the interslit distance to give a near infrared signal.

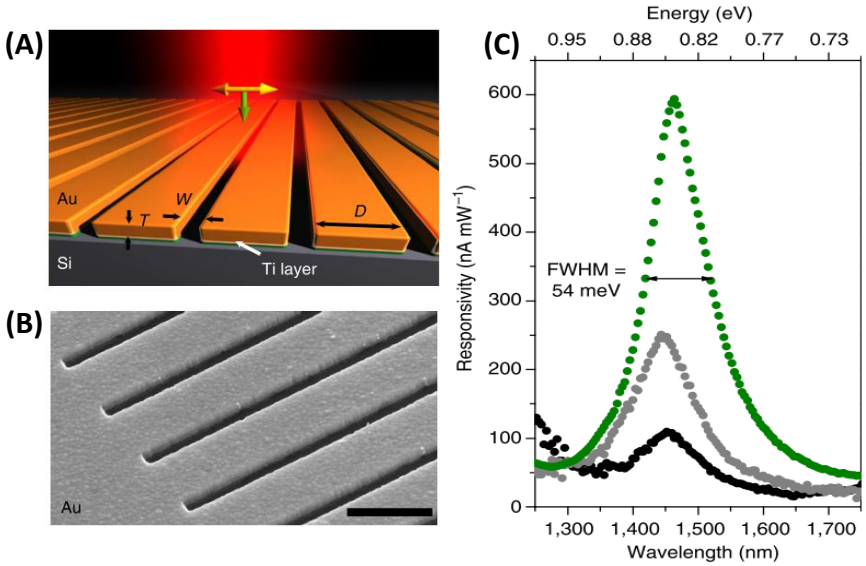

Figure 5.18: (A) A schematic illustration of the plasmonic gold fingers with incident polarized light, (B) SEM image of the gold fingers and (C) the optical responsivity of the plasmonic device [256].

Wenyi Wang et al. [257] have investigated a plasmonics photodetector working in the near-IR region based on hot electrons injection in a 2-dimensional molybdenum disulphide (MoS_2) semiconductor from interdigitated plasmonics gold nanowires. The work investigated the efficiency of hot electrons injection in plasmon photocurrent amplification. The device is irradiated with two different wavelengths, 532 nm originating from the semiconductor direct transition and 1070 nm originated from hot electrons injection, to identify the mechanism of photocurrent amplification realized in the near-IR as shown in figure 5.19. The device shows near-IR responsivity of 5.2 A/W with hot electron current amplification factor of 1.05×10^5 which is comparable to the silicon-based hot electron photodetectors reported by Knight et al. [255].

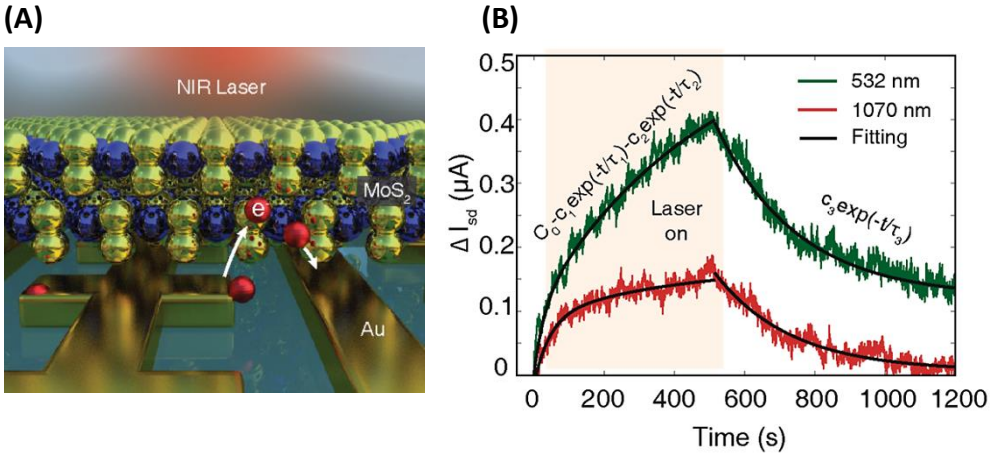

Figure 5.19: (A) a 3D schematic illustration of a MoS_2 layer on top of plasmonic gold wires. (B) Current transient measurements of the same device irradiated above the band gap with a transition wavelength of 532 nm and the plasmonic resonance wavelength of 1070 nm. Both transients show similar time constant values for the rising current [257].

The injection of hot electrons from colloidal gold nanorods decorating a single ZnO nanowire (NW) device was investigated in comparison to a bare ZnO NW device by Pescaglini et al. [258] The hybrid device, shown in figure 5.20-A, actively detected light at wavelengths 650 and 850 nm based on the plasmonic resonance of gold nanorods as shown in figure 5.20-B. The study shows that the photoconductance of ZnO in the visible (650 nm) is enhanced by a strong localized plasmonic effect from the gold nanorods which internally excite the trapped electrons at the ZnO surface defects. On the other hand, photoconductance at 850 nm is only realized in the hybrid device according to direct hot electron injection from the gold nanorods. This study also suggests the possible coupling between the near-field enhancement of plasmonic nanostructures with the sub-band gaps defects in the metal oxide semiconductors leading to a boost in photoconductivity as illustrated in figure 5.20-C.

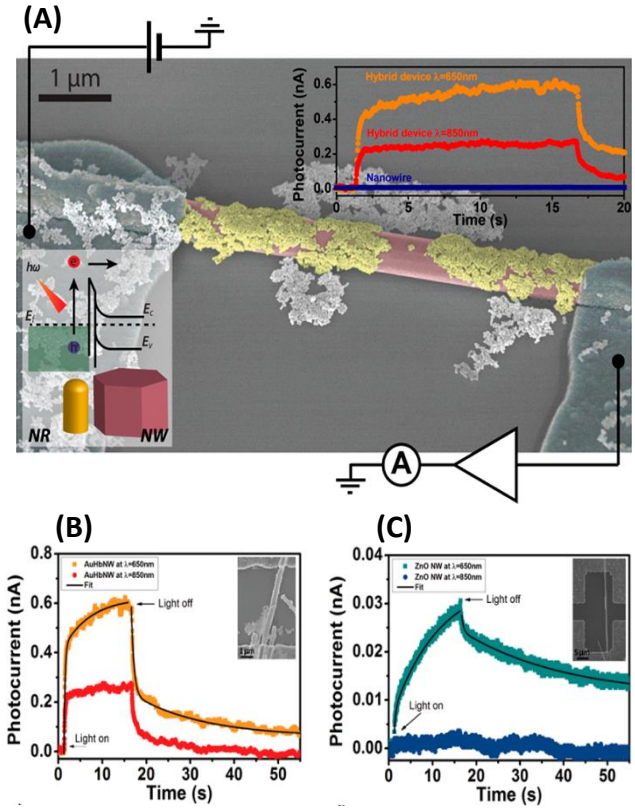

Figure 5.20: (A) A SEM image of the hybrid device where the ZnO NW is coloured in pink and the gold nanorods in yellow for clarity. The inset shows the photocurrent and band diagram of the proposed device. (B) and (C) show the photoconductance in the visible and near IR from both the hybrid device and the bare ZnO device respectively [258].

In a work by Mohammad Amin Nazirzadeh et al. [259], plasmonics photoconductivity in the near-IR is realized using randomly distributed gold nanoislands on top of silicon. An aluminium doped ZnO layer is deposited on top of the gold nanoislands working as a transparent electrode and also electrically connecting the gold islands. The gold film is annealed at different temperatures to control the islands shape and size distribution. A photoresponse of 2 mA/W is achieved with 155 nm gold islands size indicating the importance of big islands in improving the plasmonics resonance absorption and hence hot electrons generation and injection.

5.8 Methodology

5.8.1 Device fabrication

Devices were fabricated following a simple vertical configuration structure. The devices were built on pre-patterned 100 nm ITO fingers (20 Ω / square) evaporated on a 20 nm coating of SiO_2 (synthetic quartz) overlying a 20×15 mm^2 polished soda-lime, float glass substrate bought from Ossila. Each working device consists of three ITO fingers, each of 100 μm in width by 10 mm in length, all connected to a 2 mm wide ITO pad. Each substrate has 8 working devices, 4 on each side of the substrate, and we can switch between devices by moving the needle probe to a different ITO pad. The substrate was cleaned thoroughly followed by UV/Ozone treatment for 3 min, to remove any organic and impurities remaining on the surface and to improve surface wettability, and then coated by spin-casting a 30 nm (poly(3,4-ethylene dioxythiophene) polystyrene sulfonate) PEDOT:PSS layer in air at 2000 rpm for 30 sec followed by thermal annealing at 150 °C for 10 min in air. High purity gold thin film of thickness ≈25 nm was thermally evaporated on top of the PEDOT: PSS and ITO (described below in table 5.1) with a 0.1 A/sec evaporation speed at 5×10^{-7} mbar using an HHV Auto 500 multifunctional evaporator. Additional substrates simulating the investigated devices were evaporated simultaneously for the absorption and AFM measurements. Devices were fixed at about 30 cm from the gold crucible on a rotating holder inside the evaporator chamber to prevent any excess heating to the PEDOT: PSS layer. The gold layer deposited on ITO and PEDOT: PSS in devices 2 and 4 respectively were treated similarly. Thereafter, a 120 nm (± 5nm) thickness of ZnO NPs was deposited by spin coating at 2000 rpm for 30 sec from a suspension (2.5 wt.%) dissolved in chloroform. This was followed by annealing the device at 150 °C in air for 10 min. The device was

then irradiated with 2 min UV/Ozone to remove any ligands attached to the ZnO NPs before evaporating a 150 nm thick Al back electrode.

Visible photocurrent measurements were performed using a high intensity, 150 W Xenon white light solar simulator bought from Abet Technologies (model 10500) as a light source covering the wavelengths from 400 nm to 1800 nm. Narrow spectral bands were selected using a set of dielectric bandpass filters, bought from Thorlabs with 10 nm bandwidth (±3 nm) and peak wavelengths of 600nm, 650nm, 700nm, 750nm, 800nm, 850nm, 900nm and 950nm. On the other hand, UV photocurrent measurements at 363 nm were recorded using the Xenon lamp equipped with the monochromator. The light intensity was measured using a digital compact power and energy meter console with calibrated photodiode sensors from Thorlabs (PM100D). The devices were irradiated with a normally incident light beam covering the whole device area shown in figure 5.21. I-V and photocurrent transients were recorded using two electrical needle probes connected to a 2400 Keighley source meter interfaced with a PC using the BenWin+ software. All I-V and photocurrent measurements were conducted at room temperature unless stated otherwise.

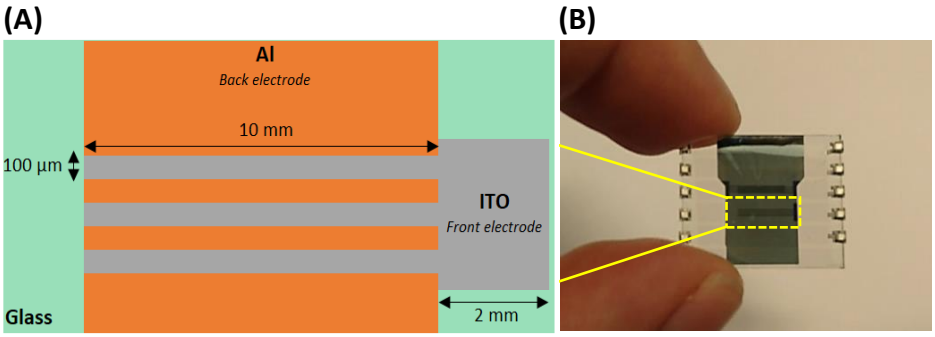

Figure 5.21: (A) A schematic illustration of the plasmonic working device giving the ITO finger dimensions and (B) an image of the actual substrate to show the active working device used in this work.

5.9 Results

5.9.1 Photodetection devices

In this chapter, four photodetection devices were chosen to investigate the near infrared (IR) photoactivity realized by the incorporation of gold nanoislands. The devices were numbered from 1 to 4 and described below in table 5.1. Devices 2 and 4 investigate the plasmonic induced photocurrent in the near-IR with and without the insertion of a hole transport/electron blocking layer represented by the organic PEDOT: PSS between the gold nanostructures and the ITO electrode. On the other hand, devices 1 and 3 are the respective control devices. All devices were prepared at the same time following the same experimental procedures for data consistency and comparison reasons. The devices were irradiated from the side of the gold islands to provide two important advantages. Firstly, light directly targets the gold-ZnO interface which helps to generate more hot electrons. Secondly, gold islands scatter the incident light which helps to maximize the light absorption.

Table 5.1: Layer structure of the photodetector devices used in this work.

Device No.	Device structure
1	ITO/ZnO NPs/Al
2	ITO/Au islands/ZnO/Al
3	ITO/PEDOT: PSS/ZnO/Al
4	ITO/PEDOT: PSS/Au islands/ZnO/Al

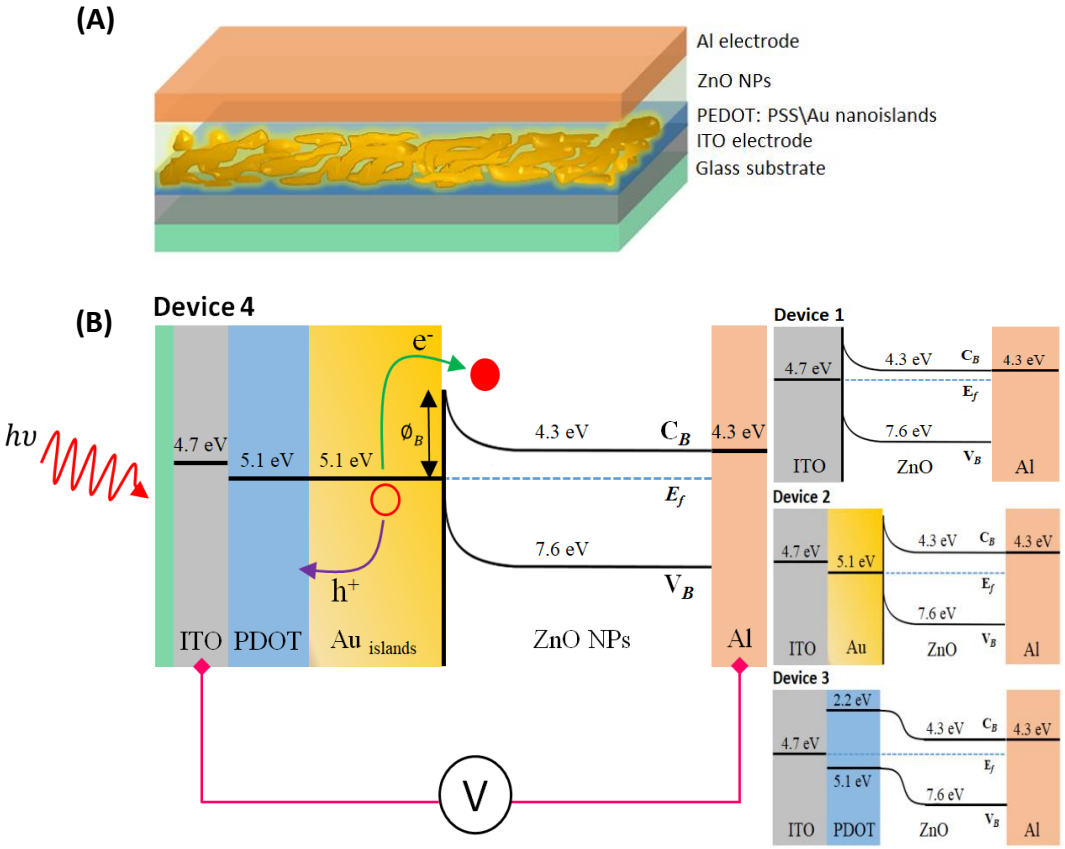

Figure 5.22: (A) a representation of the plasmonic near-IR photodetector device incorporating gold nan-islands evaporated on top of a PEDOT: PSS layer. Each working device consists of three devices as in (A) connected to the same ITO pad. (B) Energy band diagrams showing the energy levels offset for the four devices investigated in this work. The interface energies are shown in (B) of ITO, PEDOT: PSS, Au, ZnO NPs and Al were based on references [260,78].

A schematic representation of device 4 in addition to the energy band diagrams of the four devices are shown in figure 5.22-A and B. Photocurrent is normally carried out by the dominant charge carriers passing the device, which are either electrons or holes. Since ZnO is an n-type semiconductor, current is mainly carried by electrons flow. ZnO is a wide band gap semiconductor with a band gap of 3.3 eV at room temperature. Therefore, it is only expected to have photoactivity when irradiated in the UV. Upon light illumination, charge carriers are normally generated in such devices by either crossing the Schottky barrier (hot electrons injection from the gold nanoislands) or by ZnO band to band transition or by both. Therefore, by choosing the right irradiation

wavelength, we can control the generated photocurrent. For carriers generated by crossing the barrier, useful wavelengths should be in the range $\emptyset_B < hv < E_g$ where $\emptyset_B$ represents the Schottky barrier height, hv and E_g are the incident photon energy and band gap respectively. A Schottky barrier is expected to form when ZnO brought in to contact with ITO as a result of the energy bands difference between the ZnO conduction band (4.3 eV) and the work function of ITO (4.7 eV) [260,78]. On the other hand, an ohmic contact is expected to form on the other side of the device where ZnO NPs layer interfaces the Aluminium (Al) due to the similarity between the ZnO conduction band and the metal work function (4.3 eV) [78]. A Schottky junction is expected to be established when ZnO NPs interfaces the gold nanoislands whose barrier height could reach 1 eV depending on the junction quality and interface conditions [78]. Whereas, a p-n junction is formed when ZnO NPs with n-type conductivity interfaces PEDOT:PSS with p-type conductivity as illustrated in figure 5.22-B [261]. PEDOT: PSS is a highly conductive p-type organic semiconductor that helps transporting holes to the anode due to its suitable HOMO (highest occupied molecular orbital which is equivalent to the valence band in inorganic semiconductors) energy level of 5.1 eV [260]. However, PEDOT: PSS dose not conduct electrons due to its high LUMO (lowest unoccupied molecular orbital which represents the conduction band in inorganic semiconductors) energy level of 2.2 eV which make it impossible for electrons to cross through. Hence it is often used as an electrons blocking layer in optoelectronic devices. The workfunction of gold is similar to that of PEDOT: PSS (5.1 eV) so any barriers for holes transport to the ITO electrode are lower in energy than that for electrons at the Au/ZnO NPs interface.

5.9.2 Gold nanoislands formation

An atomic force microscope (AFM) was used to image the surface profile of the gold nanostructures films deposited on top of ITO and PEDOT: PSS spare samples prepared together with the actual working devices. The easy and cost-effective way to fabricate surface Plasmon-supported gold nanoislands is by direct thermal evaporation of gold thin film at very low evaporation speed [262,263,264]. This enables gold atoms to form 3-dimensional islands with nanoscale edges having a random size distribution much bigger than the deposited thickness [265]. The mechanism by which gold islands formed is fundamentally based on the interaction between gold atoms and the surface. During the evaporation process, gold atoms arrive at the substrate surface and undergo physisorption leading to weakly attaching to the surface. Gold atoms are normally diffuse (based on their kinetic and vibrational energies which provided by the given temperature of the atom) on the surface looking for high binding energy sites which therefore increase the probability of nucleation growth resulting from the high bonding force between gold-gold atoms compared to gold-surface atoms [266]. In our devices, gold films were only annealed at 150 ºC for 10 min in the air after spin coating the ZnO NPs on top of the gold layer. Figure 5.23-A and B show the AFM images of a 2×2 μm scan area in 2D, 3D in addition to the phase image (a powerful AFM technique recorded simultaneously with surface morphology to indicate the difference in surface composition based on surface stiffness and/or softness and the adhesion force between the surface and the AFM tip) of gold nanoislands films evaporated on top of PEDOT:PSS and ITO respectively. The resolution of the AFM image is 1024×1024 data points. There is an obvious difference in the gold film morphology when deposited on PEDOT:PSS and ITO despite the similar evaporation process. The gold thin film on PEDOT:PSS shows irregular and complex shapes of connected islands distributed

irregularly on the surface. Furthermore, nanogap distances (in the range 10-50 nm as calculated by AFM) between gold islands were also realized. The inset in figure 5.23-A represents a magnified image in addition to the red circles showing an example of the nanogap distance between two gold islands. These gaps form hot electromagnetic spots which help confine and intensify the applied electromagnetic field in the in-between gap [267]. On the other hand, gold deposited on top of ITO shows well packed, non-uniform, spark-shaped nanoislands in domains with random orientation covering almost the whole ITO surface. Gold nanoislands formed on top of PEDOT: PSS are bigger in size and shape and with an average height of about 30 nm compared to the gold nanostructure formed on ITO which appears to be smaller and denser with an average height of about 20 nm. However, both sets of gold nanoislands are still within the mean free path of plasmonic hot electrons transportation in gold (35 nm) [268,269] which ensures a possibility for a high number of hot electrons to cross the Schottky barrier towards the ZnO NPs. The distance between the nanoislands is important to help create a three-dimensional Schottky interface with the ZnO NPs layer which will boost the hot charge separation and transportation. The difference in the gold surface profile may be related to the surface energy of the substrate and its texture. The formation of well-defined islands when gold film deposited on PEDOT: PSS could be resulting from the molecular scale nanostructures of PEDOT: PSS surface composition which helps promote gold nucleation process and highly impacting the film formation dynamics. A similar observation is realized when gold film deposited on a transparent optical polymer [270]. This will hinder the spreading of gold atoms on the surface leading to the formation of islands. On the other hand, gold atoms on ITO surface (with a surface roughness of 1.8 nm) have more freedom to diffuse, especially after cleaning the ITO

substrate with 3 min UV/Ozone which increase the surface energy and therefore gold forms almost a continuous packed film.

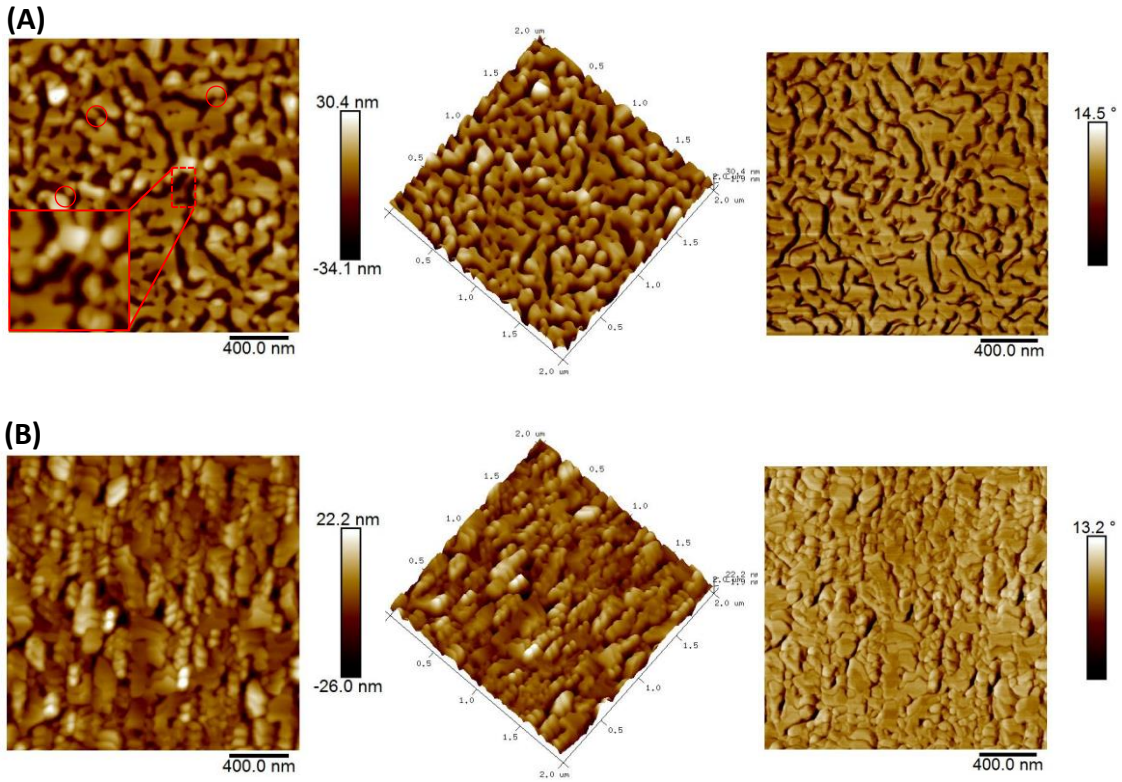

Figure 5.23: AFM images of the thin gold nano-islands evaporated on top of (A) PEDOT: PSS and (B) ITO. The magnified inset image in (A) in addition to the red circles show examples of the nanogap distances exists between the gold nanoislands. Gold films were annealed for 10 min in air at 150 °C. The topography AFM in A and B above is accompanied by a 3D illustration and a phase image for the same location.

5.9.3 Optical absorption

We now examine the absorbance of the four structures to investigate plasmonic enhancements below the band-edge. Figure 5.24 shows the absorption spectrum from the actual devices before evaporating the aluminium back electrode. Figure 5.24-A shows the absorption spectrum of gold nanoislands deposited on ITO and on ITO\PEDOT: PSS layer in order to confirm the responsibility of gold nanostructures on the broad absorption in the near-IR. The plot shows similar increases in near-IR absorption when gold nanoislands are deposited on ITO and PEDOT: PSS with a small

shift in the absorption peak position towards longer wavelengths for the latter. This high absorption in the near-IR can be related to the combination of light scattering and a plasmonic resonance caused by local interactions between the neighbouring gold islands. Similar absorption in the near-IR from the gold islands is also realized by Chen et al. [271]. Furthermore, spin coating the ZnO NPs on top of the gold nanoislands layer extends the absorption spectra in the UV because of ZnO band absorption.

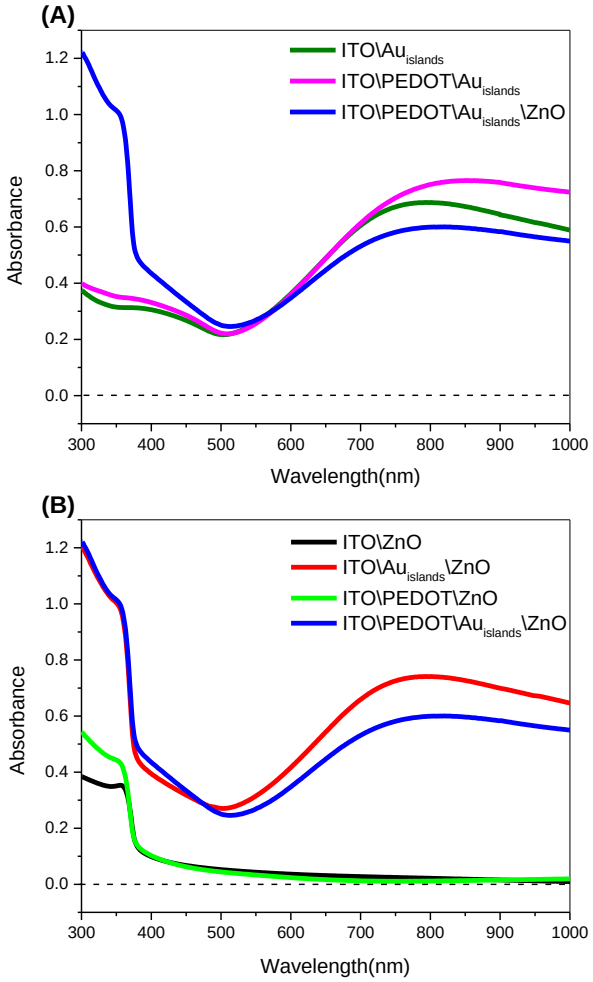

Figure 5.24: The absorption spectrum of (A) gold nanoislands combined with the ZnO and PEDOT:PSS confirming that absorption in the near-IR originates from the gold nanoislands. (B) The four actual devices investigated in this work before depositing the Al back electrode.

In figure 5.24-B, the absorption spectra of ZnO NPs deposited on top of the ITO front electrode, PEDOT: PSS and gold nanoislands are presented. The ZnO NPs absorption spectra on top of ITO and PEDOT: PSS show the fundamental interband transition in the UV region (at about 360 nm) with an absorption tail in the visible and no absorption activity is realized after 700 nm. Moreover, the absorption peak intensity of the ZnO is higher when deposited on top of PEDOT: PSS compared to ITO, implying an increased ZnO thickness when deposited on the former. We suggest that an even thicker ZnO layer is formed when deposited onto gold islands, explaining the significant increase in absorption of ZnO in the UV for the two samples containing gold nanoislands. Moreover, a noticeable increase in absorption is also realized in the visible region (from 400 nm to 500 nm) for both samples, possibly related to the light scattering by the gold nanoislands inside the device leading to absorb most of the incident light in the UV by ZnO [272]. The strength of the near-IR plasmonic resonance is different for the samples with and without PEDOT: PSS, possibly because of differences in the gold morphology, as shown in figure 5.23-A and B.

5.9.4 Photocurrent observation

The four photodetector devices, illustrated in table 5.1 were electrically characterized by measuring the dark and photocurrent on irradiation with light of photon energy ranging from 1.3 eV to 2.1 eV (600 nm to 950 nm) in addition to the UV, to identify the charge generation and injection process through the device. Figure 5.25 shows the dark I-V characteristics of the 4 devices. For each device, the current was measured relative to change the direction of current flow over the electrodes (measuring the dark current through the device when electrons injection sides are exchanged between the Al and ITO electrodes). The VB maximum of ZnO has an energy ≈ 7.6 eV, so there is a very large barrier for injection of holes at both electrodes. Therefore we assume that the

current in devices 1 and 2 is electronic in nature. PEDOT: PSS has a high LUMO energy of 2.2 eV which introduces a similarly large barrier for injections of electrons at one electrode. A Schottky barrier of about 0.4 eV is believed to be formed between the ZnO and the ITO electrode due to the difference in energy level alignment. An ohmic contact may be expected to form on the other side of the device with the Al due to the similar work function of ZnO to the Al (4.3 eV). Furthermore, a change in the barrier height formed is expected when gold islands, with a work function of 5.1 eV, are incorporated in the device. Figure 5.25-A and B respectively show the dark current versus the applied voltage for devices 1 and 2 with and without gold nanoislands between the ITO and ZnO NPs. Without the gold nanoislands, device 1 shows almost symmetric behaviour in the forward and reverse biased voltages with a low rectification trend. Interestingly the current is slighter higher with electron injection into the ITO electrode where a higher Schottky is expected. This may be caused by the development of a thin aluminium oxide layer at the Al-ZnO interface, so the contact is not ohmic. Such a layer is observed using TEM to develop during storage in the air by co-workers at the Aluminium interface of titanium dioxide nanoparticles (Dr E. Verrelli, private communication). A linear I-V characteristic with a substantially higher current is observed for device 2. This suggests that there may be some small areas of contacts between the Au aggregates (see figure 5.23-B AFM) and the Al electrode which could short-circuit the device.

Both devices 3 and 4 contain a PEDOT: PSS layer with an overlying gold layer only in device 4. Figure 5.25-C and D shows the dark I-V of devices 3 and 4 respectively with different applied voltages polarity. Both devices show a substantially lower current than devices 1 and 2 since PEDOT: PSS blocks electrons. Furthermore, the I-V characteristics become asymmetric as electrons can only be injected from the Al

electrode and holes from the other. Device 3 shows diode-like characteristic with a turn-on voltage of about 1 V. This behaviour is reflected by the junction established between the ZnO NPs and PEDOT: PSS as illustrated in figure 5.22-B [261]. Device 4 shows a steep rectifying behaviour compared to device 3, when forward biased, with higher dark current and the turn-on voltage of about 0.3 V which is much lower than device 3. This indicates that the Schottky junction formed with the ZnO NPs dominates the device working principle since the other contact with Al is considered to be semi-ohmic. Recombination of electron-hole may be more efficient at the gold-ZnO NPs than the PEDOT: PSS interface. Furthermore, the dark current in device 4 shows 3 orders of magnitude higher compared to device 3 in addition to a leakage current in the negative part of the I-V plot when forward biased as indicated by the black line shown in figure 5.25-D.

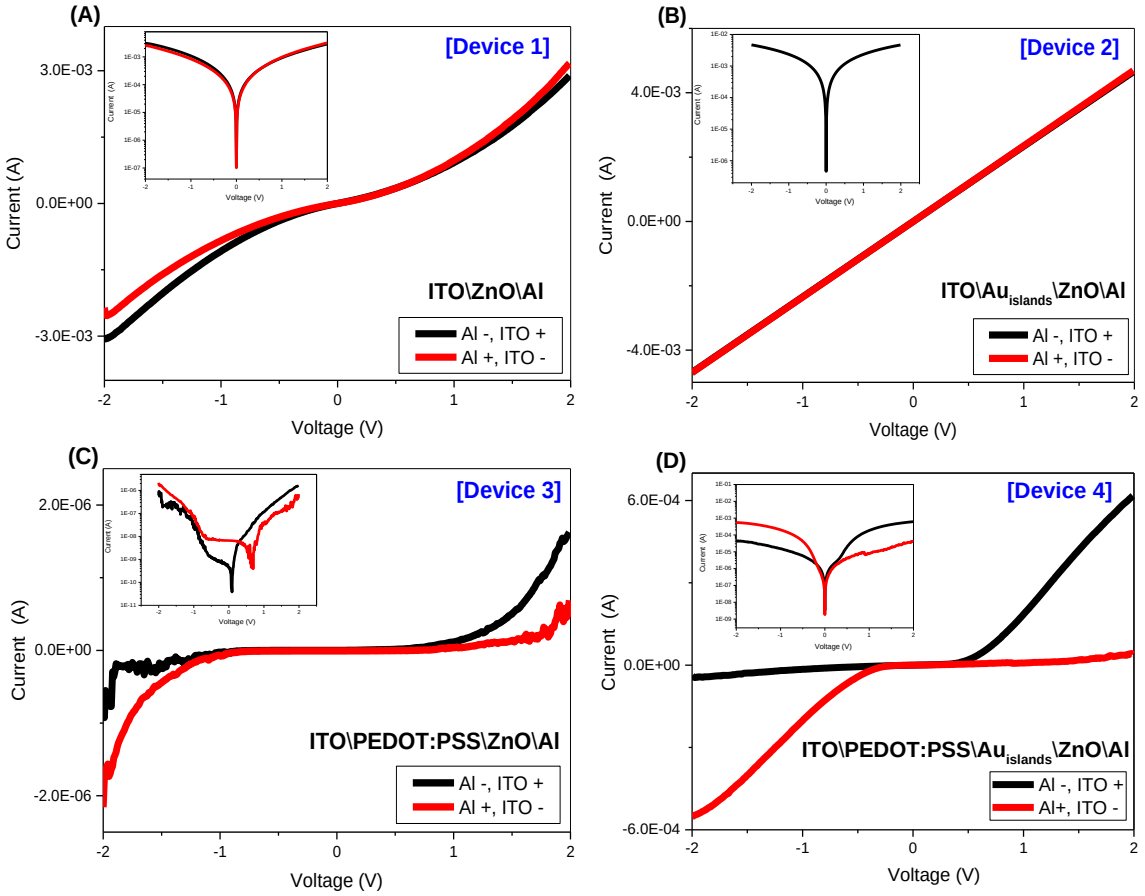

Figure 5.25: I-V characteristics of devices 1 to 4 in the dark. The labels indicate the electrode polarity under forwarding bias. The insets illustrate the dark I-V characteristics using a semi-log plot.

The diode-like behaviour of devices 3 and 4 have different ideality factors (a factor describing the similarity or how close the current rectification in the examined devices to an ideal diode's current). The ideality factor for both devices was determined by measuring the slope of the linear part of ln(I) versus applied voltage when the device was forward biased following ref. [273,274]. Its value for devices 3 and 4 was 2.9 and 5.7 respectively. Generally, a higher value of ideality factor indicates trap assisted charge tunnelling, current leakage and multiple charge recombination sites. These most likely originate from surface trap states at either the ZnO-gold interface or gold-PEDOT: PSS interface or both [275,276]. Furthermore, the high value of ideality factor could also

indicate the non-uniform interface and lateral inhomogeneity of the Schottky barrier at the interface between the gold nanoislands and the ZnO NPs.

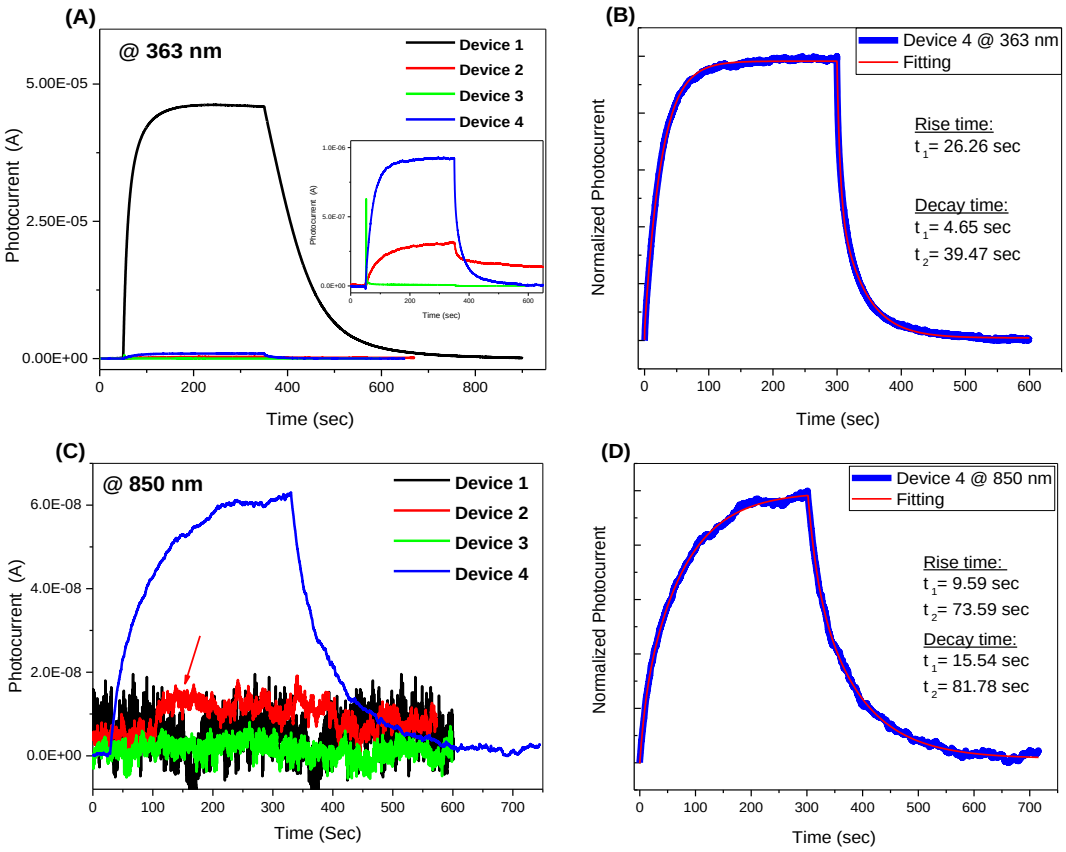

Figure 5.26: (A) Photocurrent transient comparison of the four photodetector devices investigated in this work on irradiation with UV light (363 nm) with a power density of 0.31 mW/cm^2. (B) The fitted photocurrent transient of device 4 on irradiation with UV light. (C) Photocurrent transient of the same devices as in (A) on irradiation with near-IR wavelength (≈850 nm) light with a power density of about 6 mW/cm^2, and (D) photocurrent transient from device 4 at 850 nm fitted with a double exponential function. A bias of 10mV was applied across the devices which were irradiated for 5 minutes.

Photoconductivity can be defined as the increase in conductivity of a material upon light absorption. The photocurrent transient behaviour of four photodetector devices was investigated by irradiation with UV (363 nm) light with a power density of 0.31 mW/cm^2 and near-IR (850 nm) light with a power density of 6 mW/cm^2 as shown in figure 5.26. As discussed in the optical measurements in section 5.8.1, a bandpass filter

was used to select the appropriate near-IR wavelength range. A forward biased voltage of 10 mV was applied to all devices prior to the measurement. Devices were also measured with – 10 mV and found to have almost symmetric photocurrent for devices 1 and 2 and asymmetric current transient for device 3 when measured in the UV. Furthermore, device 4 also shows asymmetric behaviour at – 10 mV with less photocurrent when irradiated in the UV and near-IR due to electrons injection blocking by the PEDOT: PSS. Figure 5.26-A shows the time-dependent photocurrent upon irradiating the four devices at 363 nm for 5 min in air. The figure inset represents the photocurrent as a function of time for devices 2, 3 and 4 for clarity. All devices show a photocurrent response with UV light as expected from ZnO. However, the photocurrent values are different. The highest photocurrent was observed in device 1 with 4.6×10^{-5} A, followed by device 4 with 9.2×10^{-7}A, device 2 with 3.1×10^{-7} A and finally device 3 with 9.3×10^{-9} A. Interestingly, the observed photocurrents are lower than the measured dark current showing in figure 5.25. This drop in photocurrent below the dark could be originated from the presence of adsorbed species such as –OH which could be removed upon testing the device with UV. Such adsorbents increase the dark current which is lowered after device irradiation. The temporal response of device 1 is similar to devices discussed in chapter four, although in this case, the device configuration is vertical rather than planar. The energy band diagrams of the four devices are illustrated earlier in figure 5.22-B. When UV light is on, light transmits through the ITO electrode and gets absorbed by the ZnO NPs layer leading to photocurrent generation. Photocurrent in ZnO NPs is carried out by the excess electrons which normally have long lifetimes since holes being trapped at the surface as discussed earlier in chapter four, section 4.1. Herein, photogenerated holes could also be trapped at the ZnO NPs surface and/or collected by the anode. When UV light is switched off, the photocurrent

decays gradually depending on the lifetime of the electrons. The slow decay of the current is a characteristic phenomenon of the persistent photocurrent in ZnO as a result of multiple electron decay processes such as recombination, electrons trapping by either defects or adsorbed atmospheric species.

Device 2 (red line), where a gold nanostructured layer is introduced between the ITO and the ZnO NPs, has a much lower UV temporal response than device 1(about two orders of magnitude lower). This device shows a substantial dark current which could be linked to possible electrical contacts between the gold agglomerates and the Al back electrode. This, however, will introduce recombination centres which limit the photocurrent by reducing the number of electrons and holes. By switching off the light, the current decays in two distinctive independent mechanisms, very fast and long decays, a signature of charge trapping effects possibly originated from native defects and/or adsorbed surface species. Device 3 represented by the green line shows a very low UV photoresponse and a different temporal response compared to devices 1 and 2 as shown in green line in figure 5.26-A. The device shows a large current spark when switching on the light followed by a steady low photocurrent. This large current spark could be resulting from a fast recombination process stimulated by the trapped species at the PEDOT: PSS/ZnO interface. Device 4, represented by the blue line, shows the second-best UV photoresponse similar to device 1 with lower photocurrent magnitude.

The same four devices discussed above were also irradiated with the near-IR light at 850 nm to investigate the plasmonic resonance absorption and its corresponding photocurrent as shown in figure 5.26-C. Devices with gold nanoislands (devices 2 and 4) showed high enough photocurrent for a direct measurement without the need for a current amplifier when irradiated at the near-IR. Device 2 (red line) shows spiky dark current followed by a small current increase (indicated by the red arrow) which could be

a noise since current increase occurs sometime after near-IR light switched on. On the other hand, device 4 shows a significant photocurrent response to the near-IR light indicated by a gradual increase in current until reaching the maximum of 6×10^{-8}A. When the light is switched off, the photocurrent decrease relatively fast followed by slow decay until the dark current value is restored. On the other hand, devices 1 and 3 (without the gold nanoislands) do not show obvious photocurrent response with irradiation at near-IR, thus supporting the assignment of the IR photocurrent to plasmonic effects.

To get insight into the lifetime of the photogenerated carriers, the photoresponse of device 4 at the two wavelengths, 363 nm and 850 nm were fitted. Figure 5.26 B and D shows the temporal response of the normalized photocurrent in device 4 when irradiated at 363 nm and 850 nm respectively. When the device was irradiated with UV light, the photocurrent growth can be described using a mono-exponential function used earlier in chapter three (equation 3.7), while the decay transient is best fitted with a double exponential function, given by equation 3.10. When the same device irradiated at 850 nm, the rise and decay time constants were best fitted by using equations 3.8 and 3.10 respectively.

Time constants for both wavelengths are gathered below in table 5.2. The photocurrent rise and decay times at 850 nm are much slower than what is normally recorded from plasmonic hot electrons shown elsewhere [252,277], where hot electrons have very short relaxation times in the timescale of femtoseconds [278,279].

Table 5.2: The time constants used to fit the temporal response of device 4 at the UV and near-IR.

Irradiation wavelength (nm)	Rise time constants		Decay time constants	
	τ_1 (sec)	τ_2 (sec)	τ_1 (sec)	τ_2 (sec)
363	26.26	----	4.65	39.47
850	9.59	73.59	15.54	81.78

The device shows a single component of the current growth when irradiated with 363 nm compared to the slow rising time represented by the two components when irradiated at 850 nm, this possibly because current density in the near-IR is low so that deeper traps in the ZnO are filled first. This phenomenon is realized and explained in chapter three when ZnO irradiated with different UV power densities. The biexponential decay time constant values in the near-IR are about double the time constants when device irradiated in the UV. This shows that the rise and decay of the temporal response in the near-IR are substantially lower than the UV. This phenomenon is also observed in gold nanostructures (with similar size as in our device) supported plasmonics photocurrent in GaN photodetector device [251]. The device also shows two exponential components to the current decay indicating two independent charge trapping/ losses by a possible recombination and/or interaction with surface species.

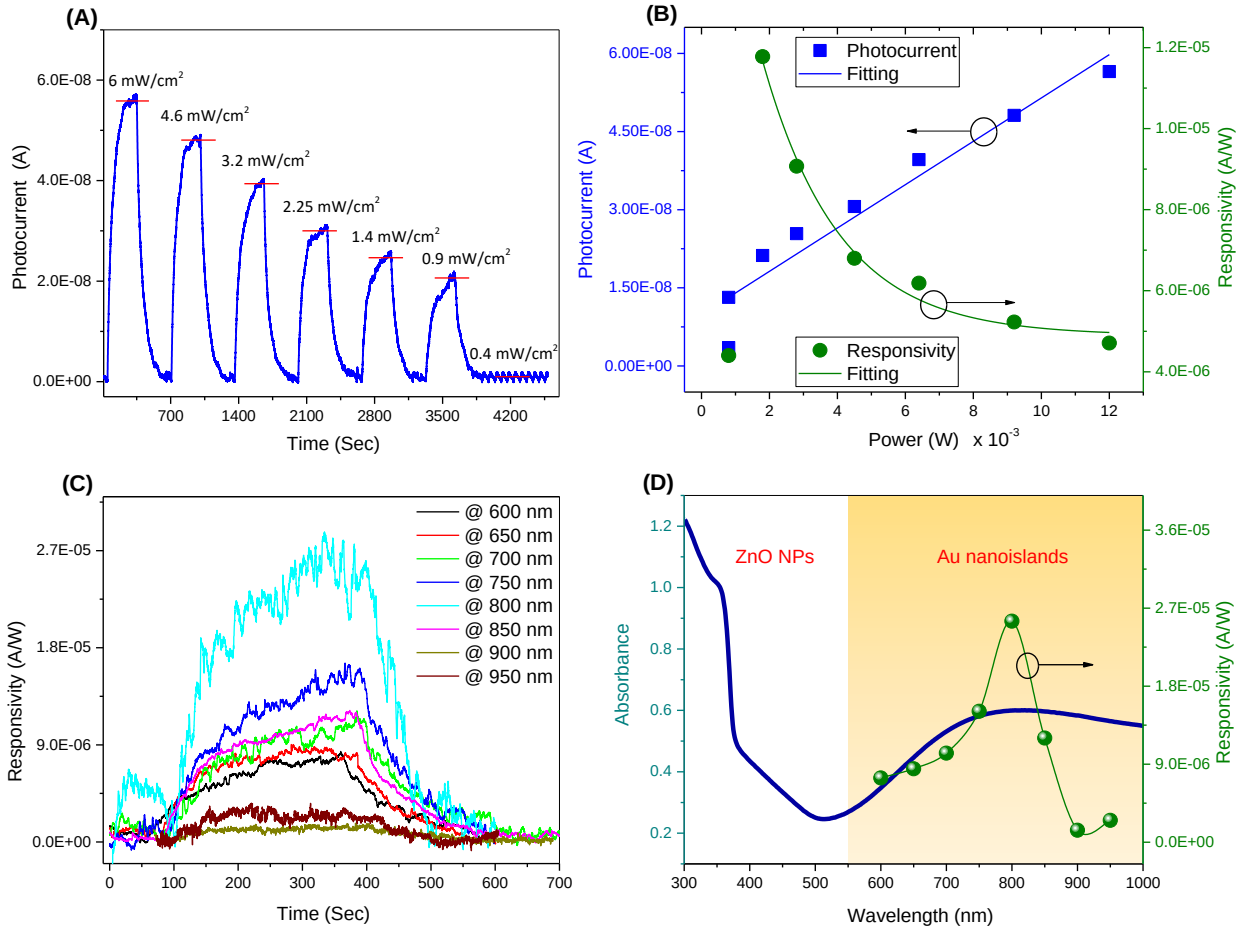

Figure 5.27: (A) Photocurrent at 850 nm as a function of time on irradiation with light of different intensities. The light intensity was controlled using a range of natural density filters. (B) Photocurrent and responsivity at 850 nm as a function of incident power calculated from (A). (C) The responsivity of device 4 as a function of wavelengths with a 10 mV bias and a set of bandpass filters with 10 nm (± 3nm) FWHM. (D) The absorption spectrum of device 4 combined with the responsivity measured at different wavelengths.

To get more insight of the near-IR photoactivity, device 4 was irradiated with 850 nm and a photocurrent transient was recorded for a set of irradiation periods of 5 min as shown in figure 5.27-A. The photocurrent is reproducible in shape and time despite the change in light power, using a set of different natural density filters. The light band at 850 nm was found to have the highest power density (about 6 mW/cm^2) compared to the other wavelengths after using the bandpass filters in front of the solar simulator. Therefore, we chose this wavelength to better clarify the power dependent photocurrent using a range of natural density filters. The device photocurrent increases sub-linearly

with incident power density following the absorption spectrum except at 0.4 mW/cm^2 where no photocurrent signal is recorded probably related to the low photocurrent signal compared to the background current noise. Increasing the light power generally leads to increasing the number of photogenerated hot electrons by a single photon/hot electron generation process with photon energy higher than the Schottky barrier [280]. The sub-linear increase in photocurrent with incident light power indicates that some of the injected hot electrons are getting trapped in ZnO NPs where the sub-linear dependence of photocurrent in ZnO is already been reported [133]. The photocurrent responsivity (R), defined earlier in chapter one as the generated photocurrent (I_{ph}) divided by the incident light power (P_{in}) and given by: $R = \frac{I_{\mathrm{ph}}}{P_{in}}$ extracted from 5.27-A is plotted as a function of incident light power and given in figure 5.27-B. The device responsivity in the near-IR is decreases with light power. This could be explained by the slow electrons reimbursement provided from the gold nanostructures so that hot electrons can be sustained and injected in the ZnO. Increasing the incident power means that high number of incident photons strike the plasmonic metal leading to increase the hot electrons emission. However, the concentration of hot electrons emission is limited by the hot electrons regeneration rate in the metal nanostructure. The electrical neutrality of the gold nanostructures is possibly maintained by the PEDOT: PSS layer which transport the photogenerated holes to the ITO, balancing the charge and sustain the electric current. Otherwise, the positively charged gold nanostructures (after hot electrons injection in the ZnO) will be sustained by possible electrochemical reactions. Photoconductivity measurements using different optical bandpass filters were performed to investigate the spectral dependence of the plasmonic induced photocurrent of the device.

Figure 5.27-C showing the time-dependent photocurrent from device 4 after irradiation with different wavelengths for 5 min. The photocurrent maximum for each wavelength is corrected with the incident light power in order to calculate the device responsivity in the visible and near-IR. Given that the responsivity is nonlinear, care was taken to ensure that R was measured using roughly the same intensities, i.e. 0.9-1.1 mW/cm^2 for all wavelengths. As figure 5.27-D also show, the plasmonic resonance absorption from device 4 extends from 550 nm to beyond 1 μm. Note the absorption measurement was made before evaporating the back aluminium electrode. The photocurrent responsivity shown in figure 5.27-D gradually increases with wavelength from 600 nm until it peaks at 800 nm with a responsivity of 2.5×10^{-5} A/W. However, the responsivity values show a rapid decrease with irradiation at longer wavelengths of 850nm, 900nm and 950nm. The plasmonic effect is known to excite hot electrons with broad energy distribution in the metal nanostructures depending on the metal size and shape especially in the case of gold nanoislands. Therefore, this sharp decrease could be related to the insufficient photon energy to excite enough electrons above the Schottky barrier with the ZnO NPs. Additionally, it could also be related to the lack of carrier concentration.

5.10 Discussion

The results suggest that the near-IR photocurrent observed in this work is stimulated by a plasmonic resonant excitation of gold nanoislands between the PEDOT: PSS and the ZnO NPs. Absorption occurs at the plasmonic resonance energy in the gold nanoislands, which leads to energy transfer to the surrounding medium when appropriate conditions are satisfied. Energy could be transferred in the form of hot electrons injection or by near-field enhancement around the gold nanostructure by the presence of hot spots which increase the absorption in the neighbouring medium. The mechanism of charge

generation and separation when device 4 is irradiated with UV and near-IR is different. At photon energy of 3.4 eV ($hv > E_g$), light is mainly absorbed in the ZnO NPs leading to an interband transition and electron-hole generation. In comparison, when the device is irradiated in the near-IR with photon energy of 1.45 eV (850 nm) ($hv < E_g$), light is mainly absorbed by the gold nanoislands through the effect of the strong near electromagnetic field enhancement originating from the synchronized oscillation of the conduction electrons in the metal with the incident electromagnetic field. This resonance oscillation will decay non-radiatively after a very short time (in the femtosecond time scale) and give rise to hot electrons. Hot electrons generated in areas close to the surface may have enough energy to overcome the Schottky barrier and relax in the conduction band of the ZnO NPs or become trapped in the defects states. This gives them long lifetime similar to the timescales for persistent UV photoconductivity in ZnO NPs observed in chapters three and four. The close behaviour of the temporal responses at both wavelengths (850 and 363 nm), as shown in figure 5.26-B and D, indicates the similarity in electrons trapping mechanisms. This support our assumption that photocurrent at 850 nm results from electron transfer from the gold nanoislands to the ZnO NPs. This scenario is also supported by a recent work of Ran Jia et al. [251] with their interesting findings revealing the plasmonic photoelectric enhancement by the polarization field of GaN (without the need of absorption overlap between GaN and gold nanostructures) originating from the lack of charge inversion symmetry from the Ga to the N terminated surfaces. The coupling between localized surface plasmons and the defects states in the surrounding medium is also supported by other research groups such as Hwang et al. [281] and Lian et al. [282].

Gold film deposited on top of the PEDOT:PSS shows a completely different morphology compared to the film deposited directly on ITO as shown in the AFM

images in figure 5.23-A and B. Gold islands on PEDOT: PSS are found to improve the plasmonic photocurrent in the near-IR which is consistent with results by Lee at al. [252]. They realized a significant plasmonic photocurrent generated by connected nano-sized gold islands compared to a continuous gold film when both are brought into contact with TiO_2. This current enhancement is inversely proportional to the interface area with the semiconductor owing to the localized surface plasmons effect. Therefore, we believe that PEDOT: PSS layer in device 4, plays a significant role in providing better interface areas between the ZnO NPs and gold nanoislands provided by the spaces between the gold islands which are much smaller in device 2. Furthermore, PEDOT: PSS layer will also help to extract the hot holes towards the ITO electrode. The incorporation of PEDOT: PSS as a hole transport layer (HTL) has been found to play a crucial role in the charge transporting in organic photovoltaic devices [283].

The number of hot electrons injected in the ZnO is highly affected by the Schottky barrier height. Generally, it is not easy to calculate or predict the barrier height with ZnO owing to the variation of surface states with its rich defects chemistry. However, we have tried to estimate the barrier height following the photoelectric measurements demonstrated in ref. [57] by plotting the square root of the photocurrent responsivity ($R^{1/2}$) recorded from plasmonic device 4 with incident photon energy ($h\upsilon$). A straight line region should be obtained by the plot. The extrapolating value of this region with the photon energy axis gives roughly the corresponding Schottky barrier height. A barrier height of about 1.3 eV was estimated between the Au nanoislands and ZnO NPs in device 4 as shown in figure 5.28. This value is about 48% higher than what is normally expected to the Schottky barrier between the gold and ZnO which is 0.8 eV. This high barrier value could be attributed to the existence of voids between the particles and the gold nanoislands resulting from the round and flat shapes of the ZnO

particles and gold nanoislands respectively which might affect the interface area. However, hot electrons irradiated with near-IR until the 900 nm can still overcome the barrier height.

Similar values of Schottky barrier heights were observed by Pescaglini et al. [258]. They found that the barrier height can vary with the gold nanorod density and/or coverage of the zinc nanorod as shown earlier in figure 5.20. Another study by Halas et al. [284] and Nordlander et al. [241] indicated that the excited hot electrons can have an energy of more than 1 eV above the Fermi level.

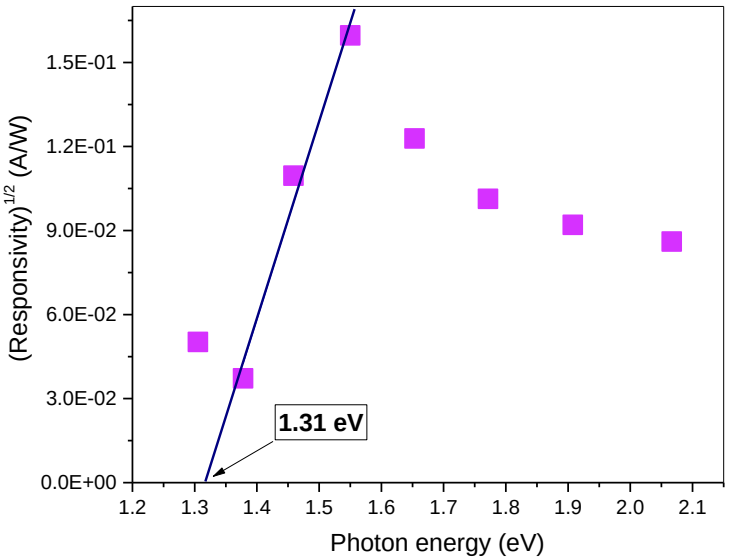

Figure 5.28: The square root of the photocurrent responsivity versus the incident photon energy for the plasmonic photodetector device 4. The Schottky barrier height is represented by the intercept point between the fitting line and the photon energy axes following ref [57].

The evaporated gold nanoislands deposited on top of the PEDOT: PSS layer, showing in figure 5.23-A, formed random sophisticated geometries with relatively sharp edges distributed all over the device. When the device irradiated with the resonance wavelength, the strong field enhancement originated by the localized plasmonic

resonance generate what is called hot spots regions. Those regions are formed as a result of plasmonic fields coupling of the neighbouring gold islands when brought into a very close distance leading to intensifying the applied electromagnetic field in the small gap between them. Such systems are reported to generate unusually large numbers of hot charge carriers due to their complex geometry shapes and by enhancing the optical absorption in the surrounding medium [219,272,285,286,287,288]. The small distances between the gold islands indicated in AFM image (figure 5.23-A) together with hot electrons injection process could be the responsible of the near-IR photoactivity observed in device 4. The intensity of the hot spot regions will mainly be governed by the inter-islands distance which found to be in the range of 10-50 nm calculated from AFM. Therefore, ZnO NPs located in between the gaps and within a short distance of the plasmonic near-field would likely to couple leading to increase the absorption cross-section of the ZnO NPs in the resonance wavelength.

5.11 Summary

A high photocurrent in the near-IR has been directly measured, without the need of current amplifier, below the band gap of ZnO NPs owing to hot electrons photoemission from gold nanoislands by localized surface plasmon effect. Those electrons are energetic enough to cross the Schottky barrier with the ZnO NPs leading to photocurrent generation. The plasmonic photocurrent measured in our device has a direct correlation with the gold nanoislands structures and the incorporation of hole transport layer (PEDOT: PSS) interfacing the gold nanoislands with the ITO front electrode.

A responsivity of 2.5×10^{-5} A/W has been recorded in the near-IR from device 4 explained on the basis of hot electrons injected into ZnO NPs and relax in its defects

states causing persistent photoconductivity. In comparison, Nazirzadeh et al. [259] have reported a much higher photoresponsivity in the near-IR of 2 mA/W using bigger plasmonic gold islands distributed randomly on top of the silicon. Furthermore, we also attributed the near-IR photoactivity to the contribution of electromagnetic hot spot regions formed between the gold nanoislands. The coupling between the plasmonic field of those regions with the nearby ZnO NPs leads to generate extra charge carriers which contribute to the overall photocurrent.

The formation of gold nanoislands did not require high-temperature annealing after deposition (only annealed at 150 ºC for 10 min after depositing the ZnO NPs) which opens the possibility of applying the same approach to flexible substrates. The formation of gold nanoislands structures is mainly caused by the impact of substrates rather than annealing at high temperatures for a long time as usually followed in literature. The simple structure of the hybrid device presented in this work offers a new design rule of using 3D nanoislands which opens new possibilities towards developing tuneable photodetectors covering the spectrum from the UV to the IR. Additionally, the low-cost device scheme presented in this work could easily be adopted by low processing temperature optoelectronics technology to enhance the performance of photovoltaic devices over a wide solar spectrum. Our work shed light on the performance of connected plasmonic metal nanostructures as an easy way to light harnessing and energy conversion.

Chapter 6

Conclusion and Future Work

6.1 Conclusion

Devices made from solution-processed ZnO nanostructure films have gained considerable interest as the next generation of the transparent semiconductor in a variety of applications such as photodetectors, transistors, solar cells and flat screens. However, device stability and reliability are highly threatened by the interaction with atmospheric surface species, such as water and/or surface carbonates during and/or after device fabrication. A full understanding and controlling of this issue is crucial for low cost and efficient device fabrication. This chapter summarizes and discusses the results drawn from three experimental chapters in separate sections to put in context the importance of our findings to the field of ZnO photodetection.

Chapter three: This chapter describes the investigation of changes in UV photoconductivity of solution-processed ZnO NP films induced by different experimental fabrication conditions. FTIR and XPS measurements indicate the variation of the surface composition when ZnO NPs are prepared and annealed in nitrogen and air. These variations identified as the remains acetate group and organic ligands which are sufficiently and partially removed by annealing in air and nitrogen respectively. The removal of these species paves the way to new organic complexes and carbonates to be

built on the surface by electrochemical reactions involving atmospheric CO_2 leading to high density of surface states. In terms of device stability, our photoconductivity measurements show that preparing, annealing and testing the ZnO NP device in nitrogen have promising impact on the photocurrent sustainability while following the later procedure in air help create quenching centres which affect the photocurrent by possible photoreactions with the surface. Results from contact angle measurement of ZnO NP films support the involvement of surface carbonates in promoting surface wettability. This contradicted with literature which mainly attributed surface wettability of ZnO NP film with water absorption. It was our aim to identify the mechanism by which persistent photoconductivity works. We showed that oxygen adsorption/desorption process do not govern all the UV photoconductivity mechanism of ZnO as it is normally suggested in literature.

Chapter four: In this chapter, we study the unusually narrow green photoconductivity observed from solution-processed ZnO NPs films. We show that this spectrally narrow PC can be attributed to electronic transitions involving deep defect states and shallow donors with discrete energy levels. A model supporting this theory is presented and correlated with temporal current response and spectroscopic evidence. It may be applicable to other semiconductors materials as well as ZnO. We also show that environmental effects such as annealing and storing in different environments can be used to enhance the green light photoconductivity. Hence the spectral response can be laterally patterned. We demonstrate a new pixelated photodetector with dual (ultraviolet and green) and single (ultraviolet only) wavelength detecting ZnO pixels produced on the same substrate.

Chapter five: This chapter discusses the deep red/infrared PC from ZnO NPs stimulated by the incorporation of gold nanoislands of random-size in a vertically

configured photodetector. The photodetector has a simple structure based on gold nanoislands film directly evaporated on top of PEDOT: PSS layer and an overlying ZnO layer. The localized surface plasmon resonance of the gold nanostructures stimulates hot electron injection from the gold to ZnO NPs. This accounts for the steady state photocurrent observed in the near-infrared

6.2 Future work

Throughout this study, we investigated the possibility of extending the photoconductivity of ZnO NPs to cover part of the visible and near-IR in addition to the UV by experimenting with different fabrication environments and surface treatment. During the course of this research, some areas are realized that could be a focus of further investigation.

Based on our findings, ZnO NP films used in this work could be further investigated as a CO_2 or H_2O sensor. The photolithographic process could be adopted to fabricate a solution processed full-colour imaging device with different pixels on the same substrate using a suspension of gold and/or aluminium nanostructures with different sizes and shapes to locally tune the optical response of ZnO NPs pixels based changing the plasmonics optical absorption resonance which stimulate hot electrons injection to the semiconductor. The pixilation process could be explored further by considering more sophisticated approaches such as a vertically displaced device configuration for compact imaging device applications. The proposed mechanism for below band-edge, spectrally narrow photoconductivity could also be investigated in terms of photocatalysis applications in the visible. Along with this, it would be very beneficial to investigate the narrow-band, green photoconductivity of different ZnO nanostructures such as nanowires and nanorods using similar or modified preparation methods.

Persistent plasmonic photoconductivity could be a useful method to study surface defects in wide band-gap semiconductors.

Bibliography

(1) Lorenz, M.; Ramachandra Rao, M. S.; Venkatesan, T.; Fortunato, E.; Barquinha, P.; Branquinho, R.; Salgueiro, D.; Martins, R.; Carlos, E.; Liu, A.; Shan, F. K.; Grundmann, M.; Boschker, H.; Mukherjee, J.; Priyadarshini, M.; DasGupta, N.; Rogers, D. J.; Teherani, F. H.; Sandana, E. V; Bove, P.; Rietwyk, K.; Zaban, A.; Veziridis, A.; Weidenkaff, A.; Muralidhar, M.; Murakami, M.; Abel, S.; Fompeyrine, J.; Zuniga-Perez, J.; Ramesh, R.; Spaldin, N. A.; Ostanin, S.; Borisov, V.; Mertig, I.; Lazenka, V.; Srinivasan, G.; Prellier, W.; Uchida, M.; Kawasaki, M.; Pentcheva, R.; Gegenwart, P.; Miletto Granozio, F.; Fontcuberta, J.; Pryds, N. The 2016 Oxide Electronic Materials and Oxide Interfaces Roadmap. *J. Phys. D. Appl. Phys.* **2016**, *49* (43), 433001.

(2) Kröger, F. A.; Vink, H. J. The Origin of the Fluorescence in Self-Activated ZnS, CdS, and ZnO. *J. Chem. Phys.* **1954**, *22* (2), 250–252.

(3) Yearian, H. J.; Howe, J. D. Scattering of High Speed Electrons of Varying Energy. *Phys. Rev.* **1935**, *48* (4), 381–382.

(4) Harrison, S. E. Conductivity and Hall Effect of ZnO at Low Temperatures. *Phys. Rev.* **1954**, *93* (1), 52–62.

(5) Morko, H.; Zgr, M. *Zinc Oxide*; Wiley-VCH Verlag GmbH & Co. KGaA: Weinheim, Germany, 2009; Vol. 44.

(6) Coleman, V. A.; Jagadish, C. Basic Properties and Applications of ZnO. In *Zinc*

Oxide Bulk, Thin Films and Nanostructures; Elsevier, 2006; pp 1–20.

(7) Duffy, J. A. Ionic-Covalent Character of Metal and Nonmetal Oxides. *J. Phys. Chem. A* **2006**, *110* (49), 13245–13248.

(8) Allen, M. W. Schottky Contact Formation to Bulk Zinc Oxide, University of Canterbury, 2008.

(9) Tang, C.; Spencer, M. J. S.; Barnard, A. S. Activity of ZnO Polar Surfaces: An Insight from Surface Energies. *Phys. Chem. Chem. Phys.* **2014**, *16* (40), 22139–22144.

(10) Huang, M. H. Room-Temperature Ultraviolet Nanowire Nanolasers. *Science (80-.).* **2001**, *292* (5523), 1897–1899.

(11) Koole, R.; Groeneveld, E.; Vanmaekelbergh, D.; Meijerink, A.; de Mello Donegá, C. Size Effects on Semiconductor Nanoparticles. In *Nanoparticles*; de Mello Donegá, C., Ed.; Springer Berlin Heidelberg: Berlin, Heidelberg, 2014; pp 13–51.

(12) Look, D. C.; Claflin, B.; Alivov, Y. I.; Park, S. J. The Future of ZnO Light Emitters. *Phys. Status Solidi C Conf.* **2004**, *1* (9), 2203–2212.

(13) Pearton, S. J.; Norton, D. P.; Ip, K.; Heo, Y. W.; Steiner, T. Recent Progress in Processing and Properties of ZnO. *Prog. Mater. Sci.* **2005**, *50* (3), 293–340.

(14) Wang, Z. L. Piezoelectric Nanogenerators Based on Zinc Oxide Nanowire Arrays. *Science (80-.).* **2006**, *312* (5771), 242–246.

(15) Look, D. C.; Reynolds, D. C.; Sizelove, J. R.; Jones, R. L.; Litton, C. W.; Cantwell, G.; Harsch, W. C. Electrical Properties of Bulk ZnO. *Solid State*

Commun. **1998**, *105* (6), 399–401.

(16) Tsukazaki, A.; Ohtomo, A.; Kawasaki, M. High-Mobility Electronic Transport in ZnO Thin Films. *Appl. Phys. Lett.* **2006**, *88* (15), 152106.

(17) Ryu, Y. R.; Lee, T. S.; White, H. W. Properties of Arsenic-Doped P-Type ZnO Grown by Hybrid Beam Deposition. *Appl. Phys. Lett.* **2003**, *83* (1), 87–89.

(18) Oba, F.; Togo, A.; Tanaka, I.; Paier, J.; Kresse, G. Defect Energetics in ZnO: A Hybrid Hartree-Fock Density Functional Study. *Phys. Rev. B - Condens. Matter Mater. Phys.* **2008**, *77* (24), 3–8.

(19) Pöppl, A.; Völkel, G. ESR and Photo-ESR Investigations of the Vmath Image Centre in ZnO Raw Material and Li-Doped ZnO Ceramic Powder. *phys. stat. sol.* **1990**, *121* (1), 195–204.

(20) Simpson, J. C.; Cordaro, J. F. Characterization of Deep Levels in Zinc Oxide. *J. Appl. Phys.* **1988**, *63* (5), 1781–1783.

(21) Naoki Ohashi, Tomokazu Nakata, Takashi Sekiguchi, Hideo Hosono, Masafumi Mizuguchi, Takaaki Tsurumi, J. T. and H. H. Yellow Emission from Zinc Oxide Giving an Electron Spin Resonance Signal at g=1.96. *Jpn. J. Appl. Phys.* **1999**, *38* (Part 2, Number 2A), L113–L115.

(22) Laufer, A.; Volbers, N.; Eisermann, S.; Potzger, K.; Geburt, S.; Ronning, C.; Meyer, B. K. Determination of Secondary Ion Mass Spectrometry Relative Sensitivity Factors for Polar and Non-Polar ZnO. *J. Appl. Phys.* **2011**, *110* (9), 94906.

(23) Nieminen, M. J. P. and R. M. Theory of Positrons in Solids and on Solid

Surfaces. *Rev. Mod. Phys.* **1994**, *66* (3), 841–899.

(24) Lany, S.; Zunger, A. Dopability, Intrinsic Conductivity, and Nonstoichiometry of Transparent Conducting Oxides. *Phys. Rev. Lett.* **2007**, *98* (4), 2–5.

(25) Janotti, A.; Van De Walle, C. G. New Insights into the Role of Native Point Defects in ZnO. *J. Cryst. Growth* **2006**, *287* (1), 58–65.

(26) Janotti, A.; Van de Walle, C. G. Native Point Defects in ZnO. *Phys. Rev. B* **2007**, *76* (16), 165202.

(27) McCluskey, M. D.; Jokela, S. J. Defects in ZnO. *J. Appl. Phys.* **2009**, *106* (7), 0–13.

(28) Freysoldt, C.; Grabowski, B.; Hickel, T.; Neugebauer, J.; Kresse, G.; Janotti, A.; Van De Walle, C. G. First-Principles Calculations for Point Defects in Solids. *Rev. Mod. Phys.* **2014**, *86* (1), 253–305.

(29) Schmidt-Mende, L.; MacManus-Driscoll, J. L. ZnO - Nanostructures, Defects, and Devices. *Mater. Today* **2007**, *10* (5), 40–48.

(30) Janotti, A.; Van de Walle, C. G. Fundamentals of Zinc Oxide as a Semiconductor. *Reports Prog. Phys.* **2009**, *72* (12), 126501.

(31) Clark, S. J.; Robertson, J.; Lany, S.; Zunger, A. Intrinsic Defects in ZnO Calculated by Screened Exchange and Hybrid Density Functionals. *Phys. Rev. B - Condens. Matter Mater. Phys.* **2010**, *81* (11), 1–5.

(32) Reynolds, D. C.; Look, D. C.; Jogai, B.; Morkoç, H. Similarities in the Bandedge and Deep-Centre Photoluminescence Mechanisms of ZnO and GaN. *Solid State Commun.* **1997**, *101* (9), 643–646.

(33) Reynolds, D. C.; Look, D. C.; Jogai, B. Fine Structure on the Green Band in ZnO. *J. Appl. Phys.* **2001**, *89* (11 I), 6189–6191.

(34) Kohan, A. F.; Ceder, G.; Morgan, D.; Van De Walle, C. G. First-Principles Study of Native Point Defects in ZnO. *Phys. Rev. B - Condens. Matter Mater. Phys.* **2000**, *61* (22), 15019–15027.

(35) Tuomisto, F.; Saarinen, K.; Look, D. C.; Farlow, G. C. Introduction and Recovery of Point Defects in Electron-Irradiated ZnO. *Phys. Rev. B - Condens. Matter Mater. Phys.* **2005**, *72* (8).

(36) Chen, Z. Q.; Betsuyaku, K.; Kawasuso, A. Vacancy Defects in Electron-Irradiated ZnO Studied by Doppler Broadening of Annihilation Radiation. *Phys. Rev. B - Condens. Matter Mater. Phys.* **2008**, *77* (11), 1–4.

(37) French, S. A.; Sokol, A. A.; Bromley, S. T.; Catlow, C. R. A.; Sherwood, P. Identification and Characterization of Active Sites and Their Catalytic Processes—the Cu/ZnO Methanol Catalyst. *Top. Catal.* **2003**, *24* (1–4), 161–172.

(38) Sokol, A. A.; French, S. A.; Bromley, S. T.; Catlow, R. A.; van Dam, H. J. J.; Sherwood, P. Point Defects in ZnO. *Faraday Discuss.* **2007**, *134* (0), 267–282.

(39) Thomas, D. G.; Lander, J. J. Hydrogen as a Donor in Zinc Oxide. *J. Chem. Phys.* **1954**, *25* (6), 1136–1142.

(40) Van De Walle, C. G. Hydrogen as a Cause of Doping in Zinc Oxide. *Phys. Rev. Lett.* **2000**, *85* (5), 1012–1015.

(41) Hofmann, D. M.; Hofstaetter, A.; Leiter, F.; Zhou, H.; Henecker, F.; Meyer, B. K.; Orlinskii, S. B.; Schmidt, J.; Baranov, P. G. Hydrogen: A Relevant Shallow

Donor in Zinc Oxide. *Phys. Rev. Lett.* **2002**, *88* (4), 45504.

(42) Ip, K.; Overberg, M. E.; Heo, Y. W.; Norton, D. P.; Pearton, S. J.; Stutz, C. E.; Kucheyev, S. O.; Jagadish, C.; Williams, J. S.; Luo, B.; Ren, F.; Look, D. C.; Zavada, J. M. Hydrogen Incorporation, Diffusivity and Evolution in Bulk ZnO. *Solid. State. Electron.* **2003**, *47* (12), 2255–2259.

(43) Nasiri, N.; Bo, R.; Wang, F.; Fu, L.; Tricoli, A. Ultraporous Electron-Depleted ZnO Nanoparticle Networks for Highly Sensitive Portable Visible-Blind UV Photodetectors. *Adv. Mater.* **2015**, *27* (29), 4336–4343.

(44) Park, C.; Lee, J.; Chang, W. S. Geometrical Separation of Defect States in ZnO Nanorods and Their Morphology-Dependent Correlation between Photoluminescence and Photoconductivity. *J. Phys. Chem. C* **2015**, *119* (29), 16984–16990.

(45) Zhang, X.; Qin, J.; Xue, Y.; Yu, P.; Zhang, B.; Wang, L.; Liu, R. Effect of Aspect Ratio and Surface Defects on the Photocatalytic Activity of ZnO Nanorods. *Sci. Rep.* **2015**, *4* (1), 4596.

(46) Xiong, G.; Pal, U.; Serrano, J. G. Correlations among Size, Defects, and Photoluminescence in ZnO Nanoparticles. *J. Appl. Phys.* **2007**, *101* (2), 24317.

(47) Han, N. S.; Shim, H. S.; Seo, J. H.; Kim, S. Y.; Park, S. M.; Song, J. K. Defect States of ZnO Nanoparticles: Discrimination by Time-Resolved Photoluminescence Spectroscopy. *J. Appl. Phys.* **2010**, *107* (8), 1–7.

(48) I. T. Drapak. Luminescence of a ZnO–Cu2O Heterojunction. *Semiconductors* **1968**, *2*, 624–625.

(49) Özgür, U.; Hofstetter, D.; Morkoç, H. ZnO Devices and Applications: A Review of Current Status and Future Prospects. *Proc. IEEE* **2010**, *98* (7), 1255–1268.

(50) Könenkamp, R.; Word, R. C.; Godinez, M. Ultraviolet Electroluminescence from ZnO/Polymer Heterojunction Light-Emitting Diodes. *Nano Lett.* **2005**, *5* (10), 2005–2008.

(51) Fortunato, E.; Barquinha, P.; Martins, R. Oxide Semiconductor Thin-Film Transistors: A Review of Recent Advances. *Adv. Mater.* **2012**, *24* (22), 2945–2986.

(52) Nomura, K. Thin-Film Transistor Fabricated in Single-Crystalline Transparent Oxide Semiconductor. *Science (80-.).* **2003**, *300* (5623), 1269–1272.

(53) Masuda, S.; Kitamura, K.; Okumura, Y.; Miyatake, S.; Tabata, H.; Kawai, T. Transparent Thin Film Transistors Using ZnO as an Active Channel Layer and Their Electrical Properties. *J. Appl. Phys.* **2003**, *93* (3), 1624–1630.

(54) Hoffman, R. L.; Norris, B. J.; Wager, J. F. ZnO-Based Transparent Thin-Film Transistors. *Appl. Phys. Lett.* **2003**, *82* (5), 733–735.

(55) Petti, L.; Münzenrieder, N.; Vogt, C.; Faber, H.; Büthe, L.; Cantarella, G.; Bottacchi, F.; Anthopoulos, T. D.; Tröster, G. Metal Oxide Semiconductor Thin-Film Transistors for Flexible Electronics. *Appl. Phys. Rev.* **2016**, *3* (2), 21303.

(56) Fowler, R. H. The Analysis of Photoelectric Sensitivity Curves for Clean Metals at Various Temperatures. *Phys. Rev.* **1931**, *38* (1), 45–56.

(57) Sze, S. M.; Ng, K. K. *Physics of Semiconductor Devices*; John Wiley & Sons, Inc.: Hoboken, NJ, USA, 2006.

(58) Razeghi, M.; Rogalski, A. Semiconductor Ultraviolet Detectors. *J. Appl. Phys.* **1996**, *79* (10), 7433–7473.

(59) Charles Kittel. *Introduction to Solid State Physics*, 8th Editio.; Wiley, 2005.

(60) Saleh, B. E. A.; Teich, M. C. *Chapter 17: Semiconductor Photon Detectors*; 1991; Vol. 5.

(61) Özgür, Ü.; Alivov, Y. I.; Liu, C.; Teke, A.; Reshchikov, M. A.; Doğan, S.; Avrutin, V.; Cho, S.-J.; Morkoç, H. A Comprehensive Review of ZnO Materials and Devices. *J. Appl. Phys.* **2005**, *98* (4), 41301.

(62) Physics and radio-electronics www.physics-and-radio-electronics.com.

(63) Montanari, S. Fabrication and Characterization of Planar Gunn Diodes for Monolithic Microwave Integrated Circuits ., RWTH Aachen University, 2005.

(64) Sang, L.; Liao, M.; Sumiya, M. A Comprehensive Review of Semiconductor Ultraviolet Photodetectors: From Thin Film to One-Dimensional Nanostructures. *Sensors* **2013**, *13* (8), 10482–10518.

(65) Omnes, F. Introduction to Semiconductor Photodetectors. In *Optoelectronic Sensors*; ISTE: London, UK, 2010; pp 1–14.

(66) Hockberger, P. E. A History of Ultraviolet Photobiology for Humans, Animals and Microorganisms. *Photochem. Photobiol.* **2002**, *76* (6), 561.

(67) Malinowski, P. *III-N Ultraviolet Detectors For Space Applications*, 1st ed.; Faculteit Ingenieurswetenschappen KU Leuven: UK, 2011.

(68) Morgan, T. N. Theory of the DX Center in Al X Ga 1 − X As and GaAs Crystals. *Phys. Rev. B* **1986**, *34* (4), 2664–2669.

(69) Mooney, P. M. Deep Donor Levels (D X Centers) in III-V Semiconductors. *J. Appl. Phys.* **1990**, *67* (3), R1–R26.

(70) Reemts, J.; Kittel, A. Persistent Photoconductivity in Highly Porous ZnO Films. *J. Appl. Phys.* **2007**, *101* (1), 13709.

(71) Madel, M.; Huber, F.; Mueller, R.; Amann, B.; Dickel, M.; Xie, Y.; Thonke, K. Persistent Photoconductivity in ZnO Nanowires: Influence of Oxygen and Argon Ambient. *J. Appl. Phys.* **2017**, *121* (12), 124301.

(72) Broich, B.; Heiland, G. Charge Transfer between ZnO Crystals and Dye Layers. *Surf. Sci.* **1980**, *92* (1), 247–264.

(73) Moazzami, K.; Murphy, T. E.; Phillips, J. D.; Cheung, M. C.-K.; Cartwright, a N. Sub-Bandgap Photoconductivity in ZnO Epilayers and Extraction of Trap Density Spectra. *Semicond. Sci. Technol.* **2006**, *21* (6), 717–723.

(74) Lany, S.; Zunger, A. Anion Vacancies as a Source of Persistent Photoconductivity in II-VI and Chalcopyrite Semiconductors. *Phys. Rev. B* **2005**, *72* (3), 35215.

(75) Janotti, A.; Van De Walle, C. G. Native Point Defects in ZnO. *Phys. Rev. B - Condens. Matter Mater. Phys.* **2007**, *76* (16), 1–22.

(76) Studenikin, S. A.; Golego, N.; Cocivera, M. Carrier Mobility and Density Contributions to Photoconductivity Transients in Polycrystalline ZnO Films. *J. Appl. Phys.* **2000**, *87* (5), 2413–2421.

(77) Li, Q. H.; Liang, Y. X.; Wan, Q.; Wang, T. H. Oxygen Sensing Characteristics of Individual ZnO Nanowire Transistors. *Appl. Phys. Lett.* **2004**, *85* (26), 6389–

6391.

(78) Jin, Y.; Wang, J.; Sun, B.; Blakesley, J. C.; Greenham, N. C. Solution-Processed Ultraviolet Photodetectors Based on Colloidal ZnO Nanoparticles. *Nano Lett.* **2008**, *8* (6), 1649–1653.

(79) Ahn, S. E.; Ji, H. J.; Kim, K.; Kim, G. T.; Bae, C. H.; Park, S. M.; Kim, Y. K.; Ha, J. S. Origin of the Slow Photoresponse in an Individual Sol-Gel Synthesized ZnO Nanowire. *Appl. Phys. Lett.* **2007**, *90* (15).

(80) Bera, A.; Basak, D. Role of Defects in the Anomalous Photoconductivity in ZnO Nanowires. *Appl. Phys. Lett.* **2009**, *94* (16), 163119.

(81) Kind, B. H.; Yan, H.; Messer, B.; Law, M.; Yang, P. Nanowire Ultraviolet Photodetectors and Optical Switches. *Adv. Mater.* **2002**, *14* (2), 158–160.

(82) Collins, R. J.; Thomas, D. G. Photoconduction and Surface Effects with Zinc Oxide Crystals. *Phys. Rev.* **1958**, *112* (2), 388–395.

(83) Bao, J.; Shalish, I.; Su, Z.; Gurwitz, R.; Capasso, F.; Wang, X.; Ren, Z. Photoinduced Oxygen Release and Persistent Photoconductivity in ZnO Nanowires. *Nanoscale Res. Lett.* **2011**, *6* (1), 404.

(84) Hirsch, M. T.; Wolk, J. A.; Walukiewicz, W.; Haller, E. E. Persistent Photoconductivity in N-Type GaN. *Appl. Phys. Lett.* **1997**, *71* (8), 1098–1100.

(85) Snyder, P. J.; Kirste, R.; Collazo, R.; Ivanisevic, A. Persistent Photoconductivity, Nanoscale Topography, and Chemical Functionalization Can Collectively Influence the Behavior of PC12 Cells on Wide Bandgap Semiconductor Surfaces. *Small* **2017**, *13* (24), 1700481.

(86) Di Bartolomeo, A.; Genovese, L.; Foller, T.; Giubileo, F.; Luongo, G.; Croin, L.; Liang, S.-J.; Ang, L. K.; Schleberger, M. Electrical Transport and Persistent Photoconductivity in Monolayer MoS 2 Phototransistors. *Nanotechnology* **2017**, *28* (21), 214002.

(87) Wu, N.; Wang, C.; Slattum, P. M.; Zhang, Y.; Yang, X.; Zang, L. Persistent Photoconductivity in Perylene Diimide Nanofiber Materials. *ACS Energy Lett.* **2016**, *1* (5), 906–912.

(88) Sun, B.; Sirringhaus, H. Solution-Processed Zinc Oxide Field-Effect Transistors Based on Self-Assembly of Colloidal Nanorods. *Nano Lett.* **2005**, *5* (12), 2408–2413.

(89) Pacholski, C.; Kornowski, A.; Weller, H. Self-Assembly of ZnO: From Nanodots to Nanorods. *Angew. Chemie Int. Ed.* **2002**, *41* (7), 1188–1191.

(90) Laurell-Technologies http://www.laurell.com/.

(91) Vig, J. R. UV/ozone Cleaning of Surfaces. *J. Vac. Sci. Technol. A Vacuum, Surfaces, Film.* **1985**, *3* (3), 1027–1034.

(92) Vig, J. R. UV/ozone Cleaning of Surfaces. *J. Vac. Sci. Technol. A Vacuum, Surfaces, Film.* **1985**, *3* (3), 1027–1034.

(93) Wartewig, S. *IR and Raman Spectroscopy*; Wiley-VCH Verlag GmbH & Co. KGaA: Weinheim, FRG, 2003.

(94) Jonny Arkin. Heavy Mineral Sand Analysis for Industrial Process Control http://www.usedscreeners.com/news/heavymineralsandanalysisforindustrialprocesscontrol.

(95) Leontiev, S. A.; Koshcheev, S. V.; Devyatov, V. G.; Cherkashin, A. E.; Mikheeva, É. P. Detailed XPS and UPS Studies of the Band Structure of Zinc Oxide. *J. Struct. Chem.* **1997**, *38* (5), 725–731.

(96) Einstein, A. On a Heuristic Point of View Concerning Production and Transformation of Light. *Ann. Phys.* **1905**, *322*, 132–148.

(97) Nordling, C.; Sokolowski, E.; Siegbahn, K. Precision Method for Obtaining Absolute Values of Atomic Binding Energies. *Phys. Rev.* **1957**, *105* (5), 1676–1677.

(98) Photoelectron spectrometer http://jacobs.physik.uni-saarland.de/english/instrumentation/uhvl.htm.

(99) Schlaf, R.; Murata, H.; Kafafi, Z. . Work Function Measurements on Indium Tin Oxide Films. *J. Electron Spectros. Relat. Phenomena* **2001**, *120* (1–3), 149–154.

(100) Basic principles of transmission electron microscope http://www.hk-phy.org/atomic_world/tem/tem02_e.html.

(101) Loos, J. The Art of SPM: Scanning Probe Microscopy in Materials Science. *Adv. Mater.* **2005**, *17* (15), 1821–1833.

(102) Roland Wiesendanger. *Scanning Probe Microscopy and Spectroscopy, Methods and Applications*; 1994.

(103) Bruker AFM https://www.bruker.com/.

(104) Peter Eaton and Paul West. *Atomic Force Microscopy*; Oxford University Press: Oxford, 2010.

(105) Klingshirn, C.; Fallert, J.; Zhou, H.; Sartor, J.; Thiele, C.; Maier-Flaig, F.;

Schneider, D.; Kalt, H. 65 Years of ZnO Research - Old and Very Recent Results. *Phys. Status Solidi Basic Res.* **2010**, *247* (6), 1424–1447.

(106) Mavi, H. S.; Rasheed, B. G.; Soni, R. K.; Abbi, S. C.; Jain, K. P. Photoluminescence and Raman Study of Porous Silicon Synthesized by Visible and Infrared Laser Etching. *Thin Solid Films* **2001**, *397* (1–2), 125–132.

(107) Djurišić, A. B.; Leung, Y. H. Optical Properties of ZnO Nanostructures. *Small* **2006**, *2* (8–9), 944–961.

(108) G. Sberveglieri, P. Nelli, S. G.; F. Quaranta, A. V.; Vasanelli, L. Oxygen Gas Sensing Characteristics at Ambient Pressure of Undoped and Lithium-Doped ZnO-Sputtered Thin Films. *Mater. Sci. Eng. B* **1990**, *7* (1–2), 63–68.

(109) Kang, B. S.; Heo, Y. W.; Tien, L. C.; Norton, D. P.; Ren, F.; Gila, B. P.; Pearton, S. J. Hydrogen and Ozone Gas Sensing Using Multiple ZnO Nanorods. *Appl. Phys. A* **2004**, *80* (5), 1029–1032.

(110) Takahashi, Y.; Kanamori, M.; Kondoh, A.; Minoura, H.; Ohya, Y. Photoconductivity of Ultrathin Zinc Oxide Films. *Jpn. J. Appl. Phys.* **1994**, *33* (Part 1, No. 12A), 6611–6615.

(111) Kolmakov, A.; Moskovits, M. Chemical Sensing and Catalysis By One-Dimensional Metal-Oxide Nanostructures. *Annu. Rev. Mater. Res.* **2004**, *34* (1), 151–180.

(112) Chang, J. F.; Kuo, H. H.; Leu, I. C.; Hon, M. H. The Effects of Thickness and Operation Temperature on ZnO : Al Thin Film CO Gas Sensor. *Sensors Actuators, B Chem.* **2002**, *84* (2–3), 258–264.

(113) Wang, X. H.; Ding, Y. F.; Zhang, J.; Zhu, Z. Q.; You, S. Z.; Chen, S. Q.; Zhu, J. Humidity Sensitive Properties of ZnO Nanotetrapods Investigated by a Quartz Crystal Microbalance. *Sensors Actuators, B Chem.* **2006**, *115* (1), 421–427.

(114) Zhang, Y.; Yu, K.; Jiang, D.; Zhu, Z.; Geng, H.; Luo, L. Zinc Oxide Nanorod and Nanowire for Humidity Sensor. *Appl. Surf. Sci.* **2005**, *242* (1–2), 212–217.

(115) Barsan, N.; Weimar, U. Understanding the Fundamental Principles of Metal Oxide Based Gas Sensors; the Example of CO Sensing with SnO 2 Sensors in the Presence of Humidity. *J. Phys. Condens. Matter* **2003**, *15* (20), R813–R839.

(116) Taylor, J. H.; Amberg, C. H. Infrared Spectra of Gases Chemisorbed on Zinc Oxide: CO and CO2. *Can. J. Chem.* **1961**, *39* (3), 535–539.

(117) OO, W. M. H. Infrared Spectroscopy of Zinc Oxide and Magnesium Nanostructures, Washington state university, 2007.

(118) Barsan, N.; Schweizer-Berberich, M.; Göpel, W. Fundamental and Practical Aspects in the Design of Nanoscaled SnO 2 Gas Sensors: A Status Report. *Fresenius J. Anal. Chem.* **1999**, *365* (4), 287–304.

(119) Franke, M. E.; Koplin, T. J.; Simon, U. Metal and Metal Oxide Nanoparticles in Chemiresistors: Does the Nanoscale Matter? *Small* **2006**, *2* (1), 36–50.

(120) Weisz, P. B. Effects of Electronic Charge Transfer between Adsorbate and Solid on Chemisorption and Catalysis. *J. Chem. Phys.* **1953**, *21* (9), 1531.

(121) Barsan, N.; Weimar, U. Conduction Model of Metal Oxide Gas Sensors. *J. Electroceramics* **2001**, *7* (3), 143–167.

(122) Xu, C.; Tamaki, J.; Miura, N.; Yamazoe, N. Grain Size Effects on Gas Sensitivity

of Porous SnO2-Based Elements. *Sensors Actuators B. Chem.* **1991**, *3* (2), 147–155.

(123) Ansari, Z. A.; Ansari, S. G.; Ko, T.; Oh, J. H. Effect of MoO3 Doping and Grain Size on SnO2-Enhancement of Sensitivity and Selectivity for CO and H2 Gas Sensing. *Sensors Actuators, B Chem.* **2002**, *87* (1), 105–114.

(124) Batzill, M.; Diebold, U. The Surface and Materials Science of Tin Oxide. *Prog. Surf. Sci.* **2005**, *79* (2–4), 47–154.

(125) Barsan, N.; Koziej, D.; Weimar, U. Metal Oxide-Based Gas Sensor Research: How To? *Sensors Actuators, B Chem.* **2007**, *121* (1), 18–35.

(126) Chao, C.-H.; Weng, W.-J.; Wei, D.-H. Enhanced UV Photodetector Response and Recovery Times Using a Nonpolar ZnO Sensing Layer. *J. Vac. Sci. Technol. A Vacuum, Surfaces, Film.* **2016**, *34* (2), 02D106.

(127) Yoo, D. J. Electrolysis of Water in CuO/ZnO Heterocontact Humidity Sensor. *J. Electrochem. Soc.* **1996**, *143* (4), L89.

(128) Chatman, S.; Poduska, K. M. The Effect of Synthesis Conditions and Humidity on Current−Voltage Relations in Electrodeposited ZnO-Based Schottky Junctions. *ACS Appl. Mater. Interfaces* **2009**, *1* (3), 552–558.

(129) Chen, Z.; Lu, C. Humidity Sensors: A Review of Materials and Mechanisms. *Sens. Lett.* **2005**, *3* (4), 274–295.

(130) Nahar, R. K.; Khanna, V. K.; Khokle, W. S.; Parr, R. A.; Wilson, J. C.; Kelly, R. G.; Sethna, P. P.; Lee, R. S.; Nylander, C.; Morgan, D. V; Guile, A. E.; Bektore, Y.; Rageh, M. S. I.; Morgan, D. V; Guile, A. E. Design and Development of a Cu

20-AI , 03-Al Moisture Transducer. *J. Phys. D Appl. Phys.* **1986**, *19*, 1072–1074.

(131) Noei, H.; Qiu, H.; Wang, Y.; Löffler, E.; Wöll, C.; Muhler, M. The Identification of Hydroxyl Groups on ZnO Nanoparticles by Infrared Spectroscopy. *Phys. Chem. Chem. Phys.* **2008**, *10* (47), 7092–7097.

(132) Henrik Fabricius, Torben Skettrup, and P. B. Ultraviolet Detectors in Thin Sputtered ZnO Films. *Appl. Opt.* **1986**, *25* (16), 2764–2767.

(133) Soci, C.; Zhang, A.; Xiang, B.; Dayeh, S. A.; Aplin, D. P. R.; Park, J.; Bao, X. Y.; Lo, Y. H.; Wang, D. ZnO Nanowire UV Photodetectors with High Internal Gain. *Nano Lett.* **2007**, *7* (4), 1003–1009.

(134) Afal, A.; Coskun, S.; Emrah Unalan, H. All Solution Processed, Nanowire Enhanced Ultraviolet Photodetectors. *Appl. Phys. Lett.* **2013**, *102* (4), 43503.

(135) Alenezi, M. R.; Henley, S. J.; Silva, S. R. P. On-Chip Fabrication of High Performance Nanostructured ZnO UV Detectors. *Sci. Rep.* **2015**, *5*, 8516.

(136) Lao, C. S.; Park, M.-C.; Kuang, Q.; Deng, Y.; Sood, A. K.; Polla, D. L.; Wang, Z. L. Giant Enhancement in UV Response of ZnO Nanobelts by Polymer Surface-Functionalization. *J. Am. Chem. Soc.* **2007**, *129* (40), 12096–12097.

(137) Manekkathodi, A.; Lu, M.-Y.; Wang, C. W.; Chen, L.-J. Direct Growth of Aligned Zinc Oxide Nanorods on Paper Substrates for Low-Cost Flexible Electronics. *Adv. Mater.* **2010**, *22* (36), 4059–4063.

(138) Basak, D.; Amin, G.; Mallik, B.; Paul, G. K.; Sen, S. K. Photoconductive UV Detectors on Sol–gel-Synthesized ZnO Films. *J. Cryst. Growth* **2003**, *256* (1–2), 73–77.

(139) Xu, Z.-Q.; Deng, H.; Xie, J.; Li, Y.; Zu, X.-T. Ultraviolet Photoconductive Detector Based on Al Doped ZnO Films Prepared by Sol–gel Method. *Appl. Surf. Sci.* **2006**, *253*, 476–479.

(140) Chen, K. J.; Hung, F. Y.; Chang, S. J.; Young, S. J. Optoelectronic Characteristics of UV Photodetector Based on ZnO Nanowire Thin Films. *J. Alloys Compd.* **2009**, *479* (1–2), 674–677.

(141) Jun, J. H.; Seong, H.; Cho, K.; Moon, B.-M. M.; Kim, S. Ultraviolet Photodetectors Based on ZnO Nanoparticles. *Ceram. Int.* **2009**, *35* (7), 2797–2801.

(142) Qin, L.; Shing, C.; Sawyer, S.; Dutta, P. S. Enhanced Ultraviolet Sensitivity of Zinc Oxide Nanoparticle Photoconductors by Surface Passivation. *Opt. Mater. (Amst).* **2011**, *33* (3), 359–362.

(143) Gogurla, N.; Sinha, A. K.; Santra, S.; Manna, S.; Ray, S. K. Multifunctional Au-ZnO Plasmonic Nanostructures for Enhanced UV Photodetector and Room Temperature NO Sensing Devices. *Sci. Rep.* **2015**, *4* (1), 6483.

(144) Jin, Z.; Gao, L.; Zhou, Q.; Wang, J. High-Performance Flexible Ultraviolet Photoconductors Based on Solution-Processed Ultrathin ZnO/Au Nanoparticle Composite Films. *Sci. Rep.* **2014**, *4*, 4268.

(145) Rudakova, A. V.; Oparicheva, U. G.; Grishina, A. E.; Maevskaya, M. V.; Emeline, A. V.; Bahnemann, D. W. Dependences of ZnO Photoinduced Hydrophilic Conversion on Light Intensity and Wavelengths. *J. Phys. Chem. C* **2015**, *119* (18), 9824–9828.

(146) Sun, R.-D.; Nakajima, A.; Fujishima, A.; Watanabe, T.; Hashimoto, K.

Photoinduced Surface Wettability Conversion of ZnO and TiO 2 Thin Films. *J. Phys. Chem. B* **2001**, *105* (10), 1984–1990.

(147) Hu, H.; Ji, H.-F.; Sun, Y. The Effect of Oxygen Vacancies on Water Wettability of a ZnO Surface. *Phys. Chem. Chem. Phys.* **2013**, *15* (39), 16557–16565.

(148) Stevens, N.; Priest, C. I.; Sedev, R.; Ralston, J. Wettability of Photoresponsive Titanium Dioxide Surfaces. *Langmuir* **2003**, *19* (8), 3272–3275.

(149) Rico, V.; López, C.; Borrás, A.; Espinós, J. P.; González-Elipe, A. R. Effect of Visible Light on the Water Contact Angles on Illuminated Oxide Semiconductors Other than TiO2. *Sol. Energy Mater. Sol. Cells* **2006**, *90* (17), 2944–2949.

(150) Feng, X.; Feng, L.; Jin, M.; Zhai, J.; Jiang, L.; Zhu, D. Reversible Super-Hydrophobicity to Super-Hydrophilicity Transition of Aligned ZnO Nanorod Films. *J. Am. Chem. Soc.* **2004**, *126* (1), 62–63.

(151) Yadav, K.; Mehta, B. R.; Bhattacharya, S.; Singh, J. P. A Fast and Effective Approach for Reversible Wetting-Dewetting Transitions on ZnO Nanowires. *Sci. Rep.* **2016**, *6* (1), 35073.

(152) Luo, M.; Shen, C.; Feltis, B. N.; Martin, L. L.; Hughes, A. E.; Wright, P. F. A.; Turney, T. W. Reducing ZnO Nanoparticle Cytotoxicity by Surface Modification. *Nanoscale* **2014**, *6* (11), 5791.

(153) Zhang, X.; Qin, J.; Xue, Y.; Yu, P.; Zhang, B.; Wang, L.; Liu, R. Effect of Aspect Ratio and Surface Defects on the Photocatalytic Activity of ZnO Nanorods. *Sci. Rep.* **2014**, *4*, 4596.

(154) A.V. Naumkin, A. Kraut-Vass, S. W. Gaarenstroom, C. J. P. NIST X-ray

Photoelectron Spectroscopy Database Version 4.1.

(155) A.V. Naumkin, A. Kraut-Vass, S. W. Gaarenstroom, C. J. P. NIST X-ray Photoelectron Spectroscopy Database, Version 4.1 http://srdata.nist.gov/xps/.

(156) Lin, C.-C.; Li, Y.-Y. Synthesis of ZnO Nanowires by Thermal Decomposition of Zinc Acetate Dihydrate. *Mater. Chem. Phys.* **2009**, *113* (1), 334–337.

(157) Kumari, R.; Sahai, A.; Goswami, N. Effect of Nitrogen Doping on Structural and Optical Properties of ZnO Nanoparticles. *Prog. Nat. Sci. Mater. Int.* **2015**, *25* (4), 300–309.

(158) Senthilkumar, K.; Tokunaga, M.; Okamoto, H.; Senthilkumar, O.; Fujita, Y. Hydrogen Related Defect Complexes in ZnO Nanoparticles. *Appl. Phys. Lett.* **2010**, *97* (9), 91907.

(159) Sakohara, S.; Tickanen, L. D.; Anderson, M. A. Luminescence Properties of Thin Zinc Oxide Membranes Prepared by the Sol-Gel Technique: Change in Visible Luminescence during Flring. *J. Phys. Chem* **1992**, *96*, 11086–11091.

(160) Lin, Z.; Guo, F.; Wang, C.; Wang, X.; Wang, K.; Qu, Y. Preparation and Sensing Properties of Hierarchical 3D Assembled Porous ZnO from Zinc Hydroxide Carbonate. *RSC Adv.* **2014**, *4* (10), 5122.

(161) Xiong, G.; Pal, U.; Serrano, J. G.; Ucer, K. B.; Williams, R. T. Photoluminesence and FTIR Study of ZnO Nanoparticles: The Impurity and Defect Perspective. *Phys. status solidi* **2006**, *3* (10), 3577–3581.

(162) Cun, T.; Dong, C.; Huang, Q. Ionothermal Precipitation of Highly Dispersive ZnO Nanoparticles with Improved Photocatalytic Performance. *Appl. Surf. Sci.*

2016, *384*, 73–82.

(163) Kumar, S.; Sahare, P. D. Effect of Surface Defects on Green Luminescence from ZnO Nanoparticles. *AIP Conference Proceedings*. 2011, pp 159–160.

(164) Saussey, J.; Lavalley, J.-C.; Bovet, C. Infrared Study of CO2 Adsorption on ZnO. Adsorption Sites. *J. Chem. Soc. Faraday Trans. 1 Phys. Chem. Condens. Phases* **1982**, *78* (5), 1457.

(165) Andreas J. Nuber. Reversible Wettability of Nanoscale ZnO Arrays, University of New Jersey.

(166) Kumar, S.; Sahare, P. D. Effects of Annealing on the Surface Defects of Zinc Oxide Nanoparticles. *World Sci.* **2012**, *7* (3), 1–9.

(167) Pholnak, C.; Sirisathitkul, C.; Suwanboon, S.; Harding, D. J. Effects of Precursor Concentration and Reaction Time on Sonochemically Synthesized ZnO Nanoparticles. *Mater. Res.* **2014**, *17* (2), 405–411.

(168) Limpijumnong, S.; Li, X.; Wei, S.-H.; Zhang, S. B. Probing Deactivations in Nitrogen Doped ZnO by Vibrational Signatures: A First Principles Study. *Phys. B Condens. Matter* **2006**, *376–377* (1), 686–689.

(169) Abe, T.; Takahashi, S.; Kamada, S.; Nakagawa, A.; Chiba, T.; Nakagawa, M.; Chiba, S.; Kashiwaba, Y.; Daibo, M.; Niikura, I.; Kashiwaba, Y.; Osada, H. Photoconductive Properties of Undoped and Nitrogen-Doped ZnO Single Crystals in Various Ambiences. *Phys. status solidi* **2016**, *13* (7–9), 581–584.

(170) Shinde, S. S.; Rajpure, K. Y. Fabrication and Performance of N-Doped ZnO UV Photoconductive Detector. *J. Alloys Compd.* **2012**, *522*, 118–122.

(171) Gankanda, A.; Cwiertny, D. M.; Grassian, V. H. Role of Atmospheric CO2 and H2O Adsorption on ZnO and CuO Nanoparticle Aging: Formation of New Surface Phases and the Impact on Nanoparticle Dissolution. *J. Phys. Chem. C* **2016**, *120* (34), 19195–19203.

(172) Wang, C.; Wang, H. M.; Fang, Z. Y. Influence of Mn Doping on the Microstructure and Optical Properties of CdS. *J. Alloys Compd.* **2009**, *486* (1–2), 702–705.

(173) Baltrusaitis, J.; Grassian, V. H. Surface Reactions of Carbon Dioxide at the Adsorbed Water−Iron Oxide Interface. *J. Phys. Chem. B* **2005**, *109* (25), 12227–12230.

(174) Baltrusaitis, J.; Grassian, V. H. Carbonic Acid Formation from Reaction of Carbon Dioxide and Water Coordinated to Al(OH) 3 : A Quantum Chemical Study. *J. Phys. Chem. A* **2010**, *114* (6), 2350–2356.

(175) Hatch, S. M.; Briscoe, J.; Sapelkin, A.; Gillin, W. P.; Gilchrist, J. B.; Ryan, M. P.; Heutz, S.; Dunn, S. Influence of Anneal Atmosphere on ZnO-Nanorod Photoluminescent and Morphological Properties with Self-Powered Photodetector Performance. *J. Appl. Phys.* **2013**, *113* (20), 204501.

(176) Eppler, A. M.; Ballard, I. M.; Nelson, J. Charge Transport in Porous Nanocrystalline Titanium Dioxide. *Phys. E Low-dimensional Syst. Nanostructures* **2002**, *14* (1–2), 197–202.

(177) Nelson, J.; Eppler, A. M.; Ballard, I. M. Photoconductivity and Charge Trapping in Porous Nanocrystalline Titanium Dioxide. *J. Photochem. Photobiol. A Chem.* **2002**, *148* (1–3), 25–31.

(178) Lai, C.; Wang, X.; Zhao, Y.; Fong, H.; Zhu, Z. Effects of Humidity on the Ultraviolet Nanosensors of Aligned Electrospun ZnO Nanofibers. *RSC Adv.* **2013**, *3* (18), 6640–6645.

(179) Thomas, S. R.; Pattanasattayavong, P.; Anthopoulos, T. D. Solution-Processable Metal Oxide Semiconductors for Thin-Film Transistor Applications. *Chem. Soc. Rev.* **2013**, *42* (16), 6910.

(180) Choy, W. C. H.; Zhang, D. Solution-Processed Metal Oxides as Efficient Carrier Transport Layers for Organic Photovoltaics. *Small* **2016**, *12* (4), 416–431.

(181) Guo, F.; Yang, B.; Yuan, Y.; Xiao, Z.; Dong, Q.; Bi, Y.; Huang, J. A Nanocomposite Ultraviolet Photodetector Based on Interfacial Trap-Controlled Charge Injection. *Nat. Nanotechnol.* **2012**, *7* (12), 798–802.

(182) Weintraub, B.; Zhou, Z.; Li, Y.; Deng, Y. Solution Synthesis of One-Dimensional ZnO Nanomaterials and Their Applications. *Nanoscale* **2010**, *2* (9), 1573.

(183) Sarkar, S.; Basak, D. Self Powered Highly Enhanced Dual Wavelength ZnO@CdS Core–Shell Nanorod Arrays Photodetector: An Intelligent Pair. *ACS Appl. Mater. Interfaces* **2015**, *7* (30), 16322–16329.

(184) Tak, Y.; Yong, K. Controlled Growth of Well-Aligned ZnO Nanorod Array Using a Novel Solution Method. *J. Phys. Chem. B* **2005**, *109* (41), 19263–19269.

(185) Laurenti, M.; Verna, A.; Fontana, M.; Quaglio, M.; Porro, S. Selective Growth of ZnO Nanowires on Substrates Patterned by Photolithography and Inkjet Printing. *Appl. Phys. A* **2014**, *117* (2), 901–907.

(186) Shi, R.; Huang, C.; Zhang, L.; Amini, A.; Liu, K.; Shi, Y.; Bao, S.; Wang, N.; Cheng, C. Three Dimensional Sculpturing of Vertical Nanowire Arrays by Conventional Photolithography. *Sci. Rep.* **2016**, *6* (1), 18886.

(187) Gwinner, M. C.; Vaynzof, Y.; Banger, K. K.; Ho, P. K. H.; Friend, R. H.; Sirringhaus, H. Solution-Processed Zinc Oxide as High-Performance Air-Stable Electron Injector in Organic Ambipolar Light-Emitting Field-Effect Transistors. *Adv. Funct. Mater.* **2010**, *20* (20), 3457–3465.

(188) Liang, S.; Sheng, H.; Liu, Y.; Huo, Z.; Lu, Y.; Shen, H. ZnO Schottky Ultraviolet Photodetectors. *J. Cryst. Growth* **2001**, *225* (2–4), 110–113.

(189) Ahn, S. E.; Lee, J. S.; Kim, H.; Kim, S.; Kang, B. H.; Kim, K. H.; Kim, G. T. Photoresponse of Sol-Gel-Synthesized ZnO Nanorods. *Appl. Phys. Lett.* **2004**, *84* (24), 5022–5024.

(190) Fan, Z.; Chang, P.; Lu, J. G.; Walter, E. C.; Penner, R. M.; Lin, C.; Lee, H. P. Photoluminescence and Polarized Photodetection of Single ZnO Nanowires. *Appl. Phys. Lett.* **2004**, *85* (25), 6128–6130.

(191) Choi, S.; Phillips, M. R.; Aharonovich, I.; Pornsuwan, S.; Cowie, B. C. C.; Ton-That, C. Photophysics of Point Defects in ZnO Nanoparticles. *Adv. Opt. Mater.* **2015**, *3* (6), 821–827.

(192) Kavitha, M. K.; Jinesh, K. B.; Philip, R.; Gopinath, P.; John, H. Defect Engineering in ZnO Nanocones for Visible Photoconductivity and Nonlinear Absorption. *Phys. Chem. Chem. Phys.* **2014**, *16* (45), 25093–25100.

(193) Sett, D.; Sarkar, S.; Basak, D. A Successive Photocurrent Transient Study to Probe the Sub-Band Gap Electron and Hole Traps in ZnO Nanorods. *RSC Adv.*

2014, *4* (102), 58553–58558.

(194) Bandopadhyay, K.; Mitra, J. Spatially Resolved Photoresponse on Individual ZnO Nanorods: Correlating Morphology, Defects and Conductivity. *Sci. Rep.* **2016**, *6* (1), 28468.

(195) Hsu, C. L.; Lin, Y. H.; Wang, L. K.; Hsueh, T. J.; Chang, S. P.; Chang, S. J. Tunable UV- and Visible-Light Photoresponse Based on P-ZnO Nanostructures/n-ZnO/Glass Peppered with Au Nanoparticles. *ACS Appl. Mater. Interfaces* **2017**, *9* (17), 14935–14944.

(196) Fan, Z.; Chang, P. C.; Lu, J. G.; Walter, E. C.; Penner, R. M.; Lin, C. H.; Lee, H. P. Photoluminescence and Polarized Photodetection of Single ZnO Nanowires. *Appl. Phys. Lett.* **2004**, *85* (25), 6128–6130.

(197) Kang, Y.; Nahm, H.-H.; Han, S. Light-Induced Peroxide Formation in ZnO: Origin of Persistent Photoconductivity. *Sci. Rep.* **2016**, *6* (1), 35148.

(198) Liu, L.; Zhao, H.; Andino, J. M.; Li, Y. Photocatalytic CO 2 Reduction with H 2 O on TiO 2 Nanocrystals: Comparison of Anatase, Rutile, and Brookite Polymorphs and Exploration of Surface Chemistry. *ACS Catal.* **2012**, *2* (8), 1817–1828.

(199) Vanheusden, K.; Warren, W. L.; Seager, C. H.; Tallant, D. R.; Voigt, J. A.; Gnade, B. E. Mechanisms behind Green Photoluminescence in ZnO Phosphor Powders. *J. Appl. Phys.* **1996**, *79* (10), 7983–7990.

(200) Wang, X. J.; Vlasenko, L. S.; Pearton, S. J.; Chen, W. M.; Buyanova, I. a. Oxygen and Zinc Vacancies in as-Grown ZnO Single Crystals. *J. Phys. D. Appl. Phys.* **2009**, *42* (17), 175411.

(201) Janotti, A.; Van De Walle, C. G. Oxygen Vacancies in ZnO. *Appl. Phys. Lett.* **2005**, *87* (12), 1–3.

(202) Giannakoudakis, D. A.; Arcibar-Orozco, J. A.; Bandosz, T. J. Key Role of Terminal Hydroxyl Groups and Visible Light in the Reactive Adsorption/catalytic Conversion of Mustard Gas Surrogate on Zinc (Hydr)oxides. *Appl. Catal. B Environ.* **2015**, *174–175* (2), 96–104.

(203) Kumar, S.; Sahare, P. D. Effects of Annealing on the Surface Defects of Zinc Oxide Nanoparticles. *Nano*. 2012, p 1250022.

(204) Hlaing Oo, W. M.; McCluskey, M. D.; Lalonde, A. D.; Norton, M. G. Infrared Spectroscopy of ZnO Nanoparticles Containing CO[sub 2] Impurities. *Appl. Phys. Lett.* **2005**, *86* (7), 73111.

(205) Mubeen, S.; Hernandez-Sosa, G.; Moses, D.; Lee, J.; Moskovits, M. Plasmonic Photosensitization of a Wide Band Gap Semiconductor: Converting Plasmons to Charge Carriers. *Nano Lett.* **2011**, *11* (12), 5548–5552.

(206) Zheng, B. Y.; Wang, Y.; Nordlander, P.; Halas, N. J. Color-Selective and CMOS-Compatible Photodetection Based on Aluminum Plasmonics. *Adv. Mater.* **2014**, *26* (36), 6318–6323.

(207) Boriskina, S. V.; Ghasemi, H.; Chen, G. Plasmonic Materials for Energy: From Physics to Applications. *Mater. Today* **2013**, *16* (10), 375–386.

(208) Dean, N. Colouring at the Nanoscale. *Nat. Nanotechnol.* **2015**, *10* (1), 15–16.

(209) Wu, X.; Centeno, A.; Zhang, X.; Darvill, D.; Ryan, M. P.; Riley, D. J.; Alford, N. M.; Xie, F. Broadband Plasmon Photocurrent Generation from Au Nanoparticles/

Mesoporous TiO2 Nanotube Electrodes. *Sol. Energy Mater. Sol. Cells* **2015**, *138*, 80–85.

(210) Li, X.; Zhu, J.; Wei, B. Hybrid Nanostructures of Metal/two-Dimensional Nanomaterials for Plasmon-Enhanced Applications. *Chem. Soc. Rev.* **2016**, *45*.

(211) Tian, Y.; Tatsuma, T. Plasmon-Induced Photoelectrochemistry at Metal Nanoparticles Supported on Nanoporous TiO2. *Chem. Commun.* **2004**, No. 16, 1810.

(212) Chan, G. H.; Zhao, J.; Hicks, E. M.; Schatz, G. C.; Van Duyne, R. P. Plasmonic Properties of Copper Nanoparticles Fabricated by Nanosphere Lithography. *Nano Lett. Nano Lett, Nano Lett* **2007**, *7* (7), 1947–1952.

(213) Fang, Z.; Zhu, X. Plasmonics in Nanostructures. *Adv. Mater.* **2013**, *25* (28), 3840–3856.

(214) Goykhman, I.; Desiatov, B.; Khurgin, J.; Shappir, J.; Levy, U. Locally-Oxidized Silicon Surface-Plasmon Schottky Detector for Telecom Wavelengths. In *8th IEEE International Conference on Group IV Photonics*; IEEE, 2011; pp 231–233.

(215) Nishijima, Y.; Ueno, K.; Yokota, Y.; Murakoshi, K.; Misawa, H. Plasmon-Assisted Photocurrent Generation from Visible to Near-Infrared Wavelength Using a Au-Nanorods/TiO 2 Electrode. *J. Phys. Chem. Lett.* **2010**, *1* (13), 2031–2036.

(216) Huang, L.; Tu, C.-C.; Lin, L. Y. Colloidal Quantum Dot Photodetectors Enhanced by Self-Assembled Plasmonic Nanoparticles. *Appl. Phys. Lett.* **2011**, *98* (11), 113110.

(217) García de Arquer, F. P.; Mihi, A.; Kufer, D.; Konstantatos, G. Photoelectric Energy Conversion of Plasmon-Generated Hot Carriers in Metal–Insulator–Semiconductor Structures. *ACS Nano* **2013**, *7* (4), 3581–3588.

(218) Pillai, S.; Green, M. A. Plasmonics for Photovoltaic Applications. *Sol. Energy Mater. Sol. Cells* **2010**, *94* (9), 1481–1486.

(219) Gan, Q.; Bartoli, F. J.; Kafafi, Z. H. Plasmonic-Enhanced Organic Photovoltaics: Breaking the 10% Efficiency Barrier. *Adv. Mater.* **2013**, *25* (17), 2385–2396.

(220) Flo Bullough. Nanotechnology http://blogs.egu.eu/network/4degrees/tag/nanotechnology/.

(221) Mie, G. Beiträge Zur Optik Trüber Medien, Speziell Kolloidaler Metallösungen. *Ann. Phys.* **1908**, *330* (3), 377–445.

(222) Jackson, J. D.; Fox, R. F. Classical Electrodynamics, 3rd Ed . *Am. J. Phys.* **1999**, *67* (9), 841–842.

(223) Fox, M. *Optical Properties of Solids,* Second Edi.; Oxford University Press.

(224) Maier, S. A. *Plasmonics: Fundamentals and Applications*; Springer US: Boston, MA, 2007.

(225) Larroulet, I. SPR: An Industrial Point of View. In *Introduction to Plasmonics*; Pan Stanford, 2015; pp 347–352.

(226) Langhammer, C.; Schwind, M.; Kasemo, B.; Zorić, I. Localized Surface Plasmon Resonances in Aluminum Nanodisks. *Nano Lett.* **2008**, *8* (5), 1461–1471.

(227) Olmon, R. L.; Slovick, B.; Johnson, T. W.; Shelton, D.; Oh, S.; Boreman, G. D.; Raschke, M. B. Optical Dielectric Function of Gold. *Phys. Rev. B* **2012**, *86* (23),

235147.

(228) March, A. Zur Elektronentheorie Der Metalle. *Ann. Phys.* **1916**, *354* (6), 710–724.

(229) Vial, A.; Grimault, A.-S.; Macías, D.; Barchiesi, D.; de la Chapelle, M. L. Improved Analytical Fit of Gold Dispersion: Application to the Modeling of Extinction Spectra with a Finite-Difference Time-Domain Method. *Phys. Rev. B* **2005**, *71* (8), 85416.

(230) Armelles, G.; Cebollada, A.; García-Martín, A.; González, M. U. Magnetoplasmonics: Combining Magnetic and Plasmonic Functionalities. *Adv. Opt. Mater.* **2013**, *1* (1), 2–2.

(231) Pitarke, J. M.; Silkin, V. M.; Chulkov, E. V.; Echenique, P. M. Theory of Surface Plasmons and Surface-Plasmon Polaritons. *Reports Prog. Phys.* **2007**, *70* (1), 1–87.

(232) Hertz, H. Ueber Einen Einfluss Des Ultravioletten Lichtes Auf Die Electrische Entladung. *Ann. Phys. Chem.* **1887**, *267*, 983–1000.

(233) Spicer, W. E. Photoemissive, Photoconductive, and Optical Absorption Studies of Alkali-Antimony Compounds. *Phys. Rev.* **1958**, *112* (1), 114–122.

(234) Sonnichsen, C.; Franzl, T.; Wilk, T.; von Plessen, G.; Feldmann, J.; Wilson, O.; Mulvaney, P. Drastic Reduction of Plasmon Damping in Gold Nanorods. *Phys. Rev. Lett.* **2002**, *88* (7), 77402.

(235) Li, J.; Cushing, S. K.; Meng, F.; Senty, T. R.; Bristow, A. D.; Wu, N. Plasmon-Induced Resonance Energy Transfer for Solar Energy Conversion. *Nat.*

Photonics **2015**, *9* (9), 601–607.

(236) Callahan, D. M.; Munday, J. N.; Atwater, H. A. Solar Cell Light Trapping beyond the Ray Optic Limit. *Nano Lett.* **2012**, *12* (1), 214–218.

(237) Cushing, S. K.; Wu, N. Progress and Perspectives of Plasmon-Enhanced Solar Energy Conversion. *J. Phys. Chem. Lett.* **2016**, *7* (4), 666–675.

(238) Cushing, S. K.; Li, J.; Bright, J.; Yost, B. T.; Zheng, P.; Bristow, A. D.; Wu, N. Controlling Plasmon-Induced Resonance Energy Transfer and Hot Electron Injection Processes in Metal@TiO 2 Core–Shell Nanoparticles. *J. Phys. Chem. C* **2015**, *119* (28), 16239–16244.

(239) Ng, C.; Cadusch, J. J.; Dligatch, S.; Roberts, A.; Davis, T. J.; Mulvaney, P.; Gómez, D. E. Hot Carrier Extraction with Plasmonic Broadband Absorbers. *ACS Nano* **2016**, *10* (4), 4704–4711.

(240) Liu, L.; Ouyang, S.; Ye, J. Gold-Nanorod-Photosensitized Titanium Dioxide with Wide-Range Visible-Light Harvesting Based on Localized Surface Plasmon Resonance. *Angew. Chemie Int. Ed.* **2013**, *52* (26), 6689–6693.

(241) Manjavacas, A.; Liu, J. G.; Kulkarni, V.; Nordlander, P. Plasmon-Induced Hot Carriers in Metallic Nanoparticles. *ACS Nano* **2014**, *8* (8), 7630–7638.

(242) Schuck, P. J. Nanoimaging: Hot Electrons Go through the Barrier. *Nat. Nanotechnol.* **2013**, *8* (11), 799–800.

(243) Knight, M. W.; Wang, Y.; Urban, A. S.; Sobhani, A.; Zheng, B. Y.; Nordlander, P.; Halas, N. J. Embedding Plasmonic Nanostructure Diodes Enhances Hot Electron Emission. *Nano Lett.* **2013**, *13* (4), 1687–1692.

(244) Zheng, B. Y.; Zhao, H.; Manjavacas, A.; McClain, M.; Nordlander, P.; Halas, N. J. Distinguishing between Plasmon-Induced and Photoexcited Carriers in a Device Geometry. *Nat. Commun.* **2015**, *6*, 7797.

(245) D.W. Peters. An Infrared Detector Utilizing Internal Photoemission. *Proc. IEEE* **1967**, *55* (5), 704–705.

(246) Zhao, G.; Kozuka, H.; Yoko, T. Sol—gel Preparation and Photoelectrochemical Properties of TiO2 Films Containing Au and Ag Metal Particles. *Thin Solid Films* **1996**, *277* (1–2), 147–154.

(247) Tian, Y.; Tatsuma, T. Mechanisms and Applications of Plasmon-Induced Charge Separation at TiO 2 Films Loaded with Gold Nanoparticles. *J. Am. Chem. Soc.* **2005**, *127* (20), 7632–7637.

(248) Bigot, J.-Y.; Halté, V.; Merle, J.-C.; Daunois, A. Electron Dynamics in Metallic Nanoparticles. *Chem. Phys.* **2000**, *251* (1–3), 181–203.

(249) Furube, A.; Du, L.; Hara, K.; Katoh, R.; Tachiya, M. Ultrafast Plasmon-Induced Electron Transfer from Gold Nanodots into TiO 2 Nanoparticles. *J. Am. Chem. Soc.* **2007**, *129* (48), 14852–14853.

(250) Barman, T.; Hussain, A. A.; Sharma, B.; Pal, A. R. Plasmonic Hot Hole Generation by Interband Transition in Gold-Polyaniline. *Sci. Rep.* **2016**, *5* (1), 18276.

(251) Jia, R.; Zhao, D.; Gao, N.; Liu, D. Polarization Enhanced Charge Transfer: Dual-Band GaN-Based Plasmonic Photodetector. *Sci. Rep.* **2017**, *7* (1), 40483.

(252) Lee, Y. K.; Jung, C. H.; Park, J.; Seo, H.; Somorjai, G. A.; Park, J. Y. Surface

Plasmon-Driven Hot Electron Flow Probed with Metal-Semiconductor Nanodiodes. *Nano Lett.* **2011**, *11* (10), 4251–4255.

(253) Goykhman, I.; Desiatov, B.; Khurgin, J.; Shappir, J.; Levy, U. Waveguide Based Compact Silicon Schottky Photodetector with Enhanced Responsivity in the Telecom Spectral Band. *Opt. Express* **2012**, *20* (27), 28594.

(254) Giugni, a; Torre, B.; Toma, A.; Francardi, M.; Malerba, M.; Alabastri, A.; Proietti Zaccaria, R.; Stockman, M. I.; Di Fabrizio, E. Hot-Electron Nanoscopy Using Adiabatic Compression of Surface Plasmons. *Nat. Nanotechnol.* **2013**, *8* (11), 845–852.

(255) Knight, M. W.; Sobhani, H.; Nordlander, P.; Halas, N. J. Photodetection with Active Optical Antennas. *Science (80-.).* **2011**, *332* (6030), 702–704.

(256) Sobhani, A.; Knight, M. W.; Wang, Y.; Zheng, B.; King, N. S.; Brown, L. V.; Fang, Z.; Nordlander, P.; Halas, N. J. Narrowband Photodetection in the near-Infrared with a Plasmon-Induced Hot Electron Device. *Nat. Commun.* **2013**, *4*, 1643.

(257) Wenyi Wang, Andrey Klots, Dhiraj Prasai, Yuanmu Yang, Kirill I. Bolotin, and J. V. Hot Electron-Based Near-Infrared Photodetection Using Bilayer MoS 2anmu Yang, Kirill I. Bolotin, and Jason Valentine. *Nano Lett.* **2015**, *15* (11), 7440–7444.

(258) Andrea Pescaglini, Alfonso Martín, Davide Cammi, Gediminas Juska, Carsten Ronning, E. P.; and Daniela Iacopino. Hot-Electron Injection in Au Nanorod–ZnO Nanowire Hybrid Device for Near-Infrared Photodetection. *Nano Lett.* **2014**, *14* (11), 6202–6209.

(259) Nazirzadeh, M. A.; Atar, F. B.; Turgut, B. B.; Okyay, A. K. Random Sized Plasmonic Nanoantennas on Silicon for Low-Cost Broad-Band near-Infrared Photodetection. *Sci. Rep.* **2015**, *4* (1), 7103.

(260) Sessolo, M.; Bolink, H. J. Hybrid Organic-Inorganic Light-Emitting Diodes. *Adv. Mater.* **2011**, *23* (16), 1829–1845.

(261) Lin, P.; Yan, X.; Zhang, Z.; Shen, Y.; Zhao, Y.; Bai, Z.; Zhang, Y. Self-Powered UV Photosensor Based on PEDOT:PSS/ZnO Micro/Nanowire with Strain-Modulated Photoresponse. *ACS Appl. Mater. Interfaces* **2013**, *5* (9), 3671–3676.

(262) Gaspar, D.; Pimentel, A. C.; Mateus, T.; Leitão, J. P.; Soares, J.; Falcão, B. P.; Araújo, A.; Vicente, A.; Filonovich, S. A.; Águas, H.; Martins, R.; Ferreira, I. Influence of the Layer Thickness in Plasmonic Gold Nanoparticles Produced by Thermal Evaporation. *Sci. Rep.* **2013**, *3* (1), 1469.

(263) Serrano, A.; De La Fuente, O. R.; García, M. A. Extended and Localized Surface Plasmons in Annealed Au Films on Glass Substrates. *J. Appl. Phys.* **2010**, *108* (7).

(264) Piscopiello, E.; Tapfer, L.; Antisari, M. V.; Paiano, P.; Prete, P.; Lovergine, N. Formation of Epitaxial Gold Nanoislands on (100) Silicon. *Phys. Rev. B* **2008**, *78* (3), 35305.

(265) Szunerits, S.; Praig, V. G.; Manesse, M.; Boukherroub, R. Gold Island Films on Indium Tin Oxide for Localized Surface Plasmon Sensing. *Nanotechnology* **2008**, *19* (19), 195712.

(266) Andersson, T. G. The Initial Growth of Vapour Deposited Gold Films. *Gold Bull.* **1982**, *15* (1), 7–18.

(267) Wei, H.; Xu, H. Plasmonics in Composite Nanostructures. *Mater. Today* **2014**, *17* (8), 372–380.

(268) Crowell, C. R.; Sze, S. M. Ballistic Mean Free Path Measurements of Hot Electrons in Au Films. *Phys. Rev. Lett.* **1965**, *15* (16), 659–661.

(269) Johnson, P. B.; Christy, R. W. Optical Constants of the Noble Metals. *Phys. Rev. B* **1972**, *6* (12), 4370–4379.

(270) Leosson, K.; Ingason, A. S.; Agnarsson, B.; Kossoy, A.; Olafsson, S.; Gather, M. C. Ultra-Thin Gold Films on Transparent Polymers. *Nanophotonics* **2013**, *2* (1), 3–11.

(271) Chen, H.; Liu, G.; Wang, L. Switched Photocurrent Direction in Au/TiO2 Bilayer Thin Films. *Sci. Rep.* **2015**, *5* (1), 10852.

(272) Atwater, H. A.; Polman, A. Plasmonics for Improved Photovoltaic Devices. *Nat. Mater.* **2010**, *9* (10), 865–865.

(273) Bano, N.; Zaman, S.; Zainelabdin, A.; Hussain, S.; Hussain, I.; Nur, O.; Willander, M. ZnO-Organic Hybrid White Light Emitting Diodes Grown on Flexible Plastic Using Low Temperature Aqueous Chemical Method. *J. Appl. Phys.* **2010**, *108* (4), 1–6.

(274) Dhananjay; Nagaraju, J.; Krupanidhi, S. B. Investigations on Magnetron Sputtered ZnO Thin Films and Au/ZnO Schottky Diodes. *Phys. B Condens. Matter* **2007**, *391* (2), 344–349.

(275) Sarritzu, V.; Sestu, N.; Marongiu, D.; Chang, X.; Masi, S.; Rizzo, A.; Colella, S.; Quochi, F.; Saba, M.; Mura, A.; Bongiovanni, G. Optical Determination of

Shockley-Read-Hall and Interface Recombination Currents in Hybrid Perovskites. *Sci. Rep.* **2017**, *7* (February), 44629.

(276) Xu, J.; Schubert, M. F.; Noemaun, A. N.; Zhu, D.; Kim, J. K.; Schubert, E. F.; Kim, M. H.; Chung, H. J.; Yoon, S.; Sone, C.; Park, Y. Reduction in Efficiency Droop, Forward Voltage, Ideality Factor, and Wavelength Shift in Polarization-Matched GaInN/GaInN Multi-Quantum-Well Light-Emitting Diodes. *Appl. Phys. Lett.* **2009**, *94* (1), 92–95.

(277) Lee, H.; Lee, Y. K.; Hwang, E.; Park, J. Y. Enhanced Surface Plasmon Effect of Ag/TiO 2 Nanodiodes on Internal Photoemission. *J. Phys. Chem. C* **2014**, *118* (11), 5650–5656.

(278) Lisowski, M.; Loukakos, P. A.; Bovensiepen, U.; Stahler, J.; Gahl, C.; Wolf, M. Ultra-Fast Dynamics of Electron Thermalization, Cooling and Transport Effects in Ru(001). *Appl. Phys. A Mater. Sci. Process.* **2004**, *78* (2), 165–176.

(279) Clavero, C. Plasmon-Induced Hot-Electron Generation at Nanoparticle/metal-Oxide Interfaces for Photovoltaic and Photocatalytic Devices. *Nat. Photonics* **2014**, *8* (2), 95–103.

(280) J. G. Endriz and W. E. Spicer. Surface-Plasmon-One-Electron Decay and Its Observation in Photoemission. *Phys. Rev. Lett. 24* (2).

(281) Hwang, J. D.; Wang, F. H.; Kung, C. Y.; Lai, M. J.; Chan, M. C. Annealing Effects of Au Nanoparticles on the Surface-Plasmon Enhanced P-Si/n-ZnO Nanorods Heterojunction Photodetectors. *J. Appl. Phys.* **2014**, *115* (17), 173110.

(282) Wu, K.; Chen, J.; McBride, J. R.; Lian, T. Efficient Hot-Electron Transfer by a Plasmon-Induced Interfacial Charge-Transfer Transition. *Science (80-.).* **2015**,

349 (6248), 632–635.

(283) Choi, H.; Kim, B.; Ko, M. J.; Lee, D.-K.; Kim, H.; Kim, S. H.; Kim, K. Solution Processed WO3 Layer for the Replacement of PEDOT:PSS Layer in Organic Photovoltaic Cells. *Org. Electron.* **2012**, *13* (6), 959–968.

(284) Mukherjee, S.; Zhou, L.; Goodman, A. M.; Large, N.; Ayala-Orozco, C.; Zhang, Y.; Nordlander, P.; Halas, N. J. Hot-Electron-Induced Dissociation of H 2 on Gold Nanoparticles Supported on SiO 2. *J. Am. Chem. Soc.* **2014**, *136* (1), 64–67.

(285) Kong, X.-T.; Wang, Z.; Govorov, A. O. Plasmonic Nanostars with Hot Spots for Efficient Generation of Hot Electrons under Solar Illumination. *Adv. Opt. Mater.* **2017**, *5* (15).

(286) Besteiro, L. V.; Govorov, A. O. Amplified Generation of Hot Electrons and Quantum Surface Effects in Nanoparticle Dimers with Plasmonic Hot Spots. *J. Phys. Chem. C* **2016**, *120* (34), 19329–19339.

(287) Zhang, H.; Govorov, A. O. Optical Generation of Hot Plasmonic Carriers in Metal Nanocrystals: The Effects of Shape and Field Enhancement. *J. Phys. Chem. C* **2014**, *118* (14), 7606–7614.

(288) Ma, X.-C.; Dai, Y.; Yu, L.; Huang, B.-B. Energy Transfer in Plasmonic Photocatalytic Composites. *Light Sci. Appl.* **2016**, *5* (April 2015), e16017.

(289) McCafferty, E.; Zettlemoyer, A. C. Adsorption of Water Vapour on α-Fe2O3. *Discuss. Faraday Soc.* **1971**, *52*, 239–254.

(290) FILMETRICS http://www.filmetrics.com/reflectance-calculator?wmin=200&wmax=1000&wstep=1&units=um&mmat=Au&smat=Si

O2&sptype=r.

(291) Girard-desprolet, R. Plasmon-Based Spectral Filtering with Metallic Nanostructures for CMOS Image Sensors, Universit´ e Grenoble Alpes, 2015.

(292) Willets, K. A.; Van Duyne, R. P. Localized Surface Plasmon Resonance Spectroscopy and Sensing. *Annu. Rev. Phys. Chem.* **2007**, *58* (1), 267–297.